First Principles Investigation of SrTiO$_3$ - NdNiO$_3$ Interfaces

LIONE, ALEXANDER,CHARLES

How to cite:

LIONE, ALEXANDER,CHARLES (2025) *First Principles Investigation of SrTiO$_3$ - NdNiO$_3$ Interfaces*, Durham theses, Durham University. Available at Durham E-Theses Online: http://etheses.dur.ac.uk/16104/

First Principles Investigation of $SrTiO_3$ - $NdNiO_3$ Interfaces

Alexander Lione

Supervisors: Dr. Nicholas Bristowe and Prof. Stewart Clark

ABO_3 perovskites are a popular playground for both fundamental and applied research due to their rich variety of structural and magnetic phase transitions. These properties can be manipulated by interfacing different perovskite systems, where effects like epitaxial strain, mode decay, quantum confinement, magnetic frustration, and polar discontinuities emerge. In this study, we investigate the behaviour of $SrTiO_3$ (STO) and $NdNiO_3$ (NNO), two perovskites exhibiting important prototypical phase transitions with decreasing temperature that can be influenced by interfacial effects. STO is a quantum paraelectric in bulk, but becomes ferroelectric under strain, while NNO undergoes a metal-insulator transition (MIT) with decreasing temperature that can also be controlled with strain.

Using first principles calculations based on density functional theory, we first determine how each material responds to strain in both [001]- and [111]-oriented systems. We demonstrate that strain can induce ferroelectricity in STO and modulate the MIT in NNO in either orientation.

We then build and analyse [001]-oriented NNO-STO interfaced systems, where we observe surprisingly large differences in the STO band offsets depending on the interface termination, even when NNO is metallic and STO paraelectric. In a stoichiometric system, this leads to a sizeable field across STO, which amplifies and pins the polarisation in one direction. We also observe complex polar behaviour in both STO and NNO near the interfaces.

Finally, we explore [111]-oriented interfaced systems of NNO and a wide range of substrates, discovering an unexpected polar discontinuity that arises from charge-ordering. This discontinuity offers a new mechanism for ferroelectricity via charge transfer, and combined with other interfacial effects, can result in the pinning of the breathing mode (which we propose amplifies the MIT temperature), the creation of two distinct types of two-dimensional electron gas, and the emergence of polar-metal phases.

First Principles Investigation of $SrTiO_3$ - $NdNiO_3$ Interfaces

Alexander Lione

A Thesis presented for the degree of
Doctor of Philosophy

Department of Physics
Durham University
United Kingdom
2025

Contents

Declaration

The work in this thesis is based on research carried out at the Department of Physics, Durham University, United Kingdom. No part of this thesis has been submitted elsewhere for any other degree or qualification and it is all my own work unless referenced to the contrary in the text.

Acknowledgements

I have no doubts that the work presented in this thesis would not have been completed without the assistance and support I receieved from the following people. I first thank my supervisor Nick Bristowe for his unending assistance throughout the project, without-whom I can be sure the last three and a half years would not have been productive. From the first days of the project to the last, Nick has replied without fail to my endless teams messages proposing new ideas (many of which I would quickly realise were nonsensical). I would next like to thank research collaborators Evgenios Stylianidis, Pavlo Zubko and Jorge Iñiguez-González for the many useful discussions on the topics mentioned in this thesis. Thirdly, I would like to thank the rest of the Bristowe group with whom I have shared an office over the course of this PhD for the technical support and good conversation (which perhaps wasn't always on-topic): Cameron Scott, Urmimala Dey, Paul Dirk, and Pierre-Louis Peuch. I also thank Durham University for providing access to the Hamilton8 and Bede supercomputers, through which all of the calculations in this study were undertaken, and the engineering and physical sciences research council (EPSRC) for funding the project. Lastly, I would like to thank my parents and grandparents for their support throughout and for suggesting I undertake this PhD in the first place.

CHAPTER 1

Introduction

The modern age is often coined the 'information era', due to rapid improvements in communication, and a world economy increasingly based on information technology. The primary cause of this is the rapidly-evolving electronics industry, where essential electrical components such as the transistor, diode and optical amplifier are now orders-of-magnitude smaller, more efficient and cost-effective than decades ago. In turn, we have been able to create increasingly powerful machines for communication, computation and sensing. Perhaps the most important change of all is the evolution of memory devices— electronic components that store information, usually in the form of a binary on- or off-state. The most well-known memory component is the simple FET (field-effect transistor), the building block of every electronic device. Since the 1970s, the number of transistors in an integrated circuit has doubled approximately every two years, due to the development of smaller, more-efficient, and less-volatile devices [1]. As FETs and other electronic devices have shrunk in size, we have approached the realm of the nanometer, where quantum phenomena dominate the properties of the system [2, 3]. Though increasingly complex and challenging to understand, this opens the door to a new realm of possibilities, not only for developing existing electronic devices, but also proposing new ones. As theoretical condensed matter physicists, we are tasked with the exciting journey of understanding this new realm. With high-performance computational resources available, we now have the possibility to investigate nanoscale systems from first principles, with accurate simulation of quantum-mechanical effects. Alongside the rapid development of experimental techniques, the coming decades promise an exciting journey for new discoveries in the realm of quantum materials and devices, and in-turn the electronics industry as a whole.

In the first chapter of this study, we provide a technical introduction to nanoscale systems— specifically those built from ABO_3 perovskites, a fascinating group of materials with a vast range of properties and applications. This is followed by a literature review of two particularly compelling members of this family: $SrTiO_3$ and $NdNiO_3$. These two materials have exhibited ferroelectric and metal-insulator transitions respectively— properties that have garnered interest for applications in memory and sensing devices. We then explore the physics of perovskite interfaces, where additional effects come into play that can further manipulate the properties of materials. Finally, we review various heterostructures and devices consisting of $SrTiO_3$ and $NdNiO_3$, where we highlight interesting behaviour and unanswered questions surrounding each material. In the hopes of uncovering interesting new phenomena, we propose to study how $SrTiO_3$ and $NdNiO_3$ respond to various interfacial effects, and interact with each other when interfaced together. This is with the aim of broadening our understanding of how these two materials (and any related) act in device-like environments, in the hopes of inspiring new technology. Our study objectives are summarised at the end of the chapter.

1.1 ABO_3 perovskites: theory and applications

Complex oxides undoubtedly remain the most popular avenue for discovering novel electronic devices. The simple ABO_3 perovskite is perhaps the staple of the complex oxides, where the smaller B cation lies at the centre of six O anions forming an octahedra, and the larger A cation lies between twelve O anions, such that the A—O bond lengths are approximately $\sqrt{2}$ times larger than the B—O bond lengths.

The simple cubic perovskite structure may be visualised in Fig. 1.1(a). The stability of a given combination of A and B cations may be estimated using the Goldschmidt tolerance factor t [4]:

$$t = \frac{r_A + r_{\mathrm{O}}}{\sqrt{2}(r_B + r_{\mathrm{O}})}, \tag{1.1}$$

(where $r_{A,B,\mathrm{O}}$ are the Shannon ionic radii [5] of A, B, and O respectively). The 'ideal' A and B radii yield a t of 1, where the system typically appears cubic. When $t > 1$ or < 1, the perovskite is prone to structural distortions. This is a generalisation, as many exceptions to this rule exist.

A high-symmetry, simple-cubic perovskite is extremely rare at room temperature or below. Subtle structural displacements occur which often lead to dramatic changes in the macroscopic properties of the crystal. The cause of these distortions, as well as their magnitude, is a complex question to answer, and typically depends on a variety of factors. Some common perovskite distortions are shown in Fig. 1.1(b)—(g), and are discussed in more detail over the next few sections of this chapter.

Understanding these distortions is essential for this project, so it is important to define a rigorous, first-principles classification system for the orientation of ions in a crystal. This can be achieved with symmetry analysis. A bulk crystal can be expressed more simply as a unit cell repeating infinitely along the crystallographic axes (the system can be described as having periodic boundary conditions (PBC)). The unit cell contains all the information about the structure of the bulk crystal excluding edges and surfaces. It can be described by a set of three lattice vectors $\mathbf{a}, \mathbf{b}, \mathbf{c}$ (the magnitude of which are the cell lattice parameters), and the ionic coordinates written in terms of these vectors. The unit cell is assigned a space group—a mathematical group of all the symmetry operations that leave it unchanged. The elements (symmetry operations) of a space group include all point group symmetries (identity, rotation, reflection, inversion, improper rotation), as well as translation, screw axis and glide plane operations. There are 219 distinct space groups, where bulk perovskites range from the highest symmetry simple cubic $Pm\bar{3}m$ to the lowest symmetry $P1$ (international short symbol notation). A space-group representation is a structure-preserving mapping of the symmetry elements onto a vector space.

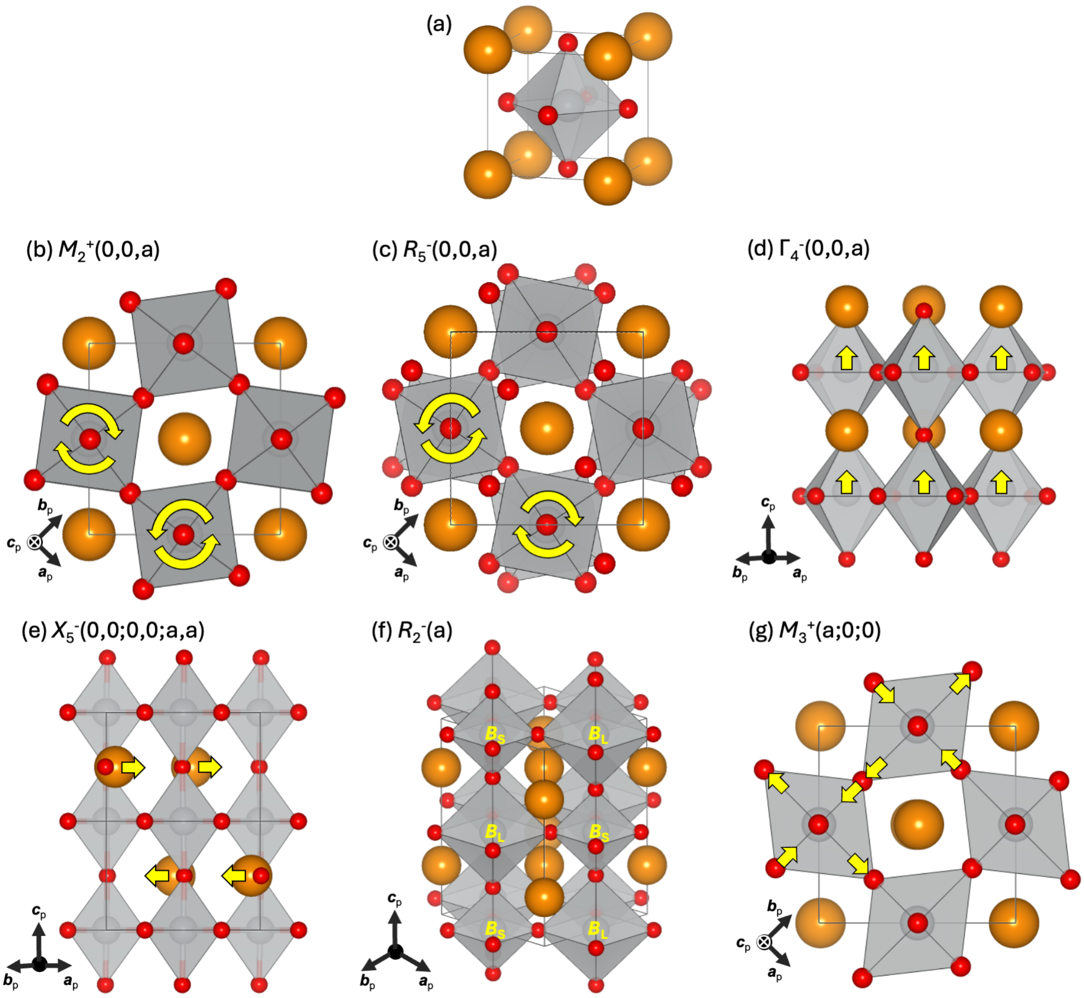

Figure 1.1: a) Simple cubic $Pm\bar{3}m$ perovskite unit cell, where gold spheres denote the A-site cations, grey spheres within octahedra denote the B-site cations, and red spheres denote oxygen anions. (b)—(g) Common perovskite distortions visualised in a $\sqrt{2} \times \sqrt{2} \times 2$ unit cell. In order from (b)—(g): in-phase octahedral tilting, out-of-phase octahedral tilting, B-site polar motion, A-site antipolar motion, breathing distortion ($B_{\mathrm{L,S}}$ denote large and small $B\mathrm{O}_6$ octahedra respectively), and Jahn-Teller distortion.

For a given vector space, the representation can be made irreducible— meaning it cannot be written as a linear combination of other irreducible representations (irreps) in the group. Structural distortions can be described by ions moving along a set of vectors, which together form a vector space. For a distortion allowed by a space group, this vector space corresponds to one of its irreps. Each irrep thus describes a specific type of allowed ionic distortion [6–8].

To more conveniently define ionic distortions, we consider our crystal unit cell in reciprocal space (k-space). In reciprocal space, the primitive cell becomes the 1st Brillouin Zone (1BZ)— the smallest cell in reciprocal space retaining all the structural properties. The three lattice vectors $\mathbf{a}, \mathbf{b}, \mathbf{c}$ are converted to reciprocal lattice vectors $\mathbf{a}_k, \mathbf{b}_k, \mathbf{c}_k$, where $\mathbf{a}_k = 2\pi \frac{\mathbf{b}\times\mathbf{c}}{\mathbf{a}\cdot\mathbf{b}\times\mathbf{c}}$ and $\mathbf{b}_k, \mathbf{c}_k$ are cyclic permutations of the indices. In reciprocal space, we consider ionic distortions by looking at the phonons— collective vibrations of ions in a crystal. If the frequency of a phonon mode oscillation is zero or imaginary (the square of its frequency is less than zero), then there is no restoring force for that vibration, meaning that the collective movement along these axes of vibration reduces the energy of the system, and the mode of distortion condenses. A mode of distortion can be defined by the high-symmetry point in the 1BZ that remains invariant under the distortion. Within the 1BZ there are various high-symmetry points depending on the cell symmetry— we define modes with respect to the high symmetry points of the simple cubic $Pm\bar{3}m$ perovskite unit cell[1]. We label the distortions of perovskites using Miller and Love's notation, which consists of the k-point corresponding to the mode, followed by a numeral subscript and possibly a '+' or '-' superscript [7], which indicates whether the distortion modes are even or odd under inversion. For example, the antiphase tilt mode is denoted by the symbol R_5^- (Fig. 1.1(c)). These are also known as irrep labels. Irrep labels for perovskites also depend on the way the unit cell is drawn— the labels change depending on whether A- or B-cations lie in the corners, as the high symmetry k-points change. For this study, we use the former orientation, with A-sites lying at the corners, as depicted in 1.1(a). The irrep labels of various common distortions

---

[1] The high symmetry points are defined differently for lower symmetry cells (besides the Γ-point, which always lies at the centre).

for this orientation are included in Fig. 1.1(b)—(g). A more detailed explanation on the perovskite irreps can be found in refs. [9–11]. We also note the direction of a distortion (known as the order parameter direction) using Mulliken symbols. Commas separate the separate cartesian components of the irrep, while semicolons separate different atoms occupying the Wyckoff positions in the structure [12]. For example, $R_5^-(0,0,a)$ denotes the anti-phase tilt mode along only the **c** axis (Fig.1.1 (c)), while $X_5^-(0,0;0,0;a,a)$ denotes the antipolar motion of the A-site cation along both **a** and **b** axes (Fig.1.1 (e)). Mulliken notations for other common perovskite distortions may be found in refs. [9–11]. Octahedral tilting can also be denoted in a more concise form using Glazer notation, where the tilt pattern along each dimension a, b, c is either in-phase (superscript '+'), anti-phase (superscript '-'), or non-tilted (superscript '0') [13]. For example, an orthorhombic tilt pattern with two anti-phase tilts of equal magnitude along two axes and an in-phase tilt pattern along the third axis is denoted as $a^-a^-c^+$. Using mode irrep analysis we can also define the magnitude of a given distortion by comparing the structure to a reference high-symmetry cell ($Pm\bar{3}m$ for perovskites). For large interfaced systems where structural distortions vary throughout the system (such that mode irrep analysis is inappropriate), we measure structural quantities layer-by-layer (where possible). Details on both procedures are discussed in the methods chapter.

In this section we have summarised a general approach for understanding the structure of perovskites. In the following sections of this chapter, we go into the details of the key perovskite distortions relevant to this project, discussing why they occur in the first place, the macroscopic consequences of them, and how they interact with each other. Generally speaking, to answer why they occur, we look to the electronic structure of the system. Thousands of different combinations of ions can be used to build stable perovskites, each with a distinct electronic structure giving rise to unique structural and electronic properties. These features often accompany a useful change in the macroscopic properties of a perovskite. Fundamentally, our goal is to discover new structural phases with useful macroscopic properties, understand why they occur, and use this knowledge to predict the appearance of these features in other systems. In this study, we are concerned primarily with two well known phenomena found in perovskites— ferroelectricity and metal-insulator transitions. These are best explained after first discussing octahedral tilting, the most common distortion in perovskites, which is heavily linked to these two effects.

1.1.1 Octahedral tilting

Schematics of in-phase and antiphase tilting are depicted in Fig. 1.1(b) and (c) respectively. Perovskites with a tolerance factor $t < 1$ often undergo tilting to 'fill the space' left by the undersized A-cation [14, 15]. The choice of tilt pattern is only indirectly related to t, though several general trends can still be identified. For systems with t slightly below 1 ($\sim$0.95), antiphase tilting often appears by itself along one ($a^0a^0c^-$) or two ($a^-a^-c^0$) axes, while for lower t ($\sim$0.9) orthorhombic tilt patterns consisting of two antiphase and one in-phase tilt ($a^-a^-c^+$) tend to appear. The latter tilt-pattern is particularly common as it can further lower the energy by allowing for the 'antipolar' A-site distortion [16]. This distortion is depicted in Fig. 1.1(e) and consists of diagonal A-site motion along the $\hat{a}_\mathrm{p} + \hat{b}_\mathrm{p}$ direction (where the in-phase tilt lies along $\hat{c}_\mathrm{p}$ direction). If t is lowered further, a rhombohedral phase can also appear, which consists of antiphase tilting along all three primitive directions ($a^-a^-a^-$), which further fills the excess space. When $t > 1$ (corresponding to an undersized B-cation), tilting is less common, and the 'excess space' is usually instead filled by B-site displacement. Tilting is also often heavily coupled with other crystal distortions, and can be the determining factor behind various phenomena appearing or not. It is worth being clear at this point about the limitations of the tolerance factor— it is an approximation based off ionic radii which are not well defined. The Shannon radii referred to above are derived approximately by measuring the bond lengths of various crystals. Regardless, the tolerance factor is a convenient approximation for introducing and explaining the trends of common perovskite distortions, while avoiding the details of the electronic structure in each case.

Structural phase transitions such as tilting may be modeled quantitatively with Landau theory— a phenomenological 'second-principles' framework for understanding phase transitions. In this model, the Landau free energy $\mathcal{F}$ is expressed as a power series in order parameters λ_i, each of which characterises a phase transition [17]. This includes symmetry breaking distortions we have quantified with mode irrep amplitudes. As an example, we can apply this model to a simple bulk system with a single distortion such as antiphase tilting λ_R:

$$\mathcal{F} = \alpha_R \lambda_R^2 + \beta_R \lambda_R^4 + \gamma_R \lambda_R^6 + ..., \tag{1.2}$$

where $\alpha_R, \beta_R, \gamma_R$ are coefficients that determine how the distortion affects the energy landscape. The allowed terms in the expansion are constrained by the symmetry of the (high symmetry) parent cell (the allowed terms can be determined via invariance analysis, which is discussed in the methods chapter). Note that in this case the odd-order terms (linear, cubic powers) have been automatically omitted from the expansion, because tilting is energetically symmetric upon changing the amplitude from $\lambda_R \rightarrow -\lambda_R$ in an ideal bulk system. The behaviour of this system in response to tilting then depends on the signs and magnitudes of $\alpha_R, \beta_R, \gamma_R$. The quadratic term determines the onset of the mode— if $\alpha_R < 0$ then tilting will develop spontaneously. If the quartic coefficient $\beta_R > 0$, λ_R is a second-order (continuous) phase transition, such that the onset of the mode gradually lowers the energy up to the minima a. If $\beta_R < 0$, and $\gamma_R > 0$, the transition is first order (discontinuous), such that there are minima for $\lambda_R = 0$ and $\lambda_R = a$, and the system must 'jump' from one to the other as to navigate the energy discontinuity. Higher order terms can also further characterise the behaviour, but are usually insignificant and negligible. In our basic bulk system only with octahedral tilting in one axis, a second-order transition is allowed by symmetry, but often there are many other features that make the transition first-order. Usually there are several other order parameters, such as coupling to other modes or strain. In these scenarios, the free energy is not only expanded in terms of each order parameter, but also in terms of the coupling terms between different order parameters. Analysing complex systems allows us to quantify how modes influence one-another. We discuss mode couplings in detail when investigating specific examples relevant to the project in the following subsections.

1.2 Ferroelectricity

The idea of a dielectric material has been well understood since the 18th century as an insulator that can be polarised by applying an electric field. A material is electrically polarised if there is a net displacement of positive bound charges relative to negative bound charges. Since then, we have uncovered other mechanisms for inducing polarisation besides an electric field, including heat (pyroelectricity) and mechanical stress (piezoelectricity). In the 1920s, perhaps the most groundbreaking type of polarised material was discovered— the ferroelectric. A ferroelectric is a material with a spontaneous and reversible polarisation. Ferroelectricity was first discovered in Rochelle salt [18], but in the decades since we have discovered ferroelectric phases in a vast range of materials. In the 1940s, $BaTiO_3$ became the first perovskite discovered to have this property [19, 20], though many more have been found since. To this day, the search for ferroelectric phases in perovskites continues.

Ferroelectricity is an extremely useful property that can be utilised in various devices. Ferroelectrics have a polar switching path that typically resembles a hysteresis loop, such that when the polarisation direction is reversed by an electric field (or another change in environment), the system can remain in that state after removing the applied field. Therefore, a ferroelectric may exist in two distinguishable states under the same conditions. Therefore, any ferroelectric is a suitable candidate for memory devices [21, 22]. The most primitive ferroelectric-based memory device is the ferroelectric capacitor, consisting of a ferroelectric sandwiched between two electrodes [23]. This system has been investigated extensively both experimentally and theoretically, and is covered in more detail when discussing interfaces later in this chapter. Other devices that have been built from ferroelectrics include field effect transistors (FETs) [24, 25], tunneling transistors [26], and Schottky junctions [27]. Ferroelectric perovskites might be particularly excellent for device applications, as they can be (relatively easily) interfaced with a wide range of other perovskites.

Fundamentally, a crystal can only be spontaneously polarised if its structure breaks inversion symmetry, and is a ferroelectric only if this polarisation is reversible. In the present day, we have discovered numerous structural and electronic pathways through which a perovskite can be a ferroelectric. The most common and relevant to this study is a net displacement of A- or B-cations (or both) relative to the oxygen anions. This type of displacement is visualised in Fig. 1.1(e), and is referred to as the polar mode in perovskites. The origin of the polar mode in perovskites has been a topic of upmost importance over recent decades. The underlying electronic driving force of the polar mode is system-dependent, but detailed explanations exist for the titanate series, consisting of the most well-known ferroelectric perovskites $BaTiO_3$ and $PbTiO_3$. The key feature of the titanates is how the unoccupied $3d$ orbitals of the Ti^{4+} sites interact within the oxygen octahedra of the perovskite. In $BaTiO_3$ and $PbTiO_3$, ferroelectricity appears as a result of hybridisation between the unoccupied Ti-$3d^0$ and occupied O-$2p$ orbitals. As the O-$2p$ orbitals are oriented toward the B-cations (which are repulsive and therefore energetically unfavourable), and the unoccupied d_{xy}, d_{yz}, d_{xz} orbital lobes lie between the oxygen sites, the hybridisation of O-$2p$ with d_{xy}, d_{yz}, d_{xz} reduces the short range Coulomb repulsion between Ti and the octahedra. As a result of this, the polar distortion is softened, as the Ti cation is increasingly able to displace towards the O-sites [28]. This feature is also known as the second-order Jahn-Teller effect [29].

However, the appearance of polar modes in the titanate series is still dependent on additional factors. The first of these is the competition with octahedral tilting. For systems with smaller tolerance factors, octahedral tilting can ‘fill the space’ left by the smaller A-site radius[2] [30, 32]. Since tilting is ubiquitous in perovskites, there are only a small number of perovskite ferroelectrics. This is also the case for orthorhombic tilt patterns, which condense for lower tolerance factors ($\sim$0.9). Because of the coupled antipolar motion that appears with the A-sites, net polar motion is naturally suppressed [16]. In the titanate series, $BaTiO_3$ and $PbTiO_3$ overcome tilting due to the size and shape of the A-sites. The polarisation is largest in $PbTiO_3$ because of the lone $6s^2$ orbital in Pb, which aligns along the direction of polarisation, increasing the tetragonality of the cell and further softening the Coulomb repulsion between Ti and oxygen sites [28]. Ba also has a sufficiently large

---

[2] On a side note, it has alternatively been shown that extremely large amounts of antiphase tilting in certain perovskites can actually cooperate with the polar mode, due to the huge increase in tetragonality [30, 31]. Generally however, tilt suppresses ferroelectricity.

ionic radius such that ferroelectricity occurs.

1.2.1 $\mathbf{SrTiO_3}$

However, with other choices of A-site cation, the system remains unable to turn polar. Sr is less chemically active than Ba and Pb, such that any Ti-d and O-2p hybridisation is not sufficient to induce a polar mode in bulk. This is contrary to predictions, as studies have shown that decreasing the tolerance factor actually increases the polar instability [16]. The reason for this is instead the increased stability of the tilting with decreasing t. In Strontium Titanate $SrTiO_3$ (STO), the tolerance factor is just small enough that octahedral tilting stabilises (along one axis) rather than the polar mode. The polar mode is suppressed as the tilting reduces the overlap between Ti-3d and O-2p orbitals preventing hybridisation. The tilt mode (λ_R) and polar mode (P) are therefore competitive— in a Landau expansion of a bulk system with these two transitions, the coefficient δ_{PR} of the biquadratic coupling term $\delta_{PR}P^2\lambda_R^2$ is greater than 0, meaning there is an energy penalty for both modes developing simultaneously [33,34]. Because of this, STO remains a paraelectric in the ground state (demonstrated experimentally for temperatures as low as 1.5 K), but only just— within the scale of quantum energy fluctuations [35–43]. It is therefore classified as a quantum paraelectric. STO is also an incipient ferroelectric, meaning it is on the verge of multiple polar transitions along different cell directions [34,44–46], which can be induced under a variety of circumstances. Polar transitions have been induced by chemical substitution [47–49], isotopic ^{18}O-substitution [50], defect engineering [51–53], mechanical stress [54, 55], as well as interfacial effects such as epitaxial strain [44, 45, 56, 57], mode mismatch [58–61], film thickness [51, 62], and formal polarisation mismatch [63].

In this study, we seek to understand how various interfacial effects trigger or interact with polar modes. Therefore, we require a material that is neither strongly polar, nor strongly non-polar, such that the subtle softening or hardening of a polar mode can be detected. STO is therefore a perfect candidate, as its transition to a ferroelectric state immediately demonstrates that a given effect cooperates with ferroelectricity (or at least polarisation, depending on the circumstance). We are able to investigate both polar and non-polar phases on an equal footing, such that we can also test the reverse of this— how interfaced systems react to the presence of the polar mode. At room temperature, STO occupies a cubic $Pm\bar{3}m$ phase, though at 110 K undergoes a phase transition to the $I4/mcm$ space group [64] consisting of antiphase octahedral tilting along one axis. As already stated, tilting is chosen by the system over polar motion due to the insufficient size of the Sr cation. The response of STO to various interfacial phenomena are discussed in length in the '$SrTiO_3$-$NdNiO_3$ interfaces' section of this chapter.

1.3 Metal-insulator transitions

The second phenomenon of interest to this study is that of the metal-insulator transition. The reasons for a given compound being insulating or metallic is system dependent, though we can still make general statements on the origins of the opening and closing of this gap, particularly for perovskites consisting of transition metal ions on the B-sites. The existence and width of the band gap in transition metal perovskites (and transition metal oxides more generally) depends on the energy levels of three components— the highest occupied Oxygen state (O-2p), and the highest occupied and lowest unoccupied transition metal (d) states [65, 66]. There exist two types of insulator: charge-transfer insulators, where the O-2p states lie between the valence and conduction bands of the transition metal, and Mott-Hubbard insulators, where the O-2p states lie below the valence transition metal bands. We can similarly say therefore that two types of metal exist in this model, firstly where O-2p states overlap the transition metal conduction band, and secondly where transition metal valence and conduction bands overlap. A more detailed explanation of this model (known more generally as the Zaanen-Sawatzki-Allen (ZSA) model of transition metal oxide band gaps), may be found in ref. [65], which correctly predicts the ground state of many perovskites. The behaviour of the d-subshell is particularly interesting in perovskites. Before including crystal distortions, the d_{xy}, d_{yz} and d_{xz} orbitals (also known as the t_{2g} states) have lobes pointing between the O-2p orbital lobes, while the $d_{x^2-y^2}$ and d_{z^2} orbitals (also known as the e_g states) have lobes pointing directly towards the O-2p lobes. This assists with crystal field splitting, where the energy difference between the e_g and t_{2g} states is amplified [66, 67]. Generally, high d-electron count transition metal oxides such as Fe^{4+}, Cu^{3+} and Ni^{3+} are predicted to be metals as the e_g states are occupied, while low d transition metal oxides such as Ti^{4+} are predicted to be insulators[3]. However, high valence systems do not particularly want to occupy these states (or at least want to lower the energy of them), which can often lead to interesting novel behaviour in many cases.

1.3.1 $R\mathrm{NiO}_3$

The ZSA scheme is not always correct however. In the case of the rare earth nickelate perovskites, with nominal Ni^{3+} sites, the systems are found to be insulators in the ground state for all choices of rare earth A-site besides La [68,69]. In fact, these systems all undergo a metal-insulator transition (MIT) with decreasing temperature. Taking NdNiO_3 as an example, the system is metallic at room temperature, but opens a gap below 200 K [70, 71]. It turns out that these systems have a clever alternative way of doing this. Nominally, as the rare-earth cations have a 3+ valence, the Ni is forced into a 3+ state, with a $3d^7$ filling. Due to crystal field splitting the occupancies are t_{2g}^6, e_g^1, corresponding to a low-spin configuration, where the e_g states have a mixed $d_{x^2-y^2}$ and d_{z^2} character. Generally, the system preferring a low- or high-spin configuration (for a d^7 filling, the high spin configuration is t_{2g}^5, e_g^2) depends on the competition between the Hund's exchange energy [72] (encouraging the high-spin setting) and the crystal field splitting (encouraging the low-spin setting). The size of the energy penalties from each effect depend on several structural and electronic features of perovskites. Varying the B-O bond lengths— which are shortened or lengthened by a larger or smaller A-site, respectively increases or decreases the effect of the crystal field splitting [65] (thus favouring or disfavouring the low-spin state). Furthermore, if the B-site charge is greater, or the B-O bonding

---

[3] In this project, we regularly refer to perovskites in terms of nominal ionic charges. It is important to note that these ionic charges are not consistently defined, because the ionic radii are not well defined. The numbers cited are an approximation, but like the tolerance factor, are a useful benchmark for introducing these concepts while avoiding the details of electronic structure.

is covalent for another reason, the crystal field splitting is similarly amplified [73]. The nickelates are charge-transfer metals in the low-spin state, where the occupied e_g states overlap with the O-2p orbitals. However, the system can reduce this overlap by introducing octahedral tilting. The metallic states are already orthorhombic, occupying the $Pbnm$ state, though as this tilt is amplified upon lowering the temperature, the bandwidths are continually decreased. It has been demonstrated through first principles calculations that there exists a critical amount of tilting to induce the MIT in the nickelates [74].

Beyond this critical amplitude of tilting, the system seeks to alter the electronic structure in some way to open this gap, to avoid the partially occupied e_g state. The nickelates achieve this by charge ordering the Ni sites [75]. The exact valences on the Ni sites in this charge ordered state are still heavily debated. Generally, the valences are $2\mathrm{Ni}^{3+} \rightarrow \mathrm{Ni}^{3+\delta} + \mathrm{Ni}^{3-\delta}$, where δ is a small amount of charge, but recent experimental and theoretical studies suggest that the 3d fillings more closely resemble $3d^8, 3d^8L^2$ (where a $3d^8$ filling corresponds to Ni^2+), where the L denotes ligand bonds with the oxygen sites [76–80]. The large $3d^8$ (denoted $\mathrm{Ni_L}$) site results in an expanded $\mathrm{NiO_6}$ octahedra, while the small $3d^8L^2$ (denoted $\mathrm{Ni_S}$) site results in a contracted $\mathrm{NiO_6}$ octahedra. As a result, the e_g state remains filled for all Ni sites, but there exists no overlap with the O-2p states in this new configuration. The system occupies a monoclinic $P2/c$ state, consisting of the all the features of the $Pbnm$ symmetry with an additional 'breathing mode' [81–84]. This distortion is visualised in Fig. 1.1(f). Within the Landau framework, the triggered mechanism can be understood via the biquadratic coupling terms between the breathing mode (λ_B), the antiphase tilting (λ_R) and the in-phase tilting (λ_M): $\delta_{BR}\lambda_B^2\lambda_R^2$, $\delta_{BM}\lambda_B^2\lambda_M^2$, and the quadratic terms $\alpha_B\lambda_B^2$, $\alpha_R\lambda_R^2$, and $\alpha_M\lambda_M^2$. It has been demonstrated via first principles calculations that $\alpha_B > 0$ while $\alpha_R, \alpha_M < 0$, such that both types of tilting are developed (and are stabilised by positive quartic coefficients) and the breathing is not [74]. However, the coupling coefficients $\delta_{BR}, \delta_{BM} < 0$, such that beyond a critical amount of tilting, the energy gain of the coupling terms outweighs the cost of the quadratic breathing term, leading to the development of the breathing mode.

Regarding the metal-insulator transitions, it is worth also mentioning orbital ordering. Transition metal perovskites typically want to remove the degeneracy in the d states for a variety of reasons, so as a result, split their energies. This can occur within the t_{2g} and e_g states separately. The result of this is distorted octahedra with varying B-O bond lengths, due to the different d orbital shapes [85, 86]. These are known as the Jahn-Teller distortions, one type of which is visualised in Fig. 1.1(g). This is also a more common method for gap opening in perovskites, as neighbouring B sites can have the same valence but different orbital character. This has even been achieved in rare earth nickelates under certain interfacial conditions [87], where the e_g states alternate between $d_{x^2-y^2}$ and d_{z^2} character.

The unique properties of the rare earth nickelates have also been utilised to build devices. Various novel electronic devices consisting of nickelates have been designed, including artificial neuromorphic systems utilising conductance switching via Ni oxidation and reduction [88], artificial neural networks built from nickelate memory capacitors (driven by rapid changes in resistivity at the MIT) [89], and sensing devices reliant on Ni charge transfer [90]. As well as the metal-insulator transitions, research into the rare-earth nickelates has greatly helped our broader understanding of several other fundamental concepts, including the nature of poorly conducting materials [91] and multiferroicity [92]. We explore the response of the nickelates to interfacial phenomena in the 'NNO-STO interface' subsection.

In this study, we seek to investigate how the metal-insulator transition is affected by interfacial phenomena. $NdNiO_3$ is a great choice for this, as it has a bulk MIT temperature near room temperature (suitable for experimental realisation), and also has a simpler magnetic ordering (alongside Pr, which has a lower MIT temperature) compared to the rest of the series. The magnetic order of the ground state charge-ordered insulating phase resembles a T, S-AFM 'spin-density-wave', consisting of large moments on the $\mathrm{Ni_L}$ sites and zero moments on the $\mathrm{Ni_S}$ sites [92–94]. The spins are ordered along (111) planes, alternating between layers of moments and zero moments. This is visualised and explored further in chapter 4 of this project. For larger A-sites however, this magnetic state only appears at lower temperatures, and after a Neél transition from a charge-ordered, paramagnetic state. We do not pursue these systems further in this study, but much of the theory proposed in this project is directly comparable to the rest of the series besides $LaNiO_3$ (LNO). We do briefly also investigate LNO in chapter 4, which is an interesting exception with a larger A-site, which leads to a rhombohedral $a^-a^-a^-$ tilt pattern with smaller tilt magnitudes that are not sufficient to trigger the MIT [69].

1.4 Perovskite interfaces

Though many perovskites are interesting in their own right as bulk crystals, a new dimension of possibility is unveiled when building precise thin films and layered heterostructures, as is typical of electronic devices. When grown in these ways a perovskite is subject to interfacial effects— additional constraints that can heavily alter its properties. Interfacial constraints are essential to take into account when designing new devices, but also very interesting in their own right as a way to manipulate systems. In the present day, we have access to experimental techniques capable of building precise interfaced systems deposited layer by layer, such as pulsed laser deposition (PLD) and molecular beam epitaxy (MBE) [2]. Regardless, some defects are inevitable, and in some situations, these can vastly affect the properties of the system. Meanwhile, using first principles calculations as in this study (discussed in chapter 2), we usually build pristine interfaced systems. This is very convenient for investigating precisely various interfacial effects, though some variation should be expected upon comparison to experiment. The degree of comparability of experiment to theory is very much system dependent— a given type of defect or limitation may have major or minor consequences, or be more or less common depending on the system. In some cases, defects can be included in first principles calculations, though this is often computationally challenging (defects usually require the doubling or quadrupling (or more) of the unit cell in-plane). To be clear however, the theoretical simulation of pristine interfaces remains highly applicable to experiment— the interfacial effects that remain present regularly dominate the systems properties.

Perovskite interfaces can be built along several crystallographic directions. The most widely used choice is the [001]-direction, where the layers alternate between

AO and BO$_2$ per formula unit (/f.u.). As well as this, systems built in the [111]-basis (as well as the [110]-basis, which is not covered in this study) are becoming increasingly commonplace, where layers alternate between AO$_3$ and B. Each orientation is interesting in its own right and applies unique constraints to any deposited films. In this study, we consider the interfacial effects present in both [001]- and [111]-oriented films and apply them to incipient ferroelectric STO and MIT-capable charge-ordered nickelate NNO. The following subsections cover a general overview of these effects, and the following section reviews relevant literature on interfaces specifically involving or related to STO and NNO.

1.4.1 Epitaxial strain

The first energetic constraint encountered when depositing a perovskite film on a substrate is caused by differences in the in-plane lattice parameters. As long as the lattice parameters of a thin film and substrate are within roughly ±4% of each other, the octahedra of the substrate and thin film can align and connect. For this to occur, the film must alter its in-plane parameters to match those of the substrate, experiencing a biaxial strain as a result. This concept is known as epitaxial strain, and is a key limit to interfacing many perovskites with one-another. Experimentally, ±4% strain is the absolute maximum before dislocations dominate the system[4] [2]. Despite this, even a small percentage of strain is enough to drastically alter the properties of perovskites. Immediately, the symmetry between in-plane and out-of-plane axes are broken, leading to cell tetragonality. In the [001]-basis, epitaxial strain splits two of the primitive directions from the third lying out-of-plane, while in the [111]-basis, strain splits the out-of-plane [111]-axis from the three other [111]-axes which lie mostly in-plane. This effect is visualised in both bases in Fig. 1.2(a).

The effect of epitaxial strain on various distortions can be modeled generally using a Landau-like energy expansion. Ginzburg and Devonshire helped extend the

---

[4] In first principles calculations, we could build a pristine interface at much higher strains, though these would certainly be unfeasible experimentally. In chapters 3 and 4, when investigating strain alone, we do regularly exceed ±4%, but only do this for the sake of understanding various physical trends with strain.

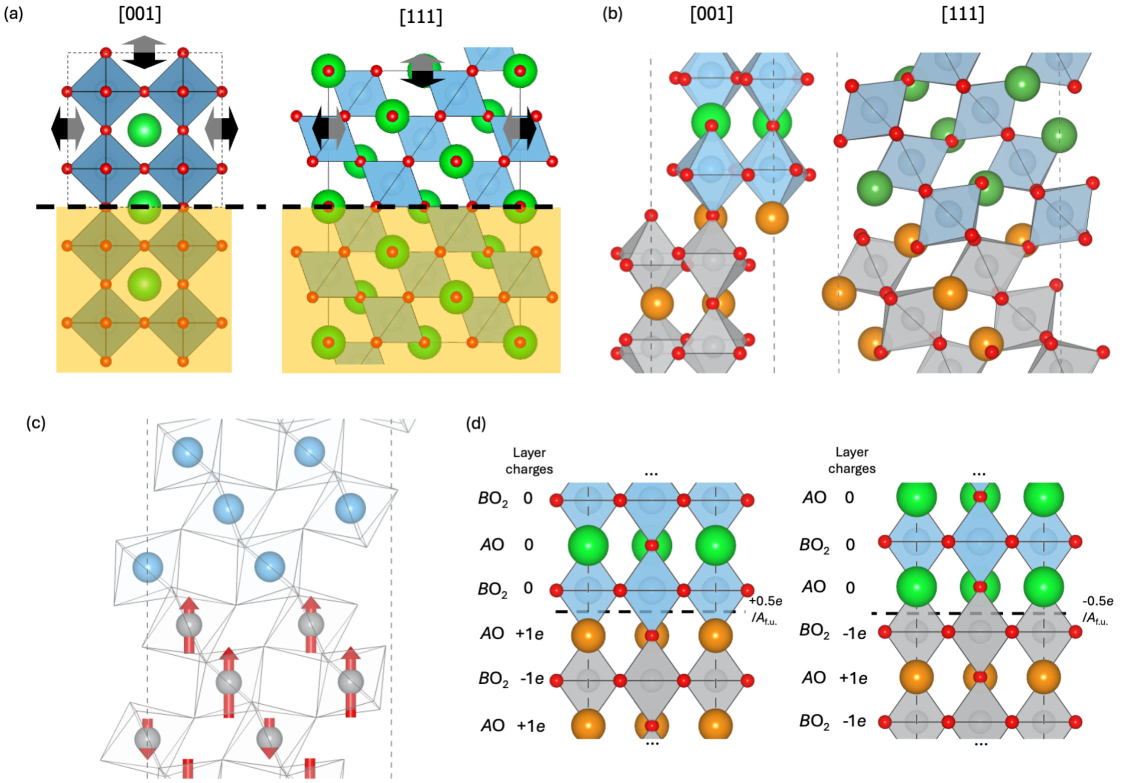

Figure 1.2: Schematics of relevant interfacial effects in various perovskite orientations. (a) Biaxial strain due to film epitaxy displayed for both [001]- and [111]-bases, where the yellow filter denotes substrate layer, and black and grey arrows denote the change in cell dimensions under tensile and compressive strains respectively. (b) Geometric differences between [001]- and [111]-interfaces that result in different mode decay lengths (where oxygen octahedra are matched for one and three oxygens respectively). (c) Magnetic frustration at the interface of a magnetic and non-magnetic system (in the [111]-basis). (d) Demonstration of the polar discontinuities between II/IV and III/III perovskite interfaces in the [001]-basis, for each choice of termination (where $A_{\text{f.u.}}$ is the in-plane area per formula unit that the interface charges are averaged over).

Landau formalism to take into account interfacial effects (alongside a range of other factors), where the former extended the model to spatial variations in the order parameters [95], while the latter considered real ferroelectric systems affected by strain and depolarising effects. To model epitaxial strain in the Landau-Ginzburg-Devonshire (LGD) formalism, we consider the two fixed in-plane strains $\epsilon_{xx}, \epsilon_{yy}$, and a free-to-relax out-of-plane strain ϵ_{zz}. In some cases, we also consider the shear components of strain ϵ_{xy}, ϵ_{xz}, ϵ_{yz}, depending on the cell symmetry. Each strain component has a quadratic term with an energy cost (with positive coefficients), coupling terms with the other strain components, and coupling terms with the structural modes present in the system [33]. The strain only terms in the free energy take the following form (excluding higher-order terms):

$$\mathcal{F}_{\text{strain}} = \sum_{j} C_j \epsilon_j^2 + \sum_{j,m} C_{jm} \epsilon_j \epsilon_m, \tag{1.3}$$

where C_j, C_{jm} are coefficients of the strain and strain-coupling terms respectively. The strain-mode coupling terms take the form of (excluding higher-order terms):

$$\mathcal{F}_{\text{strain-mode}} = \sum_{i,j} \delta_{ij} \lambda_i^2 \epsilon_j + \sum_{i \neq l} \sum_{j} \delta_{ijl} \lambda_i \lambda_l \epsilon_j \tag{1.4}$$

where $\lambda_{i,l}$ are modes, δ_{ij} are strain-mode coupling coefficients, and δ_{ijl} are strain-mode-mode (trilinear) coupling coefficients. If $\delta_{ij} < 0$, then a positive (tensile) strain favours the formation of the mode, and a negative (compressive strain) disfavours it. Vice versa applies if $\delta_{ij} > 0$. These models tend to get extremely complex, as each mode is coupled to all the other modes, and all the strain components (in some situations, higher order coupling terms also play an important role). Such models have been built for relatively simple systems such as STO, where only antiphase tilting and the polar mode (in each axis) are included alongside [001]-oriented strain. The full model may be found at ref. [34], and is composed of in- and out-of-plane tilting, in- and out-of-plane polarisation, as well as all six strain terms. In this example the coefficients are determined from experimental data, and are used to predict the strain phase diagram.

As a general rule of thumb, [001]-oriented compressive strain suppresses in-plane tilting and amplifies out-of-plane tilting in perovskites, while [001]-oriented tensile strain has the inverse effect [96,97]. This is because compressive [001]-strain reduces the 'free space' left by ionic radii along the in-plane axes (and thus lengthens the out-of-plane axis), while tensile [001]-strain creates more 'free space' along the in-plane axes (and thus shortens the out-of-plane axis). This also affects the softening of polar modes in non-orthorhombic systems, such that compressive strain softens it out-of-plane and suppresses it in-plane, and tensile strain has the reverse effect. As the polar mode is still competitive with tilting, it often remains suppressed (especially in orthorhombic systems which generally more tilted to begin with), though predictions on [001]-strained paraelectric STO suggest that the polar mode may be softened faster with strain than tilting [34].

General rules for the effect of [111]-strain on the common perovskite distortions are less established. [111]-strain expands and contracts all three primitive directions simultaneously, which we logically expect to suppress and support tilting along the primitive directions accordingly. Compressive strain might equally suppress polar distortions, while tensile strain might soften them. [111]-strain phase diagrams are generally less diverse than [001]-strain diagrams due to the uniformity of the constraint on each primitive axis [97]. Recent first principles studies suggest that the softening of the polar mode due to [111]-strain is dependent on the tolerance factor. For tolerance factors below 1 (that typically have orthorhombic tilt patterns), compressive strain softens the polar mode out-of-plane and hardens it in-plane, while tensile strain has the inverse effect. For tolerance factors close to 1 however (typically resulting in antiphase tilting and tetragonal cells), compressive strain suppresses the polar displacements both in-plane and out-of-plane, while tensile strain softens it in both directions [96].

Strain is an essential feature of interfaced systems, and is carefully investigated in chapters 3 and 4 of this study. From first principles, we are able to isolate the effect of strain from other interfacial effects by considering it on a bulk system, which is very useful for understanding complex interfaces. This is discussed further in the methods chapter.

1.4.2 Mode decay

The next problem a film encounters when deposited on a substrate is how to distort the interfacial ions. Across the interface, it is energetically unfavourable for these ions to immediately revert to a completely different structure within a layer, so usually the modes of the film and substrate average out at the interface to some extent. Moving away from the interface, the distortions gradually return to bulk-like properties. However, particularly for thinner films, sometimes this mode 'decay' from the interface is long enough to influence the properties of the entire film. In the [001]-basis, mode decay is important for in-plane tilting, because the displaced oxygen sites connect to adjacent octahedra at the interface [2]. Meanwhile, the effect of mode decay on tilting in the [111]-basis is even more extreme, where three O sites lie at the interface per octahedra, resulting in a stronger interfacial connectivity. For example, $LaAlO_3$ substrate tilts decay over at least six layers in interfaced nickelate films in this basis [98]. This is without mentioning the mode decay of other distortions, which remain less understood. The concept of mode decay in each basis, using tilting as an example is shown in Fig. 1.2(b). Mode decay can also be included in the LGD framework, where we can consider spatial variations in the order parameters via a Ginzburg term $|\nabla\lambda_i|^2$ [95,99]. In an interfaced system along out-of-plane direction z, there is an energy penalty term $\kappa_i|\frac{d\lambda_i}{dz}|^2$, where κ_i is the stiffness of λ_i. This term penalises rapid changes in λ_i across the interface. In the case where a mode is not active in a neighbouring film, such that the quadratic coefficient (of a given mode λ_i) $\alpha_i > 0$, the decay length of the mode in this region $\xi_i = \sqrt{\frac{\kappa_i}{\alpha_i}}$, and the mode follows an exponential decay: $\lambda_i(z) = \lambda_i(0)e^{-\frac{z}{\xi_i}}$.

1.4.3 Quantum confinement

The properties of films can also be heavily impacted by the finite film thickness. For ultrathin films only a few nanometers thick, the thickness approaches the scale of the De Broglie wavelength of the electronic wavefunction, such that the electrons experience confinement [100]. This leads to the discretisation of the energy landscape. This can influence the charge mobility and has been shown to induce insulating behaviour in metallic perovskites such as LNO [87].

1.4.4 Magnetic frustration

Magnetism is not discussed in length in this project, though detailed approaches exist for considering magnetic symmetry and structure for perovskites. Though the magnetic order of the rare-earth nickelates (including *A*-site moments) is non-collinear, the properties can be accurately reproduced through only considering collinear magnetic orders on the Ni-sites [74, 80]. Nonetheless, it has been shown that obtaining the correct collinear order is essential for tuning the ground state properties [101]. For any given magnetic order, an immediate termination at the interface is not usually energetically favourable. Moments become frustrated at the interface, which often results in varying moment sizes or directions. As we consider only collinear orders in this study, we are not concerned with the latter, though moment sizes are heavily linked to Ni-site occupation in the rare earth nickelates, so are a concern [80]. This effect is visualised in Fig. 1.2(c).

1.4.5 Polar discontinuities

The final interfacial effect relevant to this study is the polar discontinuity. Polar discontinuities occur not only when two systems have different amplitudes of polarisation due to cation displacements (which we refer to as ferroelectric polarisation), but also differences in the 'formal' polarisation, which depends on the layer charges of each film. When two insulating perovskites with different layer charges are interfaced together, there will be a discontinuity at the interface (alongside discontinuities caused by different inter-layer spacings and modes) [102–105]. The discontinuity in the electric displacement field **D** results in a free surface charge (lying at the interface) σ_{free}:

$$\mathbf{D}_{\text{L}} - \mathbf{D}_{\text{R}} = \sigma_{\text{free}}, \tag{1.5}$$

where $\mathbf{D}_{\text{L,R}}$ denote the displacement fields on either side of the interface. As $\nabla\mathbf{D} = \epsilon_0\nabla\mathbf{E} + \nabla\mathbf{P}$, and the change in polarisation results in an interfacial bound charge $\nabla\mathbf{P} = \sigma_{\text{bound}}$, we obtain the following expression for the change in the field from film to film:

$$\nabla \mathbf{E} = \mathbf{E}_{\mathrm{L}} - \mathbf{E}_{\mathrm{R}} = \frac{\sigma_{\mathrm{free}} - \sigma_{\mathrm{bound}}}{\epsilon_0}. \tag{1.6}$$

The fields resulting from the polar discontinuity lead to sizeable energy penalties and can significantly influence the films. A more detailed proof can be found in refs. [103,106].

To minimise the energy of the system, the interfaced layers ideally want to screen these fields in some way. This is not an easy task for insulators, which are encouraged to polarise (by how much depends on their dielectric susceptibilities). In the LGD formalism, when looking at a particular film, we include the term $-EP$ in the expansion [33], where P is the size of the polar mode, and E is the magnitude of the field across the film. This term lowers the energy when the polar mode is in the same direction as the E-field. Of course, the appearance of the polar mode is still limited by the other terms in expansion (quadratic, quartic, mode coupling, strain coupling, mode decay). However, it turns out that there are also a number of special cases where the films can come up with other clever ways to screen the fields (discussed in the following section), which have been of great interest to us over recent decades. Overall, the polar discontinuity applies an interesting constraint to the systems as a whole. This effect is visualised for the [001]-oriented interface between insulating II/IV ($A^{2+}B^{4+}$) and III/III ($A^{3+}B^{3+}$) perovskites[5] in Fig. 1.2(d).

1.5 SrTiO$_3$-NdNiO$_3$ interfaces

In this study, we are interested in how an incipient ferroelectric and a system that may undergo a MIT react to interfacial effects. We seek to understand how ferroelectricity in STO and the MIT in NNO can be induced or tuned by strain, mode decay, magnetic frustration and polar discontinuities. As well as this, we are particularly interested in how these two phenomena influence each other in an interfaced system. We therefore include a literature review of all relevant experimental and computa-

---

[5] Though we can't define ionic charges, we can find the formal polarisation of a crystal (though it is multivalued, as discussed in the 'Polarisation' subsection of chapter 2), and state that a formal polarisation corresponds to these ionic charges.

tional studies already undertaken involving interfacial STO and NNO (/RNO), as well as any related systems.

1.5.1 Interfaced STO

Starting with STO, the first ferroelectric STO phase was discovered after applying approximately 1% tensile [001]-strain, which resulted in in-plane polarisation [44,56]. This is logical considering the arguments presented above regarding [001]-strain increasing tetragonality, which is expected to soften the polar mode. Several years later, a polar STO phase was also created at 2-3% compressive strain, with polarisation out-of-plane [45, 57]. These experimental observations have been supplemented with both DFT and LGD analysis (based on experimental data), which similarly predict polar phases along these axes [34, 107, 108]. It is shown that the polar mode becomes increasingly more stable with strain than octahedral tilting, such that the polar transition temperature is predicted to exceed that of the tilts at roughly 1% compressive and 0.5% tensile strain [34]. Interestingly, first principles calculations also suggest that despite the competition between tilt modes and polar modes, extremely high tilts actually favour polar modes due to the rapid increase in cell tetragonality [43]. Polar STO phases have not been realised experimentally in the [111]-basis, but previous first principles calculations reveal a strong polar transition under tensile strain, which has components both in- and out-of-plane [109]. As the STO tolerance factor lies near 1 (such that it has only minor antiphase tilting in bulk), polarisation appearing in both axes matches predictions based on other [111]-strained perovskites [96]. However, the direction of the polarisation in this phase is not well understood, as there exist several low energy states with both in-plane and out-of-plane polarisation (in the [111]-basis). The ground state consists of polarisation with a large in-plane and small out-of-plane component, but metastable states close in energy consist of polarisation only in-plane [109]. Experimentally, STO has been grown in the [111]-basis, where high dielectric susceptibilities have been observed, but there are no reports on ferroelectric phases as of yet [110].

Aside from strain, STO has been shown to generate polar phases under other interfacial effects. Due to mode decay from interfaced ferroelectrics $BaTiO_3$ and

$PbTiO_3$, a variety of polar STO phases have been induced [58–60], which have even led to exotic polar 'vortices' under flexoelectric constraints [61]. The polar mode can also be amplified at very low film thicknesses [51, 62], and attempts to screen interfacial bound charges arising from the polar discontinuity in the LAO-STO interfaced system [63].

The now well-studied LAO-STO interfaced system is important to mention for a number of reasons. In 2004 it was shown that 2D electron gases (2DEGs) appeared near the interfaces, an unexpected result considering both LAO and STO are strongly insulating [63]. These 2DEGs have exhibited a number of interesting properties that have prompted significant research into this system— it has been shown that the 2DEGs are tunable [111], have magnetic properties [112, 113] and are superconducting [114, 115]. This is all thought to be a result of the polar discontinuity between LAO and STO, which are III/III and II/IV insulating perovskites respectively. The nominal charges and resulting formal polarisation discontinuity has been proven rigorously by calculating Wannier centres, which resulted in layer formal charges of $\pm 1e$/f.u. for LAO and $0e$/f.u. for STO in the [001]-basis [103]. In a stoichiometric system, bound charges of opposite signs exist at each type of interface (whether LaO-TiO_2 ($\sigma_{\mathrm{b}} = +0.5e/A_{\mathrm{f.u.}}$) or SrO-$AlO_2$ ($\sigma_{\mathrm{b}} = -0.5e/A_{\mathrm{f.u.}}$) where $A_{\mathrm{f.u.}}$ is the in-plane area. The system deals with this high density of charges first by polarising out-of-plane in either LAO or STO (or both, depending on the boundary conditions). Then, because of the field, the band offsets vary across the films, such that if the film thicknesses are sufficient, the valence and conduction bands of LAO and STO will overlap allowing for electrons to tunnel across the system. This principle is known as Zener tunneling, and is a feature of insulating devices where the conduction and valence bands overlap at opposite ends of a film [116, 117]. DFT calculations have verified that there exists a critical film thickness for this effect to occur [104]. In the [111]-basis, where films have a similar polar discontinuity, LAO-STO interfaces have been similarly shown to have 2DEGs present [118], which also appear to have superconducting and magnetic properties [119, 120].

On the topic of ferroelectricity (and also the instance where the interfaced film is metallic), it is important to touch on ferroelectric capacitors, which have been built from perovskites [121]. A well-known example of this involves a ferroelectric $BaTiO_3$ (BTO) layer sandwiched between metallic $SrRuO_3$ (SRO) electrodes. The electrodes allow BTO to maintain polarisation, as they screen the polarisation charges which otherwise lead to a depolarising field. Under closed circuit boundary conditions, there still exist dipoles across the interfaces which lead to a finite potential gradient across the BTO layer. At small thicknesses, the resulting depolarising field is too large and suppresses ferroelectricity [122–124], though beyond a critical thickness, BTO can retain monodomain polarisation [125]. Further study on this system additionally demonstrated that there also exists ionic motion within the metallic electrodes near the interfaces between the metallic screening charges and BTO polarisation charges, which align with the ferroelectric polarisation direction and are essential for reducing the interface dipoles [126]. The physics of the ferroelectric capacitor are applicable to any metal-ferroelectric interface, including the scenario where STO is polar and NNO metallic.

1.5.2 Interfaced NNO

NNO and other rare-earth nickelates have also been at the forefront of designing novel perovskite devices. Under [001]-strain, it has been shown experimentally that the MIT temperature may be suppressed in rare-earth nickelates [127–129]. First principles calculations have shown that both compressive and tensile [001]-strain can gradually close the gap and induce IMTs [101]. The origin of this phenomena is still somewhat ambiguous, as these calculations additionally suggest that the net tilt (which is understood to trigger the MIT) does not substantially change under strain. Interestingly, in the [111]-basis, NNO films deposited on $NdGaO_3$ (which applies a [111]-tensile strain) have a substantially amplified MIT temperature [130, 131]. Alongside strain, this might also be attributed to substrate tilt matching, though no first principles calculations have been undertaken to verify this. A particularly interesting state was observed in [111]-oriented NNO-LAO films, which apply a minimal strain, but due to octahedral tilt matching, force NNO to revert to a tilt pattern approximately resembling $a^-a^-c^0$. This tilt pattern suppresses Nd-antipolar motion, which allows for NNO to break net inversion symmetry out-of-plane and turn polar in the metallic phase [98]. Additionally, orbitally-ordered phases have been observed in ultrathin layered [111]-NNO-LAO superlattices [132].

The interfacial results listed so far mainly concern the insulating nickelate phases, but for this project it is also important to mention some well-studied interfaced systems involving metallic nickelates, particularly $\mathrm{LaNiO_3}$, which may have comparable features to metallic NNO (despite having a different symmetry). An interesting system is that of LNO and STO, which are found to remain as a metal and a paraelectric insulator respectively. From both theory and experiment, though the metallic LNO layer fully compensates any interfacial bound charges, minor band offsets still occur at each type of interface due to periodic boundary conditions [133, 134]. This effect has also been shown to occur in the [111]-oriented LNO-STO system [135]. Under certain conditions LNO can also behave similarly to NNO in the [111]-basis. In ultrathin superlattices, LNO has been demonstrated to turn insulating [87], in the exact same way NNO does in ultrathin [111]-interfaces [132]. This transition is likely driven by quantum confinement, and causes LNO to orbitally order the e_g states (such that Ni sites alternate between $d_{x^2-y^2}$ and d_{z^2} occupations) to open a gap. Orbitally ordered transitions are not observed in nickelates under any other circumstance besides extremely high [001]-tensile strains in first principles calculations, where it is also observed to open a gap [101]. We do not investigate LNO in detail in this study, as we were unable to build nickelate interfaces with it (for reasons explained in chapter 4), though we still investigate its properties as a function of [001]-strain. The phenomena of LNO are still worth keeping in mind when considering [111]-oriented NNO interfaces.

1.5.3 The STO-NNO interface and project overview

We are presented with several interesting possibilities when considering the interface between STO and NNO. We can already suggest that STO may exist in a paraelectric or ferroelectric state, while NNO may exist in a metallic or insulating state. In the above review, we discussed interfaces between materials of each of these classifications, however none that combine a perovskite that can easily switch between paraelectric and ferroelectric states, with a perovskite that can easily switch between metallic and insulating states. The superlattice built from these films may lead to a unique novel electronic device applicable to industry. An idea proposed by our experimental collaborators is that this could resemble a memristor— where resistivity follows a hysteresis loop. As both materials are insulating, it is likely that STO either remains paraelectric or turns polydomain ferroelectric (possibly depending on the amount of applied compressive strain) as to not create large depolarising fields. Upon applying a field, we might be able to revert the STO film to monodomain polarisation, which in-turn would encourage the NNO film to turn metallic (or at least form 2DEGs or 2DHGs) and screen the polarisation charges.

Measuring the (in-plane) resistivity of the NNO film at interfacial region, we might expect a rapid and sizeable change upon switching STO from polydomain to monodomain, as this could effectively induce the metallic state (and vice versa when switching from monodomain to polydomain). Switching a ferroelectric from polydomain to monodomain and back with an electric field typically follows a hysteresis path. We predict that the NNO resistivity might follow a similar hysteresis pattern, such that we could be able to easily flip between high and low resistivity states. These systems have also been realised courtesy of E. Stylianidis and P. Zubko (University College London).

Prior to investigating this system, to totally understand its properties, which we can expect to be affected by all the aforementioned interfacial effects (strain, mode decay, quantum confinement, magnetic frustration (NNO), and polar discontinuities (whether due to intrinsic effects or polarised STO)) it is necessary to isolate as many phenomena as possible and investigate them individually first. We are able to disentangle strain effects via ‘bulk-strained’ calculations, which we undertake in chapters 3 and 4 for STO and NNO (as well as LNO) respectively. We investigate the effect of strain in both [001]- and [111]-orientations, which given the reviewed literature, we expect to lead to vastly different phase diagrams.

With this established, we then extensively investigate the [001]-oriented STO-NNO interfaced system from first principles, clarifying in detail the structural and electronic properties in stoichiometric and non-stoichiometric orientations. The results of this are presented in chapter 5. In our final results chapter (chapter 6), we investigate [111]-oriented interfaces based on the STO-NNO system. For reasons explained in the chapter, we focus on interfacing NNO with a range of substrates rather than specifically STO-NNO. Given relevant literature, it is clear that this orientation is capable of inducing different behaviour to the [001]-basis, whether it be due to the different axes of biaxial strain, different interfacial matching, different polar discontinuities, differing amounts of quantum confinement or the different axis of magnetic frustration. These calculations open up a range of new possibilities not accessible in the [001]-basis, and nicely supplement the rest of our study.

1.6 Summary and project aims

We can summarise the goals of this study into several concise questions we seek to answer, which will be recapped in the final chapter of this report 'Conclusions and Outlook'.

1. Can we simulate STO and NNO using first principles techniques such that the experimental ground states are accurately recreated?

The first goal of this study is to recreate experimental observations of bulk STO and NNO using DFT, and understand any possible discrepancies. This is covered for STO and NNO in chapters 3 and 4 respectively, prior to discussing the effects of strain. For NNO, we also investigate how variation of a first principles correction term known as the Hubbard-U potential (defined in chapter 2) affects the ground state. This is also undertaken for LNO.

2. How does the ground state of STO change as a function of [001]- and [111]-oriented compressive and tensile strain?

In the latter part of chapter 3, we present an investigation into the strain phase diagrams of STO in both the [001]- and [111]-bases. Our focus is primarily towards inducing polar phases, but also the modulation of the antiphase tilt mode. We also measure how the dielectric susceptibility and polarisation (if condensed) are affected by these constraints.

3. How does the ground state of NNO change as a function of [001]- and [111]-oriented compressive and tensile strain?

Mirroring objective 2, in the latter part of chapter 4 we investigate how [001]- and [111]-strain influences the ground state of NNO, with particular focus on the stabilisation of metallic and insulating phases. We directly measure both structural and electronic properties to see how key features such as the band gap are linked to tilting, charge-ordering, and strain. We also look for changes in the ground state of LNO as a function of [001]-strain.

4. What happens when we interface an incipient ferroelectric with a material that can undergo an MIT?

In chapter 5, we address the fundamental question of this study— what happens when we interface STO and NNO (in the [001]-basis)? We investigate how the properties of each film vary layer-by-layer, and identify subtle structural and electronic features undetectable experimentally.

5. How do rare-earth nickelates behave in [111]-oriented interfaced systems?

In chapter 6, we investigate [111]-oriented interfaced nickelate systems, similarly detecting subtle structural and electronic properties not accessible through experimental means. We simulate [111]-oriented NNO on a range of substrates, in the hopes of inducing novel phases and answering unexplained experimental observations.

CHAPTER 2

Methods

Finding the ground state properties of a solid from first principles is an ongoing challenge for condensed matter physicists in the 21st century. This involves solving the many-body Schrödinger equation, which is not possible exactly for systems larger than a few particles. However, to circumvent this we can make various approximations that make the process solvable (while retaining sufficient theoretical accuracy), while also being computationally tractable for systems as large as crystal unit cells.

Density functional theory (DFT) has been shown to be consistently capable of correctly simulating the ground state properties of crystals such as perovskites, making it a suitable choice for this project. To undertake DFT calculations, we use the Vienna Ab-initio Simulation Package (VASP). In this chapter, we discuss DFT in detail, laying out the theory behind it as well as any additional corrections necessary for our systems. We also discuss the various post-processing options available for further investigating the ground state, as well as any other tools used in this project, such as those used for the group-theoretical analysis of crystals.

2.1 Density functional theory

2.1.1 The many-body problem

A crystal is an ordered arrangement of electrons and nuclei. We can define a crystal system quantum mechanically by writing out its total energy, which is expressed via the time-independent Schrödinger equation [136]:

$$\hat{H}\Psi = E_{\mathrm{tot}}\Psi, \tag{2.1}$$

where $\hat{H}$ is the system Hamiltonian, Ψ is the wavefunction, and E_{tot} is the total energy of the system. The Hamiltonian is the sum of the kinetic $E_{\mathrm{K.E}}$ and potential energy $E_{\mathrm{P.E}}$ of the system:

$$(E_{\mathrm{K.E}} + E_{\mathrm{P.E}})\Psi = E_{\mathrm{tot}}\Psi. \tag{2.2}$$

For a system of electrons and nuclei, we can define these terms as follows. The kinetic energy may be split into two expressions for electrons and nuclei:

$$E^{\mathrm{elec}}_{\mathrm{K.E}} = -\sum_{i=1}^{N} \frac{\hbar^2}{2m_{\mathrm{e}}} \nabla_i^2, \tag{2.3}$$

$$E^{\mathrm{nucl}}_{\mathrm{K.E}} = -\sum_{I=1}^{M} \frac{\hbar^2}{2M_I} \nabla_I^2, \tag{2.4}$$

where m_{e}, M_I are the masses of electrons and nuclei respectively, N, M (not to be confused with the nuclear masses M_I) are the total numbers of electrons and nuclei in the system, and $\hbar$ is Planck's constant h divided by 2π.

The potential energy term contains all the Coulomb interactions in the system. This is composed of three separate expressions— the sum of the electron-electron interactions, the sum of the nuclei-nuclei interactions, and the sum of the nuclei-electron interactions:

$$E^{\text{e-e}}_{\mathrm{P.E}} = \frac{1}{2}\frac{e^2}{4\pi\epsilon_0} \sum_{i \neq j} \frac{1}{|\mathbf{r}_i - \mathbf{r}_j|}, \tag{2.5}$$

$$E_{\text{P.E}}^{\text{Q-Q}} = \frac{1}{2}\frac{e^2}{4\pi\epsilon_0}\sum_{I\neq J}\frac{Z_I Z_J}{|\mathbf{R}_I - \mathbf{R}_J|}, \tag{2.6}$$

(where factors $\frac{1}{2}$ account for double counting),

$$E_{\text{P.E}}^{\text{Q-e}} = -\frac{e^2}{4\pi\epsilon_0}\sum_{i,I}\frac{Z_I}{|\mathbf{r}_i - \mathbf{R}_I|}. \tag{2.7}$$

The symbol e is the elementary charge, ϵ_0 is the vacuum permittivity, Z_I is the nuclear atomic mass, and $\mathbf{r}_i$, $\mathbf{R}_I$ are the coordinates of electrons and nuclei respectively. We can convert these expressions to atomic units, and write the generalised, time-independent many-body Schrodinger equation as:

$$\begin{aligned}\Bigg[-\sum_i^N \frac{\nabla_i^2}{2} - \sum_I^M \frac{\nabla_I^2}{2M_I} + \frac{1}{2}\sum_{i\neq j}\frac{1}{|\mathbf{r}_i - \mathbf{r}_j|} \\ +\frac{1}{2}\sum_{I\neq J}\frac{Z_I Z_J}{|\mathbf{R}_I - \mathbf{R}_J|} - \sum_{i,I}\frac{Z_I}{|\mathbf{r}_i - \mathbf{R}_I|}\Bigg]\Psi = E_{\text{tot}}\Psi.\end{aligned} \tag{2.8}$$

Even for a system with a few atoms, the problem with trying to solve equation 2.8 quickly becomes apparent. Taking a 5-atom simple cubic $SrTiO_3$ cell as an example, the number of electrons is $38 + 22 + 3 \times 8 = 84$, and the number of nuclei is 5. It is analytically unfeasible to solve the many-body Schrödinger equation exactly for this many particles. However, with several approximations, we can drastically simplify the problem to make it tractable for systems of this scale. Thankfully, approaches exist that have been demonstrated to accurately simulate the ground state properties of perovskites, while remaining computationally possible. Over the next few sections, we review the various theoretical shortcuts that can be applied to the many-body Schrödinger equation, which are the foundation for density functional theory (DFT)— the method used in this project for finding the electronic ground state of perovskites.

2.1.2 Born-Oppenheimer approximation

Because nuclei are so much heavier than electrons, they move far more slowly. We can make the approximation that electrons effectively move instantaneously compared to nuclei, such that upon any change of the nuclear positions, the electrons instantly respond. This is known as the Born-Oppenheimer approximation [137], and it allows us to heavily simplify equation 2.8. If the electrons respond to nuclear motion instantaneously, we can say that the electronic structure can be solved with the nuclear positions held fixed. Firstly, this allows us to say that the kinetic energy contributions of the nuclei is therefore zero, and thus omit the second term from the LHS of equation 2.8). It also means that the potential energy between nuclei now remains constant. This term may be moved to the right-hand side of the equation, where it is convenient to write $E = E_{\text{tot}} - \frac{1}{2}\sum_{I \neq J} \frac{Z_I Z_J}{|\mathbf{R}_I - \mathbf{R}_J|}$. Lastly, as the variables $\mathbf{R}_I$ are now external parameters, the nuclei-electron interaction term may be considered in terms of only electronic spatial variables $\mathbf{r}_i$: $-\sum_I \frac{Z_I}{|\mathbf{r}_i - \mathbf{R}_I|} = V_{\text{n}}(\mathbf{r}_i)$. To summarise, the many-body Schrödinger equation may now be written as:

$$\left[-\sum_i^N \frac{\nabla_i^2}{2} + \frac{1}{2}\sum_{i \neq j} \frac{1}{|\mathbf{r}_i - \mathbf{r}_j|} + \sum_i V_n(\mathbf{r}_i) \right] \Psi = E\Psi. \tag{2.9}$$

2.1.3 Independent electrons approximation

Solving equation 2.9 has been a challenge for physicists since the 1920s, mainly due to the complexity of the electron-electron interaction. In density functional theory, we undertake several steps to reduce the complexity of this term. We start by omitting it entirely, replace it with a rough but computationally tractable approximation, and then add back in the omitted physics as best we can to re-attain theoretical accuracy (to a sufficient level). The omission of the electron-electron interaction is known as the independent electrons approximation, where we simplify the Schrödinger equation to

$$\sum_i \hat{H}_0(\mathbf{r}_i)\Psi = E\Psi, \tag{2.10}$$

where

$$\hat{H}_0(\mathbf{r}) = -\frac{1}{2}\nabla^2 + V_{\text{n}}(\mathbf{r}) \tag{2.11}$$

are single-electron Hamiltonians. As the electrons are independent, the probability $|\Psi(\mathbf{r}_1, ..., \mathbf{r}_N)|^2$ of finding each electron i at their positions $\mathbf{r}_i$ must be equal to the product of the individual probabilities $|\phi_i(\mathbf{r}_i)|^2$. Therefore, in this scenario we would write the total probability as the square of the total wavefunction: $|\Psi(\mathbf{r}_1, ..., \mathbf{r}_N)|^2 = \prod_{i=1}^{N} |\phi_i(\mathbf{r}_i)|^2$,[1] where $\phi_i(\mathbf{r}_i)$ are the single-electron wavefunctions obtained by solving the single-electron Schrödinger equations

$$\hat{H}_0(\mathbf{r})\phi_i(\mathbf{r}) = \epsilon_i \phi_i(\mathbf{r}). \tag{2.12}$$

A useful property of the independent electron approximation is that we can show that the charge density n is equal to

$$n(\mathbf{r}) = \sum_i |\phi_i(\mathbf{r})|^2, \tag{2.13}$$

where we are summing the probabilities $\phi_i(\mathbf{r})$ of each electron appearing at a given position $\mathbf{r}$.

2.1.4 Mean-field approximation

Independent electrons is clearly an over-the-top approximation, as it assumes that there is no electronic interaction taking place. In the lack of this, electrons can simply bunch up and overbind to the nuclear positions. To appropriately model real systems therefore, we need to modify the above formulae to include the electronic repulsion and any quantum mechanical effects taking place. We seek to do this in a way that retains the computational simplifications that the model of independent electrons provides. Starting with the electron-electron interaction, we can approximate this by considering the average electrostatic potential generated by the electron density: $-V_{\mathrm{H}}$. V_{H} is known as the Hartree potential, and may be found using Poisson's equation:

$$\nabla^2 V_{\mathrm{H}}(\mathbf{r}) = -4\pi n(\mathbf{r}). \tag{2.14}$$

---

[1] To be clear— this expression is absolutely unusable as it violates the Pauli exclusion principle (we discuss this in the 'Exchange and correlation' subsection), but is here included to assist the discussion.

Solving this equation yields:

$$V_{\mathrm{H}}(\mathbf{r}) = \int d\mathbf{r}' \frac{n(\mathbf{r}')}{|\mathbf{r} - \mathbf{r}'|}, \tag{2.15}$$

which we add to our single electron Hamiltonians:

$$\hat{H}_0(\mathbf{r}) = -\frac{1}{2}\nabla^2 + V_{\mathrm{n}}(\mathbf{r}) + V_{\mathrm{H}}(\mathbf{r}). \tag{2.16}$$

This is the mean-field approximation [138, 139]. It remains a poor approximation on its own, as it assumes the system has a classical, continuous charge distribution, ignoring any quantum mechanical effects, which are key for understanding the properties of most systems. Regardless, compared to where we started, we have gone from a differential equation of $3N$ dimensions to one of N three-dimensional equations, which is a far more reasonable task computationally.

2.1.5 Exchange and correlation

The next step therefore is to include the quantum mechanical character of electrons as accurately as possible while retaining the computational tractability of this model. The first quantum-mechanical effect not considered in the model is the consequence of the Pauli exclusion principle, which states that no two fermions may occupy the same quantum state, meaning that the many-body wavefunction Ψ must change sign when we exchange the positions of two electrons [140]. Our previous expression for Ψ (in the 'Independent electrons approximation' section) clearly violates the Pauli exclusion principle, as Ψ does not change sign when any two electron positions are exchanged, as $\phi_1 \neq \phi_2$. The solution to this is to re-express the wavefunction Ψ in terms of single-electron wavefunctions ϕ_i in a way that still satisfies the Pauli exclusion principle, which can be achieved via the many-electron Slater determinant [141]:

$$\Psi(\mathbf{r}_1, ..., \mathbf{r}_N) = \frac{1}{\sqrt{N!}} \begin{vmatrix} \phi_1(\mathbf{r}_1) & \phi_1(\mathbf{r}_2) & ... & \phi_1(\mathbf{r}_N) \\ \phi_2(\mathbf{r}_1) & \phi_2(\mathbf{r}_2) & ... & \phi_2(\mathbf{r}_N) \\ \vdots & \vdots & \ddots & \vdots \\ \phi_N(\mathbf{r}_1) & \phi_N(\mathbf{r}_2) & ... & \phi_N(\mathbf{r}_N) \end{vmatrix}. \tag{2.17}$$

If we consider the expectation value of the exact expression for the electrostatic repulsion between electrons $\sum_{i\neq j}\frac{1}{|\mathbf{r}_i-\mathbf{r}_j|}$ with the wavefunctions with the Slater determinant present, we can derive two contributions to the energy for each pair of orbitals ϕ_i, ϕ_j. Firstly the Hartree term:

$$V_{\mathrm{H}} = \int \frac{|\phi_i(\mathbf{r}')|^2}{|\mathbf{r}-\mathbf{r}'|}, \tag{2.18}$$

(which is just a re-expression of equation 2.15), and secondly the exchange interaction term:

$$\int d\mathbf{r}' V_{\mathrm{X}}(\mathbf{r},\mathbf{r}')\phi_i(\mathbf{r}'), \tag{2.19}$$

where the Fock exchange potential V_{X} [142] is expressed as:

$$V_{\mathrm{X}}(\mathbf{r},\mathbf{r}') = -\sum_{j}^{\mathrm{occ}} \frac{\phi_j^*(\mathbf{r}')\phi_j(\mathbf{r})}{|\mathbf{r}-\mathbf{r}'|}. \tag{2.20}$$

The sum j is over all occupied ϕ_i with the same spin. The exchange potential corresponds to the repulsion experienced by electrons when approaching another electron same spin. A proof of this result may be found in Appendix A of ref. [143]. This is a computationally expensive term, but allows for the exact treatment of exchange. Hartree-Fock (HF) theory, which includes the exchange interaction exactly as well as the mean field repulsion, is a method well suited to finding the ground state of highly localised systems such as molecules. However, the mean field misses the dynamic fluctuations of the electronic potential that are key to the properties of many systems. The repulsion between electrons of opposite spin is dominated by this, as they have no exchange interaction. In the HF formalism, electrons of opposite spin only experience the mean field repulsion, which often causes electrons to over-localise. This is a big problem for systems such as metals and transition metal oxides, which heavily depend on rapid changes in the electronic potential.

The second quantum-mechanical feature to consider therefore is the electronic correlation— where electrons experience a repulsion due to their Coulomb interaction beyond what is predicted classically via the mean-field. The effect of correlation cannot be derived exactly for crystals, but can be approximated in various ways (discussed in the 'exchange-correlation functional' section below). Density functional theory (DFT) is an alternative strategy to HF that takes into account the effects of both exchange and correlation. We consider only single-electron wavefunctions $\phi_i(\mathbf{r})$ and not a total wavefunction. We replace the computationally expensive Fock exchange with an approximate exchange term V_{x}, and add in an approximate correlation term V_{c}. We combine these to form an (approximate) 'exchange-correlation' potential V_{xc}. The single-electron Hamiltonians in the DFT formalism are written as

$$\left[-\frac{1}{2}\nabla^2 + V_{\mathrm{n}}(\mathbf{r}) + V_{\mathrm{H}}(\mathbf{r}) + V_{\mathrm{xc}}(\mathbf{r})\right]\phi_i(\mathbf{r}) = \epsilon_i\phi_i(\mathbf{r}). \tag{2.21}$$

This equation is still an exact reformulation of the problem, though the exchange and correlation V_{xc} is approximated. Finding a suitable approximate V_{xc} that balances scientific accuracy with computational tractability has been a continuous task for theorists over recent decades, though expressions have been found that consistently lead to the correct ground states of perovskites (within the DFT framework discussed below). We decide on an optimal treatment of the exchange and correlation in more detail in the 'Exchange-correlation functional' subsection below, as it is best explained after covering the preliminaries of DFT.

2.1.6 Hohenberg-Kohn theorem

The framework behind DFT arises from the following observations made by Hohenberg and Kohn (1964). The energy E of the many-body Schrödinger equation is expressed as:

$$E = \int d\mathbf{r}_1...d\mathbf{r}_N \Psi^* \hat{H} \Psi = \langle\Psi|\hat{H}|\Psi\rangle\,. \tag{2.22}$$

As the formula for $\hat{H}$ remains fixed for a given system, a change in E must depend on a change in the total wavefunction Ψ. Specifically, a given many-body wavefunction Ψ uniquely determines the ground state energy E. Considering the all-electron Hamiltonian of our system of electrons and nuclei (equation 2.9), we can also say that Ψ is uniquely determined by the external potential V_{n} (which is determined by the nuclear positions).

Finally, it can be shown that V_{n} can be uniquely determined by the electron density n. This may be proven reductio ad-absurdum by considering the consequence of having two distinct external potentials V_{n}, V_{n}' generating the same density. The potentials generate different Hamiltonians $\hat{H}$, $\hat{H}'$, which will be identical besides the external potential term. Each Hamiltonian in-turn must have different total wavefunctions Ψ, Ψ'. As Ψ is the true ground state wavefunction of system $\hat{H}$, it can be shown that the energy of this system for any other wavefunction Ψ' must be higher than the energy than for the true ground state Ψ [144]:

$$E = \langle\Psi|\, \hat{H}\, |\Psi\rangle < \langle\Psi'|\, \hat{H}\, |\Psi'\rangle\,. \tag{2.23}$$

This is known as the Rayleigh-Ritz variational inequality and can equivalently be written for system $\hat{H}'$ where Ψ' is the true ground state:

$$E' = \langle\Psi'|\, \hat{H}'\, |\Psi'\rangle < \langle\Psi|\, \hat{H}'\, |\Psi\rangle\,. \tag{2.24}$$

If we sum these two results and consider that $\hat{H}$ and $\hat{H}'$ are identical besides the external potential terms, we obtain the statement $E + E' < E + E'$, which is a contradiction. Therefore, we can say that electron density n must uniquely determine V_{n}. This is known as the first Hohenberg-Kohn theorem [145]. In-turn, we can say that the density uniquely determines Ψ, and therefore E. This is the second Hohenberg-Kohn theorem, and it can be summarised by writing the ground state (0 K) energy E as a functional of the electron density only:

$$E = F[n]. \tag{2.25}$$

2.1.7 Kohn-Sham equations

This is the underlying theory utilised in DFT— that the key quantities of a system of electrons and nuclei can be written as a functional of the density. The next step is to derive expressions for these quantities. We return to our system where we have applied the independent electrons approximation, mean-field approximation, and approximated quantum mechanical effects by including an ‘exchange-correlation’ potential. In this theory, we do not consider the many-electron wavefunction, and simply write the electron density as in equation 2.13. The total energy can be expressed as follows:

$$E = E_{\mathrm{K.E}} + E_{\mathrm{n}} + E_{\mathrm{H}} + E_{\mathrm{xc}}, \tag{2.26}$$

where each component can be considered independently, and were derived by Kohn and Sham in 1965 [146]. Starting with the external potential energy E_{n}, considering equation 2.13, and that we have already demonstrated via the first Hohenberg-Kohn theorem that it is explicitly dependent on n:

$$E_{\mathrm{n}}[n] = \sum_i \langle\phi_i| V_n |\phi_i\rangle = \int d\mathbf{r} n(\mathbf{r}) V_{\mathrm{n}}(\mathbf{r}). \tag{2.27}$$

The kinetic energies and Hartree term may be expressed respectively as:

$$E_{\mathrm{K.E}} = \sum_i \langle\phi_i| -\frac{1}{2}\nabla^2 |\phi_i\rangle = -\sum_i \int d\mathbf{r}\phi_i^*(\mathbf{r})\frac{\nabla^2}{2}\phi_i(\mathbf{r}), \tag{2.28}$$

$$E_{\mathrm{H}} = \frac{1}{2}\sum_i \langle\phi_i| V_{\mathrm{H}} |\phi_i\rangle = \frac{1}{2}\int\int d\mathbf{r}d\mathbf{r}'\frac{n(\mathbf{r})n(\mathbf{r}')}{|\mathbf{r}-\mathbf{r}'|} \tag{2.29}$$

(where the $\frac{1}{2}$ prefactor is added to circumvent double counting). The currently undefined exchange-correlation term will be dealt with in the following subsection. For now we assume that we can write it as a functional of the density: $E_{\mathrm{xc}}[n]$. Overall, we can write the total energy as

$$E = -\sum_i \int d\mathbf{r}\phi_i^*(\mathbf{r})\frac{\nabla^2}{2}\phi_i(\mathbf{r}) + \int d\mathbf{r}n(\mathbf{r})V_{\mathrm{n}} + \frac{1}{2}\int\int d\mathbf{r}d\mathbf{r}'\frac{n(\mathbf{r})n(\mathbf{r}')}{|\mathbf{r}-\mathbf{r}'|}(\mathbf{r}) + E_{\mathrm{xc}}[n]. \tag{2.30}$$

Returning briefly to the single-electron Schrödinger equations (2.21), we can use these expressions to define V_{xc}. The Hohenberg-Kohn variational principle [145] states that the ground state density n_0 minimises the total energy, such that $\frac{\delta F[n]}{\delta n}|_{n_0} = 0$. Applying this to 2.30 automatically yields 2.21, and an expression for exchange-correlation potential:

$$V_{\mathrm{xc}}(\mathbf{r}) = \frac{\delta E_{\mathrm{xc}}[n]}{\delta n}|_{n(\mathbf{r})}. \tag{2.31}$$

The equations 2.21 are also known as the Kohn-Sham (KS) equations, and the solutions $\phi_i(\mathbf{r})$ are known as the KS orbitals.

We almost have the tools needed to find the ground state electron density, KS orbitals, and energy of a system of electrons and nuclei. The only remaining problem is that the quantities desire are circularly dependent— the KS orbitals depend on the potentials, the potentials depend on the density, and the density depends on the KS orbitals. Therefore, we need an initial guess for one of these quantities, for which we choose the density, as it is the easiest to estimate, and a natural starting point (it is the fundamental variable of DFT). There are several methods for this, in VASP we guess this based on precomputed charge densities for each ionic species— this is discussed in the 'Pseudopotentials' subsection. With this, and also a set of ionic coordinates (an initial guess of these may be taken from crystallographic data), we can build a self consistent field (SCF) cycle for finding the ground state properties. The process is visualised in Fig. 2.1. First, the nuclear potential V_n is calculated independently using the ionic positions. The initial density is then used to find the initial Hartree and exchange-correlation potentials. With these, the KS orbitals $\phi_i(\mathbf{r})$ may be found by solving the KS equations. Finally, the density may be recalculated using these single-electron wavefunctions. We then repeat the cycle until the calculated density matches the input within a specified tolerance. When this tolerance is achieved, we have obtained the ground state density, energy, and KS orbitals.

2.1.8 Exchange-correlation functional

Currently, no exact form of $E_\mathrm{xc}[n]$ exists, but many good approximations have been developed over recent decades. We seek a form of it that balances scientific accuracy and computational cost, which obtains the correct ground state for perovskites while remaining computationally tractable for large interfaces of several hundred atoms.

Local density approximation

The local density approximation (LDA) assumes that the energy at any point is the same as that in a uniform electron gas of the same density [147–149]. The

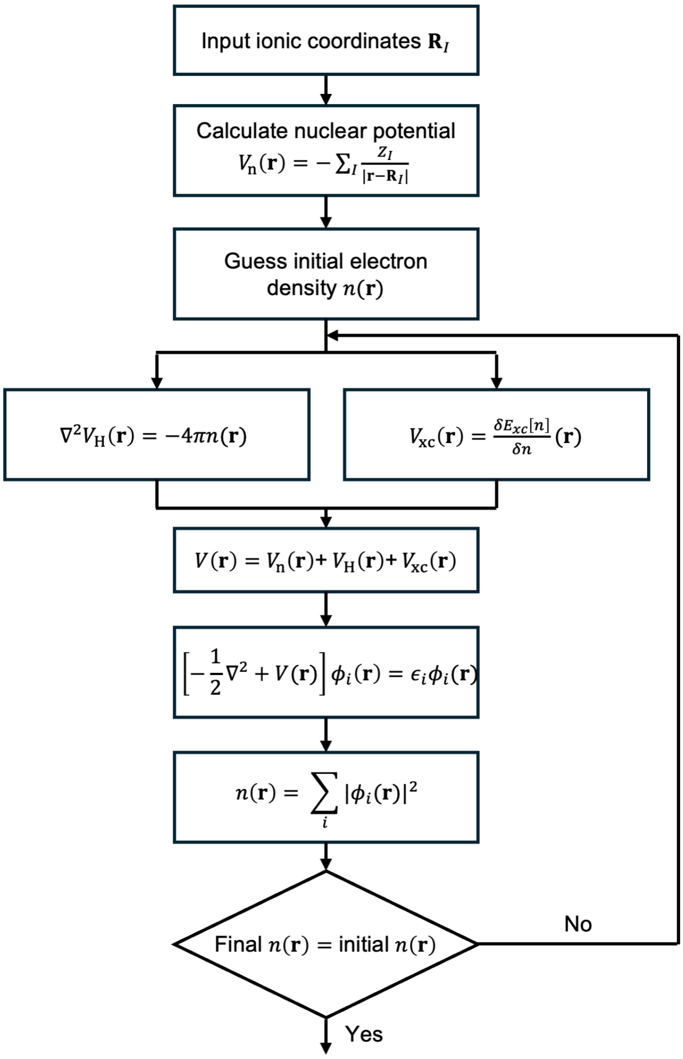

Figure 2.1: Flowchart of the self-consistent field cycle, based on Fig. 3.3 in ref. [143].

exchange correlation energy is expressed as the projection of the KS orbitals onto the exchange-correlation energy density functional of a uniform electron gas (where a gas of electrons is constrained in a box of volume Ω and the potential of the nuclei are considered constant):

$$E_{\text{xc}}^{\text{LDA}}[n(\mathbf{r})] = \int d\mathbf{r} n(\mathbf{r}) \epsilon_{\text{xc}}^{\text{unif}}[n(\mathbf{r})], \tag{2.32}$$

where $\epsilon_{\text{xc}}^{\text{unif}}[n(\mathbf{r})]$ is the energy per particle of a uniform electron gas of charge density n. The expression for $E_{\text{xc}}^{\text{LDA}}[n(\mathbf{r})]$ is found from parameterised Quantum Monte-Carlo calculations and is included in Appendix A.1.

Generalised gradient approximation

We can improve the local density approximation by rewriting E_{xc} as a functional of both the electron density n and the gradient of the electron density $|\nabla n|$ [150]. This is known as the generalised gradient approximation (GGA). Several GGA-based functionals have been proposed over the years. A popular GGA functional known as PBE (proposed by Perdew, Burke and Ernzerhof) [151], has been shown to consistently improve total energies, atomization energies, energy barriers, and structural energy differences for solids including perovskites [152,153]. It is expressed (spin-independently) in the following form:

$$E_{\text{xc}}^{\text{PBE}}[n] = \int d\mathbf{r}\, n(\mathbf{r}) \epsilon_{\text{x}}^{\text{unif}}[n] F_{\text{xc}}[n, |\nabla n|], \tag{2.33}$$

where $\epsilon_{\text{x}}^{\text{unif}}$ is the exchange energy functional of the homogeneous electron gas as specified in Appendix A.1, and F_{xc} is an enhancement factor, expressed in terms of both the density n and gradient of the density $|\nabla n|$. Though we already have expressions for $\epsilon_{\text{xc}}^{\text{unif}}$, an exact form of F_{xc} is unknown— various models have been proposed for different systems. The form of F_{xc} in the PBE approach may be found in ref. [151]. Generally, the main dilemma in building a GGA E_{xc} is that only a maximum of two of the following three conditions may be true for a given functional:

1. exact second order gradient expansion for exchange,
2. exact second order gradient expansion for correlation,

3. retention of the LDA-like linear response of a uniform electron gas.

For our calculations, we choose an option most suited to tightly-packed crystalline solids, PBEsol (Perdew, Burke, Ernzerhof) [154]. PBEsol is a refinement of the PBE functional for solids, using a modified F_{xc} from the PBE approach. With respect to the three conditions above, PBE satisfies the second and third constraint, while PBEsol satisfies the first, and approximates the second and third. PBEsol consistently obtains more accurate lattice parameters than PBE and LDA for bulk perovskites [155, 156]. A detailed description of the PBEsol functional can be found in ref. [154]. PBEsol is also computationally tractable for every system studied in this project, including large interfaces. Other functionals such as vdW-DF [157] or various hybrid functionals (which hybridise the exact treatment of exchange exactly used in HF theory with the partial treatment of exchange and correlation used in DFT [158]), typically generate more accurate lattice parameters and band gaps respectively, but these are far more computationally expensive.

2.1.9 Plane-wave basis

To compute the orbitals $\phi_i(\mathbf{r})$ it is necessary to specify a basis set. As we are dealing with a crystal unit cell with periodic boundary conditions, we can apply Bloch's theorem [159], which states that any functions within the unit cell must be equally periodic. This includes the KS orbitals ϕ_i, density $n(\mathbf{r})$ and cell potentials $V(\mathbf{r})$. We can express the KS orbitals as:

$$\phi_{i,\mathbf{k}}(\mathbf{r}+\mathbf{R}) = \phi_{i,\mathbf{k}}(\mathbf{r})e^{i\mathbf{k}\cdot\mathbf{R}}, \tag{2.34}$$

where the $\mathbf{k}$ is the reciprocal vector, i is $\sqrt{-1}$ (not to be confused with the subscript $_i$), $\mathbf{R}$ is a periodic translation and subscript k is added to $\phi_{i,\mathbf{k}}$ to denote cell periodicity (these are also referred to as Bloch functions). Given $\phi_{i,\mathbf{k}}(\mathbf{r})$ are periodic,

$$\phi_{i,\mathbf{k}}(\mathbf{r}) = u_{i,\mathbf{k}}(\mathbf{r})e^{i\mathbf{k}\cdot\mathbf{r}}, \tag{2.35}$$

where

$$u_{i,\mathbf{k}}(\mathbf{r}+\mathbf{R}) = u_{i,\mathbf{k}}(\mathbf{r}) \tag{2.36}$$

are the periodic components of the Bloch functions.

In a plane-wave basis, all periodic quantities are expressed as a set of Fourier components. Due to translational symmetry, the expansion must only include plane waves that have the periodicity of the lattice: $\mathbf{k} = \mathbf{G}$, where $\mathbf{G} = m_1\mathbf{a}_k + m_2\mathbf{b}_k + m_3\mathbf{c}_k$ and indices m are integers. The KS orbitals are therefore expressed in the form:

$$\phi_{i,\mathbf{k}}(\mathbf{r}) = \frac{1}{\sqrt{\Omega}} \sum_{\mathbf{G}} C_{\mathbf{G},i,\mathbf{k}} e^{i(\mathbf{G}+\mathbf{k})\cdot\mathbf{r}}, \tag{2.37}$$

such that

$$u_{i,\mathbf{k}}(\mathbf{r}) = \frac{1}{\sqrt{\Omega}} \sum_{\mathbf{G}} C_{\mathbf{G},i,\mathbf{k}} e^{i\mathbf{G}\cdot\mathbf{r}}, \tag{2.38}$$

where Ω is the cell volume, and $C_{\mathbf{G},i,\mathbf{k}}$ are Fourier expansion coefficients [160, 161]. The electron density and potential are expressed in the same format:

$$n(\mathbf{r}) = \sum_{\mathbf{G}} n_{\mathbf{G}} e^{i\mathbf{G}\cdot\mathbf{r}}, \tag{2.39}$$

$$V(\mathbf{r}) = \sum_{\mathbf{G}} V_{\mathbf{G}} e^{i\mathbf{G}\cdot\mathbf{r}}, \tag{2.40}$$

where $n_{\mathbf{G}}$ and $V_{\mathbf{G}}$ are expansion coefficients. It is also easy to switch between reciprocal space and real space via the Fast Fourier Transform (FFT) [162], a computationally inexpensive algorithm for converting the expansion coefficients:

$$C_{\mathbf{r},i,\mathbf{k}} = \sum_{\mathbf{G}} C_{\mathbf{G},i,\mathbf{k}} e^{i\mathbf{G}\cdot\mathbf{r}} \quad \overset{\text{FFT}}{\Longleftrightarrow} \quad C_{\mathbf{G},i,\mathbf{k}} = \frac{1}{N_{\mathrm{G}}} \sum_{\mathbf{r}} C_{\mathbf{r},i,\mathbf{k}} e^{-i\mathbf{G}\cdot\mathbf{r}}, \tag{2.41}$$

where N_{G} is the number of $\mathbf{G}$ vectors (in real space, $\mathbf{R}$) included in the summation. The summation over $\mathbf{G}$ is infinite, so must be truncated to be practical. To do this, we specify a plane-wave energy cut-off, the maximum quantum mechanical kinetic energy associated with the plane wave of the largest $\mathbf{G}$ vector:

$$E_{\mathrm{cut}} = \frac{|\mathbf{G}|^2}{2}. \tag{2.42}$$

This defines our plane-wave basis set. In practice, it is essential to undergo a plane-wave energy cut-off convergence test, where E_{cut} is varied until the properties of the system (such as the total energy, ionic forces, and stresses) converge to a suitable tolerance. We desire a plane wave cut-off that obtains sufficiently accurate results, while remaining computationally feasible. The plane-wave basis is convenient because it allows us to efficiently switch between real- and k-space using FFT's. In practice, VASP typically uses a cut-off of $2 \times E_{\text{cut}}$ specified in our results chapters, because many terms such as the density n depend on the square of the wavefunction (if the cut-off is not doubled, much of the information is lost— a factor of 2 is roughly enough to account for this). This precision is used for all calculations in this study unless specified otherwise. The plane-wave cut-off energies used in our calculations are specified in each chapter.

2.1.10 K-point sampling

The plane-wave basis is also highly convenient for dealing with the many complex integrals in the SCF cycle that cannot be solved analytically. These may be converted to integrals over the 1BZ in k-space, which can be solved numerically. We assume that the cell quantities remain approximately fixed close to a given k-point, and that we can obtain most of the information of the cell by only integrating over a finite number of k-points.

For a given system, we can further simplify any integrals over the 1BZ by only considering the irreducible Brillouin zone (IBZ), which only includes symmetrically inequivalent points of the unit cell. For an integral over a given IBZ, we evaluate only the inequivalent points and multiply by their weightings. Generally an integral over a quantity F (in k-space) can be expressed as

$$\frac{1}{\Omega} \int_{\text{BZ}} F(\mathbf{k}) d\mathbf{k} = \frac{1}{N_{\text{k,tot}}} \sum_{l} N_{\text{k},l} \times F(\mathbf{k}_l), \tag{2.43}$$

where $\mathbf{k}_l$ are the inequivalent k-points, $N_{\text{k},l}$ are the weightings of $\mathbf{k}_l$, and $N_{\text{k,tot}}$ is the total number of k-points in the 1BZ.

As with the plane-wave cut-off energy, the number of k-points and their distribution must be optimised to balance accuracy and computational cost. Therefore, we undertake a k-grid convergence test, where we vary the grid until the relevant properties (stresses, forces, total energy) converge. The k-grids used in our calculations are specified in each chapter.

A moderately sized grid is acceptable for most insulators, where quantities tend to vary smoothly across the 1BZ, though metals are far more volatile, especially around the Fermi surface, and tend to require much denser grids. In our calculations, we use an automatic meshing scheme as proposed by VASP, where we converge a k-point density rather than a fixed grid for each cell (which would require separate convergence tests for each and every cell shape we use throughout the study). The specified density automatically generates a k-point grid for a given unit cell.

2.1.11 Pseudopotentials

Another helpful approximation for greatly reducing the computational cost of DFT calculations is to simplify the effects of electrons near the cores of the ions. These electrons are strongly localized, and usually interact in a simple, predictable way. They also tend to rapidly oscillate near the core, such that they make up the majority of the computational cost. To deal with this, we replace the hard nuclear potential and the core electrons with a pre-computed potential known as a pseudopotential. The remaining valence electrons are treated as normal by DFT.

In this project, we use the PBE-generated Projector-Augmented-Wave (PAW) potentials [163, 164]. Rather than considering the KS orbitals $|\phi_{i,\mathbf{k}}\rangle$ in our calculations, we only calculate for the pseudised wavefunctions $|\tilde{\phi}_{i,\mathbf{k}}\rangle$, which are equal to $|\phi_{i,\mathbf{k}}\rangle$ outside the core but smoothed inside. The core is replaced with a predetermined function of $|\tilde{\phi}_{i,\mathbf{k}}\rangle$. The Kohn-Sham orbitals are re-expressed as:

$$|\phi_{i,\mathbf{k}}\rangle = |\tilde{\phi}_{i,\mathbf{k}}\rangle + \sum_j \left(|w_j\rangle - |\tilde{w}_j\rangle\right) \langle \tilde{p}_j|\tilde{\phi}_{i,\mathbf{k}}\rangle, \tag{2.44}$$

where $|w_j\rangle$ are partial waves— solutions to the all-electron Schrödinger equation for an isolated atom, $|\tilde{w}_j\rangle$ are pseudised partial waves equal to $|w_j\rangle$ outside the core but smooth within, and $|\tilde{p}_j\rangle$ are projectors determining the weighting of $|w_j\rangle$, $|\tilde{w}_j\rangle$. The summation is over the j all-electron partial waves $|w_j\rangle$, which are solutions to the radial scalar all-electron Schrödinger equation for a given isolated atomic species. A more detailed description of these quantities may be found in refs [163, 164].

The components $|w_j\rangle$, $|\tilde{w}_j\rangle$, and $|p_j\rangle$ are all pre-computed. The only variable term within the SCF cycle is $|\tilde{\phi}_i\rangle$, where the coefficients (with respect to the plane-wave basis) are varied. Updated expressions for the SCF cycle may also be found in refs. [163, 164].

2.1.12 Geometry optimisation

Though we now have a method for finding the energy of a given set of ionic coordinates, we require an additional procedure for finding the ground state crystal structure. At the ground state energy, the total force experienced by each nuclei will be 0 (in practice, a tolerance of 1×10^{-3} eV/Å is used unless specified otherwise). We can find the ground state structure by determining a procedure for computing the forces on each ion, and for suggesting new ionic positions that minimise these forces.

When applying the Born-Oppenheimer approximation we decoupled the electronic and nuclear motion. We can therefore make the approximation that the full many body wavefunction $\Psi(\mathbf{r}_1, ..., \mathbf{r}_N, \mathbf{R}_1, ..., \mathbf{R}_M)$ can be decomposed into two equations, one for electrons and one for nuclei. As we already have the electronic ground state for a given set of ionic positions $\{\mathbf{R}\}$, we write the total wavefunction as a product of the electron-only wavefunction $\Psi_{e,\{\mathbf{R}\}}$ and the nuclear-only wavefunction χ:

$$\Psi(\mathbf{r}_1, ..., \mathbf{r}_N, \mathbf{R}_1, ..., \mathbf{R}_M) = \Psi_{e,\{\mathbf{R}\}}(\mathbf{r}_1, ..., \mathbf{r}_N)\chi(\mathbf{R}_1, ..., \mathbf{R}_M). \tag{2.45}$$

So far, we have calculated $\Psi_{e,\{\mathbf{R}\}}$ for a fixed set of nuclear positions. If we were to allow the ions to move slightly, we can assume that the $\Psi_{e,\{\mathbf{R}\}}$ won't change much, as it only depends on $\{\mathbf{R}\}$ parametrically. Rewriting the many-body Schrödinger equation (eqn. 2.8) in terms of the electronic wavefunction (with respect to $\{\mathbf{R}\}$)

we obtain:

$$\left[-\sum_i \frac{\nabla_i^2}{2} + \sum_i V_n(\mathbf{r}_i;\{\mathbf{R}\}) + \frac{1}{2}\sum_{i\neq j}\frac{1}{|\mathbf{r}_i - \mathbf{r}_j|}\right]\Psi_{e,\{\mathbf{R}\}} = E_{e,\{\mathbf{R}\}}\Psi_{e,\{\mathbf{R}\}}, \tag{2.46}$$

where the terms in brackets make up the electronic Hamiltonian $\hat{H}_{e,\{\mathbf{R}\}}$. The many-body Schrodinger equation can therefore be rewritten as:

$$\left[-\sum_I \frac{\nabla_I^2}{2M_I} + \frac{1}{2}\sum_{I\neq J}\frac{Z_I Z_J}{|\mathbf{R}_I - \mathbf{R}_J|} + E_{e,\{\mathbf{R}\}}\right]\chi = E_{\mathrm{tot}}\chi, \tag{2.47}$$

where the three terms in the brackets can be denoted as the nuclear Hamiltonian $\hat{H}_{\mathrm{n}}$. The second and third term make up the potential energy of the nuclei U:

$$U(\{\mathbf{R}\}) = \frac{1}{2}\sum_{I\neq J}\frac{Z_I Z_J}{|\mathbf{R}_I - \mathbf{R}_J|} + E_{e,\{\mathbf{R}\}}, \tag{2.48}$$

which can be used to calculate the ionic forces. It can be observed that when computing the nuclear and electronic wavefunctions for a given potential energy profile, due to the heavier mass of the nuclei, the nuclear potential tends to be heavily localised in a narrow region of space compared the electronic wavefunction [143]. We make the assumption that the nuclei behaves more like a classical point particle, and that we can model the ionic forces classically:

$$\mathbf{F}_I \equiv M_I \frac{d^2\mathbf{R}_I}{dt^2} = -\frac{\partial U}{\partial \mathbf{R}_I}(\{\mathbf{R}\}), \tag{2.49}$$

where $\mathbf{F}_I$ are the ionic forces. The derivative of first term in U can be easily determined, while the derivative of $E_{e,\{\mathbf{R}\}}$ can be resolved using the Hellmann-Feynman theorem [165, 166], which states that the derivative of the energy eigenvalue E with respect to any variable, in this case the ionic position $\mathbf{R}_I$, can be written as the expectation value of the derivative of the Hamiltonian (in our case, the electronic one $\hat{H}_{e,\{\mathbf{R}\}}$):

$$\frac{\partial E_{e,\{\mathbf{R}\}}}{\partial \mathbf{R}_I} = \int d\mathbf{r}\Psi^*_{e,\{\mathbf{R}\}}\frac{\partial \hat{H}_{e,\{\mathbf{R}\}}}{\partial \mathbf{R}_I}\Psi_{e,\{\mathbf{R}\}}. \tag{2.50}$$

Out of the expressions in the electronic Hamiltonian, only the external potential depends on $\{\mathbf{R}\}$. The general expression for $\frac{\partial E_{e,\{\mathbf{R}\}}}{\partial \mathbf{R}_I}$ is:

$$\frac{\partial E_{e,\{\mathbf{R}\}}}{\partial \mathbf{R}_I} = Z_I \int d\mathbf{r} n(\mathbf{r}) \frac{\mathbf{r} - \mathbf{R}_I}{|\mathbf{r} - \mathbf{R}_I|^3}. \tag{2.51}$$

As we are using PAW potentials in our calculations, which are centered and thus dependent on the ionic positions $\{\mathbf{R}\}$, we also have to include a contribution $\mathbf{F}_I^{\mathrm{PAW}}$, for which expressions may be found in ref. [163]. We note that general Pulay contributions to the forces are omitted, as we are using plane waves, which besides the PAW contribution are independent of ionic positions [164]. With this considered, we obtain a general expression for the ionic forces:

$$\mathbf{F}_I = Z_I \left[\int d\mathbf{r} n(\mathbf{r}) \frac{\mathbf{r} - \mathbf{R}_I}{|\mathbf{r} - \mathbf{R}_I|^3} - \sum_{J \neq I} Z_J \frac{\mathbf{R}_J - \mathbf{R}_I}{|\mathbf{R}_J - \mathbf{R}_I|^3} \right] + \mathbf{F}_I^{\mathrm{PAW}}. \tag{2.52}$$

The ionic forces determine all the displacements within the unit cell. However, they do not consider changes outside the unit cell. The elastic strain on the cell $\epsilon_{\alpha\beta}$ must also be determined to optimise the structure, and is instead determined by the stresses $\sigma_{\alpha\beta}$:

$$\sigma_{\alpha\beta} = -\frac{1}{\Omega} \frac{\partial U}{\partial \epsilon_{\alpha\beta}}. \tag{2.53}$$

The strain tensor generally has nine unique components (in higher symmetry cells, some terms become equivalent):

$$\epsilon_{\alpha\beta} = \begin{pmatrix} \epsilon_{xx} & \epsilon_{xy} & \epsilon_{xz} \\ \epsilon_{yx} & \epsilon_{yy} & \epsilon_{yz} \\ \epsilon_{zx} & \epsilon_{zy} & \epsilon_{zz} \end{pmatrix}. \tag{2.54}$$

An equivalent expansion exists for $\sigma_{\alpha\beta}$. Generally, when we apply a strain $\epsilon_{\alpha\beta}$ to coordinate r_α, it changes to:

$$r_\alpha \rightarrow \sum_\beta (\delta_{\alpha\beta} + \epsilon_{\alpha\beta}) r_\beta, \tag{2.55}$$

where $\delta_{\alpha\beta}$ is Kronecker's delta. As with the forces, we require a general expression for the stresses, as a functional of the electron density, which is achieved by evaluating eqn. 2.53. The resulting expressions may be found in Appendix G of ref. [167].

Lastly, we need a system for suggesting new ionic positions and cell parameters based on the forces and stresses. For this we use the conjugate gradient algorithm—the details of which may be found in ref. [168]. In all, the ionic relaxation procedure can be visualised in Fig 2.2. In practice, the ground state can still be tricky to obtain for systems with flat energy landscapes, where several local minima exist that can be mistaken for the ground state. In this study, we regularly work with large interfaced systems with very low cell symmetries and many local minima. To find the ground state, it is therefore necessary to test a variety of input geometries. All possible geometries for both substrate and film should be relaxed in order to obtain a useful answer. To predict possible geometries, a prior understanding of the films in bulk or under strain alone (in the form of 'bulk-strained' calculations) is essential.

By 'bulk-strained' calculations, we are referring to the relaxation of bulk cells with the in-plane lattice parameters fixed. The relaxation procedure is completed as for any bulk system, except the in-plane stress components $\epsilon_{xx,xy,xz,yx,yy,yz}$ (and therefore the in-plane lattice parameters) are all kept fixed (while $\epsilon_{zx,zy,zz}$ may relax). This constraint was included in the geometry optimisation procedure via the 'vasp-opt-axis' patch [169].

2.1.13 Further details and corrections

Hubbard-U and Hund-J corrections

The following subsections will cover any additional corrections applied to our first principles calculations in order to improve convergence and accuracy. The first of these involves dealing with the inexactness of the exchange and correlation interactions, which can considerably affect the ground state of some systems. In LDA and GGA functionals, inaccuracies in the correlation can be large enough to substantially affect strongly correlated systems such as Mott-insulators, where the ground state is sensitive to the electron-electron interaction [170]. The errors in E_{xc} result in the under-localisation of the orbitals, which results in insulators incorrectly appearing

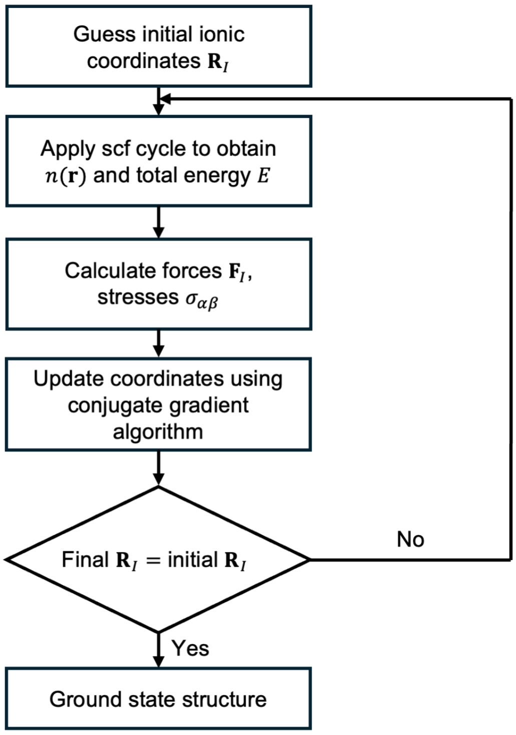

Figure 2.2: Flowchart of geometry optimisation, based on Fig. 4.4 in ref. [143]

metallic. Alongside this, the imperfect exchange contribution means that the self interaction of each electron is not completely cancelled, which further delocalises the orbitals [171].

To mitigate these errors, we introduce an additional on-site Coulomb interaction $+U$, which is equivalent to an additional Coulomb energy cost for placing two electrons on the same site. This penalises partial occupancies in a subshell, encouraging localisation. This is known as the Hubbard-U potential [172–174], and is a useful tool for systems with partially filled d- and f-states, such as the rare-earth nickelates [175–178].

It is also worth mentioning the Hund-J correction. Because of the error in the exchange interaction, systems tend to overestimate the effect of crystal field splitting (due to underestimated exchange) and encourage pair bonding, forming low-spin states. This is rather than forming high-spin states where electrons spread out into higher energy orbitals [173, 179, 180]. The $+J$ correction applies an additional energy lowering when electrons occupy different orbitals, which reduces the tendency to relax low-spin configurations rather than high-spin.

There are several implementations of these corrections with DFT, for which we test both the model of Dudarev [180], and Liechtenstein [173]. The former involves the use of an effective $U_{\text{eff}} = U - J$, while the latter allows for individual determination of U and J. Further details on the practical implementation of these methods may be found in Appendix A.2.

Magnetism

The rare-earth nickelates are spin-polarised. In this study, we found that collinear spin structures sufficiently recreate experimental observations, so do not discuss non-collinear theory (see chapter 4 for more details regarding this— the observed experimental nickelate magnetic order is non-collinear, but it has been shown previously and demonstrated again here that this is not necessary for recreating experiment). To consider magnetisation we rewrite the key quantities to have distinct spin-up ($\sigma =\uparrow$) and spin-down ($\sigma =\downarrow$) components. The KS orbitals are re-expressed as

$$|\phi_i\rangle \implies \begin{pmatrix} |\phi_i^{\uparrow}\rangle \\ |\phi_i^{\downarrow}\rangle \end{pmatrix}, \tag{2.56}$$

such that we obtain separate spin-up and spin-down densities:

$$n_\sigma(\mathbf{r}) = \sum_i \phi_{i,\sigma}(\mathbf{r})^2. \tag{2.57}$$

The single-electron effective potentials become spin-dependent:

$$V_\sigma^{\text{KS}}(\mathbf{r}) = V_{\text{n}}(\mathbf{r}) + V_{\text{H}}(\mathbf{r}) + \frac{\delta E_{\text{xc}}[n_\uparrow, n_\downarrow]}{\delta n_\sigma}, \tag{2.58}$$

such that we have separate many-electron Hamiltonians for spin-up and spin-down components:

$$\left[-\frac{1}{2}\nabla^2 + V_\sigma^{\text{KS}}(\mathbf{r})\right] \phi_{i,\sigma} = \epsilon_i \phi_{i,\sigma} \tag{2.59}$$

The equations for spin-dependent E_{xc} may be found for LDA, PBE and PBEsol in refs. [151, 154, 181].

We initialise spins in our calculations with a set of input magnetic moments chosen at our discretion. We note that converging the desired magnetic order can be very challenging given the many metastable orders present for most magnetic systems, and typically requires some trial and error with the input moments, alongside some tuning of the magnetic mixing parameters (useful controls included in VASP that alter how the moments can vary within the SCF cycle). This is particularly true for interface calculations involving the nickelates— details on this are mentioned throughout chapters 4—6.

2.2 Post processing tools

The above regard the computation of the ground state structure, energy, and magnetic order. However, there are several additional useful properties we investigate that are calculated after obtaining the ground state.

2.2.1 Structural characterisation

To analyse our ground state structure, we require a tool that characterises the symmetry and mode amplitudes from a set of ionic coordinates and lattice vectors. For bulk and strained unit cells, we are able to do this from first principles using mode irreducible representation analysis, provided by the ISOTROPY suite.

To find the symmetry of the cell, we use the 'FINDSYM' tool [182], which is able to detect the space group of a cell from a set of ionic coordinates and lattice parameters. To measure the mode irrep amplitudes with respect to a high-symmetry reference cell we use the 'ISODISTORT' tool [183, 184], which generates volume-averaged amplitudes (structural distortions are in Å, while strain modes are unitless). We have also used the 'INVARIANTS' tool [185] to generate the allowed LGD expansion terms for given cell symmetries. Further details on each procedure may be found in refs. [182–185].

For analysing large interfaced systems where structural distortions vary layer-by-layer (where mode irrep analysis is not appropriate), we directly measure the main structural quantities where possible. For this we use the python-based analysis tool

‘Perovscripts’, courtesy of O. Diéguez [186].

2.2.2 Polarisation

Modern theory of polarisation

As we are investigating ferroelectrics and polar materials, we seek to measure the polarisation of our ground state system. For this, we would need the charges and coordinates of the electrons and nuclei. Though we can define the positions and charges of nuclei, we must find a way to approximate the charge centres of an electronic wavefunction. We already made a minor shortcut by choosing valence and core electrons, where the total charge of the core electrons can be assumed to average out at the nuclear positions (we can say that the charge at each ionic coordinate is therefore the sum of the nuclear charges and core electrons specified by our PAW potentials). The remaining valence electrons make up the delocalised KS orbitals. We can find the average charge centres of the KS orbitals in real space by finding the Wannier functions $W_{i,\mathbf{R}}(\boldsymbol{r})$ [187, 188], which are the inverse Fourier transforms of the Bloch functions $\phi_{i,\mathbf{k}}$:

$$W_{i,\mathbf{R}}(\mathbf{r}) = \frac{\Omega}{(2\pi)^3} \sum_{\mathbf{k}} e^{i\mathbf{k}\cdot\mathbf{R}} \phi_{i,\mathbf{k}}(\mathbf{r}). \tag{2.60}$$

As the Wannier functions are localised, we can define an averaged centre of charge $\bar{\mathbf{r}}_i$ for each, which we refer to as a Wannier centre. These can be obtained by taking the expectation value of the position operator $\hat{\mathbf{r}}$ ($= -i\frac{\partial}{\partial \mathbf{k}}$ in momentum space) with respect to $W_{i,\mathbf{R}}(\mathbf{r})$ [189]:

$$\bar{\mathbf{r}}_i = \int W^*_{i,\mathbf{R}}(\mathbf{r})\hat{\mathbf{r}}W_{i,\mathbf{R}}(\mathbf{r})d^3\mathbf{r} = i\frac{\Omega}{(2\pi)^3}\int_{\mathrm{BZ}} d^3\mathbf{k}e^{-i\mathbf{k}\cdot\mathbf{R}}\langle u_{i,\mathbf{k}}|\frac{\partial u_{i,\mathbf{k}}}{\partial \mathbf{k}}\rangle, \tag{2.61}$$

where $u_{i,\mathbf{k}}$ are the periodic components of the Bloch functions as defined previously. In our study, we use the Wannier90 package [190, 191] to compute the Wannier functions, which are maximally localised as to minimise their spread [192]. A detailed discussion of this procedure may be found in ref. [193].

The Wannier centres of the valence electrons and ionic coordinates may be used to calculate the polarisation using the formula:

$$\mathbf{P} = \frac{1}{\Omega}\left[\sum_I q_I \mathbf{R}_I + \sum_i^{\text{occ}} e\bar{\mathbf{r}}_i\right], \tag{2.62}$$

where $\mathbf{P}$ is the polarisation in vector format, $q_I = Z_I + n_{\text{core},I}$ (where Z_I is the nuclear charge, and $n_{\text{core},I}$ are the core electrons) and $\mathbf{R}_I$ are the ionic coordinates [194–197].

As the Bloch functions are only defined within a phase factor, the Wannier centres individually are not well-defined, retaining gauge freedom. The maximal localisation procedure minimises this freedom, such that the resulting sum of the Wannier centres is well defined. The sum still remains multivalued however, meaning the polarisation is also multivalued— differing by a fixed value Q_P, known as the polarisation quantum [194–197]. This condition is equivalent to the consequences of being able to draw crystal unit cell in infinitely many ways due to translational symmetry. This is the modern theory of polarisation, and must be considered when comparing results to one-another.

Berry phase

We can also calculate this polarisation directly and avoid having to calculate the Wannier centres via the Berry phase approach. For this we consider the change in polarisation from an unpolarised state to our polarised electronic ground state [195, 196, 198, 199], which using the above expressions yields:

$$\Delta\mathbf{P} = \mathbf{P}^f - \mathbf{P}^0 = \frac{1}{\Omega}\left[\sum_I q_I^f \mathbf{r}_I^f - q_I^0 \mathbf{r}_I^0\right] - \frac{2ie}{(2\pi)^3}\sum_i^{\text{occ}} \int_{\text{BZ}} e^{-i\mathbf{k}\cdot\mathbf{R}} \langle u_{i,\mathbf{k}}^f | \frac{\partial u_{i,\mathbf{k}}^f}{\partial \mathbf{k}} \rangle - \langle u_{i,\mathbf{k}}^0 | \frac{\partial u_{i,\mathbf{k}}^0}{\partial \mathbf{k}} \rangle. \tag{2.63}$$

This is equivalent to the Berry phase obtained by the Bloch functions while evolving the state along $\mathbf{k}$, and remains modulo Q_P. It has been shown that we can measure this quantity by only considering the Bloch states of our polarised electronic ground state [195], such that the polarisation may be calculated directly in VASP from the ground state structure and KS orbitals.

2.2.3 Dielectric response

The dielectric response is the measure of how easily a system polarises under an applied electric field. This is a useful quantity for predicting the softening of the polar mode. The static dielectric tensor is simply the ratio of the applied field to the polarisation:

$$\mathbf{P} = \epsilon_0 \chi \mathbf{E}, \tag{2.64}$$

where $\chi = \chi_e + \chi_I$ is the dielectric tensor, which in our calculations is composed of electronic (χ_e) and ionic (χ_I) components respectively. We do not consider the frequency-dependent dielectric response in this study.

To find the dielectric tensor, we use density functional perturbation theory (DFPT), to measure how small periodic deviations in the electric field affect the Bloch states $u_{i,\mathbf{k}}$. This is achieved by first finding the derivative of the Bloch functions (with respect to $\mathbf{k}$) $|\partial_{\mathbf{k}} u_{i,\mathbf{k}}\rangle$ using a linear Sternheimer equation, which can be used to compute the linear response to a periodic electric field $|\partial_E u_{i,\mathbf{k}}\rangle$ using another Sternheimer equation [200, 201]. A general Sternheimer equation for a perturbation λ is written as

$$\left[\hat{H}(\mathbf{k}) - \epsilon_{i,\mathbf{k}}\right] |\partial_\lambda u_{i,\mathbf{k}}\rangle = -\partial_\lambda \left[\hat{H}(\mathbf{k}) - \epsilon_{i,\mathbf{k}}\right] |u_{i,\mathbf{k}}\rangle \,. \tag{2.65}$$

Further details of the dielectric response in the LDA and PAW formalisms using this methodology may be found in refs. [200] and [201] respectively.

2.2.4 Band structure, density of states and macroscopically averaged potential

Though the electronic band structure and density of states are calculated from the SCF cycle, it is necessary to mention a few details on their computation in this study. The band structure is simply a visual plot of the KS-orbitals as a function of k. To find the shortest possible k-path containing all the high symmetry points of a given crystal unit cell, we use the 'seekpath' tool [202, 203]. To visualise the band structure accurately, we recompute the KS-orbitals at a higher resolution along these paths, which allow for the accurate computation of the band gap E_g in insulators. We use the 'pymatgen' package for visualising the band structures and measuring E_g [204].

It is also useful to visualise the density of states (DOS), the number of states per energy. The total DOS $D(E)$ is simply

$$D(E) = \sum_i \sum_{\mathbf{k}} \delta(E - \epsilon_{i,\mathbf{k}}), \tag{2.66}$$

where E denotes energy, usually defined relative to the Fermi level E_{F}. This can easily be extended to the spin-dependent DOS by summing the spin-up and spin-down orbitals separately.

Another useful quantity to plot is the projected DOS (PDOS) $D_I(E)$, which aims to consider only the states associated with a given ionic site I. This can be achieved by applying a weighting to the states equal to the projection of an atomic-like basis function $|w_I\rangle$ onto the KS orbitals:

$$D_I(E) = \sum_i \sum_{\mathbf{k}} |\langle w_I | \phi_{i,\mathbf{k}} \rangle|^2 \delta(E - \epsilon_{i,\mathbf{k}}), \tag{2.67}$$

where the basis functions in VASP are based on the PAW formalism. These are particularly useful for estimating the density of states per layer in interfaced systems, where the PDOS may be summed for every species within a given layer. The DOS and PDOS are also plotted using the 'pymatgen' package.

When investigating interfaced systems, we also look to the macroscopically averaged potential (MAP) across the system, which makes any potential gradients easier to identify and measure. The total potential (in real space) is already calculated in the SCF cycle:

$$V_{\mathrm{tot}} = V_{\mathrm{n}} + V_{\mathrm{H}} + V_{\mathrm{xc}}. \tag{2.68}$$

To visualise the potential gradient along the $\hat{c}$ direction in an interfaced system, we can take the average potential in-plane, then macroscopically average over the interlayer distance along $\hat{c}$. The averaging procedure was completed using the 'vaspkit' package [205].

CHAPTER 3

Bulk, [001]- and [111]-strained $SrTiO_3$

Prior to studying complex interfaced systems, we seek a detailed theoretical description of $SrTiO_3$ (STO) (and equivalently $NdNiO_3$, which we discuss in the following chapter) as a bulk crystal. The ground state bulk STO structure remains subtle. As a quantum paraelectric, it is predicted that in the absence of quantum energy fluctuations, STO may stabilise a polar ground state. We present a detailed investigation into this bulk system, where we uncover a complex energy landscape alluding to the near-stabilisation of several unique phases, both polar and non-polar. We then extend our investigation to take into account the effect of epitaxial strain, where we report the phase diagrams of STO under the application of compressive and tensile [001]- and [111]-strain. In both orientations, phase transitions occur that lead to strongly stabilised ferroelectric phases. We also report a detailed investigation into the electronic properties of STO, where we find significant variation in the dielectric response and Berry phase polarisation for bulk, [001]-, and [111]-strain.

3.1 Introduction and methods

Strontium Titanate (STO) is one of the most fruitful perovskites to be discovered. It remains at the forefront of research into complex oxides and novel electronic phenomena, where the yearning for a deeper understanding of its properties has led to seemingly endless new physics. In bulk, it is a quantum paraelectric [35–42], meaning it is experimentally observed as a paraelectric down to temperatures as low as 1.5 K [35, 37], but only due to small quantum energy fluctuations (as well as subtle thermal fluctuations), which if absent, the system would be able to turn polar [38, 43]. Quantum fluctuations are estimated to be $\sim$2 meV at the ground state and are strong enough to completely suppress the polar mode (estimated to be roughly 20 K in classical models) while reducing the tilt transition temperature from 130 K to 110 K [38, 206]. The most striking feature of STO is its flat energy landscape, where it exists on the verge of several phase transitions, whether it be to polar, superconducting, or metallic states. In this study, we are most interested in STO as an incipient ferroelectric, where it exists in bulk on the verge of multiple polar transitions along different unit cell directions [34, 44–46]. Polar transitions have been induced by chemical substitution [47–49], isotopic ^{18}O-substitution [50], defect engineering [51–53], mechanical stress [54, 55], as well as interfacial effects such as epitaxial strain [44,45,56,57], mode mismatch [58–61], film thickness [51,62], and formal polarisation mismatch [63]. STO, alongside other popular perovskites $BaTiO_3$ and $PbTiO_3$, has also provided great clarity to our fundamental understanding of the ferroelectric instability in complex oxides [28]. Unlike the latter two materials however, ferroelectricity in STO is reserved only to specialised systems involving the constraints listed above. In relevance to this study are the constraints present in interfaced systems— epitaxial strain, mode mismatch, and formal polarisation mismatch. For this section of the study, we turn our focus to the effect of epitaxial strain. We investigate this here for computational practicality— where first principles techniques allow us to apply it to bulk unit cells without the need for interface calculations. This subsequently allows us to disentangle the effect of strain from other interfacial effects in said calculations.

In this results chapter, we report a thorough first principles investigation into

STO as a bulk crystal, followed by an investigation into the effect of epitaxial strain. We investigate the effect of strain on STO in both the [001]- and [111]-basis, where different geometric constraints have been shown to typically yield vastly different strain-phase diagrams [96]. This chapter provides an essential foundation to our understanding of how STO behaves in our simulations. In chapter 5, where we investigate interfaced STO, it allows us to easily identify whether phenomena are induced by strain or not. For both bulk and bulk strained calculations, we test a range of polar and non-polar phases, and report the ground state at each strain. We also discuss relevant trends in the mode amplitudes, dielectric response and Berry phase polarisation.

We performed DFT calculations within the GGA framework: utilising the PBEsol exchange-correlation functional [154], and PAW generated pseudopotentials [163] within the PBE scheme [151], implemented in the VASP [160, 161, 164]. The Sr 4*s*, 4*p*, and 5*s* (4*d* is also included, but initially left unoccupied); Ti 3*s*, 3*p*, 3*d*, and 4*s*; and O 2*s*, 2*p* electrons were explicitly included as valence, while all other electrons were frozen in the ionic cores. For all ionic relaxations, the plane-wave energy cutoff was set to 900 eV, while the K-point grid was fixed to a $5 \times 5 \times 4$ Γ-centered mesh for all calculations in the [001]-basis (where the 20 atom cell described below was used), and a $3 \times 6 \times 2$ Γ-centered mesh for all calculations in the [111]-basis (where the 60 atom cell described below was used). The polarisation was evaluated via the Berry phase approximation, in accordance with the modern theory of polarisation [194–197]. The electronic and ionic contributions to the dielectric tensor were calculated via density functional perturbation theory [201]. To quantify the structural distortions, we used symmetry adapted mode analysis as implemented in the ISOTROPY package [183]. To apply epitaxial strain, we fixed the in-plane components of the stress tensor using a stress-constraining geometry optimisation patch [169].

In this study, we tested several different phases, all of which are combinations of the R_5^- antiphase octahedral tilt mode and the Γ_4^- polar mode (as visualised in Fig. 3.1) along various axes. According to low temperature neutron diffraction data, STO has an $I4/mcm$ ground state in bulk, which consists only of antiphase tilting

Table 3.1: Structural classification of bulk phases and symmetries after applying [001]- and [111]-strain. Tilt patterns are expressed in Glazer notation.

Space Group	Tilt Pattern	Polar distortion	[001]-strain	[111]-strain
$Pm\bar{3}m$	$a^0a^0a^0$	000	$P4/mmm$	$R\bar{3}m$
$I4/mcm$	$a^0a^0c^-$	000	$I4/mcm$	$C2/c$
$R\bar{3}c$	$a^-a^-a^-$	000	$C2/c$	$C2/c$
$P4mm$	$a^0a^0a^0$	$00c$	$P4mm$	Cm
$I4cm$	$a^0a^0c^-$	$00c$	$I4cm$	Cc
$Ima2$	$a^-a^-a^0$	$aa0$	$Ima2$	$C2$
$R3c$	$a^-a^-a^-$	aaa	Cc	$R3c$
Cc	$a^-a^-c^-$	aac	Cc	Cc

around the out-of-plane axis [37]. Under [001]-oriented epitaxial strain, according to x-ray diffraction data the $I4cm$ ferroelectric phase is reported under compressive strain [45, 57], while the $Ima2$ ferroelectric phase is reported under tensile strain [44, 56]. The $I4cm$ phase consists of out-of-plane polar and tilt modes, while the $Ima2$ phase consists of in-plane polar and tilt modes. Limited experimental data exists for [111]-strained STO, though previous first-principles investigations report a strong stabilisation of the Cc phase with tensile strain, and stabilisation of non-polar phases including the metastable $C2/c$ phase with compressive strain. The Cc phase consists of polar and tilt modes along all three primitive directions, where two directions are of equal magnitude and the third unequal. The $C2/c$ phase consists only of tilting in this same pattern. In bulk, we tested 8 different phases, which are classified in terms of their available structural distortions in Table 3.1. In our bulk and [001]-strained calculations, we used a 20 atom cell with lattice vectors expressed in terms of primitive cubic cell vectors $(\mathbf{a}_\mathrm{p}, \mathbf{b}_\mathrm{p}, \mathbf{c}_\mathrm{p})$: $\mathbf{a}_{001} = \mathbf{a}_\mathrm{p} - \mathbf{b}_\mathrm{p}$, $\mathbf{b}_{001} = \mathbf{a}_\mathrm{p} + \mathbf{b}_\mathrm{p}$, $\mathbf{c}_{001} = 2\mathbf{c}_\mathrm{p}$, while in our [111]-strained calculations, we used a 60 atom cell with lattice vectors $\mathbf{a}_{111} = \mathbf{a}_\mathrm{p} + \mathbf{b}_\mathrm{p} - 2\mathbf{c}_\mathrm{p}$, $\mathbf{b}_{111} = -\mathbf{a}_\mathrm{p} + \mathbf{b}_\mathrm{p}$, $\mathbf{c}_{111} = 2\mathbf{a}_\mathrm{p} + 2\mathbf{b}_\mathrm{p} + 2\mathbf{c}_\mathrm{p}$. These two cell orientations are visualised in Fig. 3.2(b) and (c) respectively alongside a schematic showing the [111]-direction in the 5-atom simple cubic perovskite cell for clarity (Fig. 3.2(a)). We tested the same phases in Table 3.1 for both types of strain, though not all phases could be relaxed as strain often automatically breaks their symmetry. The symmetries of the bulk inputs after applying strain are also included in Table 3.1.

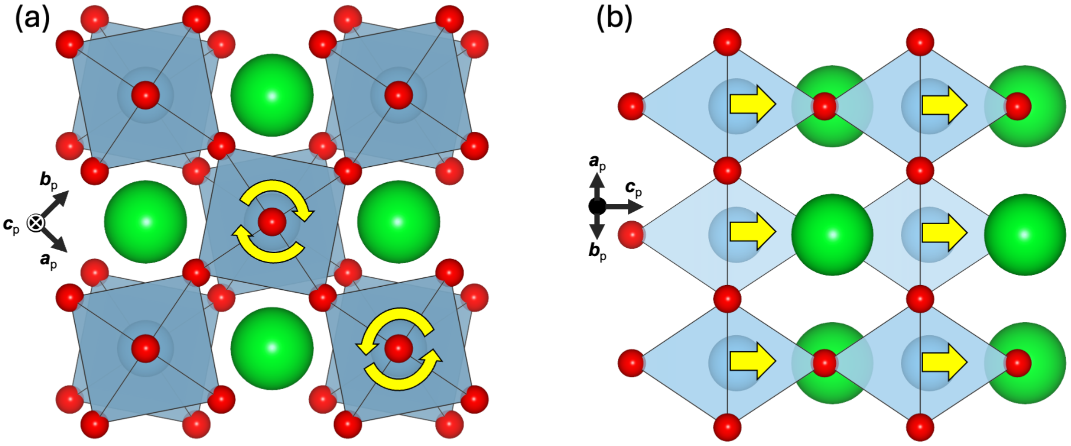

Figure 3.1: Visualisation of (a) antiphase tilt ($R_5^-(0,0,a)$) mode and (b) polar ($\Gamma_4^-(0,0,a)$) mode, where $\mathbf{a}_\mathrm{p}, \mathbf{b}_\mathrm{p}, \mathbf{c}_\mathrm{p}$ denote perovskite primitive axes.

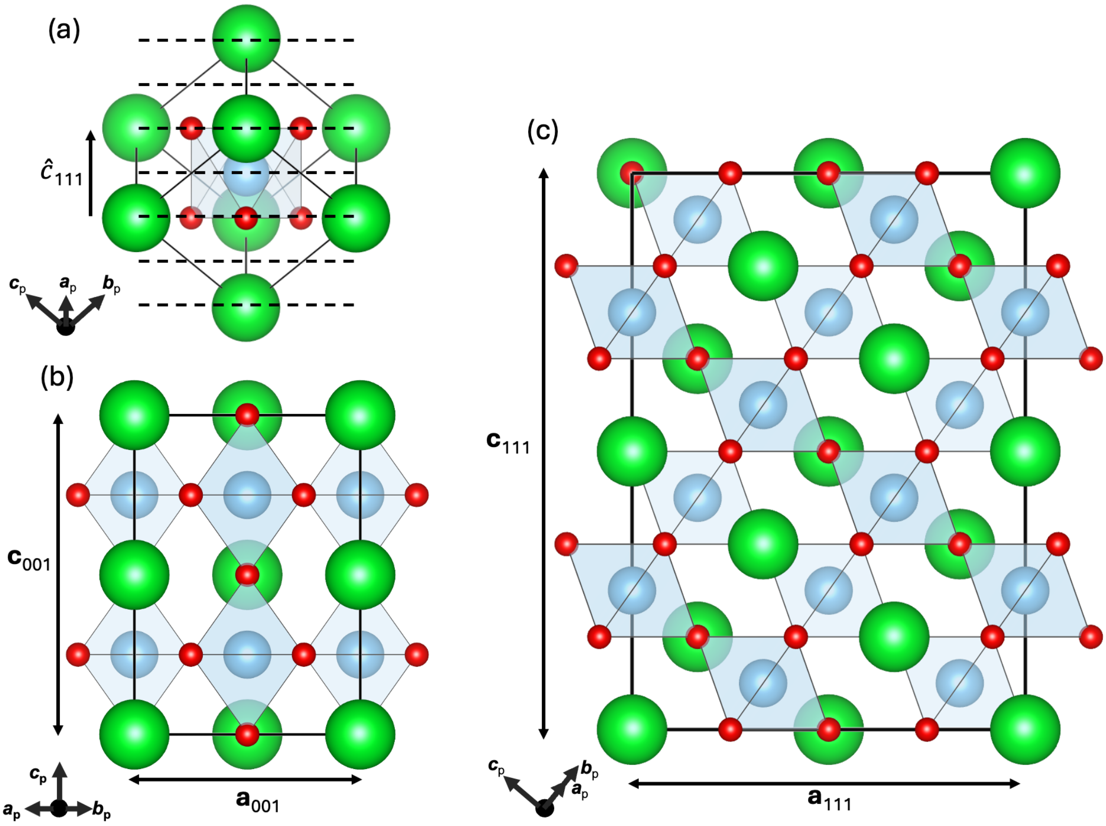

Figure 3.2: Visualisation of [001]- and [111]-oriented perovskites. (a) Rotated $Pm\bar{3}m$ primitive perovskite cell such that the direction $\hat{c}_{111}$ direction lies vertical. Horizontal dashed lines indicate (111) layers. (b) 20-atom [001]-oriented unit cell viewed from the $\mathbf{a}_{001} - \mathbf{c}_{001}$ plane. (c) 60-atom [111]-oriented unit cell viewed from the $\mathbf{a}_{111} - \mathbf{c}_{111}$ plane.

3.2 Results and discussion

3.2.1 Bulk

The bulk ground state mode amplitudes and energies are shown in Fig. 3.3. All phases listed in Tab. 3.1 were tested, and all remained in the same space group except Cc, which reverted to the higher symmetry $R3c$ phase. We find the ferroelectric $R3c$ phase to be the lowest in energy, in contrast with experiment [35,37], and most other DFT studies, which have found both paraelectric [40–42] and a range of ferroelectric [206,207] phases to be the ground state. The discrepancy between polar and non-polar ground states in different DFT calculations can be explained by the choice of exchange correlation functional. LDA-based calculations consistently yield non-polar results in bulk [40–42], while calculations using GGA and hybrid functionals (including PBE, PBEsol and HSE06) yield polar ground states [206,207]. In our study (using PBEsol), we find a polar ground state with polarisation in all three primitive axes, as seen in [206] (which tests both PBEsol and HSE06), but in contrast to the $I4cm$ ground state found in [207] (which uses PBE).

Several other phases remain extremely close in energy to the $R3c$ phase in our investigation. This includes two other polar phases $Ima2$ and $I4cm$, as well as the non-polar $I4/mcm$ phase. The three polar phases have significantly different mode amplitudes, yet remain within only 0.15 meV/f.u. of each other, while the nearest non-polar $I4/mcm$ phase, with tilt along only one primitive axis, is only 0.3 meV/f.u. higher in energy. We stress that during convergence testing, the energy difference between polar $I4cm$, and non-polar $I4/mcm$, $Pm\bar{3}m$ phases was converged to a tolerance of below 0.01 meV. Previous studies have estimated quantum energy fluctuations to be ∼2 meV/f.u. [206]. This value clearly exceeds the difference between our lowest polar $R\bar{3}c$ and non-polar $I4/mcm$ ground states. Therefore, despite yielding a polar ground state (in comparison to a non-polar experimental result), we stress that our simulations still match very well to experiment— we simply do not include quantum energy fluctuations in DFT. As previously argued in refs. [206,207], though LDA-based calculations obtain the same ground state as experiment, this is because LDA underestimates the effects of electron correlation,

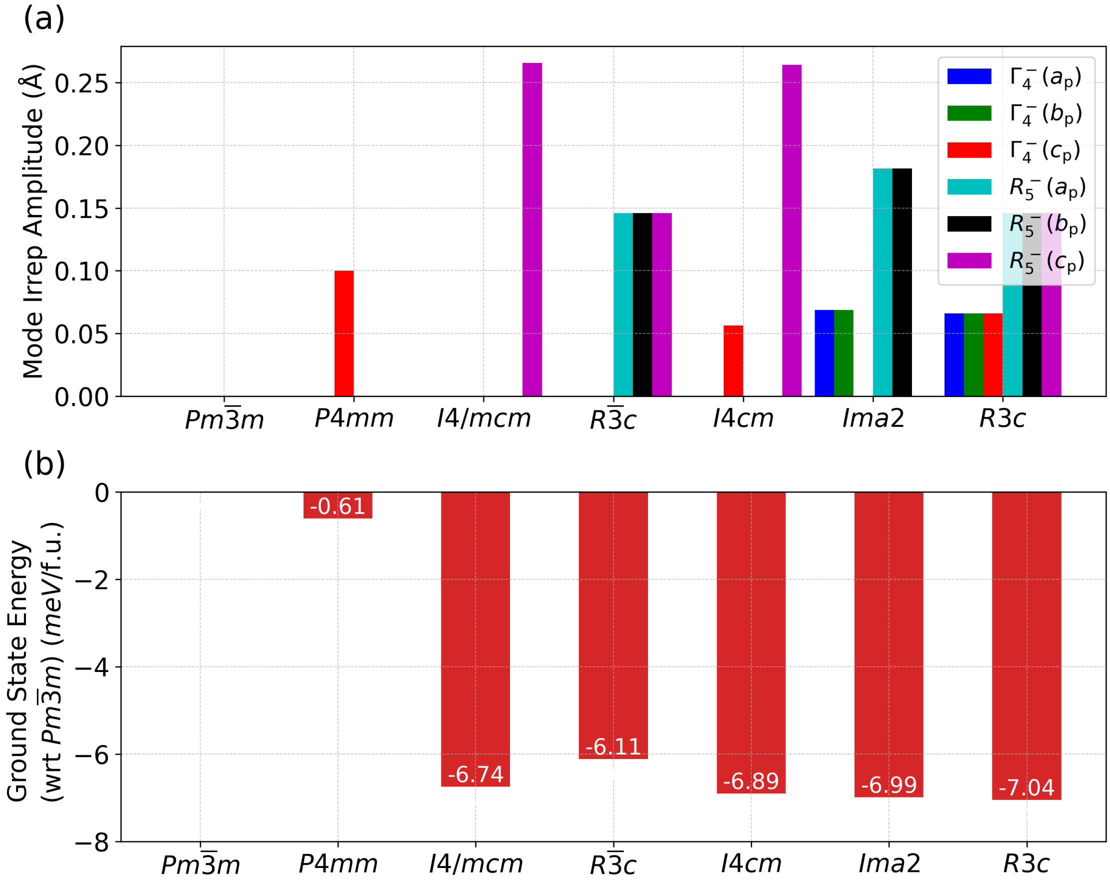

Figure 3.3: (a) Polar (Γ_4^-), antiphase tilt (R_5^-) mode amplitudes and (b) energies of various bulk phases (with respect to $Pm\bar{3}m$).

which results in the overbinding of electrons. This typically leads to the underestimation of lattice parameters and mode amplitudes, so it is no surprise that the already subtle polar distortion does not appear. As discussed in chapter 1, the polar mode depends on the hybridisation between Ti-3d and O-2p states in the Titanate series— an underestimation of correlation is bound to restrict this from happening. Though quantum energy fluctuations can be expected to suppress any of the polar phases in experiment, the minuscule energy differences between the three low-energy polar phases and non-polar $I4/mcm$ phase are intriguing for several reasons. Our results suggest an extremely flat energy landscape, such that even subtle changes in environment could easily induce dramatic changes in the ground state phase, where the mode amplitudes of the metastable phases are significantly different to the ground state.

Comparing the $I4cm$ and $R\bar{3}c$ phases, and also the three polar and tilted phases, the tilts are evidently competitive with one another, as with more tilts present, the amplitude consistently declines. The tilt modes are also responsible for the majority of the energy lowering from the cubic phase, as seen by comparing the energy of the polar-only $P4mm$ phase and tilt-only $I4/mcm$ phases. The tilt mode dominating the energy lowering is expected, where it has been demonstrated to condense in at approximately 110 K experimentally [64]. Furthermore, previous studies have shown that the tilt mode is competitive with the polar mode [30, 32], except for extremely high tilts, where the polar mode becomes less competitive due to increasing cell tetragonality. The un-tilted $P4mm$ phase shows the largest polar amplitude, which reduces by roughly 45% upon allowing for tilting in the $I4cm$ phase. Interestingly however, the tilt mode itself declines only subtly with the inclusion of the polar mode when comparing the $I4/mcm$ and $I4cm$ phases, likely due to the tilt mode dominating the energy landscape. Due to such a small contribution to the energy lowering, it is hard to say whether the polar modes are competitive with one-another, though as they are competitive with the tilt mode, and the polar mode amplitudes do not increase when switching from $Ima2$ to $R3c$, it is likely that they are (even though the polar mode increases with respect to $I4cm$, this is driven by the reduction in tilt, which has a larger effect than the competitive polar coupling). The lattice parameters for each relaxed phase are contained in Table 3.2. Our lattice parameters for metastable $I4/mcm$ match remarkably well to low temperature neutron diffraction data [37].

The Berry phase polarisation and diagonal terms of the dielectric tensor (both ionic and electronic contributions) of each phase are also contained in Table 3.2. The results for polarisation correlate closely with the Γ_4^- mode amplitude. The net polarisation is largest in the ground state phase, pointing along the [111] axis— which we can attribute to the reduction in individual tilt magnitudes in each primitive direction. The electronic contributions to the dielectric tensor remain similar regardless of phase, while the ionic components undergo colossal variation depending on the structure. We note that calculated terms for some of the metastable higher symmetry cells do not consider contributions from imaginary polar modes (as calculations were undertaken with the symmetry fixed to prevent relaxation into lower energy phases), which we expect to dominate. This applies to the $Pm\bar{3}m$ (in all three directions) and $P4mm$ (only out-of-plane polarisation was allowed) phases. Regardless, the remainder of the phases allow for the polar instability in all three axes and clearly show dramatic variation in the dielectric response. Our results demonstrate well the fascinating consequences of the flat energy landscape of STO, where even within energy changes of 0.15 meV/f.u., the dielectric coefficients can vary by the order of 100s in all three axes.

3.2.2 [001]-strain

The STO [001]-strain phase diagram is displayed in Fig. 3.4(a). For each strain point, we tested the phases listed in column 4 of Table 3.1. At many points, phases could not be relaxed— only at 3.90 Å could all three polar and tilted phases $I4cm$, Cc and $Ima2$ be relaxed simultaneously. At this point, which is extremely close to the bulk in-plane lattice parameters of each phase, it is no surprise that the energy difference is on the scale of the energy differences between the metastable bulk phases. The subtle energy differences at 3.90 Å are shown in the inset of Fig. 3.4(a). At this point we find the Cc phase to be the ground state, which is approximately equivalent to the bulk ground state $R3c$ phase, with the symmetry between in-plane

Table 3.2: Polarisation P (μC cm^{-2}), electronic, ionic dielectric tensor components (leading diagonal only) ϵ^e_{ij}, ϵ^I_{ij} (where the total dielectric tensor $\epsilon^T_{ij} = \epsilon^e_{ij} + \epsilon^I_{ij}$), and pseudo-cubic lattice parameters (Å) of bulk relaxed STO phases along [001]-oriented cell directions.

Space Group		$Pm\bar{3}m$	$P4mm$	$I4/mcm$	$R\bar{3}c$	$I4cm$	$Ima2$	$R3c$
P	$\hat{a}_{001}$	0	0	0	0	0	12.2	12.0
	$\hat{b}_{001}$	0	0	0	0	0	12.2	12.0
	$\hat{c}_{001}$	0	16.4	0	0	11.3	0	12.0
	Net	0	16.4	0	0	11.3	17.3	20.8
ϵ^e_{ij}	$\hat{a}_{001}$	6.43	6.38	6.46	6.44	6.44	6.24	6.22
	$\hat{b}_{001}$	6.43	6.38	6.46	6.45	6.44	6.35	6.25
	$\hat{c}_{001}$	6.43	6.20	6.47	6.45	6.33	6.37	6.26
ϵ^I_{ij}	$\hat{a}_{001}$	4.95	5.45	3.40	3.87	131.56	181.74	244.90
	$\hat{b}_{001}$	4.95	5.45	3.40	3.22	131.56	1126.80	324.66
	$\hat{c}_{001}$	4.95	147.77	2.16	3.06	249.84	758.63	344.68
L. P.	$\lvert\mathbf{a}_{001}\rvert/\sqrt{2}$	3.90	3.90	3.89	3.89	3.89	3.90	3.90
	$\lvert\mathbf{b}_{001}\rvert/\sqrt{2}$	3.90	3.90	3.89	3.89	3.89	3.90	3.90
	$\lvert\mathbf{c}_{001}\rvert/2$	3.90	3.91	3.91	3.89	3.92	3.89	3.90

and out-of-plane modes broken due to strain. The energy lowering from strained $Pm\bar{3}m$ to the lowest energy tilted phase and ground state (always polar and tilted) is displayed in 3.4(b). At 3.90 Å the energy lowering is still dominated by the tilt. The polar mode energy lowering is slightly larger than in bulk due to the metastable phases having different bulk lattice parameters (highlighted by vertical dashed lines), thus experiencing a slightly larger energy penalty due to strain than the Cc phase.

Compressive regime

In the compressive regime (3.70—3.85 Å), the system immediately reverts to the $I4cm$ phase, which consists only of tilt and polar modes out-of-plane. The energy difference between the polar $I4cm$ and non-polar $I4/mcm$ phases initially remains small under low compressive strains, but rapidly amplifies under higher strains. The energy difference quickly surpasses the scale of quantum fluctuations, suggesting at the very least the appearance of ferroelectricity at large strains and low temperatures. Furthermore, the energy difference appears to be increasing non-linearly, suggesting a rapid amplification if further strain were applied.

The structural properties of STO as a function of [001]-strain are presented in

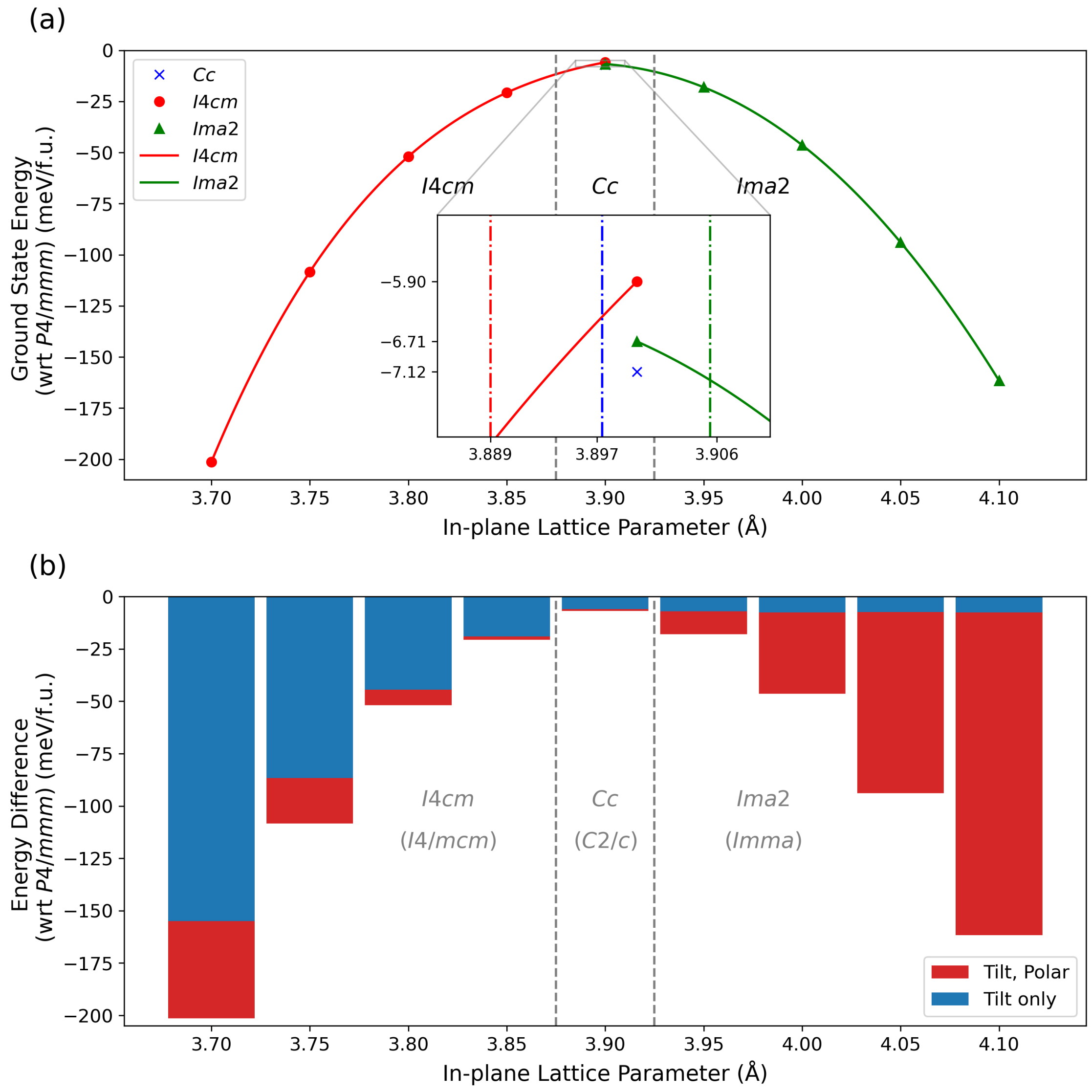

Figure 3.4: (a) [001]-strain phase diagram of STO. Inset shows subtle energy differences (also in meV/f.u.) between phases at 3.90 Å, where vertical dashed lines indicate the bulk lattice parameters of each phase. (b) Energy of lowest polar and non-polar (labelled in brackets) phases with respect to $P4/mmm$ ([001]-strained $Pm\bar{3}m$).

Fig. 3.5. The out-of-plane tilt and polar mode steadily increase in the compressive regime. As strain dramatically amplifies the tetragonality of the cell, it is unsurprising that the polar and tilt modes become increasingly stable out-of-plane, as both modes appear in bulk to fill excess space (caused by undersized *A*- or *B*-cations). Given tilting dominates the energy lowering in bulk, and that it competes with the polar mode, it might be expected that it continues to dominate under strain. However instead, the polar mode rapidly stabilises, suggesting that the cell tetragonality caused by compressive strain may favour the polar mode slightly more than tilting. Though ferroelectric STO has been induced experimentally under compressive strain [45, 57], this is consistently at temperatures lower than predicted with phenomenological LGD analysis (though this is parameterised by experimental data obtained prior to these results), which instead suggests a rapidly increasing polar transition temperature which surpasses that of the tilt mode at approximately 2% compressive strain [34]. To clarify these discrepancies, we compare the energies of the polar-only ($P4mm$), tilt-only ($I4/mcm$) and polar-tilted ground state ($I4cm$) in the compressive regime in Fig. 3.6. We find that at 3.80 Å (2.6% strain), the tilt-only phase remains significantly lower in energy than the polar-only phase, tentatively suggesting a higher tilt transition temperature than polar at this strain, matching recent experiments rather than the LGD model. At 3.70 Å however (5.1% strain), the polar-only phase is lower in energy than the tilt-only phase, which is a good indication that the polar transition temperature surpasses that of tilting near this strain. Our simulations therefore suggest that STO indeed follows a similar trend to the LGD model qualitatively, though we expect the crossover of the polar and tilt mode transition temperatures to occur at around 4—5% strain rather than the 2% strain predicted in the model. Our results appear to align closely to experiment, where tilt transition temperature amplification is reported at around 2% strain [45,57], and the polar mode is found to condense at lower temperatures. Still, we predict strains of 4—5% to significantly increase the polar transition temperature— possibly even to room temperature as predicted in the LGD model. Our studies also show parallels to arguments presented in ref. [30], where it is suggested that extremely large tilts (in bulk) could actually strengthen the polar mode due to the increased cell tetrago-

nality. It may be that colossal strains (strains that are well beyond what is typically experimentally feasible) inducing larger tilts (alongside the cell tetragonality caused by strain alone) amplify the polar mode at a faster rate than at lower strains, which is exactly as we observe. Predictably, the out-of-plane lattice parameter increases with compressive strain, while the volume decreases.

The dielectric properties of STO as a function of [001]-strain are presented in Fig. 3.7. The out-of-plane Berry phase polarisation increases proportionally with the polar mode amplitude, while the in-plane component remains at 0 μC cm^{-2}. The electronic components of the dielectric susceptibility stay relatively stable, where subtle differences in the in-plane and out-of-plane components can be attributed to minor variations in cell tetragonality and mode variation. The ionic contribution is more interesting. Upon transitioning from Cc to $I4cm$, the in-plane parameters rapidly diverge. This is clearly a result of the softening of the polar mode and subsequent freezing in of this mode beyond 3.9 Å. Experimentally, a similar divergence in the dielectric tensor is observed in the tensile regime [44] (where in-plane polarisation is observed), as quantum fluctuations suppress polarisation at 3.90 Å.

Tensile regime

The tensile regime (3.95—4.10 Å) has many parallels to the compressive regime, but also several key differences. Energetically (Fig. 3.4), the system rapidly reverts to the $Ima2$ phase, consisting of polar and tilt modes along both in-plane directions. However, unlike the compressive regime, the polar mode quickly dominates the energy lowering from the cubic phase, while the tilt energy lowering stays approximately fixed. This suggests far higher polar transition temperatures than at equivalent compressive strains. The polar mode might be expected to condense before the tilt mode even at low tensile strains, while the tilt transition temperature is likely to stay close to the bulk value of 110 K [64]. This observation matches what is seen in experiment, where in-plane ferroelectricity is present close to room temperature at a mere 1% tensile strain [44], and the LGD model [34], where a similar transition temperature is estimated. Our results also match what has been observed in previous DFT studies, where polar and tilted phases of the same space groups

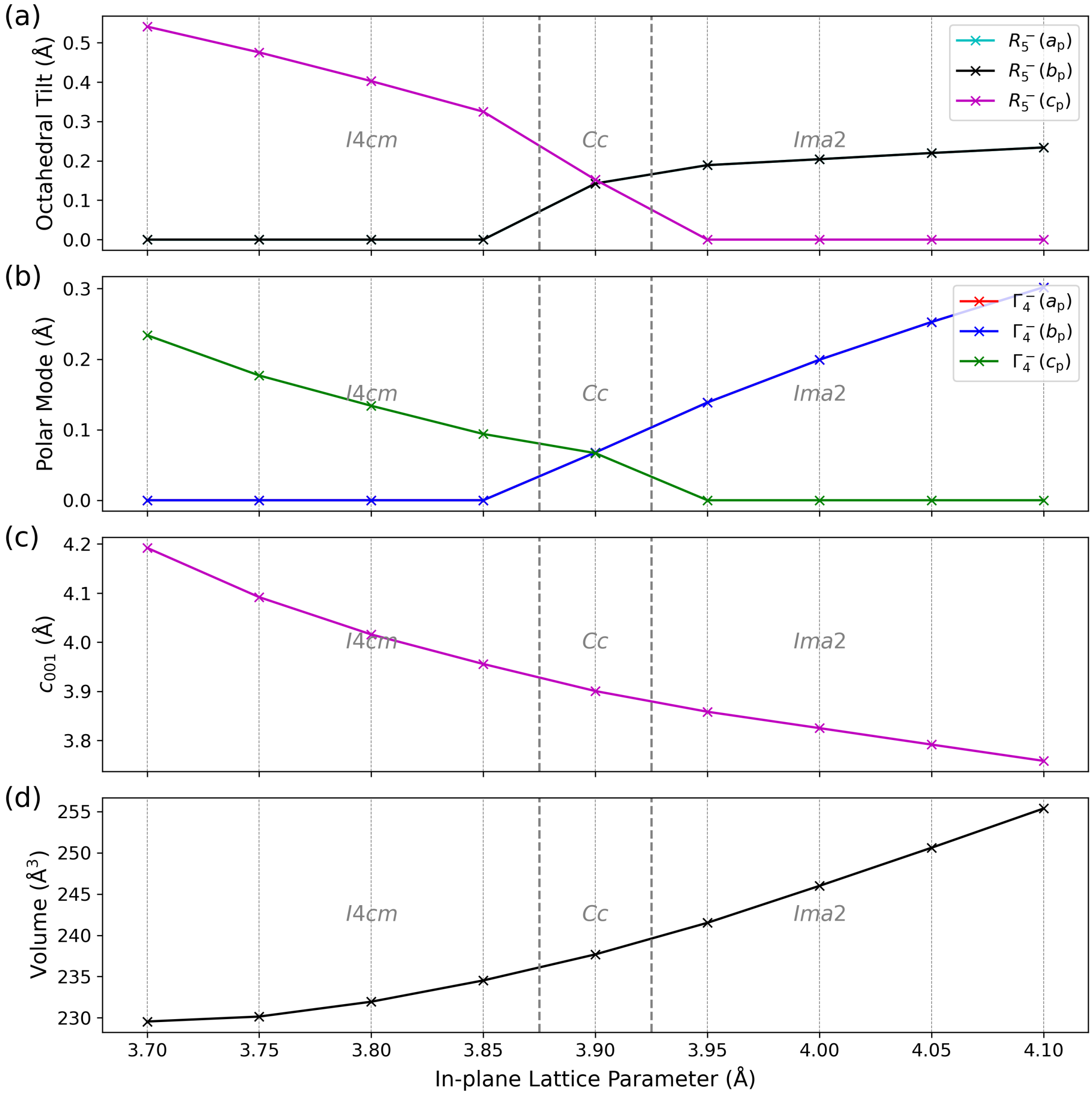

Figure 3.5: Structural properties of STO as a function of [001]-oriented epitaxial strain: (a) octahedral tilt amplitude (Å) (where $a_\mathrm{p}, b_\mathrm{p}, c_\mathrm{p}$ denote the primitive axis the tilting lies around, and tilt amplitudes around a_p and b_p are equal in magnitude for the entire regime), (b) polar mode amplitude (Å) (where displacements along a_p and b_p are equal in magnitude for the entire regime), (c) out-of-plane lattice parameter (in pseudocubic units), and (d) cell volume.

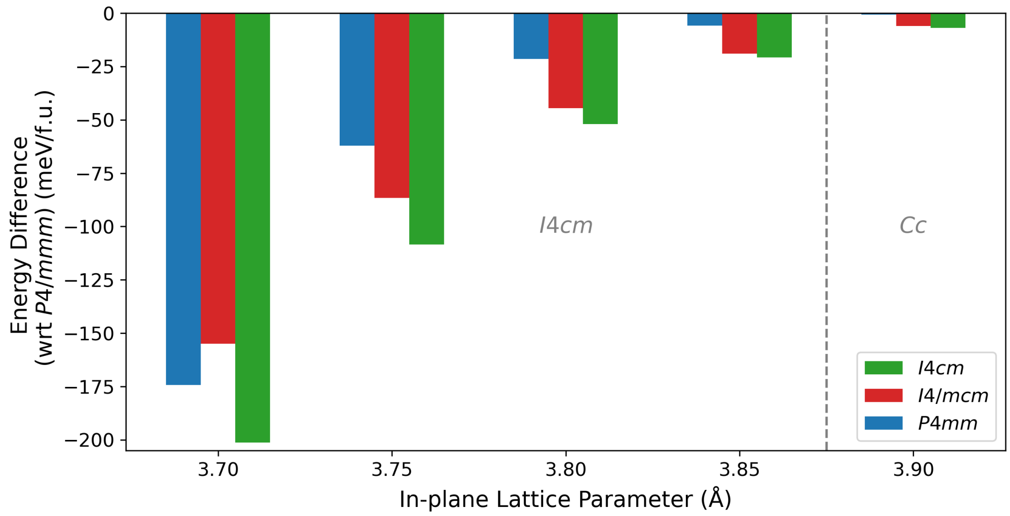

Figure 3.6: Energies of polar-only ($P4mm$), tilt-only ($I4/mcm$) and polar-tilted ($I4cm$) phases under [001]-compressive strain.

stabilise under compressive and tensile strain [107]. This is despite using the LDA exchange-correlation functional, which stabilises non-polar phases in bulk (as well as low strains). As stated previously, LDA likely obtains the correct ground state phase in bulk for the wrong reasons— the LDA functional typically over-localises electrons, which prevents subtle distortions like the polar mode from developing. Meanwhile GGA-based functionals such as PBEsol slightly delocalise electrons [154, 207], which has the opposite effect. Neither case takes into account the real cause of the suppression of the polar phase— quantum energy fluctuations [38, 206]. Structurally (Fig. 3.5), the polar modes can be seen to follow a steeper gradient than in the compressive regime, while the tilt remains approximately fixed, clearly corresponding to the above statements regarding the energy lowering. The volume and out-of-plane lattice parameter increase and decline respectively, in opposite fashion to the compressive regime.

The tensile regime is also the reverse of the compressive regime electronically (Fig. 3.7), where the polarisation once again increases proportionally to the polar mode along xx ($\hat{a}_{001}$) and yy ($\hat{b}_{001}$) directions (the total polarisation is these two in-plane values summed in quadrature). The dielectric response is also a mirror image, where the out-of-plane ionic components heavily diverge at the transition to

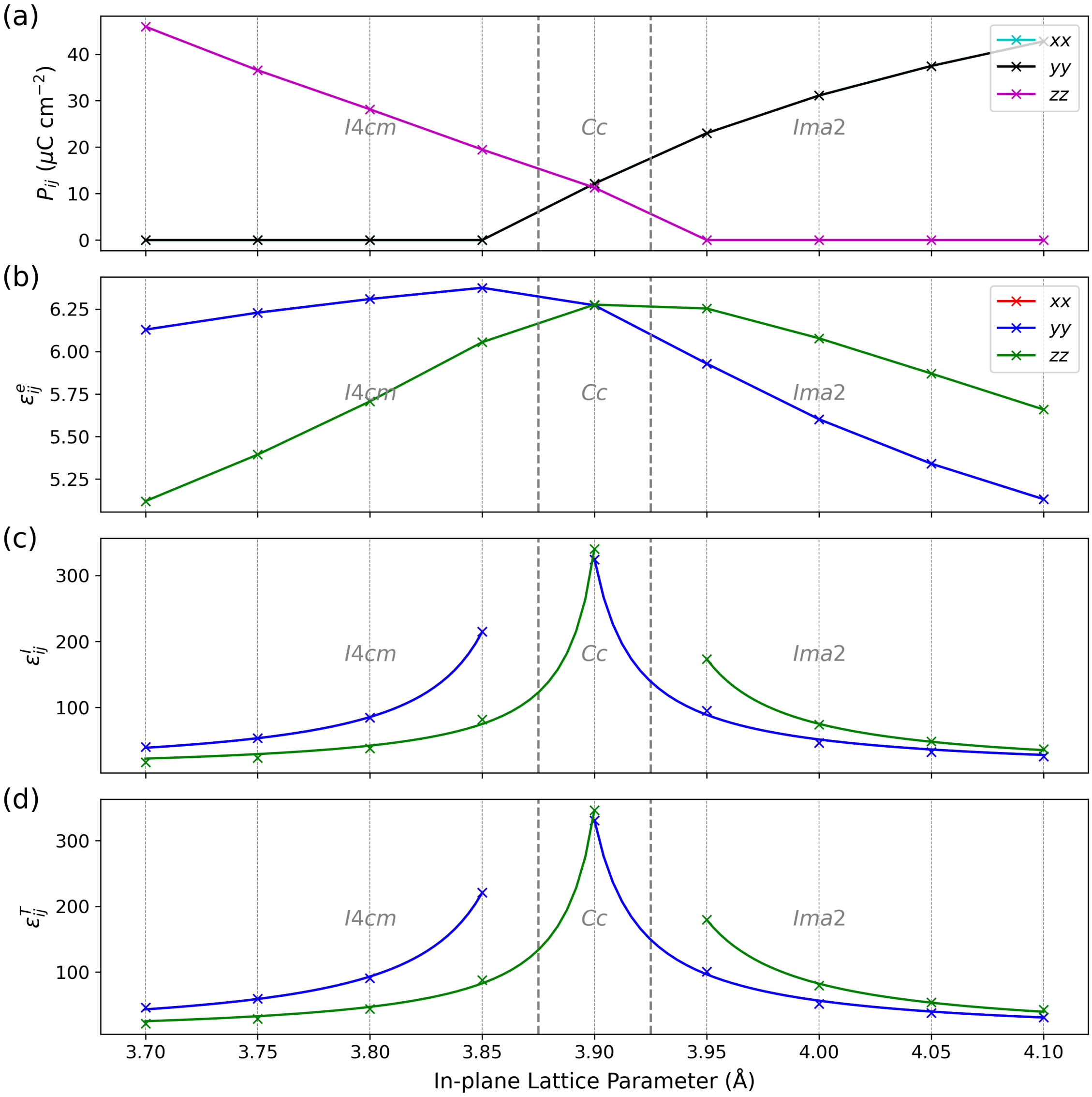

Figure 3.7: Dielectric properties of STO as a function of [001]-oriented epitaxial strain (where labels xx, yy, zz correspond to the components of the given quantity along directions $\hat{a}_{001}, \hat{b}_{001}$, and $\hat{c}_{001}$ respectively, and electronic properties along xx, yy are equal in magnitude for the entire regime): (a) Berry phase polarisation, (b)—(d) electronic (superscript e), ionic (superscript I), and total (superscript T) static dielectric tensor components ϵ_{ij} (where subscript ij corresponds to leading diagonal components xx, yy, zz defined above). All xx and yy components are equal in magnitude.

the *Cc* phase, where out-of-plane polarisation first condenses. If quantum energy fluctuations were present (as in experiment), one would expect the in-plane and out-of-plane divergence to swap places, such that the out-of-plane transition occurs in the compressive regime, the in-plane transition occurs in the tensile regime, and the system exists in a non-polar state at 3.90 Å.

3.2.3 [111]-strain

The [111]-strain phase diagram is presented in Fig. 3.8(a), where the energies of four phases that were stable or metastable for most of the regime are shown. We also investigated several other structural inputs as in Table 3.1, though these automatically reverted to one of the four phases shown. The $R\bar{3}c$ and $C2/c$ phases are tilt-only phases, with $a^-a^-a^-$ and $a^-a^-c^-$ tilt patterns respectively. The $R3c$ and Cc phases are polar and tilted phases, with $a^-a^-a^-$ and $a^-a^-c^-$ tilt patterns and *aaa* and *aac* polar modes along the primitive directions respectively. At 3.90 Å, we find the $R3c$ phase to be the ground state, where unlike the [001]-oriented system, [111]-strain does not automatically break the symmetry of the $R3c$ (nor $R\bar{3}c$) phase. The inset shows the energies of the $R3c$ and metastable Cc phases at 3.90 Å, as well as the relaxed bulk pseudocubic lattice parameters of these phases in the [111]-basis ($|\mathbf{a}_{111}|, |\mathbf{b}_{111}|$). As expected, the energy difference at this point is once again extremely subtle. The $R3c$ phase has equal bulk in-plane lattice parameters in the [111]-basis, while Cc does not. In our strain phase diagram, as we fix both in-plane parameters to be equal, it is likely that we automatically favour the $R3c$ phase for minimal strains. The $R3c$ bulk [111] in-plane parameters also lie slightly closer to 3.90 Å than those of the bulk Cc phase. We also measured the energy difference between the lowest polar and non-polar phases, where at 3.90 Å, the energy lowering from non-polar to polar remains extremely subtle, though slightly larger in magnitude than in the [001]-plot (see insets). A possible explanation for this is that the lowest-energy tilted phase is now $C2/c$ rather than $I4/mcm$ (which automatically reverts to a different $C2/c$ phase in the [111]-basis). Going from $I4/mcm$ to $I4cm$ phase introduces a polar mode in one primitive direction, while going from $C2/c$ to $R3c$ introduces polar modes in all three primitive directions, which are also each greater in magnitude than in the $I4cm$ phase. This is likely to correspond to a greater energy lowering going from non-polar to polar.

Compressive regime

In the compressive regime (3.70—3.85 Å), the system automatically reverts to the non-polar $C2/c$ phase. No polar phases could be relaxed within this regime— we find that all inputs automatically turn non-polar. Our ground state is different to that obtained in similar first principles investigations using the LDA functional, where a $P2/c$ phase (with tilt pattern $a^-a^-c^+$) with smaller tilt magnitudes is stabilised (though the $C2/c$ phase remains extremely close in energy) [109]. We could not stabilise the $P2/c$ phase in our calculations (which we find automatically reverts to the same $C2/c$ phase). This discrepancy can also be explained by the overbinding of electrons and suppression of modes in the LDA approximation, given the larger tilting in our calculations. Interestingly, the $C2/c$ phase quickly becomes significantly lower in energy than the $R\bar{3}c$ phase, which has equal tilts along all three primitive directions. In the [111]-basis, all three primitive directions are constrained equally, resulting in no additional constraint on rhombohedral phases compared to monoclinic phases. Therefore, this significant energy lowering is likely driven by the competitive tilt coupling. This competition appears to be amplified with increased compressive strain, which further amplifies the energy difference from the $R\bar{3}c$ phase. The structural properties as a function of [111]-strain may be found in Fig. 3.9. The $C2/c$ phase retains roughly the same tilt mode amplitude difference between the equal and unequal tilting axes— suggesting that [111]-strain still favours similar parameters along all three primitive directions, unlike [001]-strain, which heavily splits the in-plane and out-of-plane directions. The out-of-plane parameter c_{111} predictably increases with compressive strain, while the volume decreases.

The dielectric properties of STO as a function of [111]-strain are presented in Fig. 3.10. The compressive regime remains non-polar, though the ionic component of the dielectric response rapidly diverges along all three cell directions at 3.85 Å. This corresponds of-course to the polar transition to the $R3c$ phase, which is polarised out-of-plane. The $R3c$ system is extremely close in energy to the Cc phase, consisting of

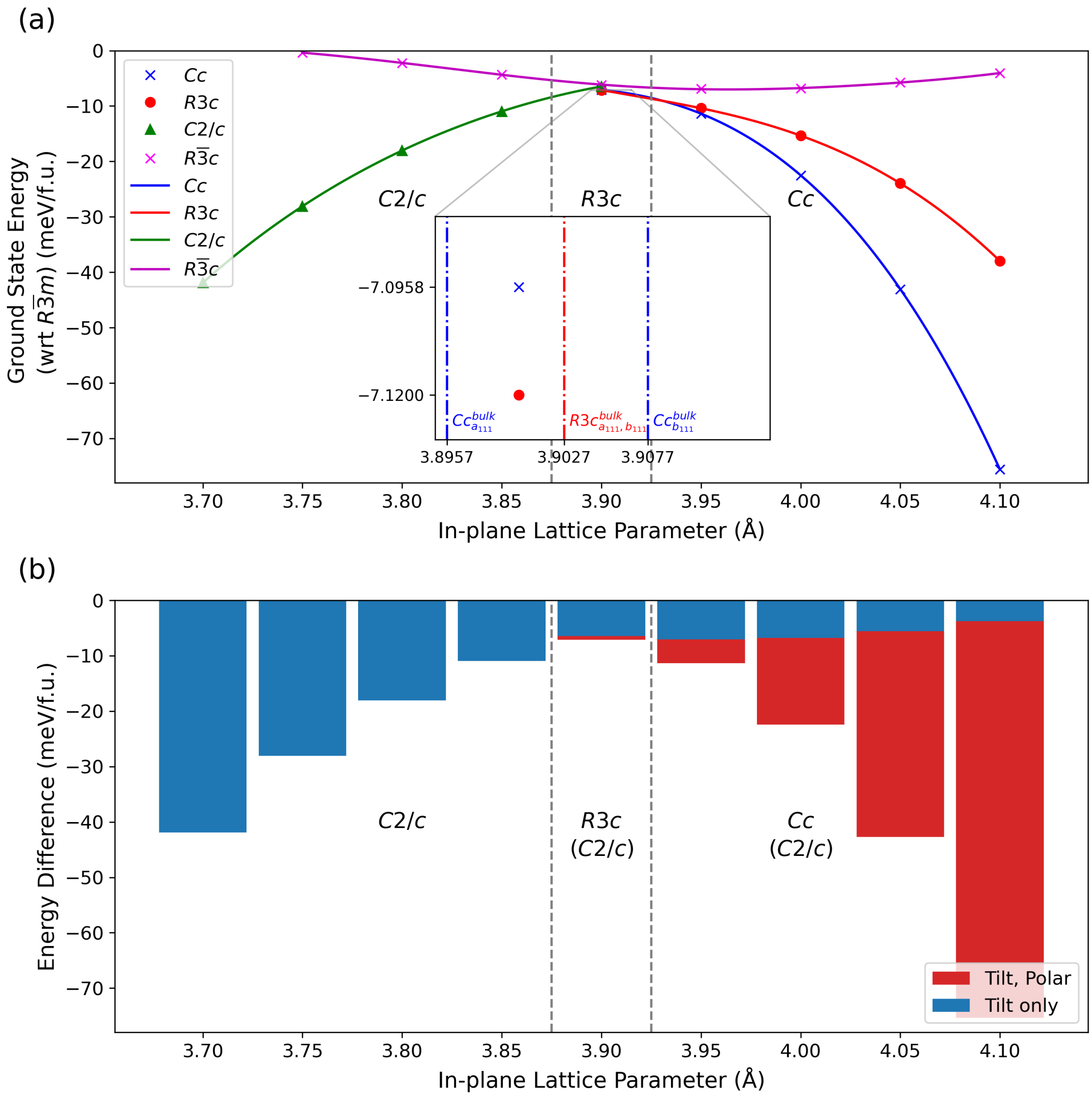

Figure 3.8: (a) [111]-strain phase diagram of STO. Inset shows subtle energy differences (also in meV/f.u.) between phases at 3.90 Å, where vertical dashed lines indicate the bulk lattice parameters of each phase. (b) Energy of lowest polar and non-polar (labeled in brackets) phases. All energies are with respect to $R\bar{3}m$ ([111]-strained $Pm\bar{3}m$).

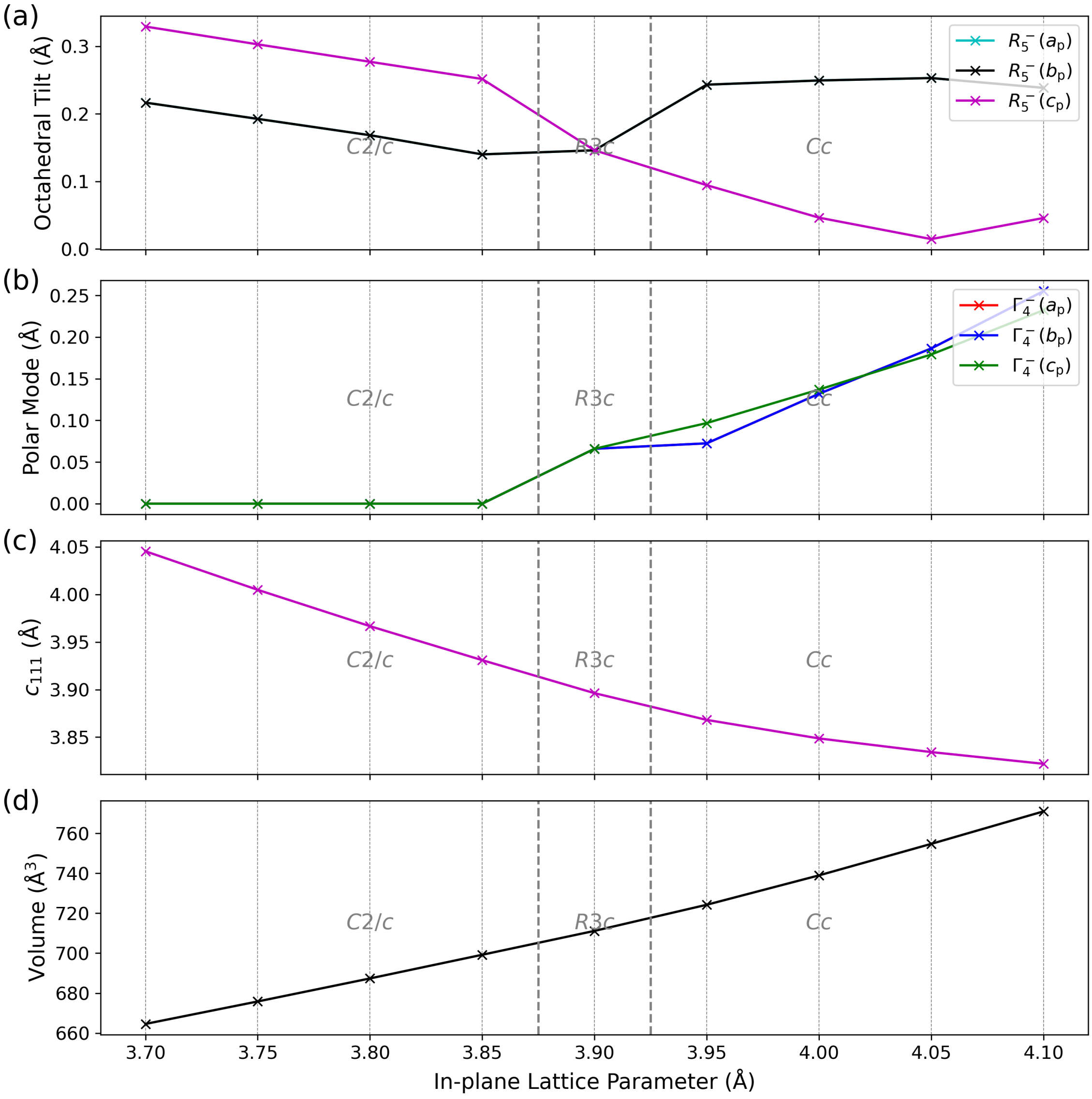

Figure 3.9: Structural properties as a function of [111]-oriented epitaxial strain: (a) octahedral tilt amplitude (where tilt amplitudes around a_p are equal to those around b_p), (b) polar mode amplitude (where displacements along a_p are equal to those of b_p), (c) out-of-plane lattice parameter (in pseudocubic units), and (d) cell volume.

polarisation along all three [111]-cell directions. In our DFT simulations with [111]-strain, we could not exactly fix the system to $R3c$, where inexact in-plane lattice parameters automatically break the symmetry to Cc. Though the system reverts to the $R3c$ phase within a tolerance of 0.01 Å change in the in-plane lattice parameters, in-plane polarisation is already present on a negligible scale at 3.9 Å. Therefore, in our dielectric runs, the in-plane components also diverge between 3.85 Å and 3.90 Å. As stressed previously however, the result for 3.90 Å is not directly comparable to experiment due to the lack of quantum fluctuations. In experiment, we might expect to see the $C2/c$ phase at 3.90 Å instead, which is the lowest energy non-polar phase here (or alternatively, the higher-symmetry $I4/mcm$ phase as seen in bulk given our calculations slightly under-bind electrons). Regardless, such divergence should be expected upon moving to the tensile regime, as explained below. Subtle variations in electronic component of the dielectric response can again be attributed to changes in the cell dimensions and structural distortions.

Tensile regime

The tensile regime (3.95—4.10 Å) displays vastly different energetic trends (Fig. 3.8) to the compressive regime, where the system quickly transitions to a polar phase, and significantly amplifies the energy difference between it and the lowest non-polar phase. We find that the system reverts to the Cc phase, consisting of an $a^-a^-c^-$ tilt pattern, and slightly different polar mode magnitudes along primitive directions, which in the [111]-basis leads to a large net in-plane distortion and small net out-of-plane distortion. Structurally (Fig. 3.9), as with the compressive regime, the system prefers split mode magnitudes along the primitive directions rather than equal, which is likely caused by mode competition. Interestingly, this appears to only affect the tilt mode significantly, as the polar modes are similar in magnitude. The energy difference between $R3c$ and Cc is less significant than that between $C2/c$ and $R\bar{3}c$ in the compressive regime. As the polar mode dominates the tensile regime, this suggests that polar modes are generally less competitive with one-another than antiphase tilt modes are. The c_{111} magnitude and cell volume decrease and increase respectively with tensile strain.

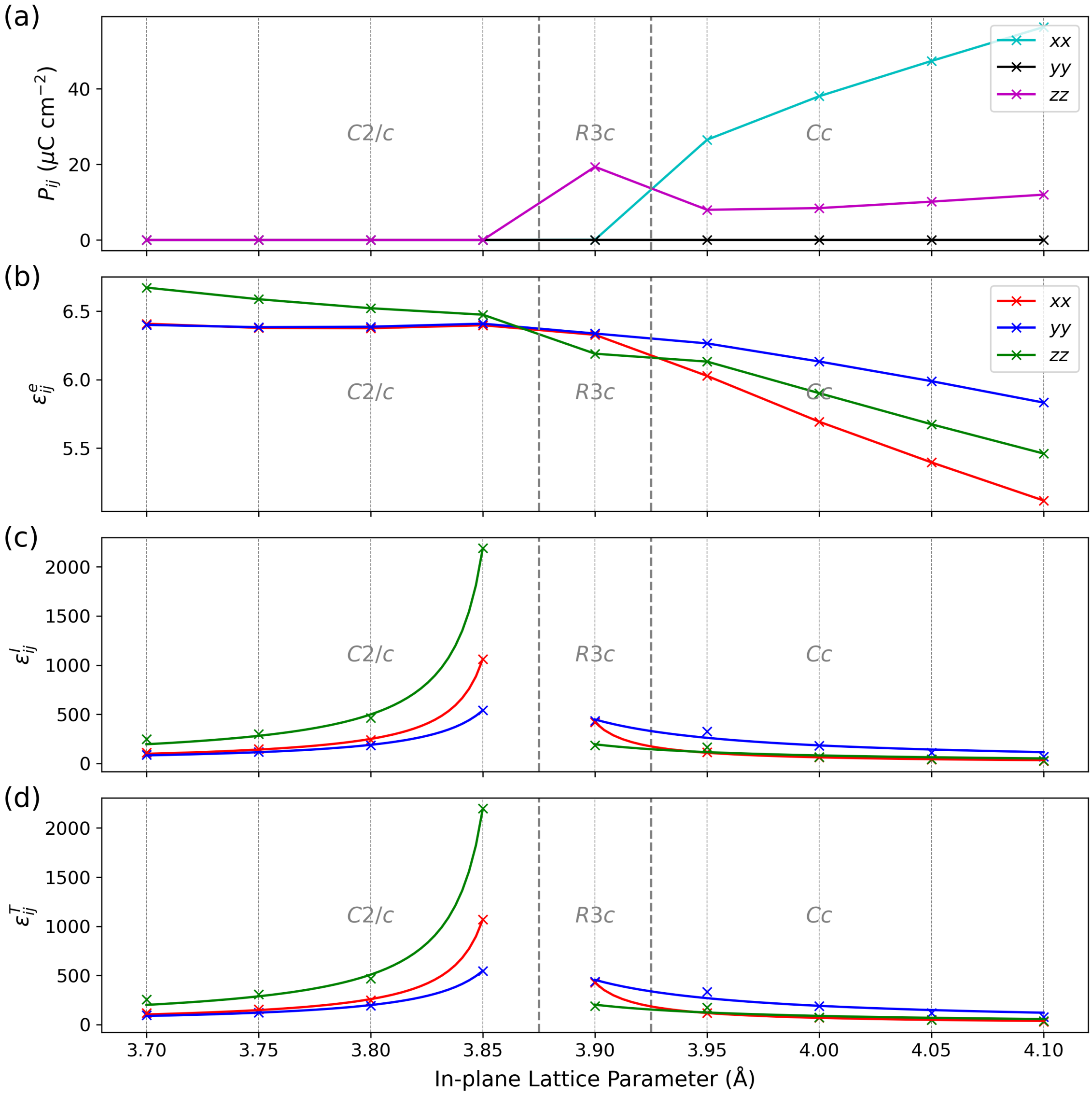

Figure 3.10: Dielectric properties as a function of [111]-oriented epitaxial strain: (a) Berry phase polarisation, (b)—(d) electronic (superscript E), ionic (superscript I), and total (superscript T) static dielectric tensor components (where labels $\mathrm{xx}, \mathrm{yy}, \mathrm{zz}$ correspond to the components of the leading diagonal of the 3×3 dielectric tensor ϵ_{ij}, calculated along directions $\hat{a}_{111}, \hat{b}_{111}, \hat{c}_{111}$).

The Cc phase has several other interesting features worth discussing. Looking to the dielectric properties (Fig. 3.10), glancing first at the polar mode plot, one might expect the Cc phase to have a similar polarisation to the $R3c$ phase. However, we find that the Cc phase cannot align all three polar modes to lie along the positive primitive directions simultaneously, such that the net polarisation lies along $\hat{c}_{111}$ (as in the $R3c$ phase). In-principle, one might expect there to be eight possible net polar directions for the Cc phase (where each polar mode in the primitive basis may align along the positive or negative primitive direction, leading to $2 \times 2 \times 2 = 8$ different net directions), where all are equivalent in energy. However, we find this not to be the case. The allowed polarisation directions of the Cc and $R3c$ phases with respect to a primitive cubic cell are highlighted in Fig. 3.11. The Cc phase instead has large in-plane and small out-of-plane polarisation components. This net direction corresponds to one of the three [111]-directions that does not lie directly out-of-plane (the fourth and final [111]-axis lies along $\hat{c}_{111}$). When we apply [111]-strain, we are breaking the symmetry between these three 'mostly-in-plane' [111]-axes and the out-of-plane [111]-axis. In our simulations, we find that the in-plane component lies entirely along the positive $\hat{a}_{111}$ direction, though based on our domain analysis, five other in-plane directions are also energetically equivalent. Because of this, we see the out-of-plane polarisation briefly spike at 3.90 Å in the $R3c$ phase, then revert to a small component after switching to the Cc phase in the tensile regime. Within the tensile regime, the electronic and ionic dielectric tensor components remain stable, where subtle variations can once again be attributed to mode and cell parameter variation. This phase has not been reported experimentally, though significant amplification in the dielectric response has been observed [110]. Previous LDA-based DFT studies also relax a Cc ground state under [111]-tensile strain with comparable in- and out-of-plane polarisations [109].

3.3 Summary

We have reported a detailed description of the electronic ground state for STO in bulk, and under the application of [001]- and [111]-oriented epitaxial strain. In

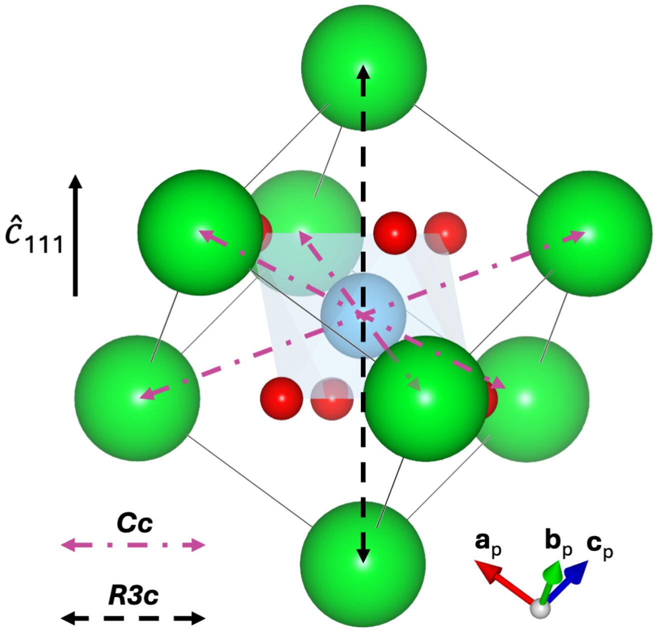

Figure 3.11: Available polarisation domains of [111]-strained Cc and $R3c$ STO phases. Cc aligns along the three predominantly in-plane [111]-directions ($2 \times 3 = 6$ polar domains), while $R3c$ aligns along the out-of-plane [111]-direction ($2 \times 1 = 2$ polar domains). $\hat{c}_{111}$ indicates the out-of-plane [111]-direction (equivalent to that in our STO [111]-oriented unit cells).

bulk, STO has an extremely flat energy landscape, where it exists on the verge of transitioning to various polar and non-polar phases, with vastly different structural and electronic features. We uncover an $R3c$ ground state, with polarisation and tilt along all primitive axes. Despite the difference in space group, we remark that our simulations map extremely well to experiment, where energy differences between polar and non-polar phases are on the scale of small thermal and quantum energy fluctuations (that are omitted from DFT calculations), thus not contradicting the classification of STO as a quantum paraelectric. Upon the application of [001]-strain, STO reverts to polar phases that match those seen in experiment— the $I4cm$ phase (polarised and tilted out-of-plane) in the compressive regime, and the $Ima2$ phase (polarised and tilted in-plane) in the tensile regime. We find that the $I4cm$ phase is dominated by the energy lowering from the tilt at strains of 1-2%, but becomes dominated by the energy lowering from the polar mode at strains of 4-5%. This matches qualitatively to LGD analysis, though we find the polar mode energy lowering only overcomes that of the tilting at strains larger than the 2%

predicted. Our findings are more in line with experimental data where a more significant amplification of the tilt transition temperature is observed, such that it remains roughly double that of the polar transition temperature at 1-2% strain. On the other hand, the energy lowering of the $Ima2$ phase is dominated by the polar mode, which is in line with both experimental results and LGD analysis. In the [111]-basis, we induce a stable non-polar $C2/c$ phase in the compressive regime, in contrast to previous LDA-based first principles studies where this phase was only metastable. We attribute this discrepancy to the choice of exchange-correlation functional. In the tensile regime, a strongly-polar Cc phase stabilises, with polarisation along the 'mostly-in-plane' [111]-axes (consisting of a large in-plane and small out-of-plane polarisation in our [111]-oriented unit cell).

Overall, this chapter provides essential information for interfacial calculations based on STO, providing a detailed, up-to-date investigation into how it responds to strain. Particularly relevant to the remainder of our study are the conditions that yield out-of-plane polarisation, which is observed under [001]-compressive and (to a minor extent) [111]-tensile strain. In the latter case, the out-of-plane component can likely be easily suppressed, as we find that the energy lowering is dominated by the in-plane component. [001]-compressively strained STO remains of essential interest to us however. In chapter 5, we build [001]-oriented interfaced systems of NNO and STO at $LaAlO_3$ strain (which is compressive for STO), and utilise our measurements of the polar mode under strain to disentangle the driving forces behind the interesting phenomena occurring in these systems.

CHAPTER 4

Bulk, [001]- and [111]-strained rare-earth nickelates

The next step of our study is to similarly investigate the bulk and strained properties of the rare-earth nickelates— both $NdNiO_3$, as a representative of the rare-earth perovskites that undergo metal-to-insulator transitions, and $LaNiO_3$, the only compound of this series to remain metallic at 0 K. We first determine suitable Hubbard-U and Hund-J corrections, such that we obtain bulk ground state phases that resemble experiment. We then investigate the effect of biaxial strain on the structural, electronic and magnetic properties of both [001]- and [111]-oriented $NdNiO_3$, as well as [001]-oriented $LaNiO_3$. We discover novel structural phase transitions not previously observed, as well as unique electronic behaviour, including amplification of the electronic band-gap, as well as insulating, charge-ordered phases with non-orthorhombic tilt patterns. To provide clarity to the trends we observe, we also investigate the coupling between the octahedral breathing mode (indicating charge-ordering) and strain, where we observe certain strains to directly favour or disfavour the stabilisation of the breathing mode. The amplification of the band gap with strain is understood in terms of a cooperative coupling between [111]-strain and the breathing mode, which expands on the recently-discovered triggered mechanism with octahedral tilting.

4.1 Introduction and methods

The rare-earth nickelates RNiO$_3$ (where R denotes a rare-earth element) are a fascinating playground for novel structural and electronic phase transitions. With the exception of La [69], all rare-earth nickelates undergo a metal-insulator transition (MIT) with decreasing temperature [70, 71]. Concomitantly, the symmetry lowers from an orthorhombic $Pbnm$ phase to a monoclinic $P2/c$ phase [81–83] with charge ordering on the Ni sites, which change from an oxidation state of $2\text{Ni}^{3+} \rightarrow \text{Ni}^{+3+\delta} + \text{Ni}^{+3-\delta}$ [84]. Research into the unique properties of the rare-earth nickelates has led us to a deeper understanding of several fundamental concepts, including the nature of poorly conducting materials [91], multiferroicity [92], MIT triggering via structural control [74], and MIT tuning via elastic strain [208]. Such phenomena have also been directly applied to designing novel electronic devices with unique properties, including artificial neuromorphic systems utilising conductance switching via Ni oxidation and reduction [88], artificial neural networks built from nickelate memory capacitors (driven by rapid changes in resistivity at the MIT) [89], and sensing devices reliant on Ni charge transfer [90].

The strain enforced on an epitaxial film provides a strategy to manipulate the properties of nickelates. [001]-oriented epitaxial strain allows for direct control of the MIT temperature, which has been shown to decline with increasing compressive [129] and tensile strain [127, 128]. DFT studies have shown that rare-earth nickelates undergo multiple phase transitions, including an insulator-metal transition (IMT) under compressive strain, and an IMT followed by a second MIT (via orbital ordering) under increasing tensile strain [101]. [111]-oriented perovskites remain significantly less studied. In other perovskites, [111]-strain has led to vastly different strain-phase diagrams in comparison to [001]-strain [96, 97]. In the case of the rare-earth nickelates, experimental studies have observed unique MIT variation under tensile [111]-strain [130, 131], the creation of A-site driven ‘polar metals’ [98], and novel orbitally-ordered phases in layered superlattices [132]. It is challenging to identify the underlying cause of these observations, whether it be strain, mode matching, interfacial dipoles, electric fields, or magnetic frustration, all of which are applicable to [111]-nickelate systems.

In identical fashion to chapter 3 with STO, we aim to provide clarity to bulk, [001]- and [111]-oriented rare-earth nickelate systems by isolating the effects of [001]- and [111]-strain. We report a first-principles investigation into the bulk ground state, as well as the effect of [001]- and [111]-strain on rare-earth nickelate $NdNiO_3$ (NNO), whose qualitative properties are consistent with the rest of the rare-earth nickelates besides La. We also investigate the properties of bulk and [001]-strained $LaNiO_3$ (LNO), which we compare and contrast to those of NNO. In our study of the bulk structures, we provide a detailed investigation into the effects of the Hubbard-U and Hund-J corrections on both NNO and LNO, where we determine a suitable choice to obtain DFT ground states that resemble experimental findings. This is followed by a detailed report of the structure and electronic properties as a function of strain for the chosen corrections. We demonstrate that both [001]- and [111]-oriented strains lead to previously-unseen nickelate phases with unique features. These findings compliment our previous understanding of how various structural distortions are coupled to one-another, as well as how they influence electronic properties such as the band gap. To obtain a deeper understanding of how the nickelates respond to epitaxial strain, we also investigate precisely its effect on the hallmark structural feature of the nickelates— the breathing mode. We measure the energy penalty of forming the breathing mode at various [001]- and [111]-strains to identify if any are cooperative or competitive. Furthermore, we search for answers regarding the driving force behind the polar nickelate phases seen in [111]-oriented interface systems [98]. To do this, we test our systems for the polar instability, by checking for inversion symmetry breaking and trends in the dielectric response with strain. This chapter provides us with a solid ground work for the complex interface systems in subsequent chapters.

Our DFT calculations resemble those of the previous chapter. The Nd $5s$, $5p$, $5d$ and $6s$ ($4f$ electrons were left frozen in the core); La $4f$ (initially unoccupied), $5s$, $5p$, $5d$ and $6s$; Ni $3p$, $3d$ and $4s$; and O $2s$ and $2p$ electrons were explicitly included as valence, while all other electrons were frozen in the ionic cores. The unit cells for the [001] and [111] basis are multiples of the cells shown in Fig. 3.2(b), (c) respectively: where the 20-atom [001]-oriented perovskite cell is doubled along both $\hat{a}_{001}$ and $\hat{c}_{001}$

to form an 80-atom cell, while the 60-atom [111]-cell is doubled along $\hat{c}_{111}$ to form a 120-atom cell. The lattice vectors of the nickelate [001]-cell are therefore expressed in terms of primitive cubic cell vectors as: $\mathbf{a}_{001} = 2\mathbf{a}_{\mathrm{p}} - 2\mathbf{b}_{\mathrm{p}}$, $\mathbf{b}_{001} = \mathbf{a}_{\mathrm{p}} + \mathbf{b}_{\mathrm{p}}$, $\mathbf{c}_{001} = 4\mathbf{c}_{\mathrm{p}}$, while those of the [111]-cell are expressed as: $\mathbf{a}_{111} = \mathbf{a}_{\mathrm{p}} + \mathbf{b}_{\mathrm{p}} - 2\mathbf{c}_{\mathrm{p}}$, $\mathbf{b}_{111} = -\mathbf{a}_{\mathrm{p}} + \mathbf{b}_{\mathrm{p}}$, $\mathbf{c}_{111} = 4\mathbf{a}_{\mathrm{p}} + 4\mathbf{b}_{\mathrm{p}} + 4\mathbf{c}_{\mathrm{p}}$. These cell sizes are necessary for expressing both the nickelate structure and magnetic order in each orientation. The K-point grid was fixed to a $3\times5\times2$ Γ-centered mesh for the 80-atom [001]-cell and a $3\times5\times1$ Γ-centered mesh for the 120-atom [111]-cell. The plane-wave cut-off was set to 900 eV for all calculations except those obtaining high-resolution band structures and dielectric tensors, where it was lowered to 550 eV to make simulations computationally tractable (while remaining well-converged). To investigate the effect of various on-site corrections, we calculated the Hubbard-U correction in accordance with both the simplified and unsimplified rotationally-invariant approaches as proposed by Dudarev et al. in ref. [180] and Lichtenstein et al. in ref. [209] respectively. We calculated the former (effective U (denoted by U_{eff})) using Cococcioni's approach as discussed in ref. [210] and the latter (U, J) using the minimum tracking approach discussed in ref. [211, 212].

Experimental studies have shown that NNO has a particularly complex magnetic order, with non-collinear AFM orders on both Ni and Nd sites at ground state [92, 94]. For simplicity, we chose to omit the Nd magnetic moment entirely (hence the omission of $4f$ electrons), as it only exhibits long range ordering below 30 K [93, 129, 213] and is not essential for the MIT and Ni charge ordering which occur at around 200 K [70, 81, 92, 214]. For computational tractability we chose not to simulate non-collinear orders on the Ni sites, as in previous bulk DFT studies, it was demonstrated that collinear T, S-AFM spin-chains with an $\uparrow\uparrow\downarrow\downarrow$ structure are lower in energy than non-collinear orders [80], and that these phases sufficiently recreate the experiment properties. With the appearance of Ni charge ordering, T, S-AFM spin chains obtain zero-moments on the lower valence $\mathrm{Ni}^{+3+\delta}$ sites (sites with nonzero moments correspond to higher valence $\mathrm{Ni}^{+3-\delta}$). This leads to alternating magnetic and non-magnetic Ni layers along the [111]-direction, where T-AFM consists of FM in-plane layers, while S-AFM consists of AFM in-plane layers. The T-, S-AFM

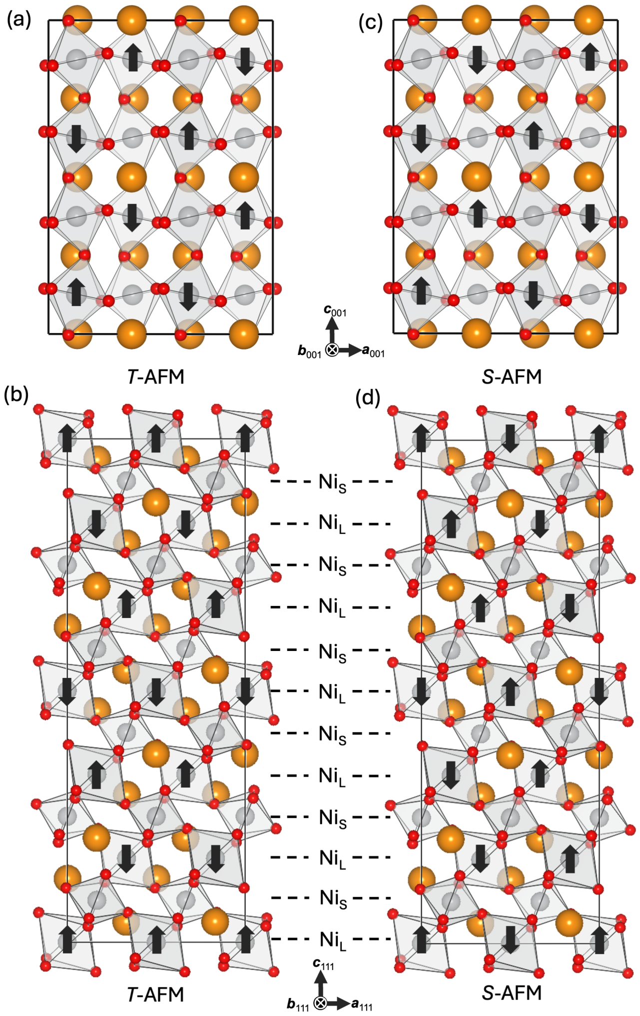

Figure 4.1: Magnetic orders of insulating, charge-ordered phases in [001]- and [111]-bases. Layers of small and large Ni valence sites are denoted by $\mathrm{Ni_S}$ ($\mathrm{Ni}^{+3+\delta}$) and $\mathrm{Ni_L}$ ($\mathrm{Ni}^{+3-\delta}$) respectively. $\mathrm{Ni_S}$ sites have no magnetic moment. (a) T-AFM magnetic order in [001]- and (b) [111]-cells, (c) S-AFM magnetic order in [001]- and (d) [111]-cells.

magnetic orders in both the [001]- and [111]-bases may be viewed in Fig. 4.1. In this study, we tested these two magnetic orders on insulating phases, and modelled the metallic phases with FM ordering as is commonly done with DFT [74, 80, 101].

We simulated a range of different structural phases for both NNO and LNO. We tested both charge-ordered and non-charge ordered inputs for two octahedral tilt patterns (written in [001]-basis Glazer notation for clarity): $a^-a^-c^+$ (corresponding to the charge-ordered, monoclinic $P2/c$ and the non-charge-ordered, orthorhombic $Pbnm$ phases), and $a^-a^-a^-$ (corresponding to the charge-ordered, triclinic $P\bar{1}$ phase, and the non-charge-ordered, rhombohedral $R\bar{3}c$ phase). A summary of these phases

Table 4.1: Space groups of various rare-earth nickelate phases, where tilt patterns are denoted in Glazer notation, charge-ordering corresponds to the presence of irrep R_2^-, and strain irrep labels correspond to the presence of [001]- (Γ_3^+) and [111]-strain (Γ_5^+). *Broken symmetry allows breathing. †Broken symmetry allows for $a^-a^-c^-$ tilt pattern. ‡Broken symmetry allows for $a^-b^-c^-$ tilt pattern.

Tilt pattern	Charge Ordering	Strain	Space group
$a^-a^-c^0$	×	×	$Imma$
		Γ_3^+	$Imma$
		Γ_5^+	$C2/m^*$
	✓	×	$C2/m$
		Γ_3^+	$C2/m$
		Γ_5^+	$C2/m$
$a^-a^-c^+$	×	×	$Pbnm$
		Γ_3^+	$Pbnm$
		Γ_5^+	$P2/c^*$
	✓	×	$P2/c$
		Γ_3^+	$P2/c$
		Γ_5^+	$P2/c$
$a^-a^-a^-$	×	×	$R\bar{3}c$
		Γ_3^+	$C2/c^\dagger$
		Γ_5^+	$C2/c^\dagger$
	✓	×	$P\bar{1}^\ddagger$
		Γ_3^+	$P\bar{1}^\ddagger$
		Γ_5^+	$P\bar{1}^\ddagger$

and the corresponding symmetry reduction induced by [001]- and [111]-strain is presented in Table 4.1, and the most significant structural distortions with their corresponding irrep label in Fig. 4.2(a)—(d). We also note that these tilt patterns occasionally reverted to higher symmetry patterns.

4.2 Results and discussion

4.2.1 Bulk

Calculation of Hubbard-U and Hund-J corrections

To find a suitable Hubbard-U and Hund-J correction for the Ni-3d sites, we first calculated the effective Hubbard-U correction (U_{eff}, as of the simplified approach) for both NNO and LNO, with the goal of finding a single U_{eff} that obtains the correct ground state for both NNO and LNO (our initial plan regarding the nickelates was

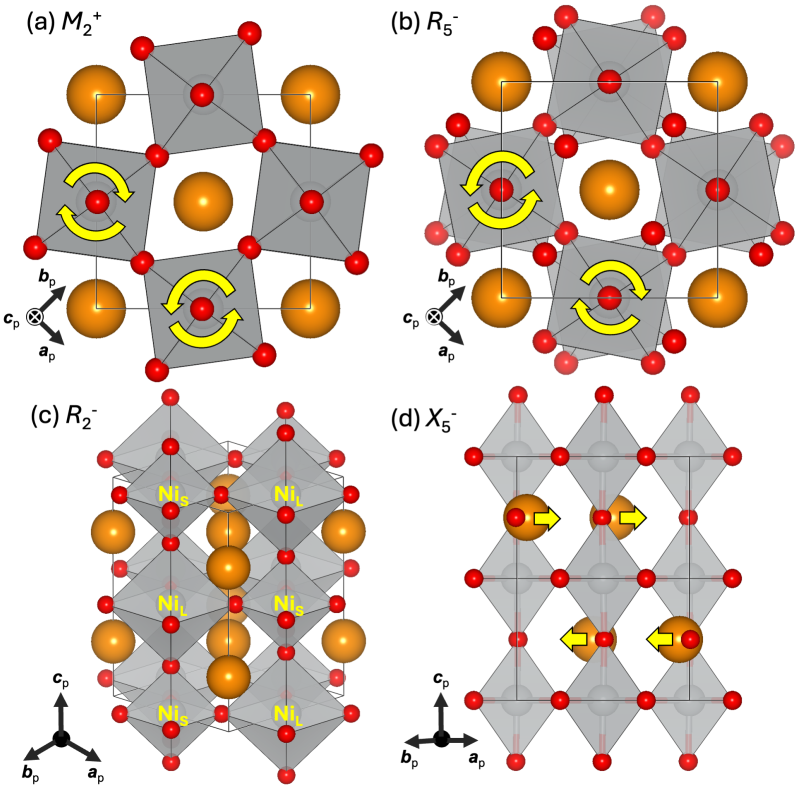

Figure 4.2: Types of structural distortions in RNiO$_3$, denoted by corresponding irrep labels and order parameter directions (with respect to the A-site origin cubic perovskite cell): (a) in-phase octahedral tilt ($M_2^+(0,0,a)$), (b) anti-phase octahedral tilt ($R_5^-(0,0,a)$), (c) breathing distortion ($R_2^-(a)$), (d) antipolar A-site motion ($X_5^-(0,0;0,0;a,a)$). Gold spheres indicate Nd sites, grey spheres indicate Ni sites, and red spheres indicate O sites.

to investigate NNO/LNO interfaces, which requires Ni-3d orbitals to have the same correction in both films). For NNO, using the experimental ground state $P2/c$ phase with T-AFM magnetic ordering, we found that $U_{\text{eff}} = 6.2$ eV for both Ni$_{\text{L}}$ and Ni$_{\text{S}}$ sites. For LNO, using the same $P2/c$ T-AFM phase, we also found that $U_{\text{eff}} = 6.2$ eV. When using the experimental ground state for LNO ($R\bar{3}c$ (FM) [69]), we found that $U_{\text{eff}} = 5.7$ eV. Therefore, to the nearest U_{eff}, the calculated correction is the same for NNO and LNO regardless of the phase being metallic or insulating. A full summary of the ground state phases for NNO and LNO as a function of U and J may be found in Table 4.2. We found that setting $U_{\text{eff}} = 6$ eV successfully obtained a metallic $R\bar{3}c$ LNO phase, but did not obtain the correct ground state for NNO. Instead, it yielded a $P2/c$ NNO state with FM order, of considerably lower energy and with different properties to the T- or S-AFM orders seen experimentally.

Table 4.2: Ground states of NNO and LNO at various Hubbard-U and Hund-J corrections.

Correction		Ground state phase	
U (eV)	J (eV)	NNO	LNO
1.50	0.75	$P2/c$ (T-AFM)	$P\bar{1}$ (T-AFM)
2.00	0.00	$P2/c$ (T-AFM)	$P\bar{1}$ (T-AFM)
	0.50	$P2/c$ (T-AFM)	$P\bar{1}$ (T-AFM)
	1.00	$Pbmn$ (FM)	$P\bar{1}$ (T-AFM)
3.00	-1.00	$P2/c$ (T-AFM)	$P\bar{1}$ (T-AFM)
	0.00	$P2/c$ (T-AFM)	$P\bar{1}$ (T-AFM)
	1.00	$P2/c$ (FM)	$R\bar{3}c$ (FM)
4.00	-1.00	$P2/c$ (FM)	$P\bar{1}$ (T-AFM)
	0.00	$P2/c$ (FM)	$P\bar{1}$ (T-AFM)
	1.00	$P2/c$ (FM)	$R\bar{3}c$ (FM)
4.90	-0.91	$P2/c$ (FM)	$R\bar{3}c$ (FM)
	0.91	$P2/c$ (FM)	$R\bar{3}c$ (FM)
5.00	0.00	$P2/c$ (FM)	$R\bar{3}c$ (FM)
$U_{\text{eff}} = 5.00$		$P2/c$ (FM)	$R\bar{3}c$ (FM)
5.99	0.83	$P2/c$ (FM)	$R\bar{3}c$ (FM)
6.00	0.00	$P2/c$ (FM)	$R\bar{3}c$ (FM)
$U_{\text{eff}} = 6.00$		$P2/c$ (FM)	$R\bar{3}c$ (FM)
6.32	0.68	$P2/c$ (FM)	$R\bar{3}c$ (FM)

Despite the larger U, FM ordering increases the band dispersion, shortening the gap to 0.14 eV, a value far smaller than that seen experimentally [215].

We next employed the 'minimum tracking approach' as mentioned above, to calculate U and J as defined in the unsimplified correction scheme. Calculating for the NNO $P2/c$ T-AFM phase obtained $U = 6.33 \pm 0.09$ eV, $J = 0.68 \pm 0.08$ eV on Ni_{L} sites, and $U = 5.99 \pm 0.04$ eV, $J = 0.83 \pm 0.04$ eV on Ni_{S} sites— a close match to the calculated U_{eff}. For the LNO $R\bar{3}c$ phase, we obtained $U = 4.9 \pm 1.1$ eV, $J = 0.9 \pm 1.1$ eV, also a good match (despite the large errors) to the values of NNO and the calculated U_{eff}. However, as with the corrections calculated with the simplified approach, these values do not obtain the correct ground state for NNO (while still performing well for LNO). As a last ditch measure, we also calculated the O-2p site corrections for the NNO, in hopes of more accurately simulating the interaction between Ni-3d and O-2p orbitals that the insulating properties depend on. Using the NNO $P2/c$ T-AFM phase, we obtained $U = 9.93 \pm 0.13$ eV, $J = 1.37 \pm 0.13$ eV for the O-2p orbitals, which once again yielded a $P2/c$ FM state for NNO (while using $U = 5.99$ eV, $J = 0.83$ eV for the Ni-3d orbitals). We also ran calculations with Nd-4f electrons included at these choices of U and J, but this did not impact the result either.

With these methods failing to capture the correct NNO ground state, we resorted to finding the ground state NNO and LNO phases for a range of U and J combinations, in the hope of finding a choice that resulted in the correct ground state. Unfortunately, we were unable to find a combination of U and J that simultaneously obtained a $P2/c$ T- or S-AFM NNO ground state and an FM $R\bar{3}c$ LNO ground state. However, we were able to find individual choices that obtained the correct ground states, allowing us to nonetheless investigate the effect of strain on these two materials, and use them in interfacial calculations (though not in the same system). For NNO, we choose a lower $U = 2$ eV correction for the Ni-3d sites, as suggested by previous studies to obtain the experimentally-observed $P2/c$ T-AFM ground state [80, 216], while for LNO, we settle for a larger $U_{\text{eff}} = 6$ eV correction (as suggested by our calculations), to obtain the correct $R\bar{3}c$ FM ground state.

Bulk NdNiO$_3$

The energy of various NNO phases at $U = 2$ eV are shown in Table 4.3. The $P2/c$ T-AFM phase (as specified in Table 4.1) is the lowest in energy, matching previous DFT studies [80,101]. We find the T-AFM magnetic order to be marginally lower in energy than the S-AFM order in our calculations. The metallic $Pbnm$-FM phase is higher in energy, while the $a^-a^-a^-$ input phases ($P\bar{1}$, $R\bar{3}c$) are higher in energy still. Details of the ground state structure and electronic properties are shown in Table 4.4 (additional details may be found in Table B.1 of Appendix B). Mode magnitudes and lattice parameters were found to be comparable to low temperature synchrotron data [84], while the band gap of the ground state $P2/c$-T phase was found to be 0.47 eV, which is comparable to values obtained from experiment [215] and previous DFT studies [80].

Table 4.3: ΔE of bulk relaxed NNO ($U = 2$ eV) and LNO ($U_{\text{eff}} = 6$ eV) phases with respect to bulk, non-magnetic $Pm\bar{3}m$.

Space Group	Mag. Order	$E - E_{Pm\bar{3}m}$ (meV/f.u.)	
		NNO	LNO
$P2/c$	T-AFM	-277	-501
$P2/c$	S-AFM	-276	-501
$Pbnm$	FM	-264	-531
$P\bar{1}$	T-AFM	-259	-503
$P\bar{1}$	S-AFM	-258	-503
$R\bar{3}c$	FM	-246	-532

Table 4.4: Structural and electronic properties of bulk NNO ($U = 2$ eV) and LNO ($U_{\text{eff}} = 6$ eV) (L. P. corresponds to Lattice Parameters). Further details for both [001] and [111] bases may be found in Table B.1 (Appendix B).

Quantity	NNO	LNO
Modes:		
$R_5^-(a_\text{p})$	0.39	0.26
$R_5^-(b_\text{p})$	0.39	0.26
$R_5^-(c_\text{p})$	0.00	0.26
$M_2^+(c_\text{p})$	0.33	0.00
R_2^-	0.06	0.00
X_5^-	0.21	0.00
L. P. (prim. basis)		
a_p (Å)	3.78	3.80
b_p (Å)	3.77	3.80
c_p (Å)	3.78	3.80
V (Å^3/f.u.)	53.79	54.73
E_g (eV)	0.47	0
Mag. Mom. (μ_B)		
Ni_L	1.18	1.28
Ni_S	0	1.28

Bulk $LaNiO_3$

The energies of various LNO phases (at the chosen $U_{\text{eff}} = 6$ eV) are also shown in Table 4.3. The metallic $R\bar{3}c$ FM phase is found to be the lowest in energy, closely followed by the metallic $Pbnm$ FM phase. Insulating phases are higher in energy, where the $P\bar{1}$ ($a^-a^-a^-$) phases are slightly lower in energy than the $P2/c$ phases ($a^-a^-c^+$). We remark that the reason for larger LNO energy differences (with respect to the non-magnetic $Pm\bar{3}m$ phase) compared to NNO is likely the choice of U correction. The modes and lattice parameters (Table 4.4, Table B.1 in Appendix B) match well to low temperature neutron diffraction data [70].

4.2.2 [001]-strain

Compressive $NdNiO_3$

The structural properties of $NdNiO_3$ as a function of [001]-strain are presented in Fig. 4.3(a)—(e). The energies of all stable and metastable phases as a function of strain (that could be relaxed) are also included in Fig. B.1 in Appendix B for reference. Starting with the compressive regime (3.60—3.75 Å), we observe the structure to initially remain in the $P2/c$ (T-AFM) phase as seen in bulk. At larger strains however, the system first reverts to the $P\bar{1}$ (T-AFM) phase at 3.65 Å, then to the metallic $I4/mcm$ (A-AFM) phase at 3.60 Å (a schematic of this magnetic order can be found in Fig. 1 of ref. [217]). These are both previously-unseen nickelate phases, though we remark that prior DFT studies have still observed an MIT at roughly this strain [101] (though this was to the $Pbnm$ (FM) phase, which we find to be metastable). We find that the system changes to the $P\bar{1}$ phase briefly during the transition— which consists of an $a^-b^-c^-$ tilt pattern (though, this is extremely close to $a^0b^-c^-$) and the breathing mode. A possible explanation for one in-plane tilt decreasing more than the other could be the energetic competition between antiphase tilts. Beyond this point, the system reverts to the $I4/mcm$ phase with an $a^0a^0c^-$ tilt pattern. This variation in the tilting is common for compressively [001]-strained perovskites (as seen the previous chapter with STO), where the suppressed in-plane and extended out-of-plane axes result in suppressed and enhanced in- and

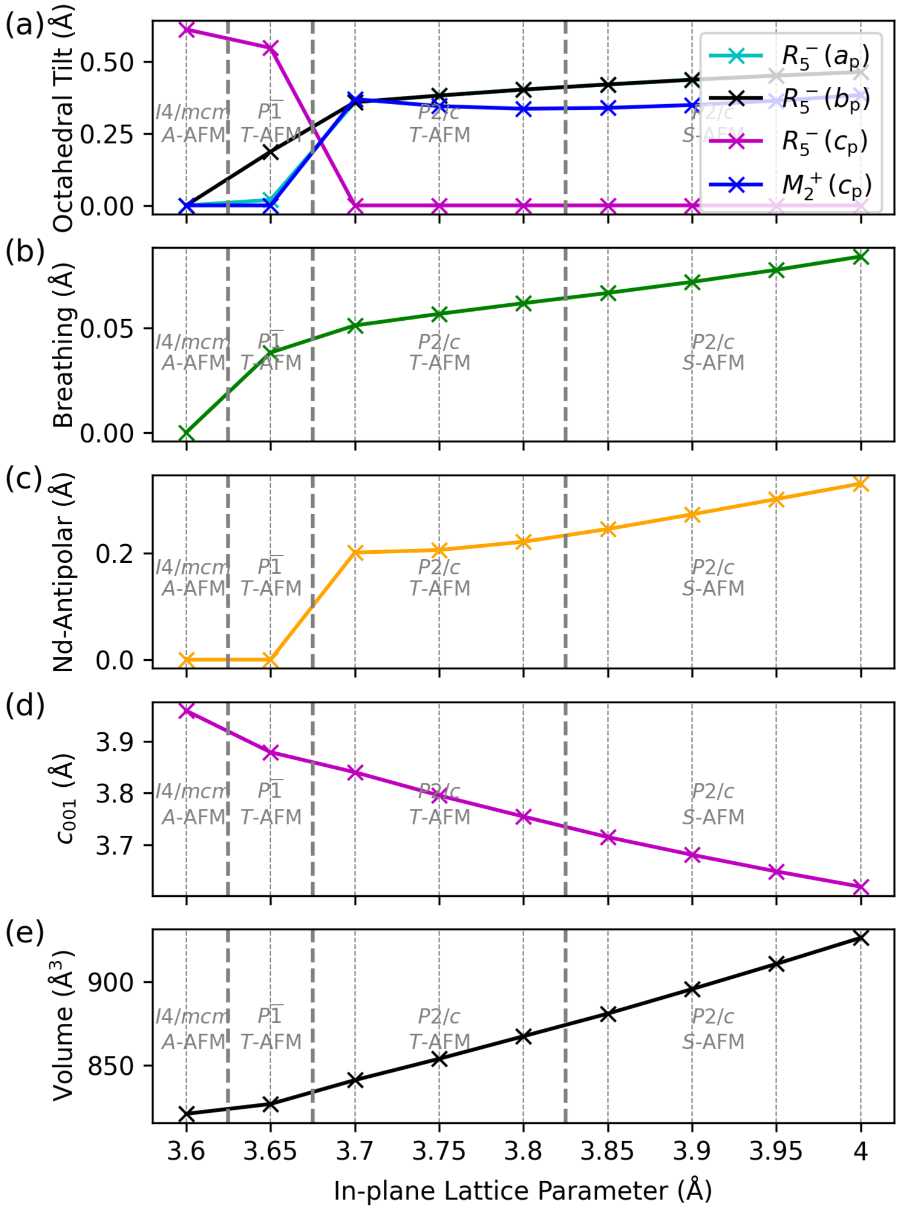

Figure 4.3: Structural properties of NNO as a function of [001]-oriented epitaxial strain: (a) octahedral tilt amplitude (where $R_5^-(a_\mathrm{p}) = R_5^-(b_\mathrm{p})$ above 3.65 Å), (b) breathing mode amplitude ($R_2^-(a)$), (c) Nd-site anti-polar mode amplitude ($X_5^-(0,0;0,0;a,a)$), (d) out-of-plane lattice parameter (in pseudocubic units), and (e) cell volume.

out-of-plane tilting respectively [96]. The breathing mode declines steadily for most of the compressive regime. Previous studies have demonstrated a cooperative coupling of the octahedral tilt modes to the breathing mode in rare-earth nickelates— such that the breathing mode becomes triggered under a critical amount of tilting [74]. Interestingly however, while in the $P2/c$ (T-AFM) phase, the tilts stay mostly fixed (on average), while the breathing mode steadily declines. This implies that the breathing mode may also be affected by a separate mechanism independent of tilting. Upon transition to the $P\bar{1}$ phase, the breathing magnitude declines more substantially, and disappears entirely beyond this. This rapid change is more likely to be (primarily) driven by the decline in tilts, where between 3.60 and 3.65 Å, the amount of tilting declines rapidly, likely to an amount below the threshold necessary for triggering the breathing mode. The A-site antipolar motion also disappears immediately upon the transition away from the $a^-a^-c^+$ tilt pattern, suggesting a typical coupling of the antipolar motion to the $a^-a^-c^+$ tilt pattern as observed in $Pnma$ perovskites [16]. With increased compressive strain, it is unsurprising that the out-of-plane lattice parameter $|\mathbf{c}_{001}|$ also increases, while the volume decreases.

The electronic properties of NdNiO_3 as a function of [001]-strain are presented in Fig. 4.4(a)—(f). To estimate the MIT temperature, we plotted the energy differences (per f.u.) ΔE_{MIT} between the lowest energy metallic and insulating phases. Interestingly, ΔE_{MIT} actually increases at mild strains, despite the decrease in breathing mode. This suggests that the nearest metallic phase ($Pbnm$ FM) becomes energetically unfavourable with compressive strain at a faster rate than the $P2/c$ phases. This is surprising, as the structural difference between the two phases— the breathing mode, declines in magnitude with strain. A possible explanation is the magnetic order— where the FM order appears to become less energetically favourable under compressive strain, as indicated by the switch to A-AFM. We tested A, C, and G-AFM orders (see ref. [217]) on $Pbnm$ phases at 3.70—3.75 Å, but found them to be higher in energy than the FM state. Regardless, beyond 3.70 Å, ΔE_{MIT} rapidly declines upon transition to the $P\bar{1}$ phase, which is most likely due to the net tilting lowering to the threshold of being too small to trigger the breathing mode. Beyond this, the system turns metallic, as observed in experiment and previous DFT stud-

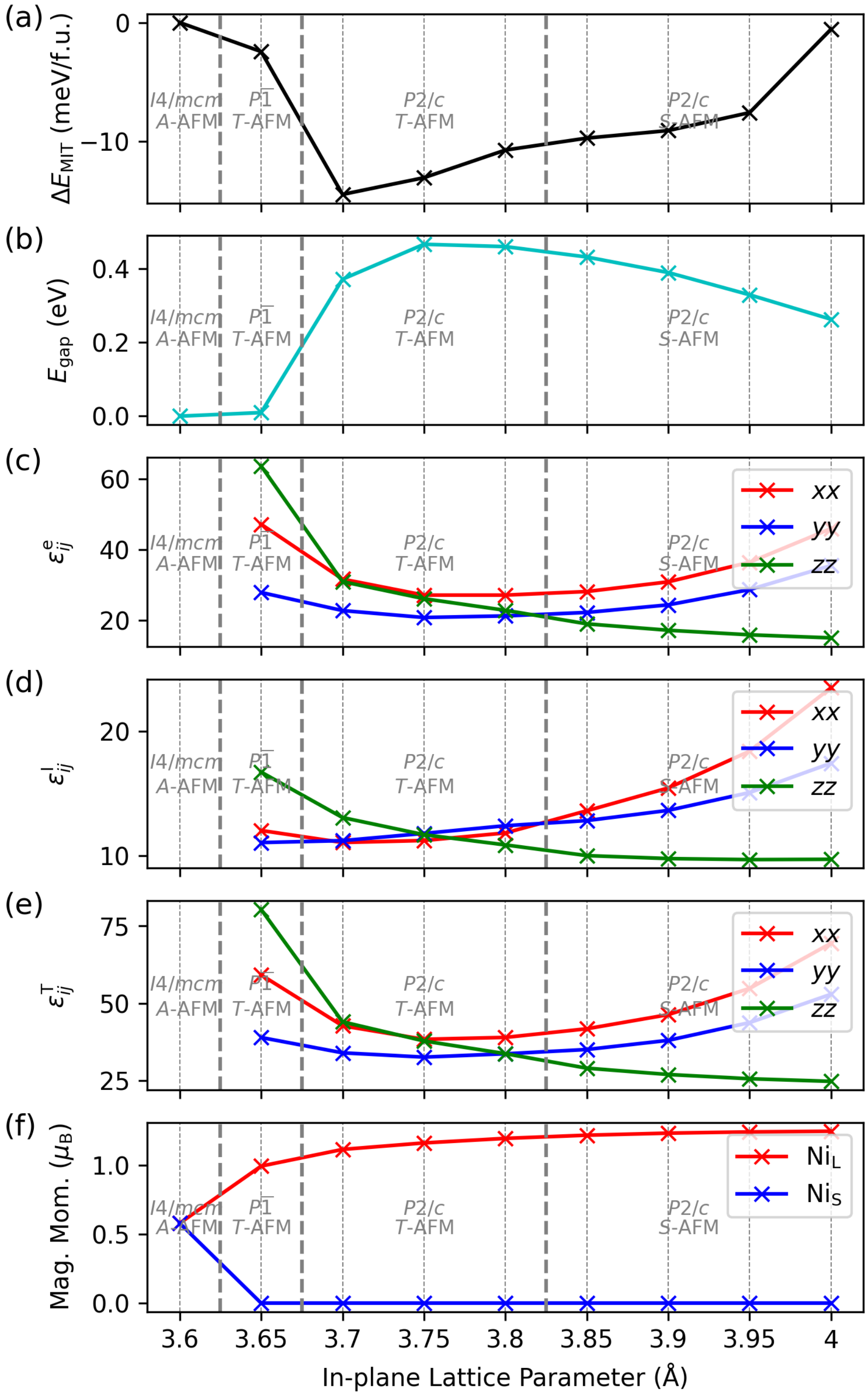

Figure 4.4: Electronic properties of NNO as a function of [001]-oriented epitaxial strain: (a) energy difference between lowest energy metallic phase and ground state, (b) electronic band gap, (c) electronic (superscript e), (d) ionic (superscript I), and (e) total (superscript T) static dielectric tensor components (where labels xx, yy, zz correspond to the components of the leading diagonal of the 3×3 dielectric tensor ϵ_{ij}, calculated along directions $\hat{a}_{001}, \hat{b}_{001}, \hat{c}_{001}$), (f) magnetic moments of large and small Ni sites.

ies [101, 128]. The width of the electronic band gap E_g is heavily coupled to the structural properties of NNO in bulk. The variation of the breathing mode amplitude directly modulates the band gap, while the tilt and Ni-O distance modulates the valence and conduction band dispersion (which in-turn moderately varies the band gap) [74]. In the compressive regime, the band gap initially declines steadily, which is unsurprising considering the breathing mode declines, and the net tilting does not increase. As the tilts and breathing mode decline further with increased strain, the band gap drops rapidly, almost to zero even within the charge-ordered $P\bar{1}$ phase, indicating that this phase is indeed on the verge of the IMT. We also computed the dielectric properties to check for polar instabilities. The electronic components ϵ^{e}_{ij} remain relatively steady until the system transitions to the $P\bar{1}$ phase, where they rapidly increase as the system approaches the IMT. This is not a surprising feature, as it becomes easier for electrons to displace as the band gap narrows. The ionic components ϵ^{I}_{ij} also vary significantly in the compressive regime, particularly out-of-plane, where there is a significant amplification with strain. This is likely a result of the increasing cell tetragonality, where the elongation of the out-of-plane parameter typically favours the appearance of out-of-plane polarisation (as seen with STO). This is likely amplified further by the net reduction in tilting, which is typically competitive with the polar mode (though the out-of-plane tilting, which affects the out-of-plane polar mode most substantially, increases) [32]. We also plot the magnetic moments, and observe clear $\mathrm{Ni_L}$ - $\mathrm{Ni_S}$ splitting in the charge-ordered insulating phases, and equal moments in the metallic phase. The system appears to favour the T-AFM magnetic order rather than S-AFM within the compressive regime, which may be driven by the strain itself, or tilt variation. It is also worth further commenting on the A-AFM order with respect to T-, S-AFM. Taking a hypothetical $\mathrm{Ni_S}$ site, and summing the magnetic moments of the six next nearest $\mathrm{Ni_L}$ sites, one finds that the sum in the T- and S-AFM regimes is always zero. This is not the case for A-AFM however (nor C- or G-AFM), where the sum is always non-zero. It is therefore unsurprising that the T-AFM and S-AFM orders are more energetically favoured by the nickelates for forming insulating phases (as a zero moment typically corresponds to a lower charge valence). We find that applying A-, C-, and G-AFM orders to the charge ordered $P2/c$ phase is enough to close the gap (though these remain higher in energy at all strains).

Tensile $NdNiO_3$

In the tensile regime (3.80—4.00 Å), the system remains in the $P2/c$ S-AFM phase, though several important structural changes occur with strain. The tilt modes increase slightly in-plane and out-of-plane, which is an unusual feature to occur under tensile [001]-strain, as out-of-plane tilting is often suppressed as $|\mathbf{c}_{001}|$ declines. The breathing mode also increases steadily. As with the moderate compressive regime, this is unlikely to be a result of tilting alone. The A-site antipolar motion also increases, which may indicate coupling with tensile strain alongside tilting. In opposite fashion to the compressive regime, $|\mathbf{c}_{001}|$ declines, while the volume increases.

The energy difference between metallic and insulating phases steadily declines for most of the tensile regime, until 4.00 Å, where it declines at a faster rate. This may seem a little surprising based on the structural results, as the breathing mode increases in magnitude. However, high [001]-strains are likely to apply a considerable energy cost to the breathing mode, as the mode relies on equal B-O bond lengths in each dimension. As an alternative, we might expect large [001]-strains to encourage orbitally-ordered Jahn-Teller phases involving split $d_{x^2-y^2} - d_{z^2}$ orbitals, which have been observed in previous DFT studies at extremely high [001]-tensile strains of around ∼9% (after undergoing an IMT at around ∼6% strain) [107]. This is not observed in our results, indicating that it is unlikely to occur within experimentally-realisable amounts of strain (4.00 Å = ∼6% strain). Our results still match the previous study qualitatively however (which uses the PBE exchange-correlation functional, and a 500 eV plane-wave cut-off), as NNO is clearly close to an IMT beyond our maximal strain. The band gap steadily declines with tensile strain. As the tilt and breathing modes stay fixed and increase respectively, this is probably a result of strain alone, where B-O bond shortening out-of-plane is likely to cause band dispersion (due to the increased overlap of Ni-3d and O-2p orbitals). Interestingly, the electronic components of the dielectric tensor steadily increase in-plane and decline out-of-plane. This is likely a consequence of the steadily-declining band gap, but suggests that electrons are more-easily able to displace along the elongated axes than compressed axes (where they appear to become more confined), contrary to what is expected regarding orbital overlap. The ionic response shows a very similar trend, though likely for different reasons— the increasing in-plane lattice parameters result in excess space that favours the formation of in-plane polar modes. This effect is likely encouraged further by the lack-of in-plane tilting amplification here, which competes with the polar mode to fill the space. Considering how close the system is to the IMT, it is unlikely that a polar phase can develop (spontaneously) with further strain. The magnetic moments subtly increase with tensile strain, which is likely a result of increased breathing mode amplitude and therefore local $\mathrm{Ni_L}$ valence.

Compressive $\mathbf{LaNiO_3}$

The properties of LNO as a function of [001]-strain are shown in Fig. 4.5(a)—(e). The energies of each stable and metastable phase as a function of strain may be found in Fig. B.2 in Appendix B. Upon applying [001]-strain, the symmetry of the rhombohedral $R\bar{3}c$ (FM) phase is immediately broken to the $C2/c$ (FM) phase, such that the in- and out-of-plane tilts are allowed to differ in magnitude (thus resulting in an $a^-a^-c^-$ tilt pattern). Under compressive strain, the in-plane tilts gradually decrease, until they disappear entirely beyond 3.70 Å, transitioning to a higher symmetry $I4/mcm$ phase. The out-of-plane tilt simultaneously increases steadily— clearly reminiscent of the NNO and STO [001]-compressive regimes. Once again, this is likely driven by increasing cell tetragonality combined with decreasing (competitive) in-plane tilts.

The system remains strongly metallic throughout the compressive regime, and retains an FM order. We also tested A-, C-, and G-AFM orders on the $I4/mcm$ phase in the compressive regime, though we found that these remained metastable. The insulating $P\bar{1}$ T-AFM phase was found to be metastable in the compressive regime, and lower in energy than the $Pbnm$ phase. It is a little surprising that we were able to relax the $P\bar{1}$ phase altogether, as this input reverted to the higher

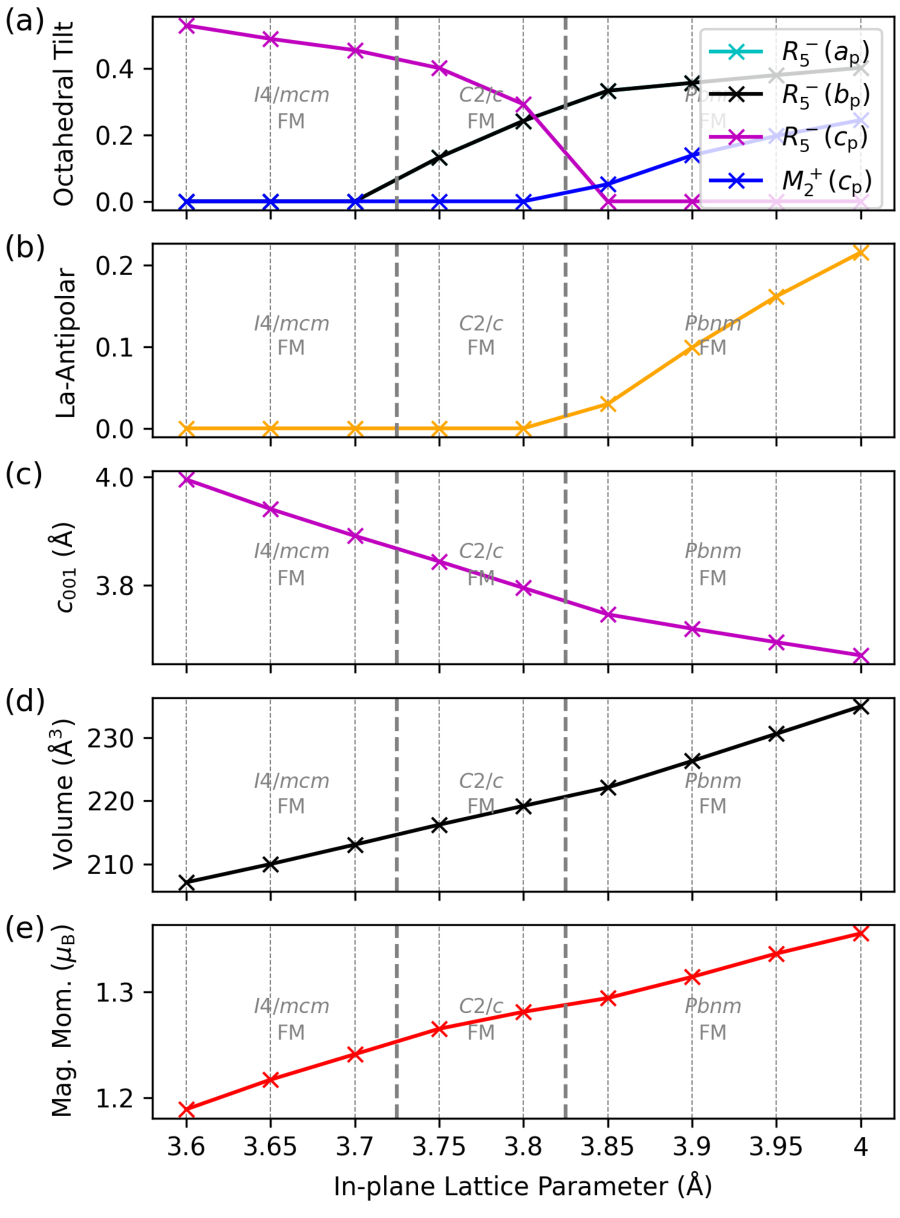

Figure 4.5: Properties of LNO as a function of [001]-oriented epitaxial strain: (a) octahedral tilt amplitude (where $R_5^-(a_\mathrm{p}) = R_5^-(b_\mathrm{p})$), (b) La-site antipolar mode amplitude ($X_5^-(0,0;0,0;a,a)$), (c) out-of-plane lattice parameter (in pseudocubic units), (d) cell volume and (e) magnetic moments.

symmetry $a^0a^0c^-$ tilt pattern at high compressive strains, yet retained the breathing mode, which based on the triggered mechanism of NNO, should not be possible. Regardless, it is higher in energy, and appears to become increasingly energetically unfavourable at higher strains— likely because of the increased energy cost of the breathing mode. The *Pbnm* input reverted to a metastable $a^0a^0c^+$ phase for high compressive strains, clearly demonstrating that antiphase tilting is preferential to in-phase along the out-of-plane axis in the compressive regime, which is logical given the former better fills the excess space caused by strain.

Tensile $LaNiO_3$

In the tensile regime, the system quickly reverts to the *Pbnm* phase— the tilt pattern changing from $a^-a^-c^-$ to $a^-a^-c^+$. This is vaguely reminiscent of the NNO tensile regime, where this tilt pattern also remains energetically stable— suggesting that tensile [001]-strain may not impose such a huge penalty on out-of-plane tilting when in-phase. Both the in- and out-of-plane tilts rise steadily, which simultaneously drives the *A*-site antipolar mode. We do not see the breathing mode stabilise, though one might predict that the system becomes more susceptible to it at moderate tensile strains, where the net tilting is larger than in bulk, and without applying a significant geometric constraint as seen for high [001]-strains. However, the net tilt amplitude ($= \sqrt{2 \times (R_5^-)^2 + (M_2^+)^2}$) at 4.00 Å for LNO (= 0.62) is larger than the net tilt at the lowest tilt NNO strain point with breathing (3.65 Å, net tilt = 0.58), which suggest that tilting is not the only factor for triggering the breathing mode in the rare-earth nickelates. A possible explanation is that the amount of $4f$ orbital filling (and therefore, *A*-site ionic radius) plays a crucial role in determining whether the breathing mode forms, as Nd clearly allows for breathing mode triggering at lower net tilt than La, which has a larger *A*-site. It is unclear whether the breathing mode can still stabilise in LNO, though previous DFT studies on interfaced LNO have observed an MIT via orbital-ordering [87], which is suggested to be driven by strain and quantum confinement. This is equivalent to the phase observed in NNO at extremely high tensile strains [101]. If it is possible to induce an MIT in LNO at higher tensile strains than tested here, the system is likely to do this through orbital-ordering rather than charge-ordering, due to the energy penalty of the breathing mode at high tensile strains. In Fig. B.2, there are no trends that suggest any of the charge-ordered insulating phases are close to stabilising.

4.2.3 [111]-strain

Compressive NdNiO$_3$

To study interfaced systems involving [111]-oriented charge-ordered nickelates, we investigated in-full the effect of [111]-strain on NNO. The structural details are reported in Fig. 4.6 (a)—(f). The energies of each phase as a function of [111]-strain may be found in Fig. B.3 in Appendix B. Starting with the compressive regime (3.60—3.75 Å), we observe the structure to remain in the $P2/c$ (T-AFM) space group, except for very high strains where the system transitions to a higher symmetry $C2/m$ (T-AFM) phase. As compressive strain is applied, the in-phase M_2^+ tilt declines steadily, while the Nd-antipolar motion declines concomitantly. Interestingly however, the two R_5^- tilts remain stable, even increasing slightly with strain. This could be explained by the competitive coupling between octahedral tilts, where the declining M_2^+ mode allows the other two tilts to increase in magnitude. The breathing mode also steadily declines throughout the compressive regime. It is plausible that the decline of the breathing mode is driven by the decline of the in-phase tilt (thus reducing the net tilt), though as the two antiphase tilts increase slightly, it is hard to conclude that tilting is the only factor causing this. Despite the predictable increase of the out-of-plane parameter $|\mathbf{c}_{111}|$, the three primitive axes decline with strain, particularly in the $\hat{c}_\mathrm{p}$ direction (likely a result of the vanishing tilt on this axis). The variation in the primitive lattice parameters is driven primarily by [111]-strain directly, which applies an equal geometric constraint on each primitive direction (though this is complicated by the effects of tilt competition here).

The electronic properties of NdNiO$_3$ as a function of [111]-strain are presented in Fig. 4.7(a)—(f). Interestingly, we could not relax any metallic phases in the compressive [111]-regime, which is surprising given the breathing mode is declining in magnitude, suggesting that the system might be approaching an IMT. Regardless,

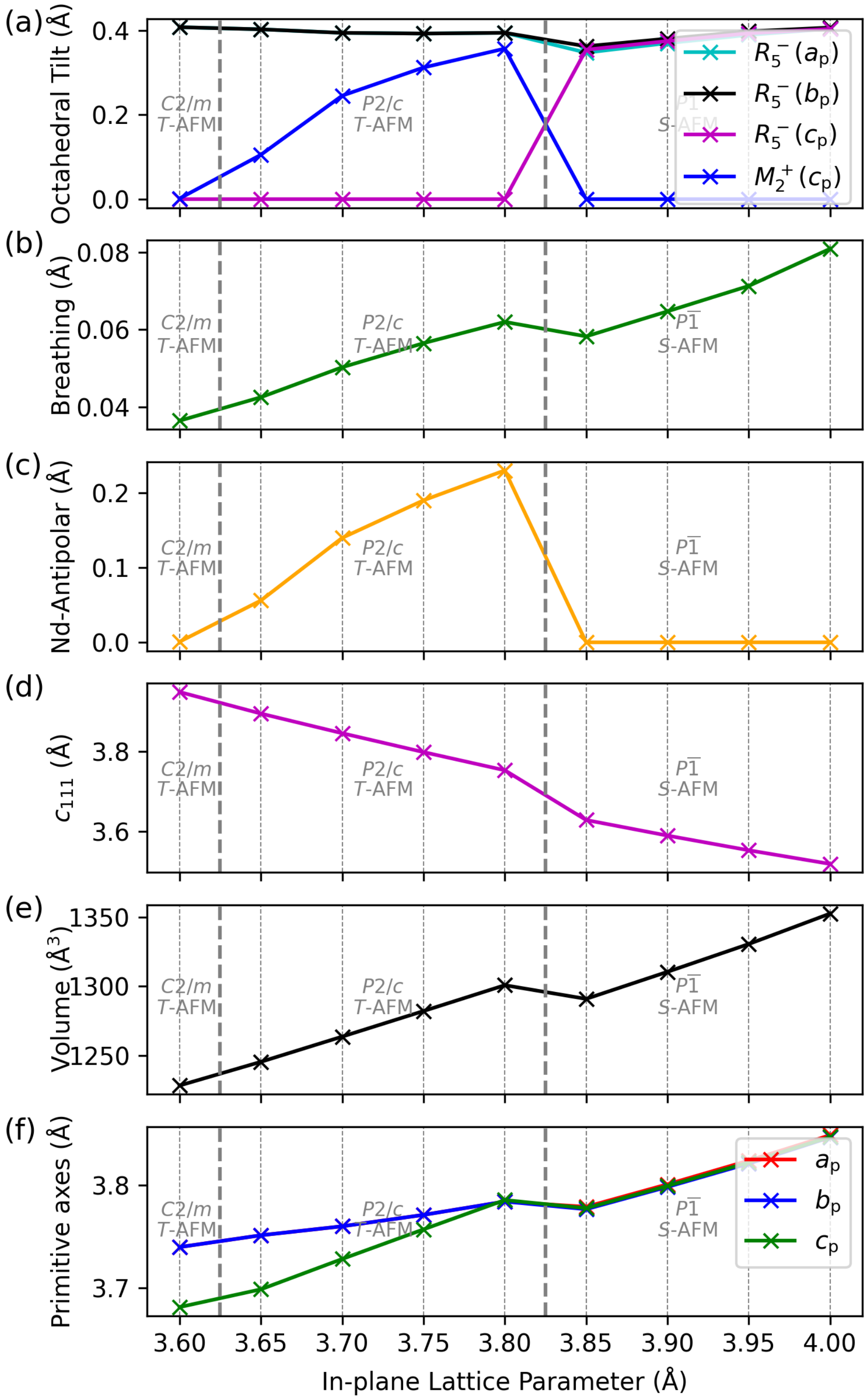

Figure 4.6: Structural properties of NNO as a function of [111]-oriented epitaxial strain: (a)—(e) are equivalent to Fig. 4.3(a)—(e) (where $R_5^-(a_p) = R_5^-(b_p)$ from 3.60 to 3.80 Å and (primitive axis magnitudes) $a_p = b_p$) (f) lattice parameters along primitive axes (in pseudocubic units).

given the net tilt and breathing mode decline, it is no surprise that the electronic band gap also steadily declines under the compressive [111]-strain. The decline is relatively moderate however— the gap remains far from closing fully. Looking to the dielectric properties, which we compute with respect to the [111]-cell axes, we find that the out-of-plane component (along $\hat{c}_{111}$) is amplified with increasing strain, while in-plane components (along $\hat{a}_{111}$ and $\hat{b}_{111}$) are also moderately amplified. This is primarily due to the electronic component, which suggests that the system may indeed be approaching the IMT. The greater amplification of the electronic component along $\hat{c}_{111}$ is likely related to the elongation of this axis (though, it appears that the compression of the in-plane axes does not strictly further confine electrons as we see in [001]-tensile strain regime, as these coefficients also rise). The ionic component is also slightly amplified along $\hat{c}_{111}$, which indicates that the system may also be marginally closer to a polar instability, which is likely also linked to the increasing cell tetragonality.

Comparison to compressive [001]-strain

There are many similarities between the results for [111]- and [001]-oriented compressive strain on NNO. Generally, the effect of compressive strain on the structure of NNO is not as extreme in the [111]-basis as in the [001]-basis, due to the varying geometric constraints on the primitive axes. [111]-strain affects the primitive axes equally, while [001]-strain splits the axes lying in-plane with the one lying out-of-plane. The latter substantially alters the tilting, particularly at larger strains, where the IMT is induced. Still, the electronic properties of the [111]-compressive regime show a striking resemblance to those of the [001]-compressive regime. Right before the IMT, the electronic dielectric components diverge to similar values as in the [111]-regime at our maximal compressive strain. This indicates that the [111]-strained system may actually be far closer to an IMT at 3.60 Å than expected, and that further compressive [111]-strain might induce this. The out-of-plane ionic component also increases in both strain regimes. In the [001]-basis this is in spite of the out-of-plane tilt mode increasing— if this could be suppressed before the IMT, the polar mode may become unstable. However, as with the [111]-basis, reducing

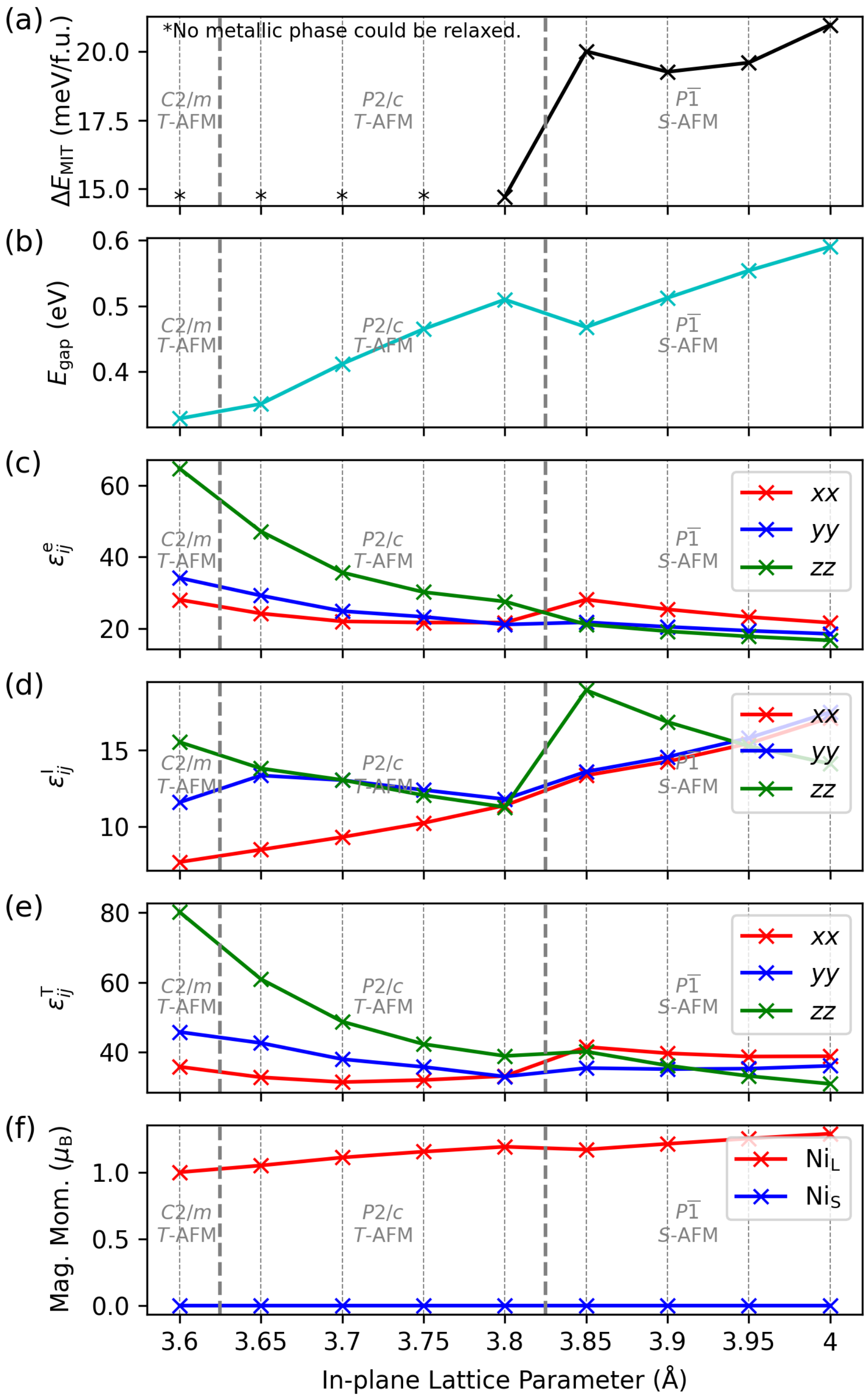

Figure 4.7: Electronic properties of NNO as a function of [111]-oriented epitaxial strain: (a)—(e) identical to 4.4(a)—(e) except dielectric tensor components are now oriented along $\hat{a}_{111}$, $\hat{b}_{111}$, and $\hat{c}_{111}$, (f) magnetic moments of large and small Ni sites.

the tilting may just induce the IMT instead. Furthermore, octahedral tilt matching (particularly out-of-plane) to a substrate in the [001]-basis typically has a much weaker effect (due to connectivity of the octahedra). Therefore, the creation of a polar NNO phase in the [001]-basis is likely to be far more challenging than in the [111]-basis.

Tensile $NdNiO_3$

In the tensile regime (3.80—4.00 Å), initially (3.80 Å) the system remains in the $P2/c$ (T-AFM) phase. However, beyond this point we observe the stabilisation of a triclinic $P\bar{1}$ (S-AFM) phase, where the in-phase tilt mode of the $P2/c$ phase reverts to antiphase, with a similar magnitude to the other two antiphase tilt modes (resulting in an $a^-a^-a^-$ pattern). Simultaneously, the antipolar mode predictably disappears as it is not induced by this tilt pattern. However, the breathing mode remains present, hinting that the model of the triggered MIT in ref. [74] also applies to non-orthorhombic tilt patterns. It was demonstrated in ref. [74] that both antiphase and in-phase tilt modes couple cooperatively to the breathing mode, so this result is not unexpected. During the phase transition to $P\bar{1}$, the breathing mode slightly decreases in amplitude. The primitive parameters, c_{111} magnitude and volume also all slightly decrease, which is surprising under tensile strain. The most likely cause is the change in tilt pattern, which is more able to fill the excess space left by strain than the orthorhombic tilt pattern. Therefore, the three primitive parameters shorten slightly, which in-turn lowers c_{111} and the volume. The breathing mode lowering is trickier to explain, though this suggests that it becomes increasingly stable for larger cell sizes (which is also seen under [001]-strain). Based on this, we can say that the $a^-a^-a^-$ tilt pattern is slightly less able (for the same tilt magnitudes) than the orthorhombic tilt pattern to trigger the breathing mode for the same strains. Regardless, beyond this transition, we see the breathing mode steadily increase. The tilts, driven by strain, only increase minimally, which is further evidence that the breathing mode is also coupled to other cell properties (which we explore in the next section).

The energy difference between metallic and insulating phases increases significantly in the [111]-tensile regime, even for lower strains. It appears to tail off at medium tensile strains, but continues increasing beyond this. This matches nicely to experiment, where the MIT temperature has been observed to enhance significantly on an orthorhombic $NdGaO_3$ substrate in the [111]-basis, which applies tensile strains of 1.8% and 4.2% to each in-plane axis [130]. The band gap steadily increases in the [111]-tensile regime, which can be attributed to the increase in breathing mode, as well as the slight increase in tilting. We note that based on the above arguments regarding tilt patterns, enforcing an $a^-a^-c^+$ pattern is likely to amplify the gap further, given the drop in magnitude when transitioning from $P2/c$ to $P\bar{1}$. The dielectric properties remain stable, with no indication of a polar mode appearing with increased tensile strain. However, we notice a significant out-of-plane ionic dielectric component amplification at low tensile strains, while the system is in the $P\bar{1}$ phase. This suggests that phases with the $a^-a^-a^-$ tilt pattern may be more cooperative with the polar mode than those with the $a^-a^-c^+$ pattern. The $a^-a^-a^-$ pattern has been shown to appear alongside polar modes in several bulk perovskites [31]. To see if we could induce a polar NNO phase, we investigated the polar instability of the metastable $P\bar{1}$ phase at 3.75 Å, the lowest compressive point it could be relaxed (higher compressive strains relax to a $C2/m$ ($a^-a^-c^0$) state). We could not relax a polar mode here, but found the out-of-plane ionic component to be 25.84, an increase from 3.85 Å (18.92). In an interfaced system, it may be possible via substrate tilt control to induce the $P\bar{1}$ phase deep into the compressive regime. At these points, where the out-of-plane axis is amplified, the resulting system is likely to be closer to the polar instability, which could tentatively lead to an exotic polar, charge-ordered nickelate phase. On a separate note, substrate tilt matching could also reduce the NNO tilt magnitudes, making a polar phase more energetically favourable (if the tilts are reduced too much however, this may prevent the triggering of the breathing mode and induce an IMT). Experimentally, on [111]-$LaAlO_3$ (which applies only a minimal tensile strain to NNO, but enforces the $a^-a^-a^-$ tilt pattern), a polar metal NNO phase has been observed— which is attributed to tilt matching [98]. Our results indeed suggest that inducing this tilt pattern in NNO moves the system closer to a polar instability, while simultaneously suppressing the

MIT. Our results also suggest that applying compressive [111]-strain could amplify this effect further. However, we emphasise that these calculations suggest that NNO is still quite far from being polar, at least from the effect of strain alone. One other interesting point to note is in regards the magnetic order. We find that in the [111]-tensile regime, the S-AFM order is lower in energy than the T-AFM order, and vice versa in the compressive regime, just as is seen in the [001]-strain phase diagram. A possible cause of this alongside the strain itself is the tilting, where increasing the tilts appears to favour S-AFM, while decreasing them favours T-AFM.

Comparison to tensile [001]-strain

As with the compressive regime, there are many similarities between the [111]- and [001]-tensile regimes. Both regimes see the breathing mode increase in amplitude, while the tilt mode amplitudes remains mostly unchanged. This suggests that both strains drive the appearance of breathing mode in ways other than the tilting. Despite this, [111]-tensile strain has a vastly different effect on ΔE_{MIT}. At our maximal tensile strain (4.00 Å), ΔE_{MIT} is significantly amplified in the [111]-basis, while rapidly decreasing in the [001]-basis. [111]-tensile strain is the only type of strain investigated in this study that shows signs of amplifying the MIT temperature rather than reducing it.

4.2.4 Coupling of the breathing mode to strain

Our results suggests that there exists an alternative driving force for the appearance of the breathing mode, besides octahedral tilting. To clarify this, we investigated the mode coupling between the breathing mode and strain itself. For several strains amplitudes, we measured the energy of the system for various breathing mode amplitudes, from 0% to 150% of the bulk ground state value. Our findings are shown in Fig. 4.8. For each curve, we measure the energy curvature based on a fitted quadratic function. A smaller curvature indicates that the breathing mode is more energetically favourable for a given strain, while a larger curvature indicates the reverse. Looking first at the effect of [111]-strain (Fig. 4.8(a)), we find the energy curvature increases with compressive strain, and decreases with tensile strain.

This matches exactly what is seen in our strain phase diagram, where the breathing mode decreases and increases in magnitude with compressive and tensile strain respectively. This also confirms that the breathing mode not only driven by tilt (which is simultaneously affected by strain), but also strain. The result for [001]-strain (Fig. 4.8(b)) is very similar, where the curvature also increases and decreases in compressive and tensile strain respectively, matching our [001]-strain phase diagram.

Interestingly, though the magnitude of the curvature is greater under compressive strain in the [111]-basis, we only observe the IMT to occur in the [001]-basis. This must be due to the differences in the tilting, where the latter sees much greater variation. Another unanswered question is the reduction of ΔE_{MIT} at high [001]-tensile strains, despite the increased favouring of the breathing mode at this strain. As mentioned, the breathing mode is likely suppressed by reduced primitive parameters—in this test we do not allow the out-of-plane parameter to relax, which might be the deciding factor for [001]-tensile strain. This could also be further affected by other modes not included here.

To further understand the situation, we also checked the allowed Landau coupling terms of various symmetries present in our study. Interestingly, upon investigating the coupling between the tilt modes ($R_5^-(a,a,0)$, $M_2^+(0,0,a)$), breathing mode ($R_2^-(a)$) and [111]-strain mode ($\Gamma_5^+(a,b,-a)$), we find that there exists a fifth-order coupling term of the form $(R_5^-)^3(R_2^-)(\Gamma_5^+)$. Though we expect this coupling term to be small relative to the couplings between [111]-strain and tilting (as well as [111]-strain and breathing), this term implies that the energy depends on the sign of the breathing mode magnitude, which structurally corresponds to alternating which sites are $\mathrm{Ni_L}$ and $\mathrm{Ni_S}$. To test this, we investigated how the energy landscape for a compressively strained system with fixed tilting and [111]-strain varies as a function of (R_2^-) (for both positive and negative amplitudes). We find that the energy is indeed asymmetric with a linear relationship for breathing amplitudes of -2% to +2% of the bulk value. This means that the choice of which sites are $\mathrm{Ni_L}$ and $\mathrm{Ni_S}$ does indeed matter to the system under [111]-strain. This difference is relatively subtle, but we show that it is non-negligible. In terms of our reported [111]-strain phase diagram, for the input $P2/c$ phases, we tested the choice of breathing order that

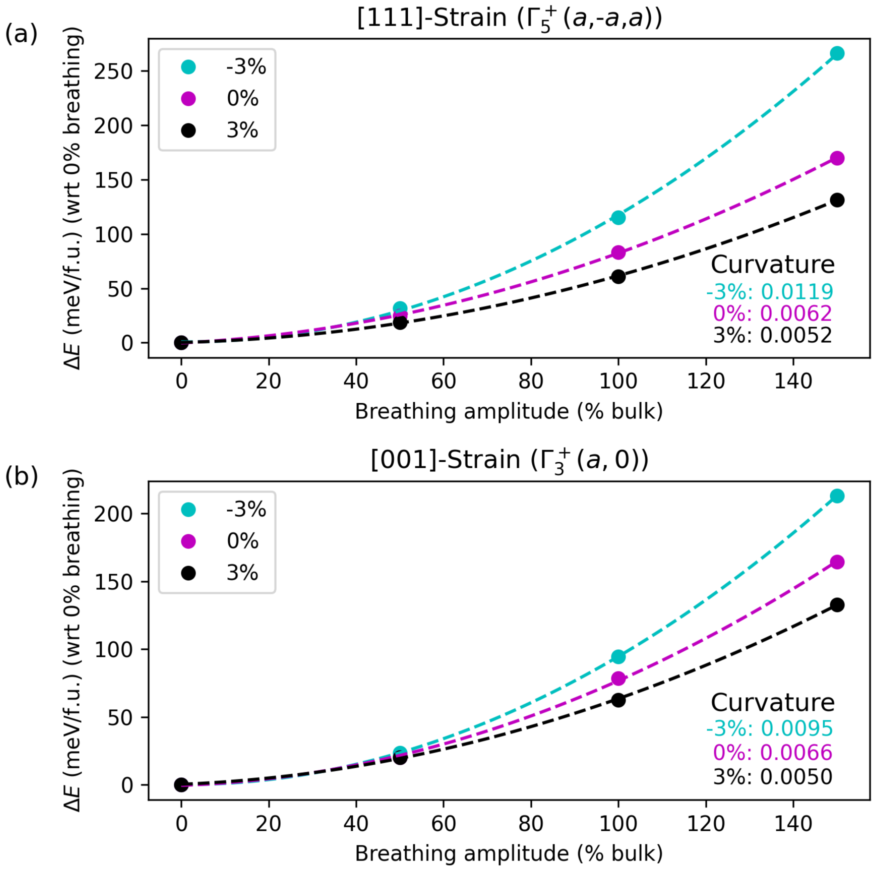

Figure 4.8: Strain-breathing mode energy curvature for (a) [111]-strain ($\Gamma_5^+(a, -a, a)$ and (b) [001]-strain ($\Gamma_3^+(a, 0)$. Curvatures are measured via second-order polynomial fits (and are thus unitless).

was lower in energy in the tensile regime, but higher in energy in the compressive regime. Given we already have a $P2/c$ (T-AFM) ground state for the compressive regime, we do not expect the qualitative features of our results to be significantly affected by this.

4.3 Summary

We have provided an in-depth investigation into several factors determining the properties of the rare-earth nickelates. We have studied both $NdNiO_3$ and $LaNiO_3$, where the former is also representative of the rest of the rare-earth nickelates. We determined suitable Hubbard-U and Hund-J correction terms for both NNO and LNO, and found that the former best matches low temperature experimental readings with a small Hubbard-U correction of 2 eV, and the latter an effective U_{eff} of 6 eV.

We then applied [001]-strain to both compounds, and find that both undergo various phase transitions. NNO undergoes an IMT under compressive strain, reverting to previously-unseen $P\bar{1}$ (T-AFM) and $I4/mcm$ (A-AFM) phases. LNO remains metallic, but reverts to novel $C2/c$ (FM), and $I4/mcm$ (FM) phases under compressive strain and a novel $Pbnm$ (FM) phase under tensile strain. We also investigate the effect of [111]-strain on NNO, and identify similarities and differences to the [001]-regime. Here, we do not observe an IMT, but the system reverts to a novel $C2/m$ (T-AFM) phase under compressive strain and a novel $P\bar{1}$ (S-AFM) phase under tensile strain.

We also investigated the coupling between strain and the breathing mode. We find that compressive [001]- and [111]-strains compete with the breathing mode, while tensile [001]- and [111]-strains cooperate with it. We also discover a fifth-order coupling term between the tilting, [111]-strain and the breathing mode within the Landau energy expansion, which we verify leads to the breathing mode having an asymmetric energy lowering depending on its sign (such that the choice of Ni_S and Ni_L site matters under this strain).

CHAPTER 5

Huge interfacial dipoles and pinned polarisation in [001]-oriented $SrTiO_3$-$NdNiO_3$ interfaces

Now we have a detailed description of how STO and NNO respond to epitaxial strain, we move to interfaced systems, which we are now able to analyse to the best of our ability. In this chapter, we report an investigation into [001]-oriented NNO-STO interfaced systems consisting of various combinations of SrO-NiO_2 and NdO-TiO_2 interfaces. We come to the interesting discovery that even when the NNO layer is metallic and the STO layer paraelectric, huge dipoles appear at the interfaces beyond what is expected from intrinsic effects. We find that these correspond to the dipole between an interfacial charge (which we identify is approximately equal to that of the well-known LAO-STO interface) and metallic screening charges of the opposite sign. To reduce the energy cost of the dipoles, the STO and NNO films behave in unique ways. When the STO film is fixed to be paraelectric, we find that the interfacial Nd- and Ni-sites shift substantially in attempt to screen the dipoles. In contrast, when STO is allowed to turn polar, it immediately stabilises and becomes pinned in the direction of the field arising from the interfacial dipoles. The STO polarisation is larger than in bulk-strained calculations, and suppresses interfacial Nd and Ni motion, which in-turn increases the NNO screening length.

5.1 Introduction and methods

Interfacing an insulating III/III perovskite (A-, B-site nominal charges are both 3+) with an insulating II/IV perovskite (A-, B-site nominal charges are 2+ and 4+ respectively) in the [001]-basis leads to interfacial polar discontinuities— high densities of bound charges at the interfaces that if left unscreened, result in sizeable electric fields throughout the system [102–105]. This often leads to unusual behaviour, as the films are encouraged to screen this charge as much as possible (or consequently experience energy penalties), which is not an easy task for insulators. Polar discontinuities were first observed in perovskites at the interface between LAO and STO— two insulators with A^{3+}, B^{3+} and A^{2+}, B^{4+} formal charges respectively [63, 111]. To deal with the huge energy cost, this system forms two dimensional electron gases (2DEGs) at the interfaces, where free carriers screen the bound charges. This can be achieved at a critical film thickness where the LAO valence and STO conduction bands overlap due to the unscreened field across the system, which allows for electron tunneling [104]. Further studies have demonstrated that LAO-STO 2DEGs possess a range of fascinating properties, including magnetism [112, 113], superconductivity at low temperatures [114, 115] and the possibility for manipulation via an external electric field [218]. Polar discontinuities exist in any system of interfaced perovskite insulators with different layer charges (which result in different formal polarisations), and lead to diverging potentials in both open- and closed-circuit systems if left unscreened. Even for systems with enough free charges to screen the discontinuity, the screening remains imperfect as the charges cannot all lie exactly at the interface. As a result, dipoles are formed from the interfacial charges and the screening charges of opposing sign (separated by the finite screening length). In closed-circuit systems (all DFT calculations, and most experiments, where short-circuiting is common due to defects), if the dipoles at either interface are inequivalent (which is the case for stoichiometric perovskite systems) then net fields still appear across the system [105].

The effect of imperfect screening is also seen in the ferroelectric capacitor, which consists of a ferroelectric film sandwiched between two metallic electrodes. Monodomain polarisation may occur here, due to the metallic screening of interfacial charges appearing from (ferroelectric) polarisation [121, 219]. However, the metallic screening remains imperfect, so inequivalent interface dipoles appear on either side of the ferroelectric, which lead to a depolarising field across the it (as well as the metal electrodes, though this is screened by the free charges). The magnitude of this field may only be reduced by increasing the ferroelectric film thickness, which in-turn lowers the energy cost for monodomain polarisation. Therefore, there exists a critical film thickness for the appearance of ferroelectricity, beyond which the field is small enough and the polar mode is energetically possible [125, 126].

In this chapter, we build closed-circuit (equivalent to periodic boundary conditions) interfaced systems of incipient ferroelectric STO and metallic NNO. Our DFT calculations use parameters as close to those used for our bulk calculations as possible where computationally feasible. We continue using the PBEsol exchange-correlation functional alongside the same pseudopotentials (within the PBE scheme) as used for Sr, Ti, Nd-, Ni- and O-sites in chapters 3 and 4. As doubling the 20-atom [001]-cell (as defined in Fig. 3.2(b)) in-plane leads to a computationally-untractable 400 atom unit cell for the film thicknesses we desire (discussed below), we choose to omit T- and S-AFM orders in the NNO film. We instead use the metallic $Pbnm$-FM structural input— though the breathing mode could be added in, it is unlikely to appear spontaneously. Experimental studies on NNO-STO interfaces directly comparable to ours have reported metallic behaviour in the nickelate layers, suggesting that a unit cell of this size is still capable of recreating all experimental properties [220]. All of our calculations used an initial FM input[1] with moments on the Ni sites set to $2\mu_{\mathrm{B}}$. We build these systems at LAO strain, in order to mimic the effect of an LAO substrate. This imposes a compressive strain of 2.5% on STO and a minor tensile strain of 0.2% on NNO. According to our calculations from previous chapters, this strain yields a polar ($I4cm$) state in STO and a metallic ($Pbnm$) FM state in NNO (out of the 20-atom cell phases— insulating $P2/c$ T-AFM is the 80-atom cell ground state). We also relaxed [001]-oriented bulk LAO (including La $4f$ (unoccupied), $5s$,

---

[1] The systems were still able to relax AFM phases, and they regularly did (the magnetic order was generally volatile during the SCF cycle). However, we made sure to re-relaxed our (metastable) structures with an FM order, which we found further lowered the energy for each system.

$5d$, $5p$ and $6s$; Al $3s$ and $3p$ electrons) in its ground state rhombohedral $R\bar{3}c$ phase ($a^-a^-a^-$ tilt pattern), and found the result to be comparable to low-temperature neutron diffraction data [221], such that we obtained in-plane lattice parameters of $|\mathbf{a}_{001}^{\mathrm{LAO}}| = 5.35$ Å and $|\mathbf{b}_{001}^{\mathrm{LAO}}| = 5.34$ Å. For computational tractability during ionic relaxations, we set the plane-wave energy cut-off to 550 eV, while the K-point grid was fixed to a $5 \times 5 \times 1$ Γ-centered mesh for all systems. We relax three systems (besides their in-plane lattice parameters, which are held fixed to those of bulk LAO), each consisting of 200 atoms, to a force convergence of 1 meV/Å. We used a Hubbard-U correction of 2 eV on the Ni-$3d$ sites as in chapter 4.

We start by investigating non-stoichiometric interfaced systems consisting of two of the same type of interface, either SrO-NiO$_2$ or NdO-TiO$_2$. This fixes net inversion symmetry if starting from a non-polar STO phase (though it is still broken locally at the interfaces), preventing STO from accessing the polar phase. Therefore, we are interfacing a paraelectric STO film with metallic NNO film, which we expect to behave in a simple manner. The system consisting of two SrO-NiO$_2$ interfaces has 8.5 NNO layers and 11.5 STO layers, while the system of two NdO-TiO$_2$ interfaces has 9.5 NNO layers and 10.5 STO layers (where each layer has the chemical formula $2ABO_3$). The layer thicknesses have to be varied slightly between systems to retain inversion symmetry, though we still see bulk-like properties in the centre of each film, meaning the systems can still be compared on an even footing.

We then extend the model to the stoichiometric system consisting of one of each interface termination. If STO is ferroelectric, we may expect a similar scenario to the ferroelectric capacitor described above, but if not, a similar result to the non-stoichiometric metal-paraelectric systems. In this system the STO thickness matters, as there may be fields across the film. Our NNO and STO films are 8 and 12 layers thick respectively (where each layer has formula $2ABO_3$). The STO film specifically consists of six [001]-unit cells as defined in Fig. 3.2(b), which is equivalent to the thickness used in previous DFT studies of the LAO-STO system [104]. We use an NNO film that is sufficiently thick to resemble bulk-like properties in the central layer.

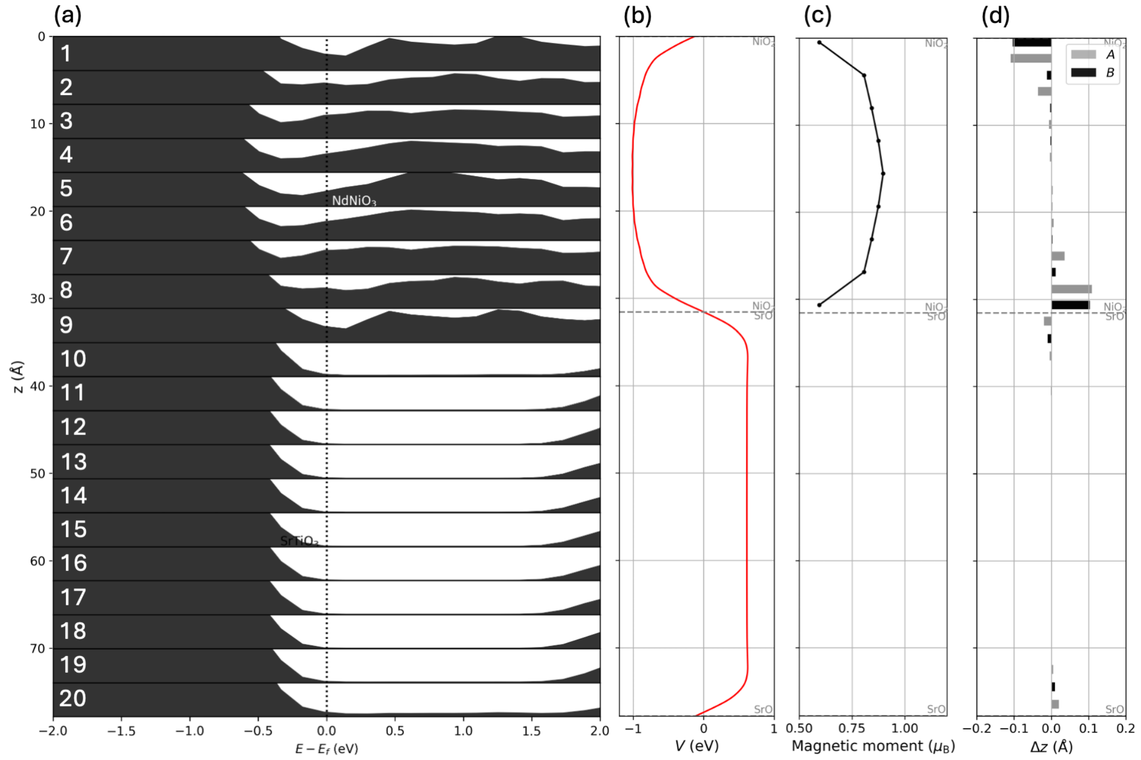

Figure 5.1: Key electronic and structural properties of non-stoichiometric STO-NNO system consisting of two SrO-NiO$_2$ interfaces as a function of z (position along $\hat{c}_{001}$): (a) layer PDOS near E_F, where each layer has chemical formula $2ABO_3$, and the y-axis of each layer plot ranges from 0 to 3 states/eV, (b) macroscopically averaged potential (averaged over STO inter-layer distance (= 4.0 Å)), (c) layer magnetic moments, and (d) A- and B-site polar displacements along $\hat{c}_{001}$.

5.2 Results and discussion

5.2.1 Non-stoichiometric systems

SrO-NiO$_2$

Starting with the SrO-NiO$_2$ non-stoichiometric system, we present the key electronic and structural properties in Fig. 5.1(a)—(d). Looking first to the layer-by-layer projected density of states (PDOS) (Fig. 5.1(a)), where each layer has the chemical formula $2ABO_3$, it is clear to see that the NNO film is metallic throughout, while the STO film remains insulating. We remark that Gaussian smearing is used to allow for partial occupancies, which are essential for simulating metallic layers (this smearing was also used for the rest of this study). We use a relatively large smearing width of 0.2 eV (as suggested by VASP) to safely simulate any metallic layers. It is important to note that this slightly compromises the shape of the conduction and valence bands of STO, though the valence band maximums (VBMs) and conduction band minimums (CBMs) can still be estimated by ignoring any long tail-offs. The VBMs of the STO layers stay fixed just below the Fermi level E_{F}. Looking next to the macroscopically averaged potential (MAP, Fig. 5.1(b)), which is averaged over the approximate bulk-like STO $B-B$ layer distance of 4.0 Å, the potential in the NNO film becomes gradually less negative near the interfaces. This is surprising, as though some intrinsic dipole between STO and NNO is expected, this appears to instead indicate an uneven charge distribution within the NNO film. Stronger evidence for this appears in the magnetic moments (Fig. 5.1(c)), which are a good indication of Ni-site valence. The moments decrease heavily at the interfaces, and decay away from the interface in similar fashion to the potential towards a fixed bulk-like value. The A, B-cation displacements along $\hat{c}_{001}$ (Fig. 5.1(d)) show a particularly interesting picture. As inversion symmetry is retained across the cell, STO cannot turn polar, though A- and B-cations may still displace at the interfaces where inversion symmetry is broken locally. Small displacements are expected given intrinsic dipoles, though surprisingly we observe the largest $\hat{c}_{001}$ displacements in the NNO film rather than the STO film, despite the latter being more energetically susceptible to polar displacements according to bulk-strained calculations (according to the $I4cm$ ground state). The interfacial Nd- and Ni-sites move a huge 0.1 Å in the direction of the interface.

Secondary structural details of the SrO-NiO$_2$ interface are shown in Fig. 5.2(a)—(f). Looking first to the BO$_6$ bond length average (Fig. 5.2(a)), which acts as a measure of the octahedra sizes (and approximately, the charge valence on the B-sites), we can see that the octahedra vary considerably layer-by-layer, especially at the interfaces, where they decrease in magnitude substantially. This trend maps closely to the potential and magnetic moments, and as STO octahedra sizes are larger, we can conclude that this is not a result of interfacial mode decay. The octahedral rotations with respect to the primitive axes are shown in Fig. 5.2(b). Each layer includes the tilts of two octahedra in all three primitive directions, with the plus and minus signs indicating clockwise or anticlockwise rotation (looking

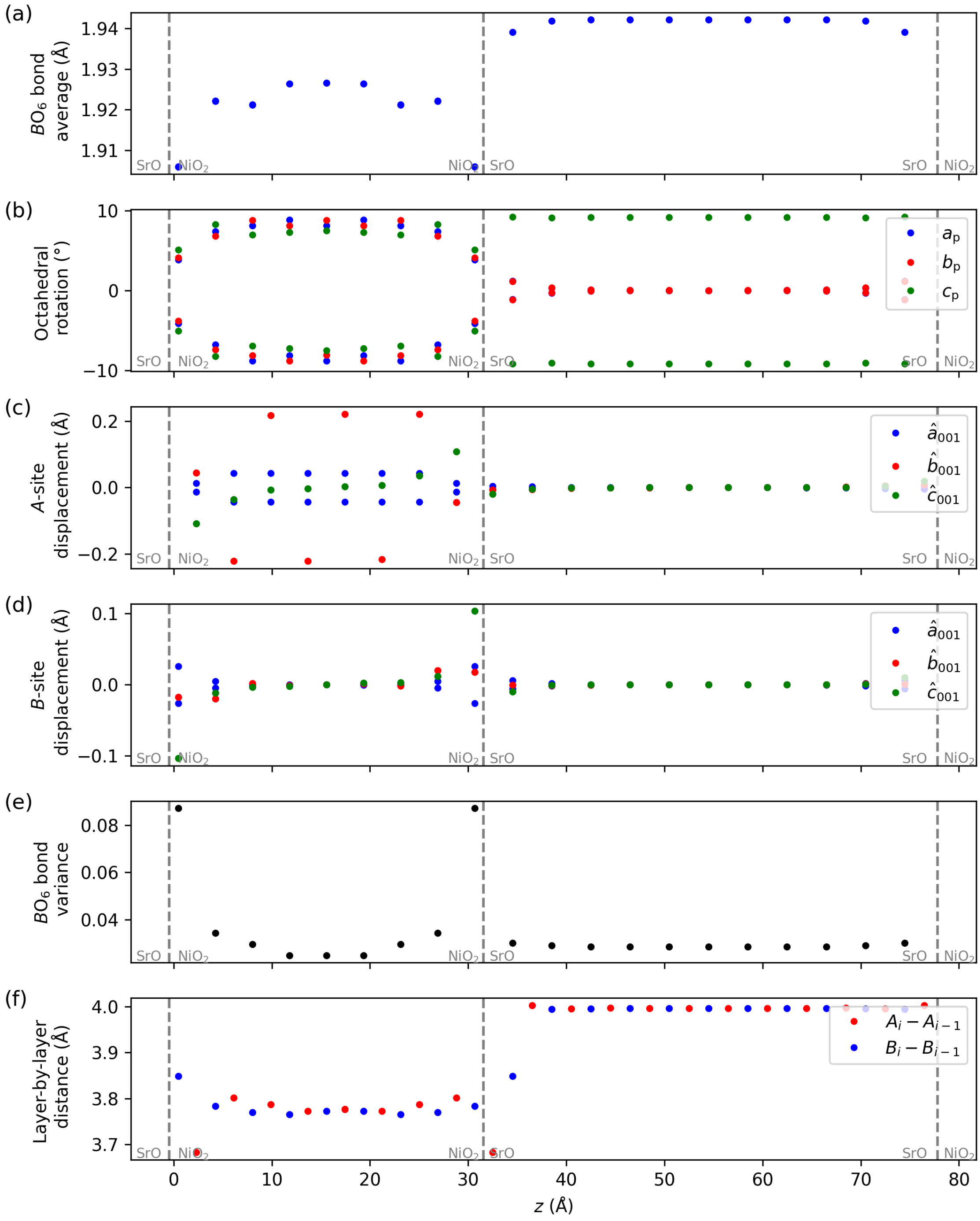

Figure 5.2: Further structural properties of non-stoichiometric STO-NNO system consisting of two SrO-NiO$_2$ interfaces as a function of z (direction along $\hat{c}_{001}$): (a) average B-O bond length within BO_6 octahedra, (b) octahedral rotations normal to primitive directions $\hat{a}_\mathrm{p}, \hat{b}_\mathrm{p}, \hat{c}_\mathrm{p}$, (c) A-site displacement along cell axis directions $\hat{a}_{001}, \hat{b}_{001}, \hat{c}_{001}$, (d) B-site displacement along cell axis directions, (e) variance of B-O bonds within BO_6 octahedra, (f) inter-layer distance, where A_i, B_i denote the z coordinate of A-, B-sites on given layer (such that A_{i-1}, B_{i-1} denote the z coordinate of the A-, B-sites on the previous layer)

along the direction of the primitive axis) respectively. The NNO layer retains its $a^-a^-c^+$ tilt pattern, while the STO layer retains its $a^0a^0c^-$ pattern, except near the interfaces. In-plane tilts typically have a larger decay length than out-of-plane tilts in the [001]-basis due to oxygen site matching [222, 223]. This can explain the non-zero in-plane tilts in the interfacial STO layers, as well as the smaller in-plane tilts in the interfacial NNO layers, but it cannot explain the lower out-of-plane tilt in the NNO layers at the interfaces, which abruptly decrease in magnitude. This variation is instead likely driven by the large Nd and Ni polar displacements at the interfaces, which are competitively coupled to the tilt mode [30, 31]. The in-plane A- and B-site displacements are shown alongside the out-of-plane displacements in Fig. 5.2(c),(d). The A- and B-site displacements are measured along the [001]-basis lattice vectors rather than the primitive directions. Alongside the large out-of-plane components discussed above, there is considerable in-plane motion, most notably in the Nd-sites. This clearly corresponds to A-site antipolar motion, which is coupled to the $a^-a^-c^+$ tilt pattern [16]. However, at the interfaces, the motion is largely reduced, which could be due to competition with the out-of-plane polar motion (and possibly the reduced tilts). The Ni-sites also slightly displace in-plane near the interfaces, which could be to compensate for the suppressed Nd-antipolar motion. We also measure the octahedral bond length variance (Fig. 5.2(e)), as a measure of Jahn-Teller-like octahedral distortion. In our system, we see a large variance only in the interfacial Ni-octahedra, which is predictable given the large polar motion and connectivity to the neighbouring TiO_6 octahedra. Finally, we plot the inter-layer distances (Fig. 5.2(f)) as a measure of the layer-by-layer tetragonality, which we estimate by plotting the $A-A$ and $B-B$ distances along $\hat{c}_{001}$. Each point corresponds to the out-of-plane distance between the cations at a given layer and those of the previous layer along $\hat{c}_{001}$. Here, the bulk-like regions of the STO and NNO layers match closely to the magnitudes of the $\mathbf{c}_{001}$ lattice vectors of relaxed bulk LAO strained $I4/mcm$ and $Pbnm$ (FM) cells respectively. However, this is not without substantial deviations at the interfaces, which are a result of the A- and B-site polar motion along $\hat{c}_{001}$, and the difference in out-of-plane lattice parameters of either film. In this system, inter-layer distances as low as 3.68 Å are observed between the interfacial Nd and Sr layers.

NdO-TiO$_2$

The key electronic and structural properties of the NdO-TiO$_2$ system are shown in Fig. 5.3(a)—(d). The properties of this system are in many ways a mirror-image of those seen in the SrO-NiO$_2$ system. The layer-by-layer PDOS once again shows NNO to be metallic and STO insulating, though in this case, the STO VBM lies at -1.59eV, far from E_F. Such a large difference in the STO band offsets indicates that the dipoles are almost certainly not only a result of intrinsic effects. This is rather surprising, as this implies the presence of a polar discontinuity of some sort, something not thought possible for anything other than an insulator-insulator interface. We explore this idea further in the following subsection. The MAP also shows a more negative region in NNO near the interfaces, as opposed to the more positive region in the SrO-NiO$_2$ system. If these regions indicate screening charges from the NNO film, it is strong evidence that they are of opposite sign depending on the interface termination. The magnetic moments mirror this trend, with large moments at the interfaces indicating a high negative charge density and a decay to bulk-like moments within a layer (aside from some minor oscillation). The A- and B-cation displacements along $\hat{c}_{001}$ also act inversely to the SrO-NiO$_2$ interface, where in this case cations displace away from the interface. This effect is once-again largest in the interfacial Nd- and Ni-sites. There still exists some displacement in the Sr-sites, though the interfacial Ti-sites are immobile, likely due to such huge displacements in the nearest Nd-sites. These interfacial Nd-sites displace by nearly 0.2 Å, almost double the displacement of the interfacial Ni in the SrO-NiO$_2$ system. It may be that the Nd-sites displace more easily than the Ni-sites along $\hat{c}_{001}$, possibly because the A-sites are already susceptible to antipolar motion in-plane (though it is not suppressed at the interfaces in this system). Other studies (in different systems) have observed polar NNO to similarly appear in the A-sites rather than the B-sites [98], suggesting that this may be a consistent feature of the rare-earth nickelates.

Secondary structural details of the NdO-TiO$_2$ interface are shown in Fig. 5.4(a)—

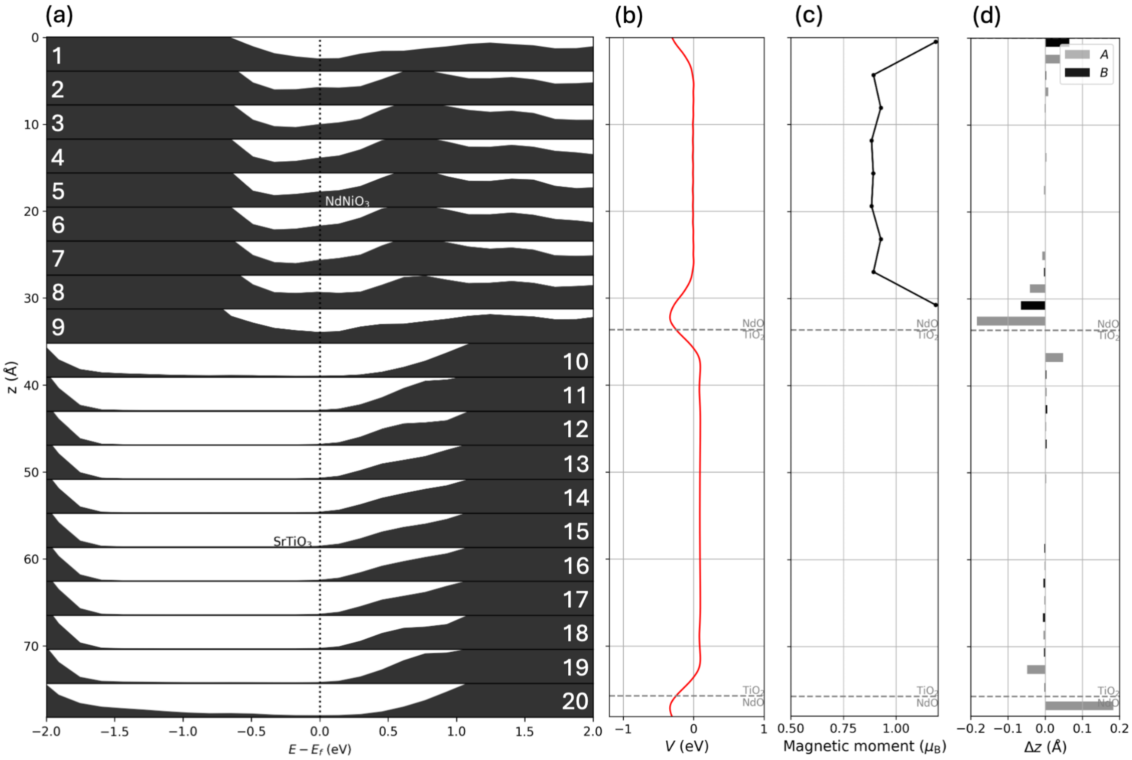

Figure 5.3: Key electronic and structural properties of non-stoichiometric STO-NNO system consisting of two NdO-TiO$_2$ interfaces as a function of z (direction along $\hat{c}_{001}$), where (a)—(d) are equivalent to Fig. 5.1.

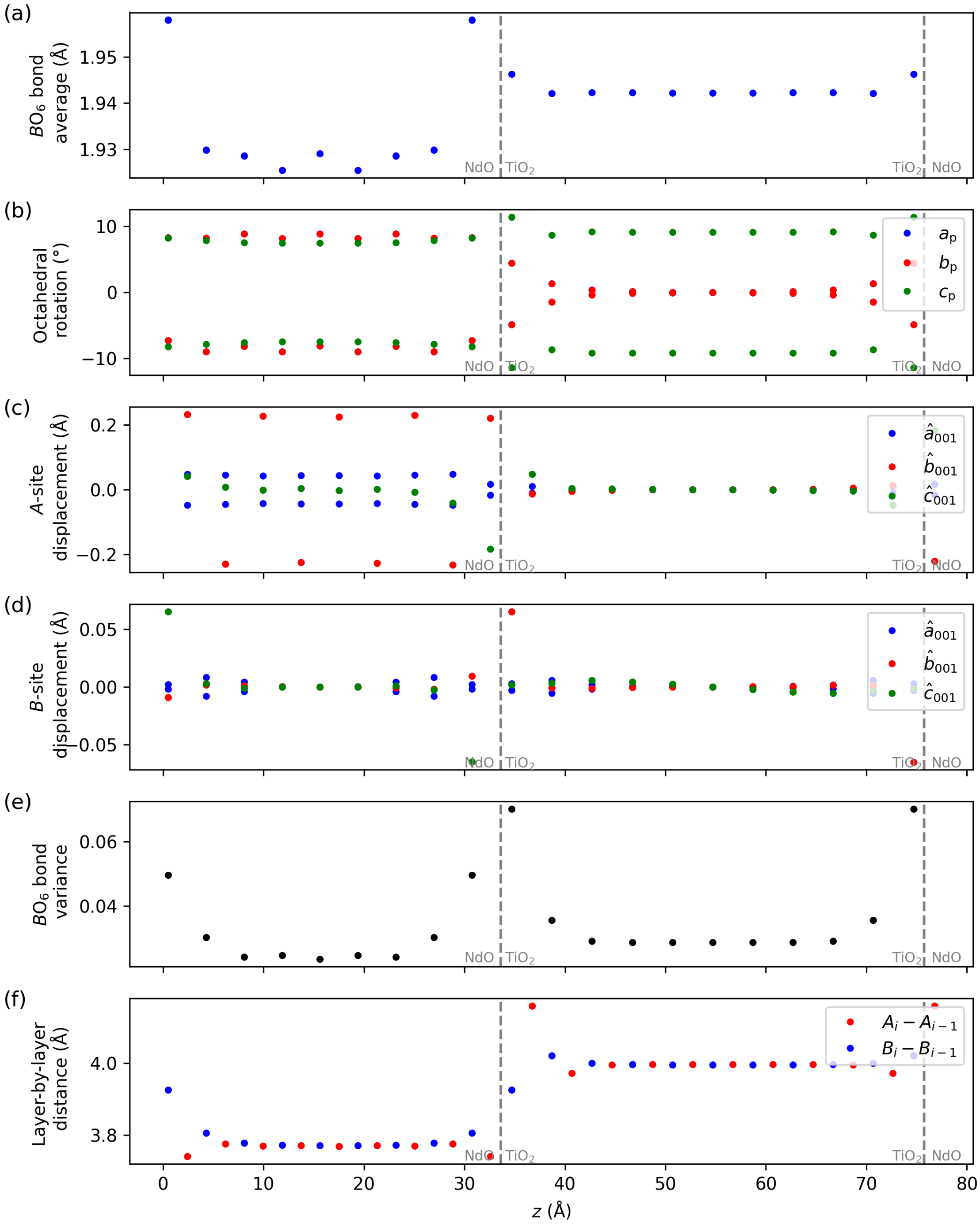

Figure 5.4: Further structural properties of non-stoichiometric STO-NNO system consisting of two NdO-TiO_2 interfaces as a function of z (direction along $\hat{c}_{001}$), where (a)—(f) are equivalent to Fig. 5.2.

(f). In this case, the NNO octahedra sizes increase significantly at the interfaces, again an indication of increased Ni valence rather than mode decay. The tilt patterns are once again $a^-a^-c^+$ in NNO and $a^0a^0c^-$ in STO besides the interfacial layers. It appears that the NNO film experiences little-to-no tilt decay from STO, which is likely a result of the nearest NiO_6 octahedra lying further from the interface. On the contrary, the STO film demonstrates more tilt variation than in the SrO-NiO_2 system, likely because TiO_6 octahedra now lie at the interface. Interestingly, the tilt is also amplified out-of-plane, which could be a local tolerance factor effect: as Nd has a smaller ionic radius than Sr, the interfacial octahedra have additional excess space to fill. The Nd- and Ni-sites remain relatively steady in-plane, such that the Nd-antipolar motion does not decay. However, the Ti-sites show reasonably large in-plane amplification at the interfaces. This could be the systems way of balancing the interfacial Nd-antipolar motion. The octahedral variance is once again largest at the interfaces, which is unsurprising given the large out-of-plane and in-plane A- and B-site motion. The inter-layer distances also vary greatly near the interfaces because of this, where distances as large as 4.16 Å exist between the interfacial Nd- and Sr-sites.

5.2.2 Interface dipoles in metal-insulator interfaces

The difference in STO band offsets between each interface interface termination is suspiciously large, and highly unlikely to only be a result of intrinsic effects. Our results also strongly indicate an uneven charge distribution within the NNO films, which are also different for each non-stoichiometric system. This only makes sense if there are large interfacial charges of opposing sign to screen. As STO is non-polar in these systems, it is tempting to think about a polar discontinuity caused by formal charge mismatch. This is well-defined for a system of two insulators, but unexpected in a system of an insulator and a metal. Polar discontinuities can be understood via the formal polarisation arising from layer charges, which can be rigorously defined for an insulator by finding the centres of the maximally-localised Wannier functions (MLWFs) [192, 193], and calculating the gauge-independent formal polarisation. Curiously, recent studies have shown that that MLWFs do exist for metals [224], though no method currently exists for finding them. In section 6.2.2, after applying Wannier analysis to the charge-ordered insulating state of NNO, we find that the gauge-independent formal polarisation in the [001]-direction is equivalent to that of a III/III insulating perovskite such as LAO (the effects of charge-ordering average out for each layer in the [001]-basis). We already know that LAO-STO interfaces yield bound charges of $\pm 0.5e$ per f.u. [106]. If our non-charge-ordered NNO film were insulating, this would be the case here too, though as it is metallic, the Wannier centres are unknown and polarisation cannot be defined. Remarkably however, our results suggest that the metallic NNO film acts similarly to a hypothetical insulating film with the same formal charges. There is no polar discontinuity here, as the net charge at the interface will always be zero for a metal. However, for the purpose of modelling the system, it seems as if we can imagine an underlying formal polarisation corresponding to a bound charge which is self-screened by NNO. As an estimate of the quantity of screening charges, assuming that the NNO film perfectly screens the polar discontinuity in each case, we measure the difference in the total magnetisation between the two systems (this is possible, as we observe the NNO film to always be a half metal). For a system of insulating III/III and II/IV perovskites, the polar discontinuity is always exactly $0.5e$. In our systems, we have $2 \times 0.5e = 1e$ per interface, so $\times 2 = 2e$ per system. Therefore, the difference in hypothetical bound charge between the two interfaced systems $(2e + 2e)$ would be $4e$, if equivalent to the LAO-STO system. If the metal is completely screening this, we expect the difference in magnetisation to be equal to this figure (our systems are ferromagnetic, and half metals, so the total magnetisation is an estimate of the total screening charges). Interestingly, we find the difference between our two non-stoichiometric systems to be $4.055\mu_{\mathrm{B}}$, a very close match. This suggests that the interface between NNO and STO has a 'bound charge' (quote marks are used to describe this charge as in reality, the net interface charge is zero due to the free metallic screening charges) extremely similar to that between LAO and STO. Like the ferroelectric capacitor, there exists a finite screening length between the screening charges and the 'bound charges' lying at the interface, which we observe with the decay of the potential and magnetic moments. The consequences of this are the

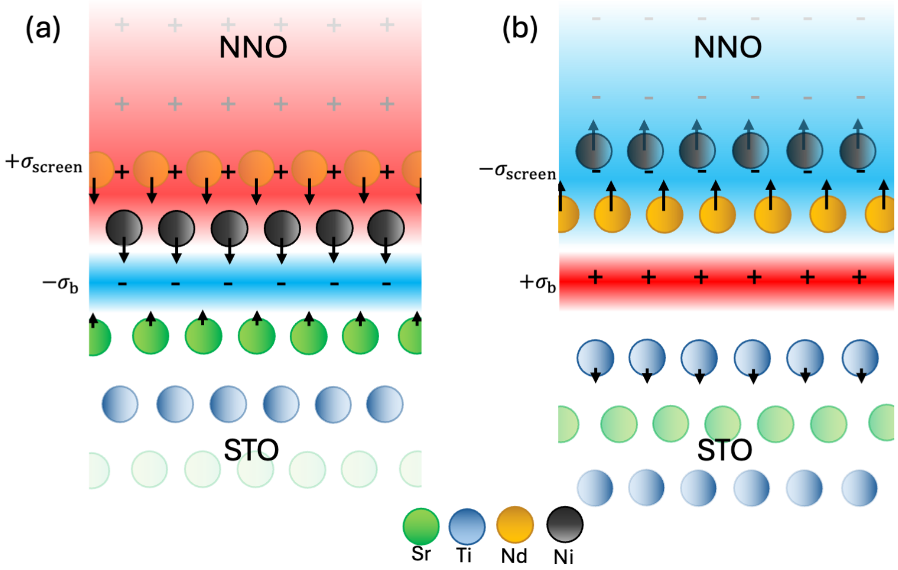

Figure 5.5: Visual schematics of the behaviour at non-stoichiometric (a) SrO-NiO$_2$ and (b) NdO-TiO$_2$ interfaces. σ_{b} denotes the interfacial 'bound charge', σ_{screen} denotes screening charge (which are separated by a finite screening length), and arrows indicate ionic displacement.

large interface dipoles observed in the potential, which differ depending on the type of interface, where the SrO-NiO$_2$ interface has a negative 'bound charge' close to $-0.5e$, and the NdO-TiO$_2$ interface has a positive 'bound charge' close to $+0.5e$. In many ways, the NNO-STO interfaces are a hybrid of the two systems discussed in the introduction— the LAO-STO system and the ferroelectric capacitor.

With this new model, we can better understand the observations in each non-stoichiometric interface. Looking first to the SrO-NiO$_2$ system, we include a visual schematic in Fig. 5.5(a). The negative 'bound charge' $-\sigma_{\text{b}}$ is screened by the free NNO film charges $+\sigma_{\text{screen}}$. As a result, the positively charged Ni- and Nd-sites experience a repulsion from the screening charges and an attraction to the bound charge, as is seen in the electrodes of ferroelectric capacitors [126]. This explains the displacement towards the interface. As the 'bound charge' is fully screened by the NNO film, the interfacial Sr- and Ti-sites only experience minor displacements. The NdO-TiO$_2$ system (Fig. 5.5(b)) is a mirror of this, where there now exists a positive 'bound charge' $+\sigma_{\text{b}}$ and negative screening charges $-\sigma_{\text{screen}}$. The Nd- and Ni-sites are now repulsed by the 'bound charge' and attracted to the screening charges, so are displaced away from the interface.

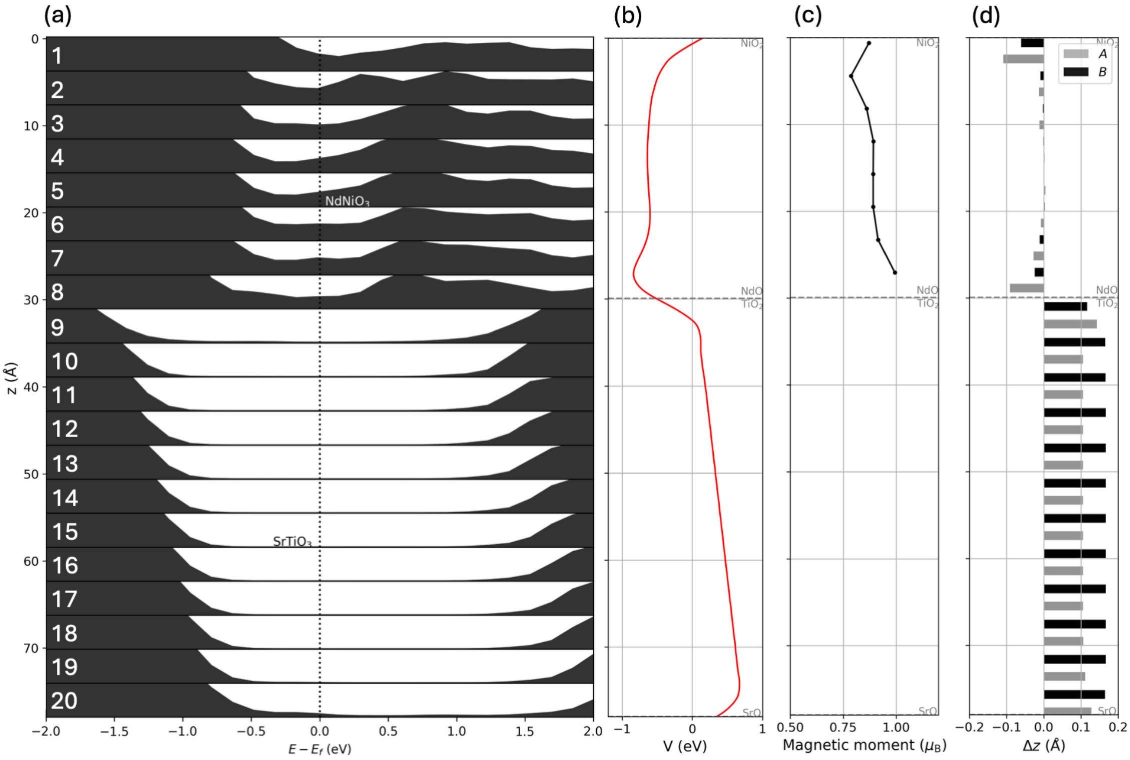

Figure 5.6: Key electronic and structural properties of stoichiometric STO-NNO system as a function of z (direction along $\hat{c}_{001}$), where (a)—(d) are equivalent to Fig. 5.1.

5.2.3 Stoichiometric

With the non-stoichiometric results analysed, we can compare the behaviour in each system to the behaviour of the same types of interface in a closed-circuit stoichiometric system. The key properties of the stoichiometric result are shown in Fig. 5.6(a)—(d). Once again, we observe the NNO film to be metallic, and the STO layers to be insulating, though here the STO band offset varies from layer to layer. The MAP shows that there is a potential gradient, and therefore field across the STO film. This means that the screening of the 'bound charges' by the metallic NNO is once again imperfect, and interfacial dipoles exist across both interfaces. Like the non-stoichiometric equivalents, the stoichiometric interfaces have more positive and more negative potential regions at the SrO-NiO$_2$ and NdO-TiO$_2$ interfaces respectively. However in this case, moving along $\hat{c}_{001}$ both interfaces have potential steps of the same sign, meaning that there must exist a field across the films such that the potential is equal at opposite ends of the cell (due to closed-circuit boundary conditions) [105]. In the NNO film, any fields are fully screened by the free charges, though across the insulating STO film this field remains unscreened. In our system, we observe exactly this, where there exists a field across STO of 0.014 eV/Å from the (positive) NdO-TiO_2 interface to the (negative) SrO-NiO_2. The magnetic moments also show an interesting picture. The sites at each interface somewhat resemble those of the non-stoichiometric cases, though the lowest moment at the SrO-NiO_2 interface now lies in the second layer of Ni-sites rather than the first as seen in the non-stoichiometric case. As this layer aligns with the positive screening charge region, this indicates that the screening charges have been pushed further from the bound charge in the stoichiometric system. A similar feature occurs at the NdO-TiO_2 interface, where there is only a slight amplification in the interfacial Ni-moments compared to the non-stoichiometric NdO-TiO_2 system, also suggesting that the screening charges do not lie as close to the interface. Both effects might be explained by net polar motion, which is now allowed due to inversion symmetry breaking. STO becomes strongly polarised along $\hat{c}_{001}$, such that the cations are displaced towards the negative bound charge (SrO-NiO_2) and away from the positive bound charge (NdO-TiO_2). There are several interesting features that come as a result of this. Firstly, the cation displacement is larger in this system (0.166 Å) than in bulk LAO-strained (*I4cm*) STO (0.145 Å) by 14.5%, which matches well to experimental results that observe amplified STO tetragonality in this system [220] (which heavily suggests the presence of large cation displacements). Secondly, this cation motion acts to oppose the formation of the electric field, such that it points from the SrO-NiO_2 interface to the NdO-TiO_2 interface. We also tried to relax this system with the initial STO cation motion pointing in the opposite direction, though we found this automatically reverted to the orientation seen here, meaning this is certainly not only a result of strain. Therefore, the STO polarisation is pinned in one direction, and amplified. This feature also maps exactly to what is observed experimentally, where the STO polarisation is unswitchable [220]. In regards the screening charge decay lengths, at the SrO-NiO_2 interface it is possible that the positive screening charges are repulsed due to the positive Sr-, Ti-motion towards the interface, such that the screening charges appear to lie closer to the second layer

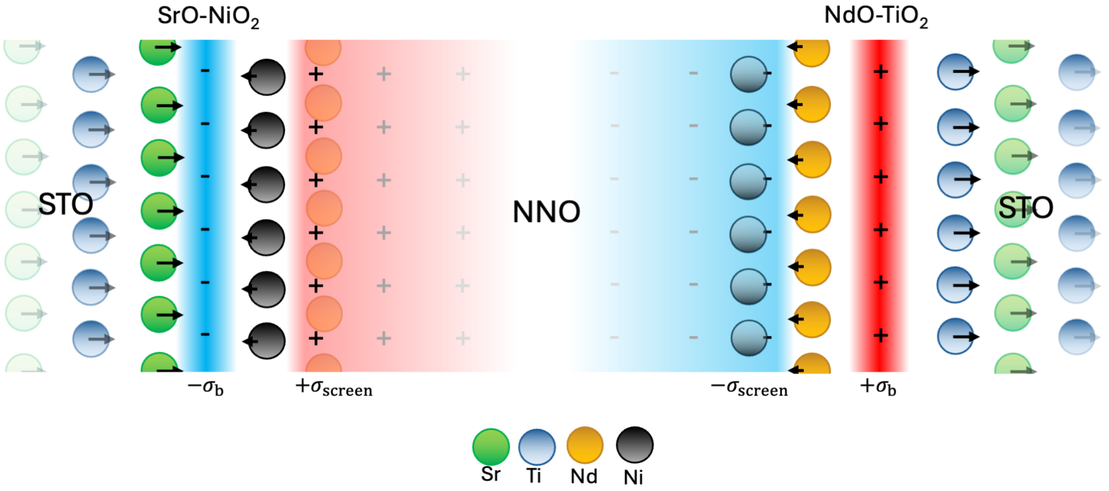

Figure 5.7: Visual schematic of the behaviour at each interface in the stoichiometric NNO-STO system.

of Ni-sites. Similarly, at the NdO-TiO$_2$ interface there now exists a less positive region near the interface due to the movement of Sr- and Ti-sites, possibly repulsing the negative screening charges. Another explanation is that this is just a result of the field caused by closed circuit boundary conditions, which also exists across NNO prior to screening. This can be easily screened by the NNO film, though the charge distribution may vary from the non-stoichiometric interfaces lacking the field. The polar STO motion also greatly affects the Nd- and Ni-cation motion between the screening and bound charges, which are heavily reduced in the stoichiometric system at both interfaces. This effect corresponds to an additional Ginzburg term (mode decay) in the Landau energy model, and may be a further driving force behind the large band offsets. The STO cation motion competes with the Nd- and Ni-displacements at the interfaces as they point in opposite directions. The properties of the stoichiometric system are summarised visually in Fig. 5.7.

Additional structural properties of the stoichiometric NNO-STO system are shown in Fig. 5.8(a)—(f). The octahedral sizes are notably different to what is seen in the equivalent non-stoichiometric systems. At the SrO-NiO$_2$ interface, the lowest-valence Ni-site now lies at the second layer of octahedra rather than the nearest, which again supports the hypothesis that the positive screening charges lie further

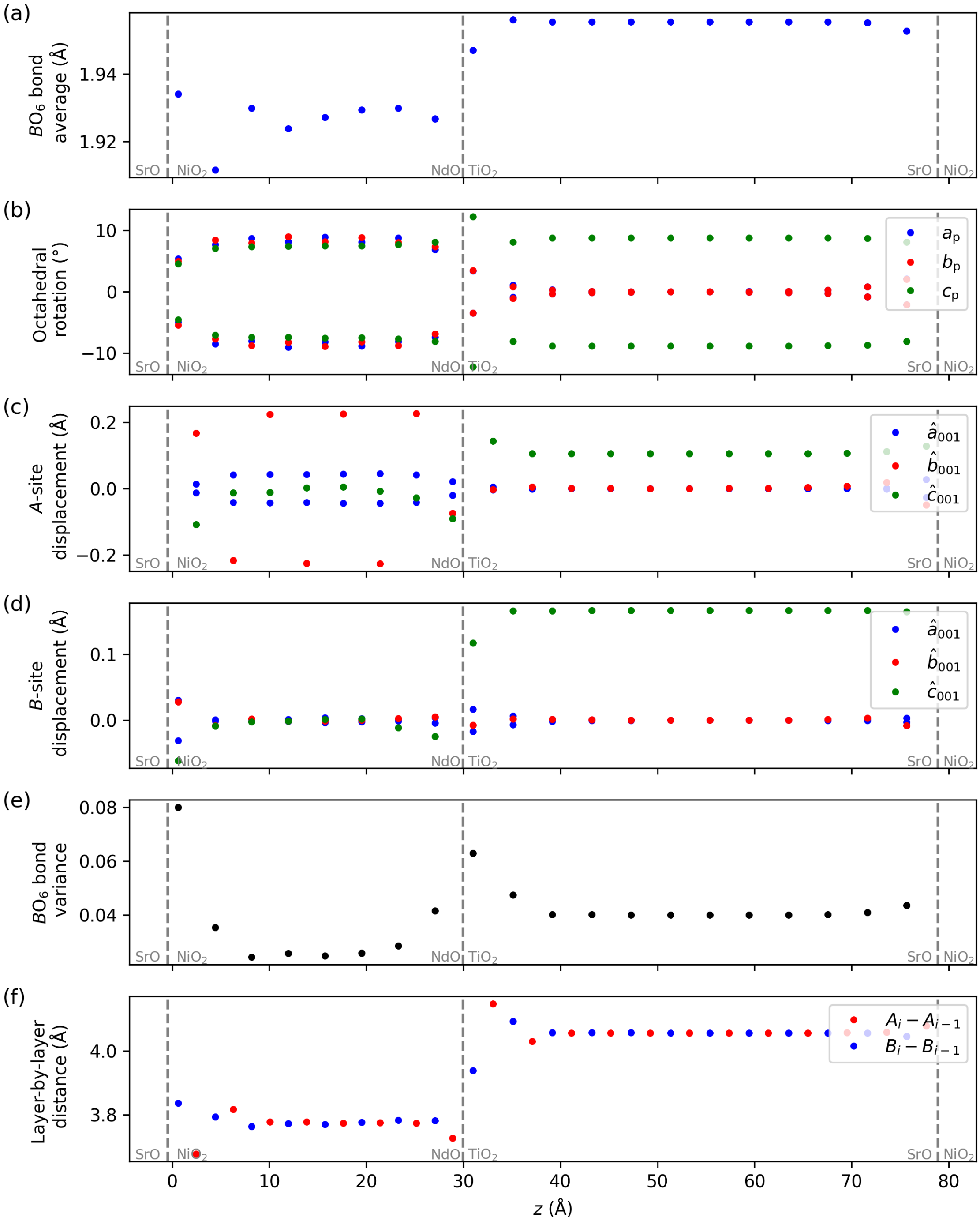

Figure 5.8: Further properties of stoichiometric STO-NNO system as a function of z (direction along $\hat{c}_{001}$), where (a)—(f) are equivalent to Fig. 5.2.

(on average) from the interface than in the non-stoichiometric system. The octahedral sizes at the NdO-TiO_2 interface are also different to the non-stoichiometric system, where the interfacial Ni are smaller in this case, again suggesting that the negative screening charges are similarly affected. The tilts very much resemble the trends seen in the two non-stoichiometric systems for each equivalent interface, though in STO, the out-of-plane tilt is considerably reduced, which is inevitably a result of competition with the net polarisation allowed by inversion symmetry breaking. Despite the differences in A- and B-cation motion out-of-plane, their in-plane motion is very similar to that seen in the non-stoichiometric systems. The only exception might be the Ti-motion at the NdO-TiO_2 interface, which appears to now be suppressed, likely due to competition with the out-of-plane polar motion. The octahedral variance is once again generally amplified at the interfaces, but also generally within the STO film, which is clearly a result of the polar mode. The $A - A$ and $B - B$ distances are also heavily amplified at the interfaces, but also within the STO film (the STO inter-layer distance in the bulk-like region is 4.057 Å) with respect to the bulk LAO-strained distance (4.045 Å).

5.3 Summary

We have found the ground state properties of non-stoichiometric and stoichiometric NNO-STO closed-circuit interfaced systems. We discover that there are uncharacteristically large STO band offsets corresponding to huge interface dipoles, beyond what is expected from intrinsic effects. It is tempting to model these as being due to interfacial 'bound charges' arising from a finite formal polarisation in the NNO film, despite it being metallic. We suggest that these 'bound charges' are fully screened by the free NNO charges, but only imperfectly, such that there still exists a screening length and in-turn interface dipoles. We find indirectly that the sum of the screening charges at each interface is extremely close to $\pm 0.5e$/f.u., which is the amount required to screen the bound charge in the LAO-STO interfaced system.

In the stoichiometric NNO-STO system, the dipoles combined with closed-circuit boundary conditions lead to a field across the system, which is screened in NNO, but finite across STO. The STO polar mode is also now allowed to appear due to net inversion symmetry breaking, and condenses in to directly oppose the field generated by the interfacial dipoles and closed circuit boundary conditions. The polar displacement is 14.5% larger than in bulk LAO strained STO, which matches well to experiment. It is also pinned to one direction. This polarisation suppresses Nd- and Ni-cation motion at the interfaces, such that the screening length of the NNO charges increases (though this may alternatively be a result of the (screened) field that now appears across the NNO film).

Overall, this study highlights the interplay in closed-circuit interfaced systems built from a metallic film and an incipient ferroelectric. If more computational resources become available in the future, a further interesting study could be to simulate the same system doubled in-plane so T-, and S-type AFM bulk ground state NNO phases may be considered, such that the breathing mode and MIT may appear more easily. Regardless, considering the strong match of our results to experiment, this study suggests that this is unlikely to be the case. Alternatively, thicker NNO films that are increasingly unlikely to remain metallic throughout could be considered. In this study, we have used a relatively large STO thickness (by DFT standards) such that polarisation may appear more easily, though investigating lower or higher thicknesses may also be of interest in the future, such that the STO field is larger or smaller, in-turn possibly controlling the magnitude of STO polarisation.

CHAPTER 6

Unique polar discontinuity and screening mechanisms in [111]-oriented $NdNiO_3$-substrate interfaces (substrate = $CaTiO_3$, $NdGaO_3$, $LaAlO_3$)

In the final results chapter of this study, we investigate [111]-oriented nickelate-based interfaced systems. We demonstrate that the polar discontinuity for nickelates in [111]-interfaces is very different to that in [001]-interfaces, such that it is dependent on the presence of charge ordering and choice of large and small Ni-sites. We use this to explain a variety of novel phenomena that occur when the nickelate is interfaced with different substrates in this basis. Interfaced with $CaTiO_3$, we are able to pin the nickelate breathing order, such that a metallic phase becomes increasingly energetically unfavourable (such that we predict the MIT temperature to amplify). Interfaced with $NdGaO_3$ and $LaAlO_3$, we encounter large polar discontinuities that force the nickelate layer to form interfacial 2DEGs, which can be achieved by suppressing the breathing mode or doping the charge-ordered state via Zener tunneling. We test both ultrathin and larger film thicknesses, where the former is dominated by interfacial effects, and the latter allows us to observe bulk-like behaviour in the centre of the film.

6.1 Introduction and methods

[111]-Oriented interfaced systems of perovskites remain far less studied than [001]-systems. In chapters 3 and 4, we demonstrated that epitaxial strain may have a vastly different effect on the properties of STO and NNO in the [111]-basis. Other interfacial effects have also been demonstrated to behave differently here, including mode decay, where the tilt mode has been shown to decay far more slowly in the [111]-basis due to bond connectivity [98]. The polar discontinuity is also different, as any bound charge is averaged over a larger in-plane area— precisely $\sqrt{3}$ ($\times A_{001} = A_{111}$) times larger than [001]-interfaces (for a given system) [225, 226]. Furthermore, the screening mechanisms that exist for a system in the [001]-basis may not be as energetically favourable or available at all in the [111]-basis. Various interesting behaviour has been observed experimentally for nickelate films in this basis, including amplified MIT temperatures [130], polar metallic phases [98], and proximity-induced metal-insulator transitions [87].

In this chapter, we investigate some of these systems from first principles, and suggest new ones that may have interesting properties. We build stoichiometric [111]-oriented superlattices of NNO with several common substrates— $CaTiO_3$ (CTO), $NdGaO_3$ (NGO) and $LaAlO_3$ (LAO). CTO is chosen in hopes of isolating the effect of a polar discontinuity on NNO in this basis, as it is a II/IV perovskite (nominally) and has similar lattice parameters and modes (besides the breathing mode) to NNO. NGO and LAO meanwhile are nominally III/III perovskites, so we do not expect a polar discontinuity. NGO has similar modes to NNO (besides the breathing mode), so we expect a relatively well-behaved system, besides perhaps some strengthening of the insulating phase due to the sizable tensile [111]-strain it applies (as discussed in chapter 4). LAO applies only a minor tensile strain, but has an $a^-a^-a^-$ tilt pattern, which has been demonstrated experimentally to decay slowly in NNO films [98]. Overall, each choice of substrate imposes distinct interfacial constraints on [111]-oriented nickelates, potentially giving rise to novel behaviour. We omit STO from this investigation due to time and computational limits— STO is also a II/IV perovskite, though we predict the behaviour of NNO on STO to be more complex than on CTO, as STO applies a large tensile strain, and has a very different tilt pattern to NNO. We nonetheless believe that our results for the three substrates tested here provide a solid groundwork for understanding [111]-oriented NNO, and can be used to make reasonable predictions for the behaviour of NNO on STO in this basis.

As in chapter 5, our DFT calculations use parameters close to those used for our bulk calculations where computationally feasible. We use the PBEsol exchange-correlation functional alongside the same PBE scheme pseudopotentials. The Ca $3p$ and $4s$; Ti $3p$, $3d$ and $4s$; Ga $4s$ and $4p$; La $4f$ (unoccupied), $5s$, $5p$, $5d$ and $6s$; and Al $3s$ and $3p$ electrons were explicitly included as valence, while the same valence electrons were used for Nd, Ni and O as in previous chapters, and all other electrons were frozen in the ionic cores. We once again applied a Hubbard-U correction of 2 eV to the Ni-$3d$ orbitals. For computational tractability during ionic relaxations, we set the plane-wave energy cut-off to 550 eV, while the K-point grid was fixed to a $3 \times 5 \times 1$ Γ-centered mesh for all systems (see below for cell sizes). We build interfaced systems based on the 60-atom [111]-oriented cell shown in Fig. 3.2(c), and relax to a force convergence of 1 meV/Å. The in-plane lattice parameters are fixed to those of the substrate. For each choice of substrate, we test NNO films built of one or two stacked 60-atom [111]-unit cells. We use a single 60-atom [111]-cell for the substrate in all calculations, which we verify is large enough to show bulk-like properties in the centre for all three choices of substrate (such that the system properties are unaffected by the substrate thickness). This is verified by building 120-atom [111]-oriented superstructures for each substrate, fixing two layers (where each layer has chemical formula $2ABO_3$) to the geometry of bulk NNO, and relaxing all other layers, such that the mode decay lengths can be observed and determined. We find that no modes have a decay length longer than two layers in any substrate, meaning six-layer substrates are sufficiently large and can be expected to display bulk-like properties in the central two layers. In the [111]-basis, we are able to simulate insulating NNO phases, as $T-$ and $S-$AFM magnetic orders are allowed by either choice of film thicknesses (though it is not allowed in bulk, the substrate layer allows us to build these orders in a 60-atom film). For each interface, we test a variety of nickelate phases primarily based on those defined in Table 4.3. These are clarified in further detail below.

6.2 Results and discussion

6.2.1 Pinning of the breathing order in NNO-CTO superlattice

We start by building interfaces of NNO and CTO. Experimentally, CTO has been observed to have a close structural match to rare-earth nickelates besides the presence of charge ordering. We start by relaxing CTO in its experimental *Pbnm* phase in the 60-atom [111]-cell, to obtain a suitable input structure and lattice parameters. Our result is comparable to low temperature neutron diffraction data [227], such that we obtain lattice parameters of $|\mathbf{a}_{111}^{\mathrm{CTO}}| = 9.29$ Å ($/\sqrt{6} = 3.79$ Å), $|\mathbf{b}_{111}^{\mathrm{CTO}}| = 5.45$ Å ($/\sqrt{2} = 3.85$ Å), and $|\mathbf{c}_{111}^{\mathrm{CTO}}| = 13.11$ Å ($/2\sqrt{3} = 3.78$ Å). As found in chapter 4, the (DFT) NNO pseudocubic bulk in-plane [111] lattice parameters are $|\mathbf{a}_{111}^{\mathrm{NNO}}| = 9.26$ Å ($/\sqrt{6} = 3.78$ Å), $|\mathbf{b}_{111}^{\mathrm{NNO}}| = 5.33$ Å ($/\sqrt{2} = 3.77$ Å), and $|\mathbf{c}_{111}^{\mathrm{NNO}}| = 26.17$ Å ($/4\sqrt{3} = 3.78$ Å). Therefore, the CTO substrate imposes a tensile [111]-strain on NNO, but only significantly in one in-plane axis. Considering the results of our bulk-strained calculations, we might expect from strain alone either a $P2/c$ T-AFM or $P\bar{1}$ S-AFM NNO ground state, though based on previous studies examining the effect of tilt decay across [111] interfaces, and given CTO is orthorhombic, it is more plausible that NNO remains in the $P2/c$ structure. We might also expect a polar discontinuity of some kind, given CTO is a II/IV perovskite and NNO a III/III perovskite (besides charge ordering). This could be similar to that in the [001]-STO-NNO interfaces, where NNO is encouraged to shift to a metallic state to screen interfacial bound charges.

Starting with the one 60-atom [111]-cell thick NNO film, we test two NNO structural inputs interfaced with the relaxed CTO input. We choose the insulating $P2/c$ T-AFM phase (we found that S-AFM is generally more difficult to converge in such a thin film, and that the T-AFM phase has approximately the same properties) and the metallic *Pbnm*-FM phase. Given more time, we would test more phases, though we find that these are enough to uncover a range of interesting features in this system. Fascinatingly, we find that both inputs relax to a charge-ordered phase. This resulting from a *Pbnm*-FM input phase is particularly surprising, as the $P2/c$-FM phase never spontaneously appeared in our bulk [111]-strained calculations. This suggests that the charge-ordered phase is additionally encouraged here. Furthermore, we find that both phases automatically revert to the same order of large and small Ni-sites. In the [111]-basis, the $\mathrm{Ni_L}$- and $\mathrm{Ni_S}$-sites lie on alternating layers, and we find that the $\mathrm{CaO_3}$-Ni interface always consists of $\mathrm{Ni_S}$-sites, while the nearest Ni layer to the $\mathrm{NdO_3}$-Ti interface always consists of $\mathrm{Ni_L}$-sites. If the energy difference between this and the phase with reversed Ni-sites at each interface was minor, this could be attributed to the slight energy bias of the breathing order caused by [111]-strain (discussed at the end of chapter 4), but upon rerunning the system with the reversed breathing order, we find that it could not be relaxed— it instead automatically reverted to the opposite order. This all suggests a much stronger energy bias towards one breathing orientation beyond the effects of [111]-strain.

This immediately prompts us to undertake a deeper investigation into the polar discontinuity in [111]-oriented NNO-based interfaces. The fact that $\mathrm{Ni_L}$- and $\mathrm{Ni_S}$-sites lie on different layers in this basis automatically means that the polar discontinuity will be slightly different to a II/IV-III/III interface, though our results suggest that this is by a sizeable amount, as the NNO film appears to disfavour non-charge-ordered metallic phases, contradicting what is expected from a large polar discontinuity. Mode decay is also unlikely to play a major role here, as the *Pbnm* CTO substrate if anything would encourage equal-sized octahedra at each interface. Magnetic frustration may play a role, though is unlikely to have such a major impact, as there is no obvious reason for it to affect T-AFM magnetic orders (as is present in charge-ordered phases) less or more than a FM order (as present in non-charge-ordered phases).

6.2.2 The polar discontinuity in [111]-oriented nickelate systems and a possible new type of ferroelectricity

Before continuing our analysis of NNO-CTO interfaces, we closely examine the formal charges of the charge-ordered NNO phase to help clarify the polar discontinuities and explain our results. CTO is an insulating II/IV perovskite (like STO), and we have suggested in the previous chapter that metallic (*Pbnm*) NNO can be thought of as having an underlying polar structure similar to a III/III perovskite that is self-screened by the metallic carriers. In the [111]-basis however, we find that the NNO film is encouraged to switch to the charge-ordered insulating state. As already mentioned, Ni-sites no longer average to the same nominal charges in-plane when in the charge-ordered phase in this basis. The exact nominal charges of the $\mathrm{Ni_S}$- and $\mathrm{Ni_L}$-sites are not well defined in literature due to the highly covalent character of the Ni valence charge [76–80]. To clarify this, we calculate the MLWFs of the occupied states of the bulk (insulating) charge-ordered NNO phase, as well as their centres. By grouping the Wannier centres around the Ni-sites, we find the gauge-independent formal polarisation corresponds to that calculated when modelling the Ni-site valences as precisely $\mathrm{Ni_L^{2+}}$ and $\mathrm{Ni_S^{4+}}$. We verify that our calculated MLWFs correspond to our DFT ground state by comparing the band structures from each calculation, where we find the valence states closely resemble each other (we do not calculate the MLWFs of unoccupied states). The overlay of the two can be found in Fig. C.1 in Appendix C. These nominal charges mean that in comparison to a III/III perovskite, exactly one electron has moved to an adjacent Ni layer along $\hat{c}_{111}$ for every two Ni layers (per two formula units). We can identify the consequences of this by calculating the bulk formal polarisation of NNO in this [111]-basis. In Fig. 6.1, we calculate the formal polarisation P_F for [111]-oriented perovskite films with varying A- and B-site formal charges. All calculated P_F's are modulo the quantum of polarisation $e|\mathbf{c}_{111}|/\Omega$ (where Ω is the cell volume). When creating surfaces (as is necessary when building interfaces), P_F (within a set modulo the quantum) becomes well-defined. Equivalently, when building a stoichiometric interfaced system of two or more perovskites, the change in P_F (and therefore the polar discontinuity) remains

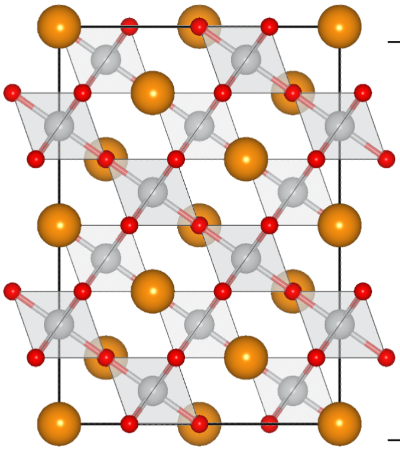

	$A^{3+}B^{3+}O$	$A^{2+}B^{4+}O$	$A^{3+}B^{2+,4+}O$	$A^{3+}B^{4+,2+}O$
B^2	3	4	4	2
AO_3	-3	-4	-3	-3
B^1	3	4	2	4
AO_3	-3	-4	-3	-3
B^2	3	4	4	2
AO_3	-3	-4	-3	-3
B^1	3	4	2	4
AO_3	-3	-4	-3	-3
B^2	3	4	4	2
AO_3	-3	-4	-3	-3
B^1	3	4	2	4
AO_3	-3	-4	-3	-3
P_F	1.5	2	1	2

Figure 6.1: Formal polarisation (P_F, in units $e|\mathbf{c}_{111}|/\Omega$ per (in-plane) f.u., where Ω is the cell volume) of [111]-oriented perovskite layers with varying formal charges. '$A^{3+}B^{3+}O_3$' is equivalent to NGO, LAO and approximately metallic (non-charge-ordered) NNO, '$A^{2+}B^{4+}O_3$' is equivalent to CTO (as well as STO), while '$A^{2+}B^{2+,4+}O_3$' and '$A^{2+}B^{4+,2+}O_3$' are equivalent to insulating charge-ordered NNO films with different interfacial Ni valences— $\mathrm{Ni_L}$ and $\mathrm{Ni_S}$ respectively. All values in are modulo the quantum of polarisation in bulk, which is equal to $e|\mathbf{c}_{111}|/\Omega$.

fixed and equal to the differences between the displayed P_F values. Therefore, for example, the difference between P_F's for CTO (II/IV) and LAO or NGO (III/III) is always $0.5e$/f.u.. Interestingly, we find that the discontinuity between the charge-ordered nickelate and a III/III perovskite is also always $0.5e$/f.u.. Furthermore, the polar discontinuity between the nickelate and a II/IV perovskite can be zero for a certain orientation of $\mathrm{Ni_L^{2+}}$ and $\mathrm{Ni_S^{4+}}$. To distinguish each state in our interfaced systems we consider the interfacial Ni layer (the top layer in Fig. 6.1), where we find that if the interfacial Ni layer is $\mathrm{Ni_S^{4+}}$, $P_\mathrm{F} = 1$, and if the first Ni layer is $\mathrm{Ni_L^{2+}}$, $P_\mathrm{F} = 2$. In a bulk system, these values would be modulo the quantum, making the two orientations equivalent, but in an interfaced system of fixed terminations, the polar discontinuity varies depending on the breathing order.

This feature has interesting consequences. Firstly, we can immediately identify why one breathing order is preferential in the NNO-CTO system, as the P_F's are equal for both films when the interfacial Ni layer (at the $\mathrm{CaO_3}$-Ni interface) has a valence of $\mathrm{Ni_L^{2+}}$, while there is a polar discontinuity when the interfacial Ni have a valence of $\mathrm{Ni_S^{4+}}$ or the NNO film is not charge-ordered. This information is greatly useful for disentangling the NNO-CTO system in the following subsection, and also the NGO- and LAO-NNO systems, which we expect to have a polar discontinuity when NNO is an insulator, and not whilst metallic.

Before delving into this, we highlight another very interesting property of NNO films in the [111]-basis (which is also a property of all charge-ordered perovskites). Within a relatively small energy range in bulk, we have access to a wide range of P_{F}'s, meaning that via manipulation of the environment, it may be possible to switch between these states. In a stoichiometric film, if we are able to switch the $\mathrm{Ni_L}$-sites to $\mathrm{Ni_S}$ (and vice-versa), which may be possible with an applied E-field, we could consider the system ferroelectric. This would be a previously-undiscovered type of ferroelectricity driven purely by charge transfer. We do not investigate possible switching mechanisms here, though on the surface one might predict an intermediate $\mathrm{Ni}^{3+}/\mathrm{Ni}^{3+}$ state within the switching process. This might prevent ferroelectricity entirely, as the NNO film may have to briefly convert to a less energetically-favourable metallic phase. Alternatively however, this may add another interesting layer of complexity to the system, where if IMT occurs intermediately, we would expect the dielectric response to briefly diverge before settling to a finite value in the opposite charge-ordered state. Another possibility is that the nickelate forms in-plane breathing domains in the [111]-basis as to avoid polar discontinuities (this phase is discussed briefly at the end of the chapter), where the domains alternate between $\mathrm{Ni_L}$- and $\mathrm{Ni_S}$-sites lying on the same (111)-plane. In this scenario, upon applying a field, we might expect domain wall motion along the [111]-direction corresponding to the movement of electrons between $\mathrm{Ni_L}$- and $\mathrm{Ni_S}$-sites, which would result in the net movement of charge along the [111]-direction and therefore a change in the net polarisation.

Alongside our direct calculation of polarisation via the MLWFs, as a sanity check, we also calculate the Berry-phase polarisation for insulating charge-ordered and non-charge-ordered perovskites. There are some practical considerations for demonstrating this. Firstly, we must investigate bulk unit cells (rather than interfaced systems), so the quantum of polarisation must be considered in any calculated value. As the difference per formula unit between a regular III/III perovskite and the breathing NNO phase is $0.5e|\mathbf{c}_{111}|$, we require unit cells that only have one formula unit in-plane to distinguish between these two states. Therefore, we cannot use the ground state $P2/c$ NNO phase, as the doubled (in-plane) cell will double the difference in the polarisation, which will be equal to the polarisation quantum ($2 \times 0.5/\text{f.u.} = 1$), and thus indistinguishable. Secondly, we cannot investigate metallic systems, so require an insulating III/III perovskite to replace the metallic nickelate phase.

To circumvent these problems, we first calculate the Berry-phase polarisation for the charge-ordered [111]-oriented $P\bar{1}$ T-AFM NNO phase, which can be represented by a hexagonal unit cell consisting of one formula unit per layer. To represent the non-charge-ordered phase, we use bulk III/III perovskite insulator LaGaO_3, in both the $C2/c$ and undistorted $Pm\bar{3}m$ phases (which can be made in the same hexagonal cell basis). We find that the Berry-phase polarisation for the $C2/c$ and $Pm\bar{3}m$ LGO phases are the same, showing that symmetry breaking (as long as inversion symmetry is retained) does not affect the formal polarisation in this basis, as expected. We find that the charge-ordered $P\bar{1}$ phase differs from these values by precisely $0.5e|\mathbf{c}_{111}|/\Omega$. In the hexagonal $P\bar{1}$ T-AFM unit cell consisting of twelve NdNiO_3 layers (to allow for T-AFM in bulk), a change of $0.5e|\mathbf{c}_{111}|/\Omega$ is equivalent to moving six electrons a distance of $\frac{1}{12}|\mathbf{c}_{111}|$ along $\hat{c}_{111}$ each, which is exactly equivalent to transitioning from $2\text{Ni}^{3+} \rightarrow \text{Ni}^{2+} + \text{Ni}^{4+}$ in this basis. Therefore, our Berry-phase polarisations exactly match our predictions for P_F using MLWFs.

We do not explore the idea of charge-transfer ferroelectricity further in this study, though these results for P_F are verified further by our interfacial calculations, where we observe several interesting consequences that arise from this.

6.2.3 Analysis of [111]-oriented NNO-CTO superlattices

60-atom thick NNO film

The primary structural and electronic properties of the ground state 60-atom thick NNO-CTO interfaced system are shown in Fig. 6.2. Looking first to the layer PDOS (Fig. 6.2(a)), we can see that the system is insulating throughout. We remark that due to Gaussian smearing, the valence and conduction bands appear very close to the Fermi level, though we highlight that this is also observed in our bulk NNO strained calculations with the same smearing, where the system is in fact insulating, and the band gap is measured to be roughly 0.5 eV. There are slight band offsets at the interfacial NNO layers, though these appear to be of very similar magnitude, and can be attributed to intrinsic differences typical of interfaces between any two perovskites. Considering the stable valence band maximums of the films, we can say that there is no net field across either film, which for a closed-circuit system, means that any interfacial dipoles are well-screened. This is confirmed further by the MAP (Fig. 6.2(b)), where there is no noticeable gradient across the layers. The out-of-plane A-, B-site displacements (Fig. 6.2(c)) are also relatively stable, though we do note a slight net polar shift in the B-sites of the CTO layer, and uneven polar motion around the interfaces in the NNO film. Both of these effects are likely the system attempting to screen the minor differences in interface dipoles, and given the lack of sloping in the MAP, we can say that these displacements (alongside any other minor effects) are sufficient in doing this. Polar motion more-readily appearing in CTO rather than NNO (while both have orthorhombic tilt patterns) might be because Ti is more polarisable than Ni (given the smaller ionic radii), or because the breathing mode suppresses B-site polar motion. There is also a general antipolar A-site motion in both films, which clearly corresponds to the antipolar motion typical of systems with $a^-a^-c^+$ tilt patterns [16], though this same distortion leads to partial out-of-plane components in the [111]-basis. Lastly, the magnetic moments are displayed visually in Fig. 6.2(d), which clearly resemble the charge-ordered T-type AFM order.

We also include further structural details of our system in Fig. C.2(a)—(f) in Appendix C. The octahedra sizes verify that the NNO film is charge ordered, where the sizes clearly vary layer-by-layer. We can also see that there is no noticeable decay from NNO into CTO, suggesting that there is not a huge energy cost for interfacing a breathing system with a non-breathing system in this basis. We find that the tilting (measured along the primitive directions) in both films is indeed of the $a^-a^-c^+$ order, and as they are very close in magnitude, there is negligible

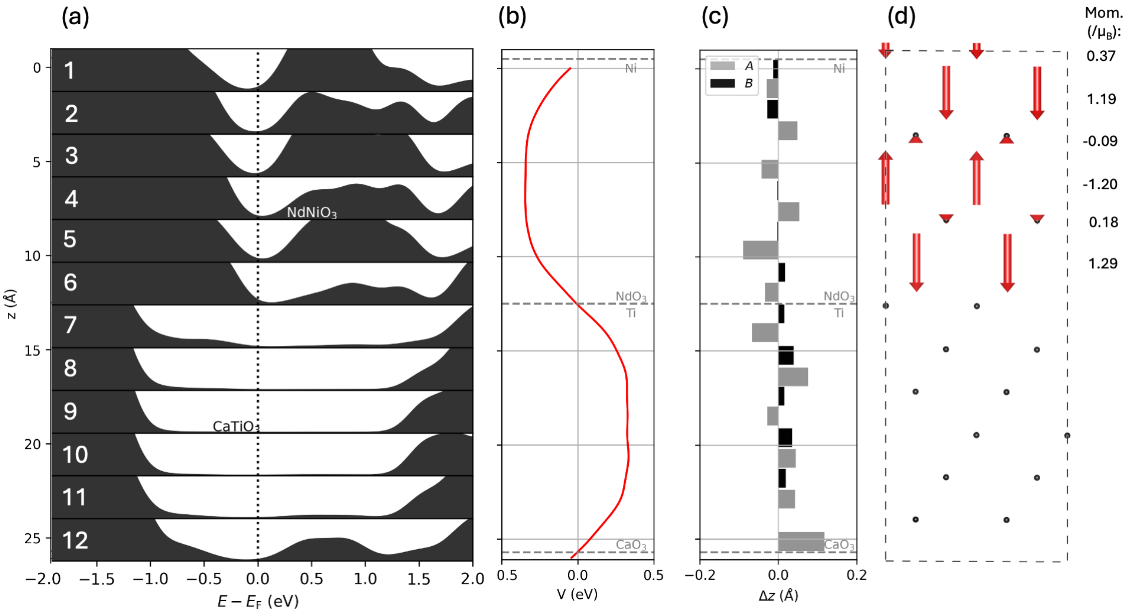

Figure 6.2: Key electronic and structural properties of stoichiometric 60 atom thick NNO-CTO system as a function of z (direction along $\hat{c}_{111}$): (a) projected layer density of states, (b) macroscopically averaged potential, (c) out-of-plane A- and B-site displacements, and (d) magnetic order and moments.

tilt mode decay in this system. The in-plane A-site ionic distortions are relatively large, clearly a result of the antipolar A-site motion, which has components along all [111]-cell axes. The B-site motion appears to be largely disordered and small in magnitude, and is likely a knock-on effect of mode decay and interfacial dipole screening. The octahedral variances and inter-layer distances are also predictable. The variances are typically larger at the interfaces due to minor polar displacements, while the inter-layer distances can be attributed to the antipolar A-site motion. In all, we can say that our result strongly matches our predictions from counting formal charges, as we see a clearly charge-ordered, insulating $P2/c$ T-AFM NNO ground state.

120-atom thick NNO film

We also investigate whether increasing the NNO film thickness affects the properties of the film. For the 60-atom NNO-CTO system, there are only minor interfacial effects and therefore minor differences in the NNO film with respect to bulk, meaning that a larger thickness is unlikely to have a major effect. However, generally this is an extremely thin film, and in other systems with more substantial interfacial effects, it may be hard to understand what is occurring. Larger thicknesses will help disentangle this. Regardless, we also investigate the thicker NNO film in this system, where CTO is kept at the same 60-atom thickness, and the NNO film is doubled out-of-plane.

The primary structural and electronic properties of the 120-atom NNO-CTO interfaced system are shown in Fig. 6.3. The layer PDOS once again shows an insulating NNO film, with a clear gap opening on every layer, and no major changes in the band offsets. Looking at the MAP, there does appear to be minor sloping across the NNO film, suggesting a very small field remains present. This is understandably due to two differing intrinsic dipoles in combination with closed-circuit boundary conditions, though the fact that it appears here means that it likely also exists in the 60-atom system, and cannot be clearly resolved in the averaged potential due to film thickness. Regardless, this field is virtually negligible, and the 120-atom film otherwise clearly resembles the 60-atom film. The A-site and B-site displacements once again vary at the interfaces in attempt to screen the minor interface dipoles. Polar motion is most prevalent in the CTO film, where there is a net displacement throughout. There appears to be an asymmetric response depending on the termination, which might be explained by the location of the nearest Ni-site: at the NdO_3-Ti interface, the nearest Ni^{2+}-site lies a layer away, while at the CaO_3-Ni interface the nearest Ni^{4+}-site is directly present. The more negative Ni^{2+} layer at the NdO_3-Ti interface attracts the interfacial Nd-sites (which are reversed from the direction expected by the antipolar mode, and additionally repulsed by the more positive CTO region), while the next-nearest Nd-site is repulsed as a result of this (it does not feel the more positive CTO region). The CaO_3-Ni interface is more difficult to explain. Here the nearest Ca-site is strongly attracted to the NNO film, despite the nearest Ni^{4+}-site being more positive. The MAP suggests that this region of the NNO film is slightly more negative, which could be a knock on effect of intrinsic dipoles and polar screening in CTO, where there appears to be less of a net field. The effect is relatively minor so is not explored in more detail here. Finally, the magnetic moments clearly resemble the charge-ordered T-AFM $P2/c$

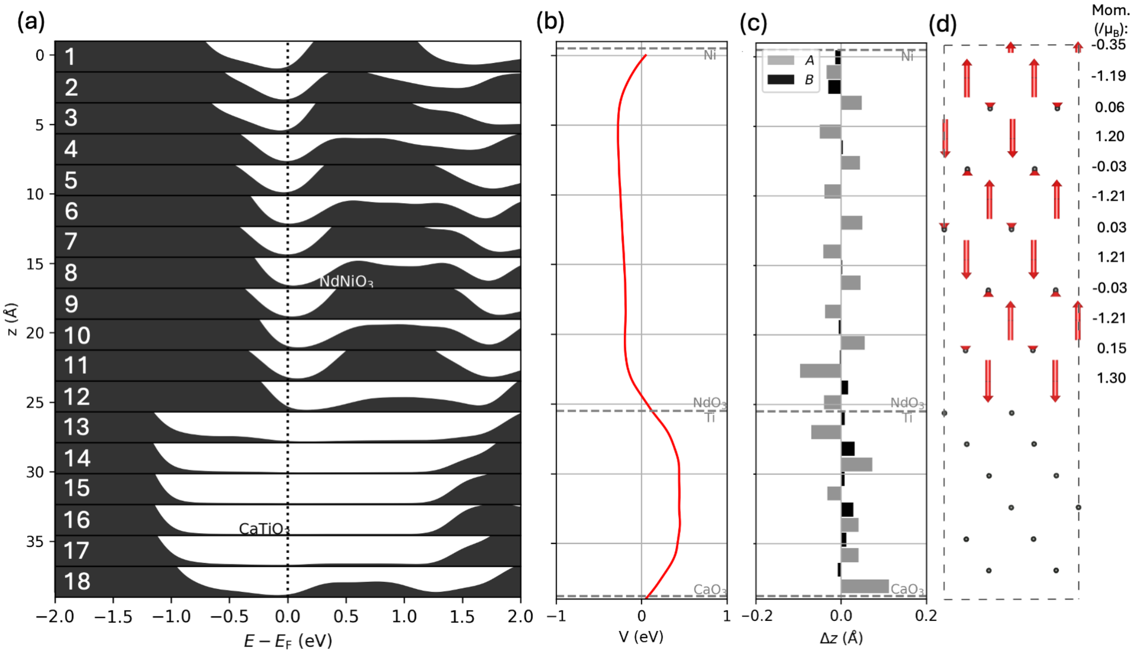

Figure 6.3: Key electronic and structural properties of stoichiometric 120 atom thick NNO-CTO system as a function of z (direction along $\hat{c}_{111}$), where (a)—(d) are equivalent to Fig. 6.2(a)—(d).

state. Additional structural features are included in Fig. C.3 (Appendix C). On the whole, the NNO film still clearly resembles the $P2/c$ symmetry predicted and the CTO film the $Pbnm$ phase besides interfacial effects and minor net polar motion.

Overall, it is clear that the CTO substrate can fix NNO to its bulk ground state, with the breathing mode specifically ordered such that the Ni-sites lying at the Ni-CaO$_3$ and Ti-NdO$_3$ interfaces are $\mathrm{Ni}_{\mathrm{L}}^{2+}$ and $\mathrm{Ni}_{\mathrm{S}}^{4+}$ respectively, matching our formal charge model. This may be a powerful new mechanism for controlling the properties of the nickelates. Using the polar discontinuity, we are able to pin the film to the charge-ordered insulating state, as there is an added energy penalty for forming the metallic state. We believe therefore that the NNO MIT temperature can be greatly amplified in [111]-oriented NNO-CTO superlattices, or in fact any [111]-oriented superlattice consisting of a charge-ordered insulating rare earth nickelate and an insulating II/IV perovskite (ideally with similar lattice parameters and modes to avoid possible energy penalties from strain and mode decay). We hope to see this verified experimentally in the future.

6.2.4 Unique metallic charge-ordered phases in NNO-NGO superlattices

60-atom thick NNO film

We now investigate the interface between NNO and III/III insulating perovskite NGO, which according to our model, is expected to have large polar discontinuities when the NNO film adopts a charge-ordered state. If the NNO film adopts this state, we expect the bound charge to be exactly $0.5e$ per f.u., averaged over $A^{\mathrm{NGO}}_{111,\text{ f.u.}}$ (where $A^{\mathrm{NGO}}_{111,\text{ f.u.}} = \sqrt{3}A^{\mathrm{NGO}}_{001,\text{ f.u.}}$) [225]. If the film occupies a non-charge-ordered metallic state on the other hand, there will be no polar discontinuities. We start by relaxing a bulk 60-atom NGO cell in the [111]-basis, which we find adopts the $Pbnm$ ground state. The resulting in-plane DFT lattice parameters are $|\mathbf{a}^{\mathrm{NGO}}_{111}| = 9.44$ Å ($/\sqrt{6} = 3.85$ Å) and $|\mathbf{b}^{\mathrm{NGO}}_{111}| = 5.56$ Å ($/\sqrt{2} = 3.93$ Å)). The NGO substrate therefore applies a large tensile [111]-strain to NNO, which we have previously shown increases the MIT energy and leads to a $P\bar{1}$ S-AFM ground state in bulk. Given the orthorhombic NGO ground state however, we predict that NNO phases with $a^-a^-c^+$ tilt patterns are instead preferred due to mode decay. In chapter 4 we predicted the $a^-a^-c^+$ phases to have slightly larger band gaps and possibly larger MIT energy differences than the $a^-a^-c^-$ phases for the same amount of strain. Experimentally, this has been observed in relatively thick NNO films deposited on NGO in the [111]-basis, where the film adopts a $P2/c$ space group and has an amplified MIT temperature [130]. All considered, strain and mode decay encourage NNO to be insulating, while the expected polar discontinuity encourages NNO to turn metallic. This presents a complex picture with no obvious outcome.

On the whole, finding the ground state of the [111]-oriented NNO-NGO system proved to be extremely challenging, as we found a huge range of metastable phases. It was necessary to test a wide range of structures and magnetic orders (both charge-ordered and non-charge-ordered), which we found were extremely volatile and a challenge to relax to the desired phase. After extensive investigation, we find a rather ambiguous ground state, which appears to have features from several bulk NNO phases. The primary features of this lowest energy state are shown in Fig. 6.4.

The layer PDOS suggest that NNO has turned metallic, as there is a clear presence of states at E_F beyond what can be attributed to smearing (as in the NNO-CTO systems). Interestingly however, we can also see that there is a slight variance in the band offsets of the insulating NGO film, indicating the possible presence of a field. This is confirmed in our MAP, where we see a gradient across not only NGO, but also NNO. A field in the latter suggests that NNO is not able to perfectly screen the field arising from differing interface dipoles and closed-circuit boundary conditions, which is not out-of-question given the low film thickness. This situation is ambiguous to understand, as NNO in its metallic state (without charge-ordering) should not have a polar discontinuity with NGO. However, the magnetic order suggests that NNO may retain some semblance of charge-ordering. The order is roughly FM, though the spins flip on layer 5 and vary in size throughout. We also relaxed this system with a completely FM order though found it to be higher in energy. Near the NdO_3-Ni interface, the system appears to have some amount of charge ordering, while at the NdO_3-Ga interface, the moments appear to be uniform. As the magnetic order is not T- or S-AFM, we predict that charge-ordered NNO states would still be metallic (according to our bulk calculations), which is what is observed here. However, the question remains as to why the system would do this rather than form a completely non-charge-ordered NNO film.

Out of the other structural features of this system (Fig. C.4, Appendix C), the most important to mention are the octahedra sizes. We see that our theory of a partially charge-ordered metal is supported, where we observe (minor, compared to the NNO-CTO system) charge-ordering at the NdO_3-Ni interface, which appears to gradually disappear upon approaching the NdO_3-Ga interface.

120-atom thick NNO film

Overall, the 60-atom system is very difficult to disentangle. Clearly, there is a different polar discontinuity here to the NNO-CTO systems, supporting our discussion above, but as the interfacial effects dominate in such thin films, so it is tricky to come to any strong conclusions to how this system is dealing with it. We investigate the thicker NNO film on NGO to shine light on this.

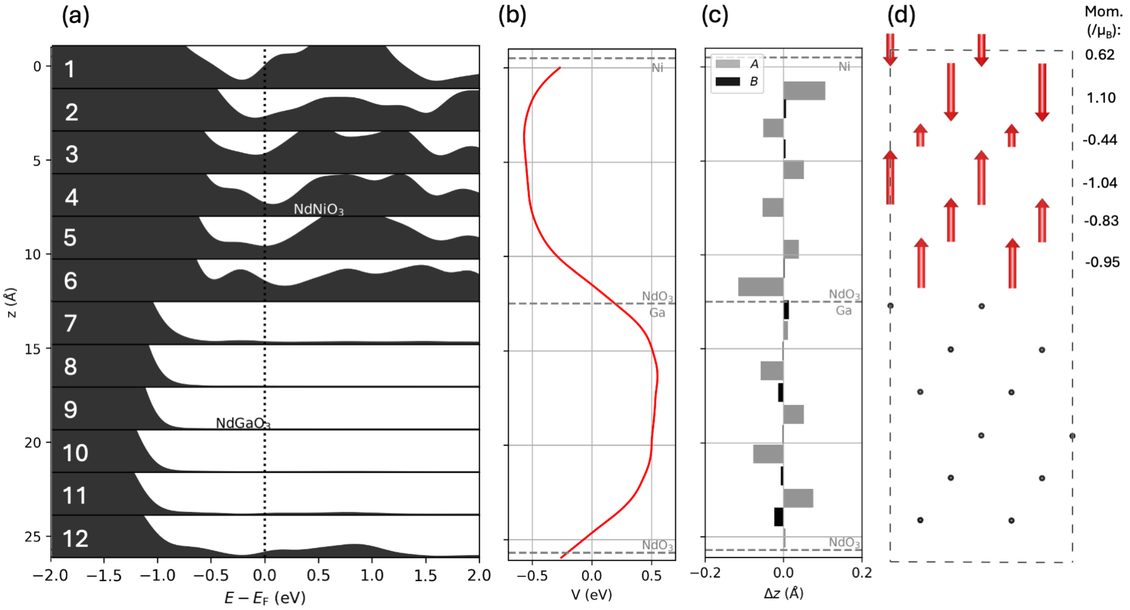

Figure 6.4: Key electronic and structural properties of stoichiometric 60 atom thick NNO-NGO system as a function of z (direction along $\hat{c}_{111}$), where (a)—(d) are equivalent to Fig. 6.2(a)—(d).

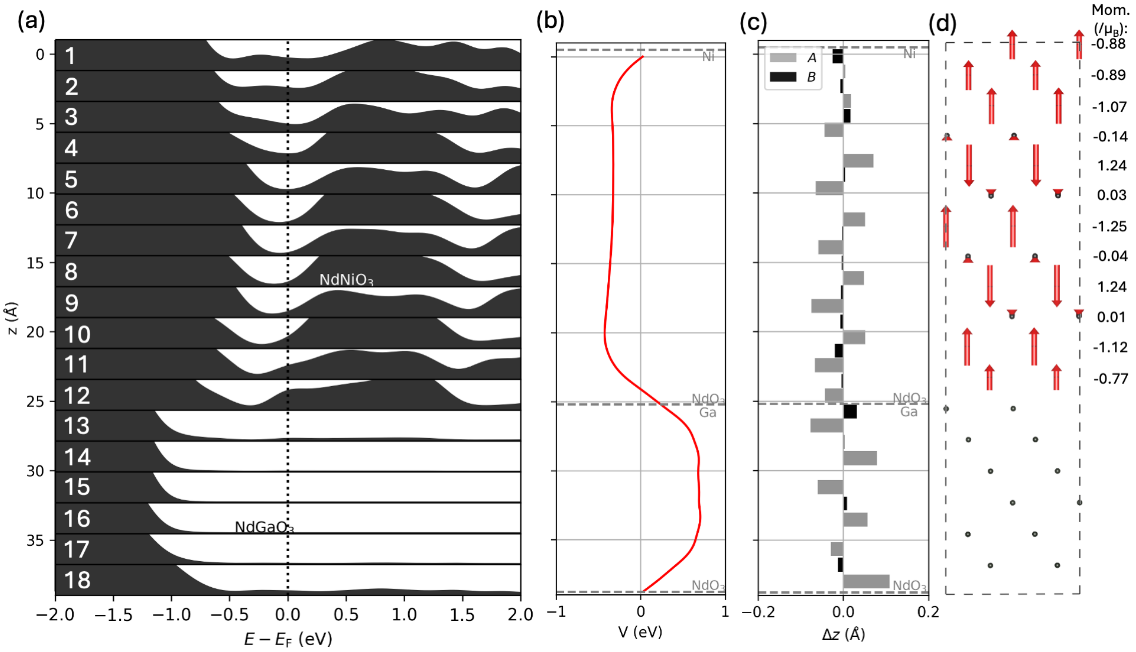

Figure 6.5: Key electronic and structural properties of stoichiometric 120 atom thick NNO-NGO system as a function of z (direction along $\hat{c}_{111}$), where (a)—(d) are equivalent to Fig. 6.2(a)—(d).

Finding the ground state of this system was also exceptionally difficult, as many metastable states appeared. The key properties of this system are displayed in Fig. 6.5. In this case, we immediately see that the film opens a gap roughly 3—4 layers from each interface, suggesting that the system is returning to bulk-like properties. The behaviour at the interfaces resembles more closely what is happening in the 60-atom film system. It is clear that these interfacial effects occur over at least three layers, which explains the lack of bulk-like behaviour in the 60-atom film. At the NdO_3-Ni interface, the first four layers appear to be metallic, while the NdO_3-Ga interface also has states at the Fermi level, but this appears to be a result of the band offset rather than the gap closing (as there still appears to be an energy region without states in these layers). The MAP also shows an interesting trend. There is a smaller measured gradient in the NNO film here (compared to the 60 atom system, though we remark that the larger x-axis scale makes this somewhat tricky to determine from our plots), and none in the NGO film, suggesting that any polar discontinuities are better screened. The shape of the NNO curve, which also vaguely resembles the band offsets in the layer PDOS, is rather unusual, and almost appears to be slightly curved rather than a linear slope as is typical for an interfaced insulator. This is likely a result of the different screening mechanisms at each interface. At the NdO_3-Ni interface, we see a flatter slope, and a layer PDOS resembling 2DEGs (layers 1—4 have no obvious gap as seen in layers 5—12), which suggests that the system has turned strongly metallic here. The system has closed the gap here by simply removing any charge-ordering at this interface. Meanwhile, at the NdO_3-Ga interface the potential curves, which seems to allow for the conduction states of the interfacial nickelate layers to cross the Fermi level. This phenomenon resembles Zener tunneling, where the conduction and valence bands overlap at opposite ends of a film due to the band offsets (as is observed in LAO-STO interfaces) [116, 117]. However, we do not strictly see Zener tunneling here— only the overlap of the conduction band minimum and the Fermi level. As a result, the NNO film is able to remain in the charge-ordered state at this interface, but becomes doped from this overlapping. With this in mind, and looking to the magnetic moments, the MAP can be explained more easily. The moments show charge-ordering throughout most of the film, besides the first two layers where a 2DEG has formed (arguably the final layer is also a 2DEG, though the large moment may just be down to interfacial magnetic frustration rather than a change in valence). Near the NdO_3-Ni interface, the nearest charge-ordered site (layer 3) has a larger moment, suggesting a negative polar discontinuity, which we expect to be screened by positive charges, which we see in the MAP. Near the NdO_3-Ga interface, the nearest Ni-site moments are small, corresponding to a positive discontinuity and negative screening charges, which again matches the MAP. The A- and B-site displacements are similar to the 60-atom film in bulk, but have slightly different responses to the interfaces. These are a little easier to explain in this system, where cations appear to be attracted to the NdO_3-Ni interface, and repulsed from the NdO_3-Ga interface. This makes sense if the former has a negative bound charge and positive screening charges, while the latter has a positive bound charge and negative screening charges. The 60-atom system can be explained to behave differently because of the interfacial effects dominating the system, which results in a complicated mess of screening mechanisms and charge-ordering.

Additional structural properties are shown in Fig. C.5 (Appendix C), where there are a few interesting features worth discussing. The octahedra sizes match our predictions from the moments, though strange behaviour is observed in the tilts, where the in-phase tilting is heavily suppressed near the interfaces of the NNO film. We also observe the Nd-site antipolar motion to decrease in-plane at these regions, and the Ni-site in-plane motion to increase. These effects are all structurally coupled to one-another, though it is not obvious which is the driving force. Initially, we might have considered it a result of the disappearance of breathing at the interfaces, though it occurs on either side and does not appear in the 60-atom film. Another possibility is that the in-plane Nd-motion is suppressed by the 2DEGs forming, such that the tilts decrease and Ni-sites compensate by displacing more. Finally, there may be a hidden structural energy penalty that depends on the direction of the in-phase tilt we have overlooked (as we saw for the breathing mode under [111]-strain). This may affect the NNO and NGO films differently, due to the tensile strain or the breathing mode present in NNO.

Aside from the interfaces, in the bulk regions, our film resembles what is seen in the NNO-CTO films, and also experimental reports of [111]-oriented NNO films on NGO (of larger thicknesses) [130], where the insulating $P2/c$ phase is observed. In these reports NNO is shown to be strongly insulating and have an amplified MIT from bulk. We cannot determine the amplified MIT, though given the effect of [111]-tensile strain, the bulk film here likely resembles our [111]-tensile bulk-strained results, which we have previously shown are likely to have an amplified MIT. However, these experimental readings (ref. [130]) are unlikely to be able to resolve the subtle interfacial behaviour seen in our results, which we suggest occur within roughly 8 Å from the interfaces. Overall however, we can say that our results match well to experiment, despite some ambiguity regarding the screening mechanisms. Still, we believe that this system warrants further experimental investigation, in hopes of observing either type of 2DEG seen here. Given the significant interest in the behaviour of the 2DEG lying at the LAO-STO interface (the doped charge-ordered interface seen here might resemble this), the 2DEG accessed by closing the gap might have very different properties— perhaps it is more or less susceptible to an electric field, has different superconducting capabilities, or has different magnetisation (as has been observed in previous studies of [001]- and [111]-oriented systems) [63,112,114,118–120]. In addition to our ground state phase, we also found some interesting metastable states, and propose some alternatives not realisable in this study due to cell size constraints. These apply to both the NNO-NGO and the following NNO-LAO systems, and are therefore discussed in the last subsection of this results section.

6.2.5 Polar metal phases in NNO-LAO superlattices

60-atom thick NNO film

Finally, we simulate [111]-oriented NNO films on an LAO substrate. LAO is a III/III perovskite just like NGO, but with a different ground state phase. Experimentally LAO occupies a rhombohedral $R\bar{3}c$ ground state with an $a^-a^-a^-$ tilt pattern, with similar lattice parameters to NNO [221]. Relaxing LAO in the [111]-basis, we obtain lattice parameters of $|\mathbf{a}_{111}^{\mathrm{LAO}}| = 9.27$ Å ($/\sqrt{6} = 3.79$ Å) and $|\mathbf{b}_{111}^{\mathrm{LAO}}| = 5.35$ Å ($/\sqrt{2} =$ 3.79 Å)), which are comparable to experimental measurements [221]. This applies a minor tensile strain to NNO. When using an $a^-a^-a^-$ tilt pattern input, we find that LAO remains in this tilt pattern, but surprisingly, we also uncover an LAO phase with an $a^-a^-c^0$ pattern that is marginally lower in energy. Previous DFT studies on LAO (also using the PBEsol functional) have found similar results, where these two tilt patterns (as well as $a^-a^-c^-$ and $a^-b^-c^-$) are found to be degenerate [228]. Experimentally, LAO is observed to remain in the $a^-a^-a^-$ (or at least, $a^-a^-c^-$) tilt pattern in [111]-interfaces with NNO [98]. To retain applicability to experiment, we therefore do not consider in detail any results where LAO occupies a vastly different tilt pattern to these. This complicates our investigation slightly, as this $a^-a^-c^0$ state is inevitably more energetically favourable for LAO when NNO occupies any orthorhombic ($a^-a^-c^+$) tilt pattern. Therefore, in this report we primarily consider NNO phases which have the $a^-a^-a^-$ or $a^-a^-c^-$ tilt pattern (inducing the same pattern in LAO). For completeness, we still tested the $a^-a^-c^+$ NNO inputs, but found they consistently resulted in $a^-a^-c^+$ LAO tilt patterns, which we believe to be unrealistic, so are omitted from the discussion.

As with the NNO-NGO systems, we find the energy landscape to have an extreme amount of local minima, so test a variety of NNO input structures and magnetic orders. The primary structural and electronic properties of the lowest energy structure that consist of $a^-a^-a^-$ or $a^-a^-c^-$ tilt patterns are shown in Fig. 6.6. The layer PDOS show that NNO is clearly metallic, and LAO unsurprisingly insulating, much like the NNO-NGO system. Interestingly however, we see that the band offsets hardly vary within the insulating LAO layer as they do in the NGO-NNO systems, suggesting that any fields arising from dipoles are better screened here. This is confirmed by the MAP, where there exists only a near-negligible amount of sloping in the LAO film, and none in the NNO film. This suggests that the NNO film has indeed sufficiently screened any fields (despite the film thickness). Interestingly, the magnetic order is the same as in the NGO-NNO system, but the moment sizes are noticeably different. We also relaxed an FM order here, but once-again found it to be higher in energy. A small amount of charge-ordering may be present (regarding the boundary between spin-up and spin-down regions), but on the whole we can say that the system is approximately non-charge-ordered. This suggests that the drive to become charge-ordered and insulating is not as strong as in NGO-interfaced systems. This might be explained by a few factors, firstly the lack of tensile strain, which is far smaller for LAO compared to NGO, and has been shown to amplify the energy difference between the lowest insulating and metallic phases. Secondly, given the lower amplitude of tilting in LAO (compared to the bulk-strained $P\bar{1}$ and $C2/c$ NNO phases), the bands of the NNO film are likely more dispersed, such that the triggering of the breathing mode is weaker. If this is the case, only minor intrinsic dipoles exist at the interfaces as in the NNO-CTO system, which should not be difficult to screen with ionic displacements. Another difference from the NGO-NNO case can be seen in these (A-, B-site) displacements, where A-site antipolar modes are no longer present due to the choice of tilt pattern. Previous experimental studies have reported polar NNO films in NNO-LAO interfaces due to the suppression of the antipolar motion [98], but this is not seen greatly here. There are minor displacements at the interfaces, which likely exist to screen the interface dipoles. A possible explanation for this discrepancy is the behaviour of LAO while using the PBEsol functional— as stated above, the $a^-a^-a^-$ tilt pattern appears not to be as stable in our calculations as in experiment. We state this as there are no reports of an $a^-a^-c^0$ tilt pattern appearing near the ground state in literature (besides DFT studies utilising the same functional as we have used [228]). Given the polar mode is primarily driven by the LAO tilt decay, it is plausible to say that the driving force behind this effect is underestimated in our calculations.

Secondary structural features are shown in Fig. C.6 (Appendix C), and support our explanation. The octahedra sizes are relatively uniform, such that any variation can be attributed to interfacial connectivity, dipole screening and possibly very minor charge ordering. Looking to the tilts, we verify that the tilting is lower in LAO than in bulk-strained NNO $P\bar{1}$ and $C2/c$ phases, confirming it as a possible driving mechanism for the stabilisation of metallic non-charge-ordered phases.

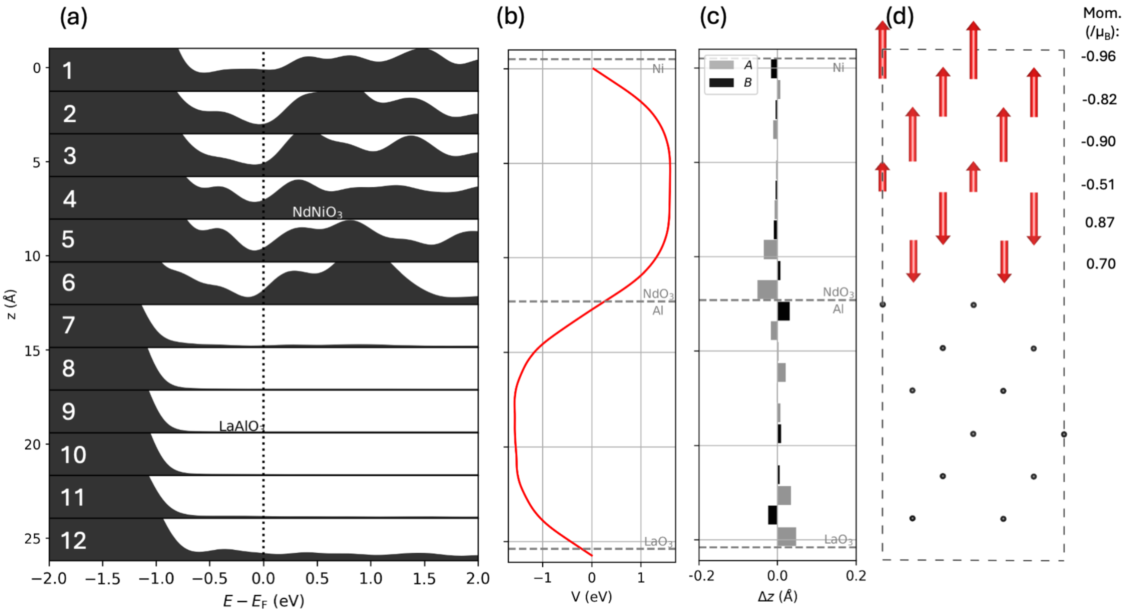

Figure 6.6: Key electronic and structural properties of stoichiometric 60 atom thick NNO-LAO system as a function of z (direction along $\hat{c}_{111}$), where (a)—(d) are equivalent to Fig. 6.2(a)—(d).

120-atom thick NNO film

The 120-atom NNO film is also simulated on LAO. The results are shown in Fig. 6.7, where we observe remarkably different behaviour to the 60-atom film. In this case, NNO appears to have turned to a charge-ordered phase throughout, where the band offsets vary layer-by-layer, clearly due to an unscreened field. Because of the film thickness, the valence and conduction bands can be seen to overlap at opposite ends of the film, allowing for Zener tunneling. This is reflected by the MAP also, where sloping can be seen across both films. Furthermore, there appear to be larger polar displacements here than in the 60-atom film, especially in the A-sites, which are likely driven by the field. The moments also demonstrate the condensing of the breathing phase throughout, though we could not relax a perfect T-AFM order across the entire film (one layer is flipped leading to nonzero moments on the small sites). Regardless, this is a huge change from the thinner film system, but is not unfounded, given the thinner film would not be able to access Zener tunneling due to lower NNO film thickness. Our result partially matches what is observed experimentally, where inversion symmetry breaking is observed in metallic

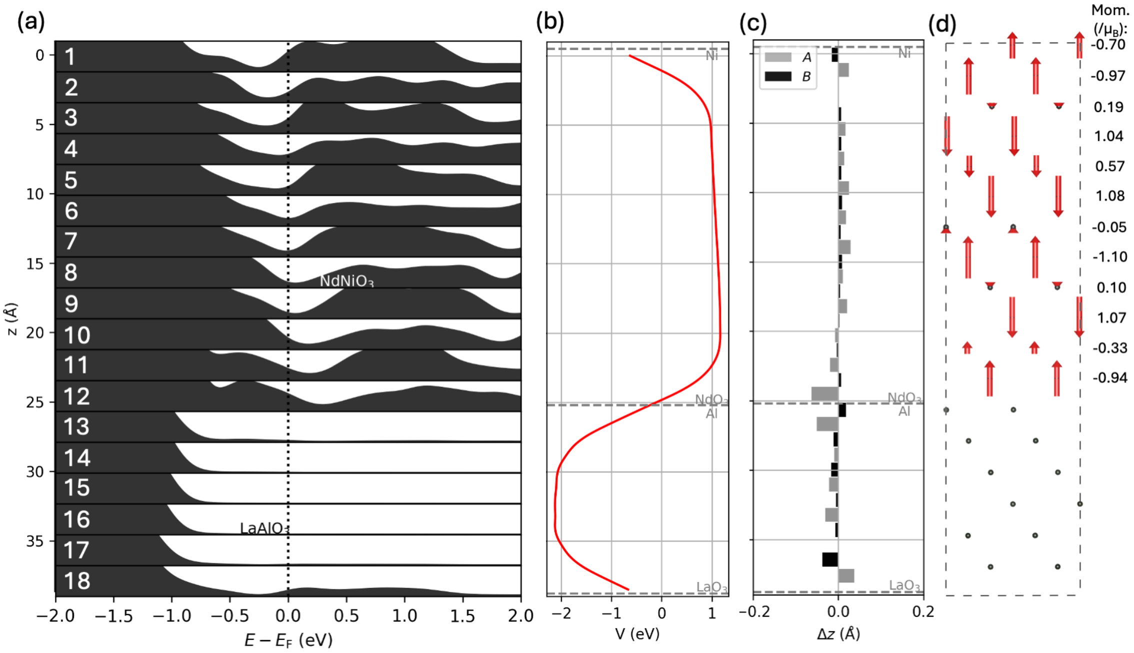

Figure 6.7: Key electronic and structural properties of stoichiometric 120 atom thick NNO-LAO system as a function of z (direction along $\hat{c}_{111}$), where (a)—(d) are equivalent to Fig. 6.2(a)—(d).

NNO films [98]. We remark that this is not solely down to tilt matching, which we expect fixes NNO to the $P\bar{1}$ state seen here, but also due to the unexpected polar discontinuity. Regardless, we cannot be sure of this, as experimental readings are obtained at higher temperatures where charge-ordering may have disappeared (which would severely reduce any polar discontinuities).

Aside from experiment, given the results of the 120-atom NGO-NNO system, this is still a surprising result. We may have expected this state to appear in the NGO-NNO system as well. In that system there does appear to be a band offset driven 2DEG at one interface, but not the other, so perhaps an additional stable or metastable state exists that resembles this result. Alternatively, the opposite is true, and there are states for the LAO-NNO system with 2DEGs at the interfaces instead. Additional structural details can be found in Fig. C.7 (Appendix C), where there are no major surprises.

Comparison to [001]-oriented NGO,LAO-NNO interfaces

To supplement our findings, we also investigated [001]-oriented NGO- and LAO-NNO interfaces. In this case, we built NNO-substrate films from the 80-atom cell defined in chapter 4 for insulating nickelate phases. This corresponds to a 160-atom unit cell consisting of an 80-atom NNO film and an 80-atom NGO or LAO film interfaced along $\hat{c}_{001}$. The layer PDOS, MAP, and A-, B-site displacements for each system may be found in Fig. D.1 (Appendix D). We find that the NNO film occupies the T-AFM $P2/c$ ground state in both systems. We highlight that the system is insulating, despite the smearing in the layer PDOS where it appears as if states are present at the Fermi level (we verified the system is insulating by checking the layer PDOS of bulk [001]-strained NNO systems (which we know are insulating from computation of the band structure), and find that the layer PDOS are almost identical). Overall, besides minor band offsets, which can be attributed to intrinsic dipoles, there appear to be no major interfacial screening effects nor fields across the system. This is completely in-line with what is expected here, where the breathing phase adds no further polar discontinuity due to Ni valence averaging in-plane. Only minor interfacial effects occur, on the scale of those in the CTO-NNO systems, which also have no major discontinuity.

The fact that this is not the case in the [111]-oriented NGO-, LAO-NNO interfaces is strong evidence that an additional polar discontinuity is present there. We have demonstrated several ways that the system can deal with this, though stress that screening typically occurs over several layers and drastically alters the properties of the film, especially for lower thicknesses.

6.2.6 Further possible phases for NNO on III/III perovskite substrates

In regards this polar discontinuity in NGO- and LAO-NNO systems, it is also worth highlighting some additional metastable phases we managed to relax, as well as ideas for phases that are not realisable in our cells due to size. The first of these involves the transfer of exactly one electron from the interfacial Ni^{2+} layer to the interfacial

Ni^{4+} layer, such that $2\mathrm{Ni}^{4+}/2\mathrm{Ni}^{2+} \rightarrow \mathrm{Ni}^{4+} + \mathrm{Ni}^{3+}/\mathrm{Ni}^{2+} + \mathrm{Ni}^{3+}$ (where the / denotes the Ni-sites at either interface). Due to this charge transfer, the polar discontinuity is screened. We managed to relax this state in the NGO-NNO system for a $P\bar{1}$ tilt pattern, though remark that it took many attempts due to the volatility of the SCF cycle. This state was metastable, and could not be relaxed for the $P2/c$ tilt pattern. It could be that the system struggles to relax this phase due to the proximity of Ni^{3+}-sites to Ni^{4+}- and Ni^{2+}-sites, where a gap may locally close relatively easily, causing the system to revert to regular 2DEGs (where all interfacial sites are likely to be Ni^{3+}).

Another interesting possibility that could not be considered is to transfer two electrons per every four interfacial Ni-sites, but double the valence: $4\mathrm{Ni}^{4+}/4\mathrm{Ni}^{2+} \rightarrow 3\mathrm{Ni}^{4+} + \mathrm{Ni}^{2+}/3\mathrm{Ni}^{2+} + \mathrm{Ni}^{4+}$. In this case, it may be that the difference in interfacial valence means the system can avoid forming 2DEGs and retain the lower-energy insulating character in the bulk of the film. This phase requires the doubling of the unit cell in-plane, so we have not extensively tested this. This could be an interesting phase for a variety of reasons— the lone $\mathrm{Ni}^{2+}/\mathrm{Ni}^{4+}$-sites at each interface might be polarons that form interesting patterns, and may be mobile with an electric field in-plane.

Finally, another alternative not accessible in our cells is the idea of 'breathing domains', which would be ordered in-plane, such that domains of Ni^{2+} and Ni^{4+} would average in-plane a 3+ nominal charge. As a result, only minor polar discontinuities would exist at the interfaces between domains, rather than a large net field across the system.

Overall, [111]-oriented NGO- and LAO-NNO interfaced systems are exceptionally interesting, and we heavily encourage further experimental investigation, particularly towards the behaviour at interfaces and ultrathin films, where a variety of interesting phases exist on the verge of stability.

6.3 Summary

In this chapter, we have demonstrated novel behaviour in NNO when interfaced in the [111]-basis. We discover an unexpected polar discontinuity for charge-ordered NNO in this basis, where we first demonstrate that a certain breathing order is preferential when interfaced with II/IV perovskite CTO, then show that the formal polarisation of NNO in the charge-ordered phase (in the [111]-direction) corresponds to $\mathrm{Ni_{L,S}}$ formal charges of 2+ and 4+ respectively (which appear on separate (111)-layers). As a result, the breathing is pinned to a particular order when NNO is interfaced with a II/IV perovskite as the formal polarisations match. This is such that an additional energy cost appears when reverting to the metallic NNO phase—we expect the MIT temperature to be amplified significantly in these systems. We then investigate NNO films on III/III perovskites NGO (orthorhombic tilt pattern, large tensile strain) and LAO (rhombohedral, small tensile strain). We find an extremely complex energy landscape with many metastable phases in both cases. We observe significant interfacial screening mechanisms in these systems, which is clear evidence of a sizeable polar discontinuity. We find the systems have a variety of available screening mechanisms, including 2DEGs and Zener tunneling-like conduction band overlap. Overall, besides ultrathin films, our results suggest that the NNO films seek to retain their charge-ordered, insulating character as much as possible, which it is able to do in the bulk of the film. This matches experimental readings, though we suggest a deeper investigation to the behaviour at the interfaces, which we suggest have a large polar discontinuity, and as a result some interesting and possibly novel screening mechanisms.

CHAPTER 7

Conclusions and outlook

To conclude this report, we review the project aims set at the end of the introduction. For each question, we briefly recap our findings, then suggest next steps for further study. I also provide my own outlook on the project as a whole.

1. Can we simulate STO and NNO using first principles techniques such that the experimental ground states are accurately recreated?

We obtain a ferroelectric $R3c$ STO ground state rather than the paraelectric phase observed experimentally, but only due to the lack of quantum energy fluctuations not present in first principles calculations. Our ground state is only marginally lower in energy than the lowest non-polar phases, which matches the description of STO as a quantum paraelectric. We do not expect investigation with more accurate functionals such as hybrids to yield a qualitatively different picture to what is seen here.

For NNO, we obtain a charge-ordered, insulating $P2/c$ ground state with a T-AFM magnetic order, which are the key experimental features for correctly simulating the MIT. We find that a small Hubbard-U correction of 2 eV on the Ni-$3d$ orbitals is optimal for NNO, but find this to be insufficient for LNO, where a 5 eV correction is required to obtain a metallic, $R\bar{3}c$ ground state comparable to experiment. Because of this, it is unfortunately not possible to investigate NNO-LNO interfaces from first principles. A useful future study would be to find a single set of DFT parameters that obtain the correct ground state for all rare-earth nickelates. We particularly suggest an investigation into the intersite Coulomb interaction $+V$, which might improve the energy cost of the MIT (which depends on the stability of the breathing phase, which in-turn depends on mostly-covalent electrons between Ni-3*d* and O-2*p* orbitals). Alternatively, given more computational resources, one could investigate the ground state nickelate phases with higher accuracy exchange-correlation functionals, or even investigate the effect of other subtle features such as non-collinear spin orderings and *A*-site magnetic order.

2. How does the ground state of STO change as a function of [001]- and [111]-oriented compressive and tensile strain?

We find that compressive and tensile [001]-strain strongly stabilises polarisation out-of- and in-plane respectively, matching experimental observations. The stability of the polar mode rapidly increases with strain, at a higher rate than the antiphase tilt mode. We find that tensile [111]-strain stabilises polarisation both in- and out-of-plane (in the [111]-basis), while compressive [111]-strain suppresses it.

For obtaining strongly polar STO states, we suggest theoretical and experimental investigation into high [001]-strains (within experimental feasibility), where we predict increasingly more stable polar phases. [111]-oriented tensile-strained STO systems could also be of interest experimentally, to see whether STO polarisation in- and out-of-plane can be realised simultaneously, and to verify the domain structure. We also suggest varying the magnitude of strain applied to each in-plane direction, which is not tested here, and could be achieved experimentally with non-cubic substrates. Furthermore, investigation into [110]-strain could be of interest, as it may induce polarisation along other unique axes to those seen here.

3. How does the ground state of NNO change as a function of [001]- and [111]-oriented compressive and tensile strain?

Under compressive [001]-strain, the in-plane tilts are quickly suppressed, which prevents the triggering of the charge-ordered phase, thus inducing an IMT. Under tensile [001]-strain the insulating phase is more stable, but experiences a large energy penalty for the breathing mode at high strains (where ΔE_{MIT} rapidly declines). Compressive [111]-strain gradually decreases the NNO tilting and band gap, while tensile [111]-strain gradually amplifies the gap and MIT energy difference, while inducing novel $a^-a^-c^-$ breathing phases. The breathing mode is competitively coupled to compressive strain, and cooperative with tensile strain in both bases. We also discover an odd-order coupling term between [111]-strain, tilting and the breathing mode, which we confirm corresponds to an energy penalty depending on the choice of large and small Ni-sites.

Further investigation into the energy penalties of the breathing mode under [111]-strain could be useful for uncovering new phases that may have been missed here. We also suggest further investigation into the many available nickelate tilt patterns, especially those consisting of in-phase tilts (such as $a^+a^+c^+$) which are not explored. Furthermore, we predict novel metallic phases to appear under high [111]-compressive strains, which could not be relaxed here (besides the undistorted $R\bar{3}m$ system). Experimentally, tensile [111]-strained NNO systems would be particularly interesting to investigate further if realisable at high strains, as our results suggest a significant amplification of the band gap and MIT temperature. The trends with strain observed here are likely to be applicable to the rest of the series aside from LNO, though separate investigation into these may still be worthwhile (especially those that have Neél transitions, which may stabilise different magnetic orders at ground state under strain). As with STO, non-cubic in-plane strain and [110]-strain may also induce further novel behaviour in the rare-earth nickelates.

4. What happens when we interface an incipient ferroelectric with a material that can undergo an MIT?

Due to computational limitations, we are unable to investigate the insulating NNO phase, but find that the available metallic state matches experimental observations. In non-stoichiometric systems, where STO is fixed as a paraelectric, we discover an unexpectedly large difference in the band offsets depending on the choice of layer termination. This is due to the metallic screening of an underlying interfacial 'bound charge' approximately equivalent to that seen in LAO-STO interfaces. In a stoichiometric system with inversion symmetry broken, we find that the STO film becomes strongly polarised, moreso than in equivalent bulk-strained calculations. We find that the polarisation acts to minimise the field generated by the large inequivalent interface dipoles and closed-circuit boundary conditions, such that it becomes pinned in one direction.

Given more computational resources, a further interesting study could be to simulate the same system doubled in-plane so T-, and S-AFM NNO phases may be considered, such that the breathing mode and MIT are more able to occur. Considering the strong match of our results to experiment, this study suggests that this is unlikely to be the case for these thicknesses. Regardless, thicker NNO films might be able to do this by forming 2DEGs at the interfaces and retaining insulating behaviour in the centre of the film. Varying the STO thickness could also have interesting consequences— as in contrast to traditional ferroelectric-electrode devices, we predict smaller thicknesses to amplify the polarisation and larger thicknesses to diminish it.

More generally, we suggest further investigation into the cause of the dipole appearing between metals and insulators. A good starting point might be to test a variety of metals and MIT-capable materials interfaced with insulators (or simply STO), which may reveal different magnitudes of dipoles and band offsets, shining light on the problem. To precisely understand this situation, one could develop a method for finding the Wannier centres of metallic phases, which may be possible along certain axes where electrons are immobile. It may be that this can be done for the [001]-direction in nickelates, and can be used in-turn to calculate any underlying formal polarisations (that become screened by the free charges).

5. How do rare-earth nickelates behave in [111]-oriented interfaced systems?

When interfaced in the [111]-direction, we find that charge-ordered perovskites have a different polar discontinuity to that seen [001]-oriented systems. When interfaced with II/IV (insulating) perovskite CTO, we find that nickelate films prefer a particular breathing order, and that metallic phases are energetically penalised. When interfaced with III/III perovskites NGO and LAO, we find novel interfacial behaviour occurring over several layers. In ultrathin films (13 Å), we find that interfacial effects dominate the system completely, while for thicker films (26 Å) we observe bulk-like (insulating, charge-ordered) behaviour near the centre of the film and screening effects near the interfaces. We find a vast range of previously-unseen nickelate structures, consisting of several distinct screening mechanisms, including 2DEGs and Zener tunneling. We also discuss other possible screening mechanisms that might appear experimentally, involving Ni charge transfer and breathing domains. In addition to this, we uncover a possible new type of ferroelectricity due to charge-ordering along the [111]-direction. Changing which Ni-sites are large or small alters the formal polarisation along this direction, which may be switchable with an applied electric field.

Overall, we heavily encourage further study into the [111]-oriented nickelate film. Experimental realisation of the NNO-CTO system could be an easy way to verify our theory of the polar discontinuity, where we expect the NNO MIT temperature to be amplified significantly. The NGO- and LAO-NNO systems are also worth further clarifying experimentally, particularly in regard the interfacial behaviour, where we predict several interesting mechanisms. The ferroelectric NNO phase could be tested experimentally by interfacing it with metallic electrodes. Other charge-ordered perovskites such as $BaBiO_3$ and $BiNiO_3$ could also be tested, which we predict to have the same feature.

Investigating the [111]-oriented NNO-STO interface may also be worthwhile. In this case, the system has the same discontinuity as in the NNO-CTO system, but depending on the choice of substrate (that applies strain), STO might add additional complications. Under any [111]-strain STO has a tilt pattern resembling $a^-a^-c^-$, which is likely to be induced in NNO, and under tensile strain, STO is polarised in- and out-of-plane. This might be suppressed by the polar discontinuity, or induce polar phases in the insulating nickelate. Alternatively, NNO might be more likely to turn polar in an interface with $BaTiO_3$, which has a larger polar mode than STO.

Personal outlook

I believe that investigation into complex oxide interfaces from first principles could be one of the most fruitful studies in condensed matter physics over the coming decades, as theoretical methods and computational resources continually improve. Currently, we understand the effects of interfacial phenomena primarily from what can be detected experimentally, as most interfaced systems are too large to simulate from first principles. Experimental studies are rarely capable of resolving many of the structural and electronic features of these systems due to their subtlety. As we have shown in the latter chapters of this project however, often novel complex behaviour is occurring at the interfaces that we are not detecting. This information is essential for understanding these materials and can undoubtedly be utilised for designing new devices.

Using this project as an example, we have shown that huge dipoles can exist between metals and insulators, and that an unexpected polar discontinuity exists in [111]-oriented charge-ordered systems. Both effects completely change our understanding of these systems, and result in complex interfacial effects that had not been detected experimentally. STO and NNO are two of the most interesting materials out there, and in this study alone we have induced novel behaviour in each. I am hopeful that these materials and interfaced systems based on them are continually investigated, and that they eventually reach industry.

I believe condensed matter physics in this day and age will be looked back on as a golden era in centuries to come. We exist at a time where theoretical and experimental methods have only just become capable of accurately probing materials at the quantum level. We are rapidly discovering endless new physics across countless systems, providing humanity with a toolbox of possible phenomena that can be harnessed through precise manipulation.

APPENDIX A

Further methods details

A.1 Energy functional of a uniform electron gas

The exchange and correlation components of the LDA energy of the uniform electron gas may be considered independently:

$$\epsilon_{xc}^{\text{unif}} = \epsilon_{x}^{\text{unif}} + \epsilon_{c}^{\text{unif}}. \tag{A.1.1}$$

The exchange component of the energy can be found exactly [147, 149, 229]:

$$E_{\text{x}}^{\text{LDA}} = \int n(\mathbf{r})\epsilon_x^{\text{unif}}[n(\mathbf{r})]d\mathbf{r} = -\frac{3}{4}\left(\frac{3}{\pi}\right)^{\frac{1}{3}} \int n^{\frac{4}{3}}(\mathbf{r})d\mathbf{r}, \tag{A.1.2}$$

and the correlation may be parameterised as

$$E_{\text{c}}^{\text{LDA}} = n\Omega \cdot \begin{cases} 0.0311 \ln r_s - 0.0480 + 0.002 r_s \ln r_s - 0.0116 r_s & \text{if } r_s < 1 \\ -0.1423/(1 + 1.0529\sqrt{r_s} + 0.3334 r_s) & \text{if } r_s \geq 1 \end{cases}, \tag{A.1.3}$$

where r_s is the Wigner-Seitz radius [230,231]. The Wigner-Seitz radius is the radius of the spherical volume occupied by each electron:

$$r_s = \left(\frac{3}{4\pi n} \right)^{\frac{1}{3}}. \tag{A.1.4}$$

A.2 Hubbard-U and Hund-J

To investigate the effect of various on-site corrections, we calculated the Hubbard-U correction in accordance with both the simplified and unsimplified rotationally-invariant approaches as proposed by Dudarev et al. as in ref. [180] and Lichtenstein et al. as in ref. [209] respectively. We calculate the former (effective U, U_{eff}) using Cococcioni's approach as in ref. [210] and the latter (U, J) using the 'minimum tracking approach' as in ref. [211,212].

APPENDIX B

Further bulk and bulk-strained nickelate details

Table B.1: Further structural and electronic details of bulk NNO ($U = 2$ eV) and LNO ($U_{\text{eff}} = 6$ eV).

Quantity	NNO	LNO
L. P. ([001]-basis)		
a_{001} (Å)	3.78	3.77
b_{001} (Å)	3.77	3.83
c_{001} (Å)	3.78	3.80
L. P. ([111]-basis)		
a_{111} (Å)	3.78	3.83
b_{111} (Å)	3.77	3.83
c_{111} (Å)	3.78	3.74
D. T. ([001]-basis)		
χ^e_{xx}	26.21	-
χ^e_{yy}	20.33	-
χ^e_{zz}	24.16	-
χ^I_{xx}	11.48	-
χ^I_{yy}	12.10	-
χ^I_{zz}	11.22	-
χ^T_{xx}	37.69	-
χ^T_{yy}	32.43	-
χ^T_{zz}	35.38	-
D. T. ([111]-basis)		
χ^e_{xx}	21.62	-
χ^e_{yy}	22.33	-
χ^e_{zz}	28.57	-
χ^I_{xx}	10.84	-
χ^I_{yy}	12.15	-
χ^I_{zz}	11.68	-
χ^T_{xx}	32.46	-
χ^T_{yy}	34.48	-
χ^T_{zz}	40.25	-

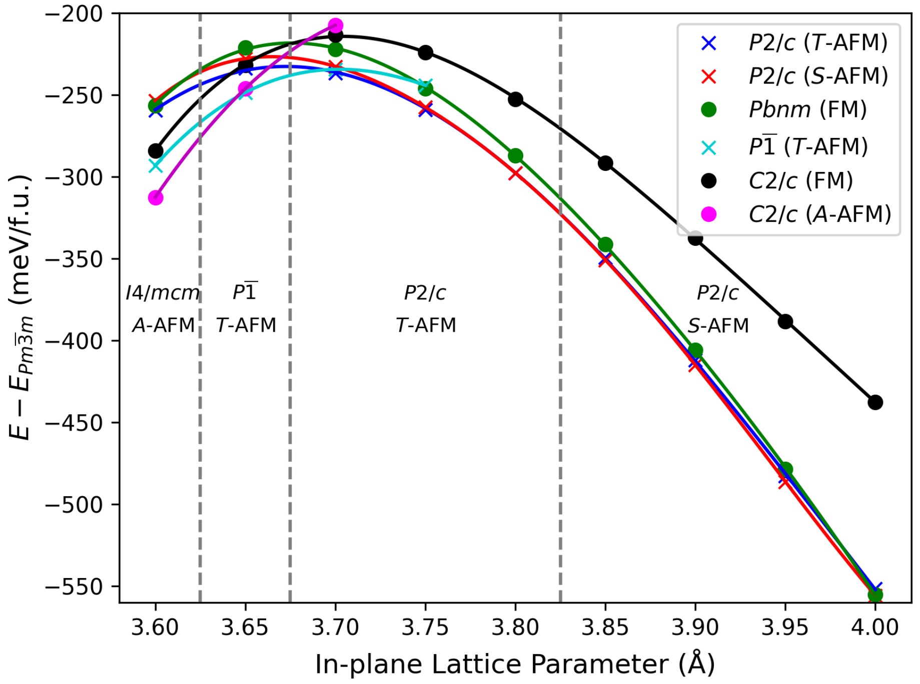

Figure B.1: Energy of various NNO phases as a function of [001]-strain. Insulating and metallic phases are indicated by crosses and circles respectively.

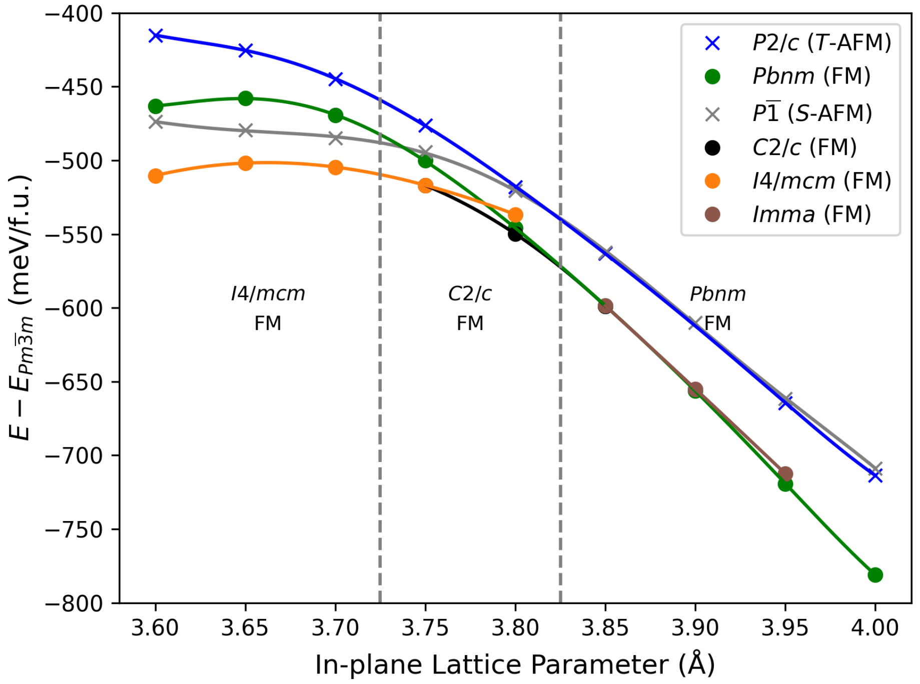

Figure B.2: Energy of various LNO phases as a function of [001]-strain. Insulating and metallic phases are denoted in the same way as in Fig. B.1.

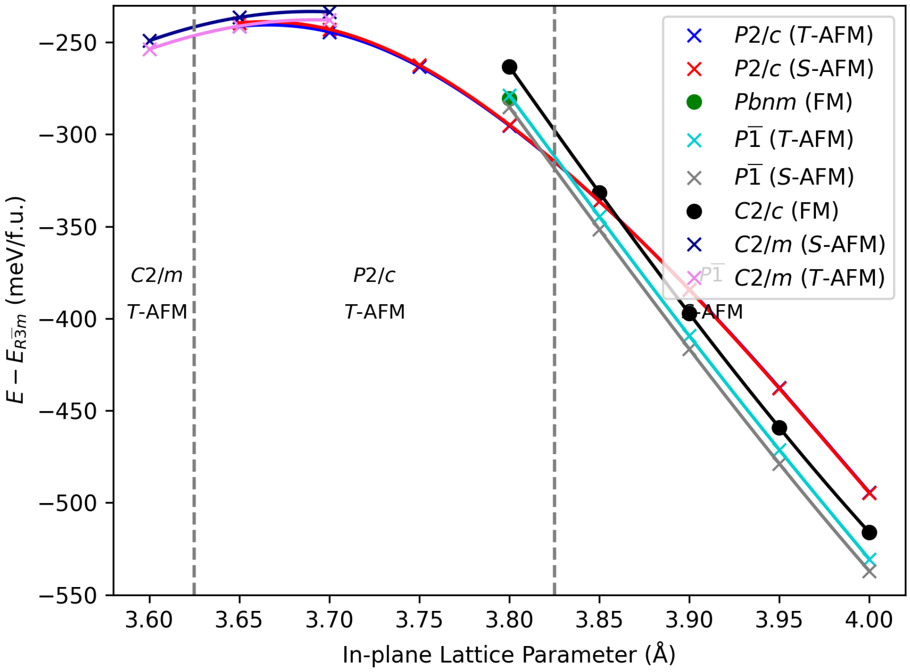

Figure B.3: Energy of various NNO phases as a function of [111]-strain. Insulating and metallic phases denoted in the same way as in Fig. B.1.

APPENDIX C

Additional details of [111]-oriented NNO-based systems

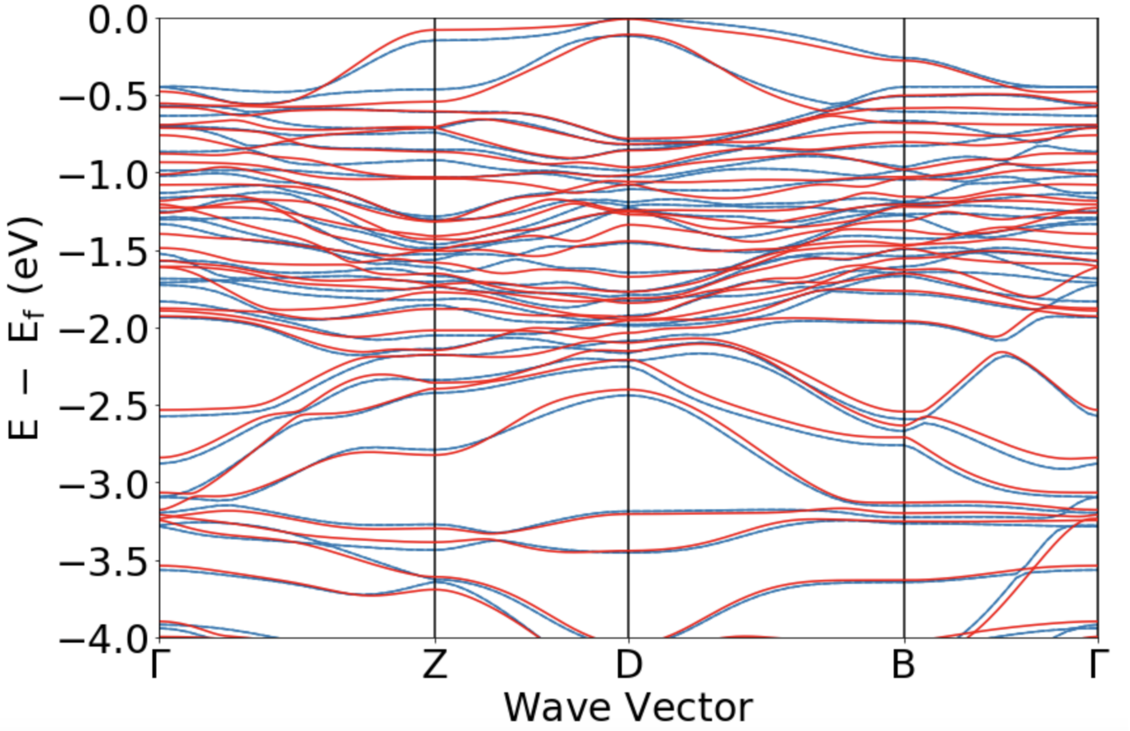

Figure C.1: Overlay of the bulk, charge-ordered $P2/c$ NNO valence band structure calculated in VASP (blue bands) and Wannier90 (red bands). The Wannier functions were generated using the Bloch functions obtained from the VASP calculation.

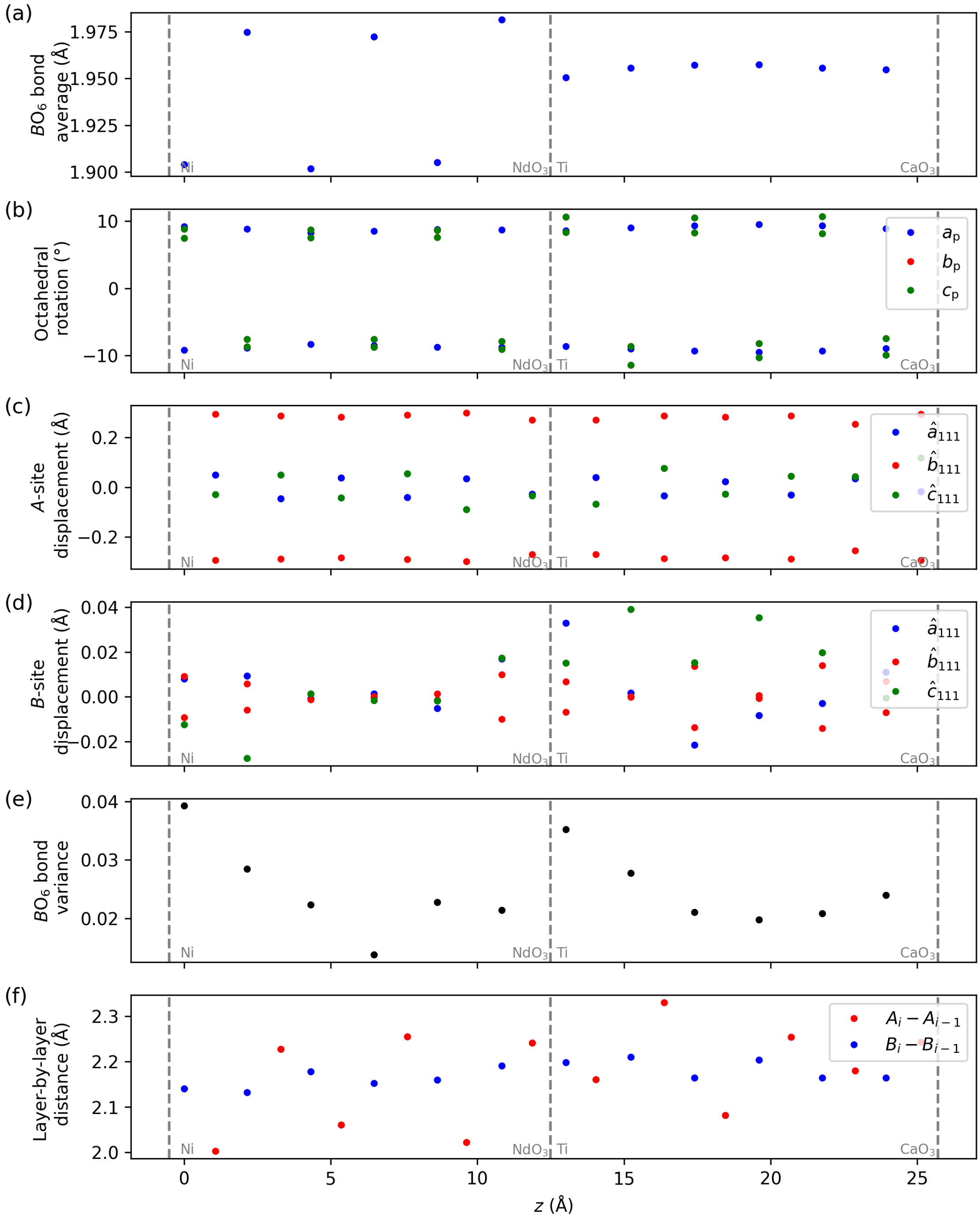

Figure C.2: Further structural properties of non-stoichiometric 60-atom NNO-CTO system as a function of z (direction along $\hat{c}_{111}$): (a) average B-O bond length within BO_6 octahedra, (b) octahedral rotations around primitive directions $\hat{a}_\mathrm{p}, \hat{b}_\mathrm{p}, \hat{c}_\mathrm{p}$, (c) A-site displacement along cell axis directions $\hat{a}_{111}, \hat{b}_{111}, \hat{c}_{111}$, (d) B-site displacement along cell axis directions, (e) variance of B-O bonds within BO_6 octahedra, (f) inter-layer distance, where A_i, B_i denote the z coordinate of A, B sites on given layer (such that A_{i-1}, B_{i-1} denote the z coordinate of the A, B sites on the previous layer)

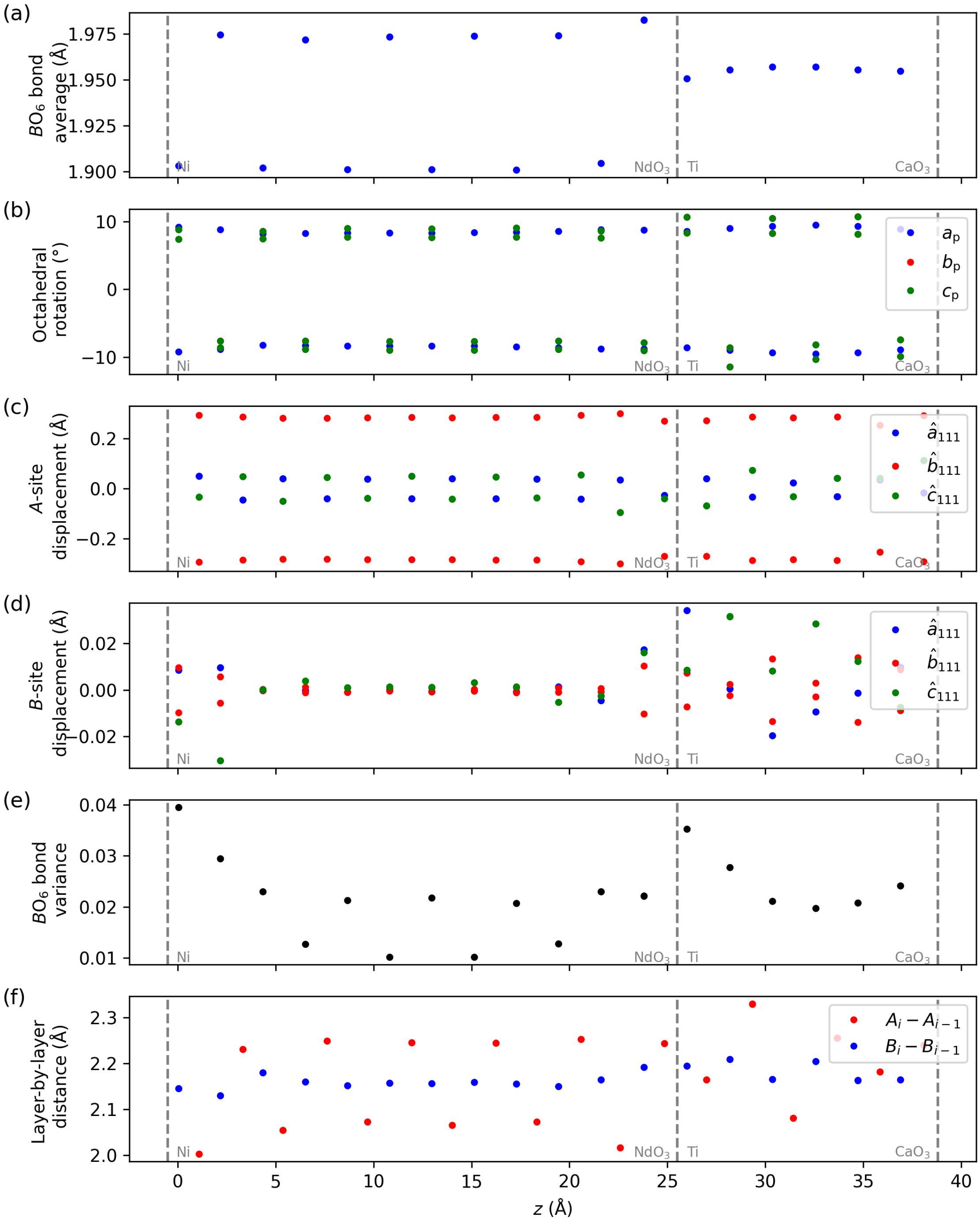

Figure C.3: Further structural properties of 120-atom NNO-CTO as a function of z (direction along $\hat{c}_{111}$), where (a)—(f) are equivalent to Fig. C.2.

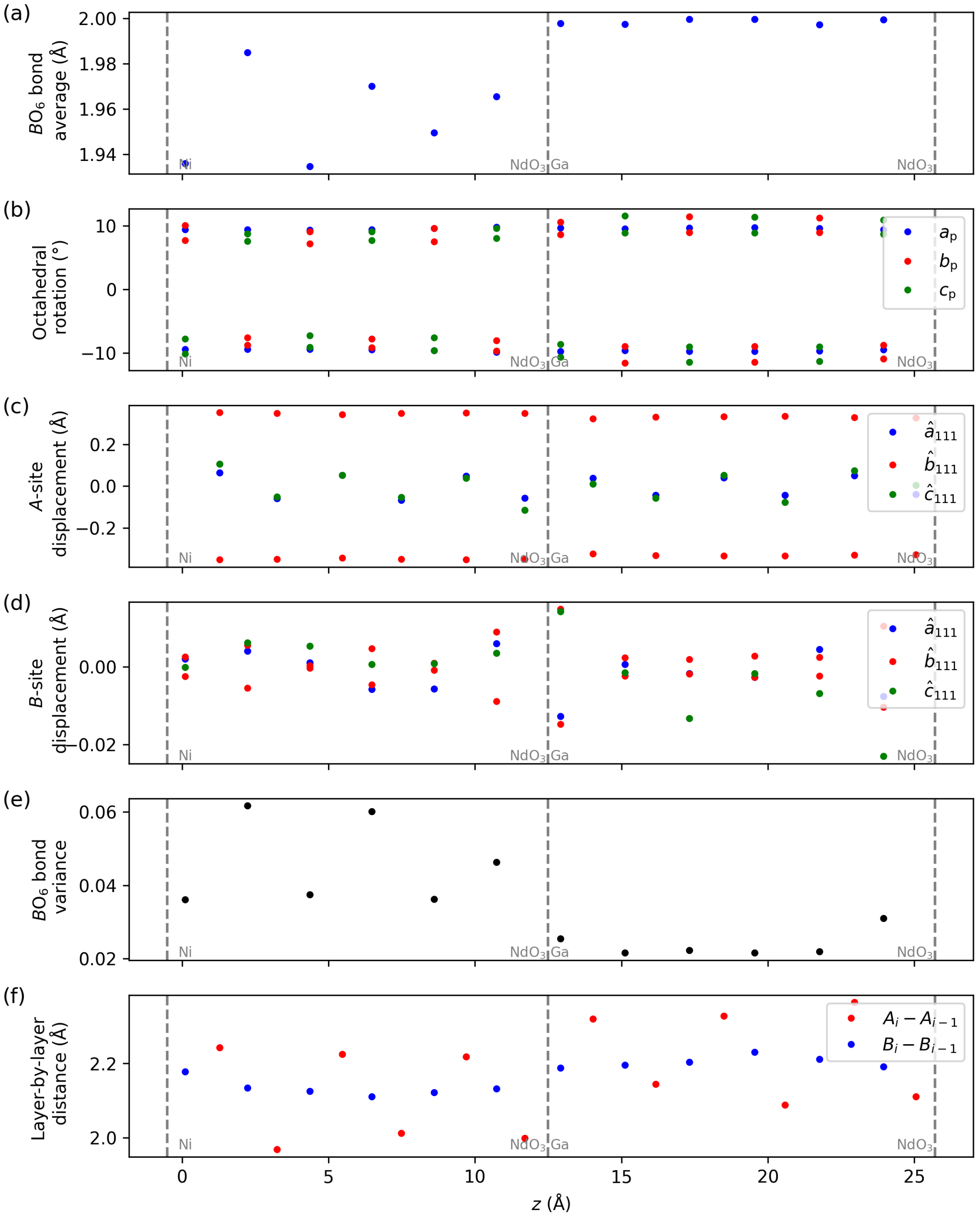

Figure C.4: Further structural properties of 60-atom NNO-NGO as a function of z (direction along $\hat{c}_{111}$), where (a)—(f) are equivalent to Fig. C.2.

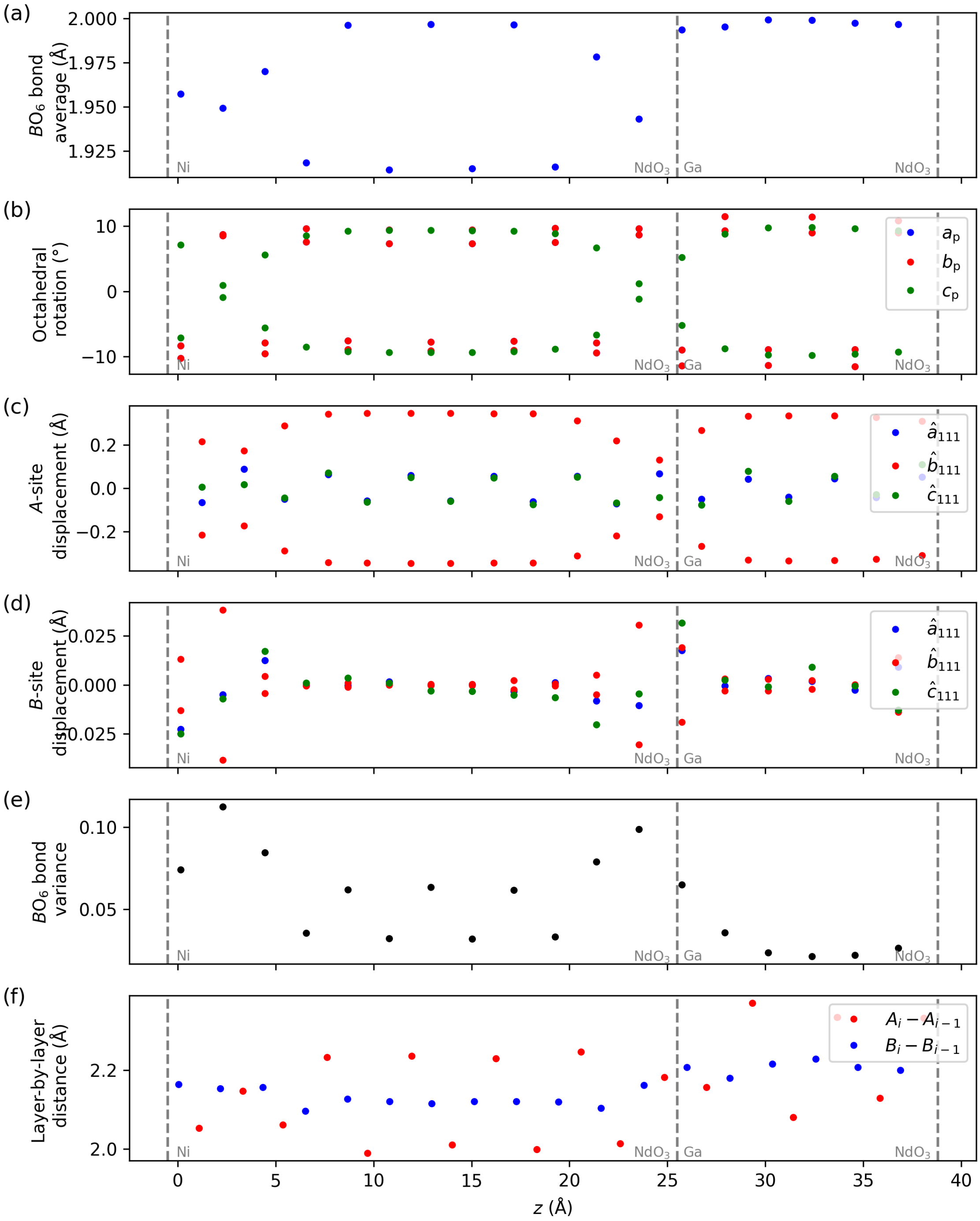

Figure C.5: Further structural properties of 120-atom NNO-NGO as a function of z (direction along $\hat{c}_{111}$), where (a)—(f) are equivalent to Fig. C.2.

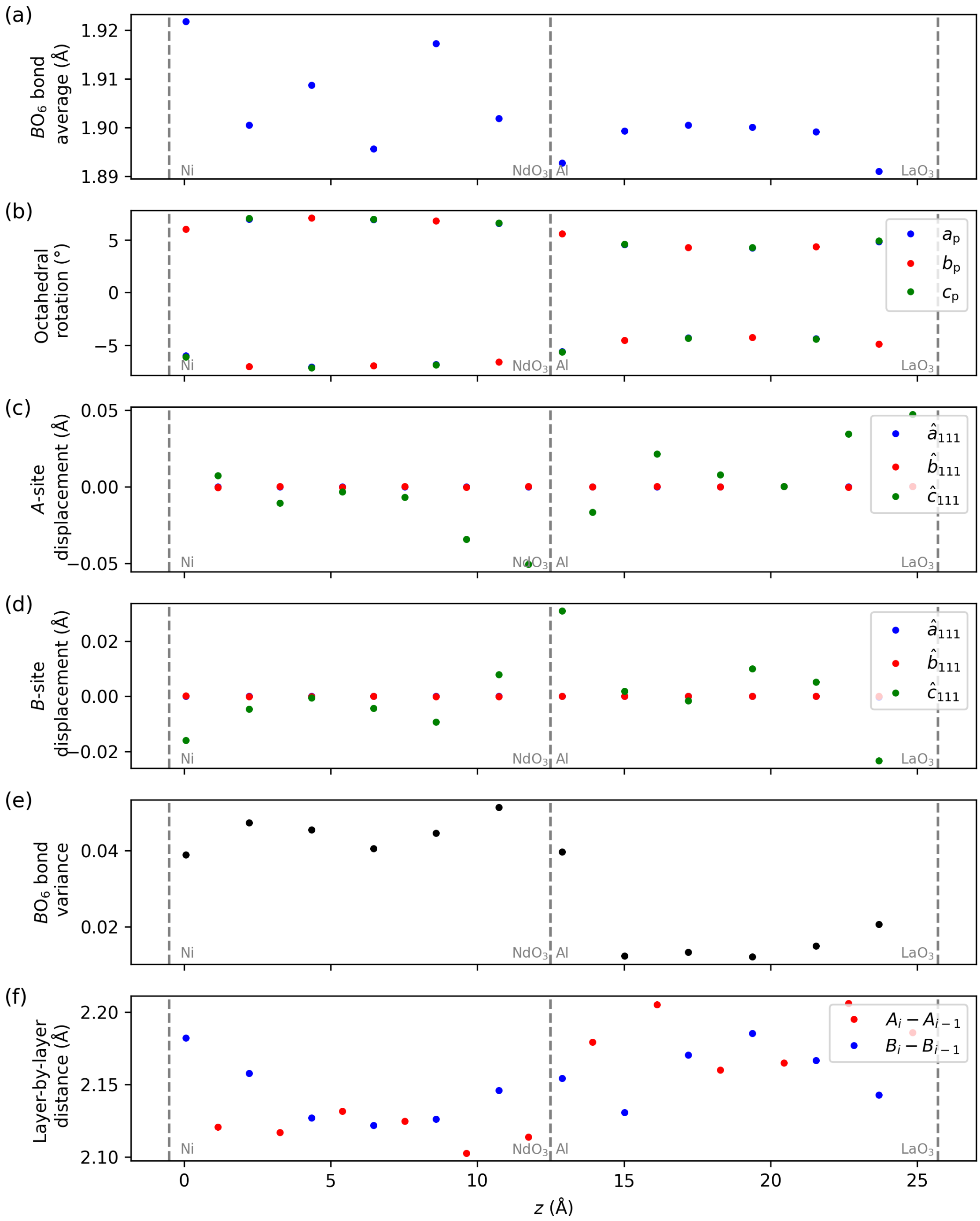

Figure C.6: Further structural properties of 60-atom NNO-LAO as a function of z (direction along $\hat{c}_{111}$), where (a)—(f) are equivalent to Fig. C.2.

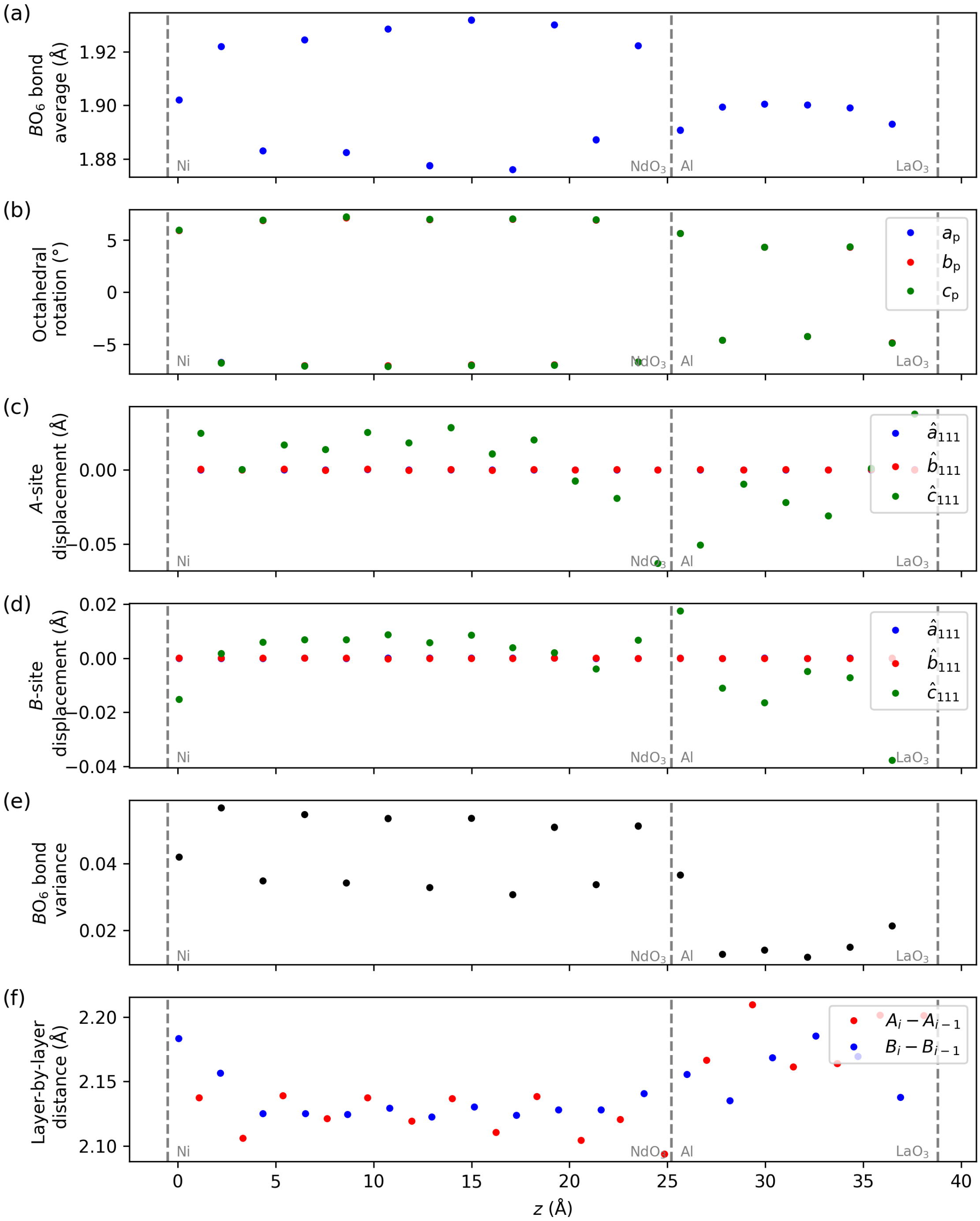

Figure C.7: Further structural properties of 120-atom NNO-LAO as a function of z (direction along $\hat{c}_{111}$), where (a)—(f) are equivalent to Fig. C.2.

APPENDIX D

[001]-oriented NGO- and LAO-NNO interfaces

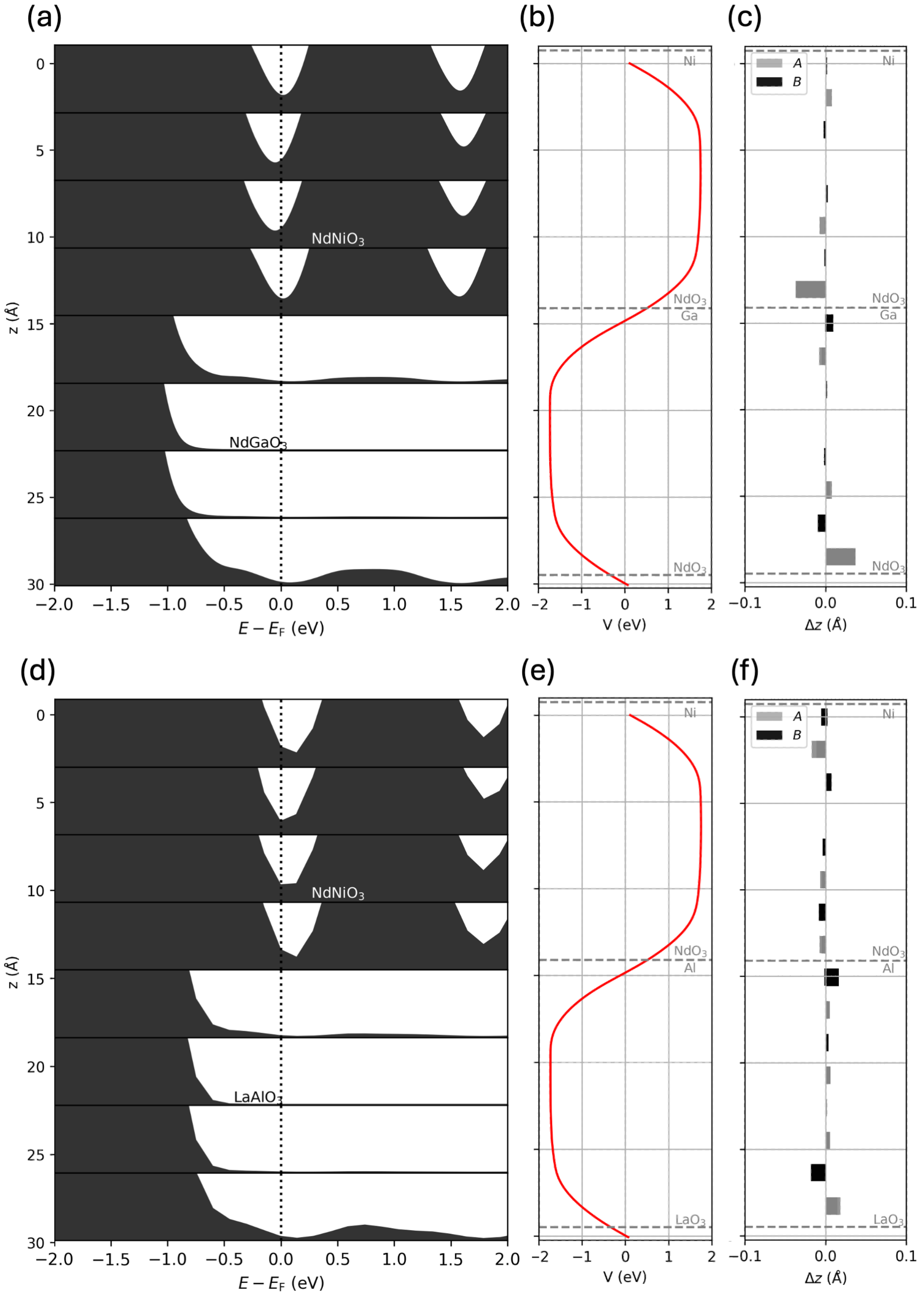

Figure D.1: Properties of [001]-oriented NGO- and LAO-NNO interfaced systems. Layer PDOS (where each layer has formula $4ABO_3$), MAP and A-, B-site displacements along $\hat{c}_{001}$ as a function of z (direction along $\hat{c}_{001}$) for (a)—(c) NGO-NNO, and (d)—(f) LAO-NNO.

Bibliography

[1] G. E. Moore *et al.*, “Cramming more components onto integrated circuits,” 1965. 1

[2] P. Zubko, S. Gariglio, M. Gabay, P. Ghosez, and J.-M. Triscone, “Interface physics in complex oxide heterostructures,” *Annu. Rev. Condens. Matter Phys.*, vol. 2, no. 1, pp. 141–165, 2011. 1, 1.4, 1.4.1, 1.4.2

[3] S. Ismail-Beigi, F. J. Walker, A. S. Disa, K. M. Rabe, and C. H. Ahn, “Picoscale materials engineering,” *Nature Reviews Materials*, vol. 2, no. 11, pp. 1–17, 2017. 1

[4] V. Goldschmidt, “Crystal structure and chemical constitution,” *Transactions of the Faraday Society*, vol. 25, pp. 253–283, 1929. 1.1

[5] C. E. Shannon, “Communication in the presence of noise,” *Proceedings of the IRE*, vol. 37, no. 1, pp. 10–21, 1949. 1.1

[6] C. Bradley and A. Cracknell, “The mathematical theory of symmetry in solids, Clarendon,” 1972. 1.1

[7] H. T. Stokes, B. J. Campbell, and R. Cordes, “Tabulation of irreducible representations of the crystallographic space groups and their superspace extensions,” *Foundations of Crystallography*, vol. 69, no. 4, pp. 388–395, 2013. 1.1

[8] A. P. Cracknell and B. Davies, *Kronecker product tables*, vol. 4. Springer, 1979. 1.1

[9] C. J. Howard and H. T. Stokes, “Group-theoretical analysis of octahedral tilting in perovskites,” *Structural Science*, vol. 54, no. 6, pp. 782–789, 1998. 1.1

[10] C. J. Howard and H. T. Stokes, “Structures and phase transitions in perovskites–a group-theoretical approach,” *Foundations of Crystallography*, vol. 61, no. 1, pp. 93–111, 2005. 1.1

[11] M. S. Senn and N. C. Bristowe, “A group-theoretical approach to enumerating magnetoelectric and multiferroic couplings in perovskites,” *Foundations of Crystallography*, vol. 74, no. 4, pp. 308–321, 2018. 1.1

[12] R. S. Mulliken, “Intensities of electronic transitions in molecular spectra iv. cyclic dienes and hyperconjugation,” *The Journal of Chemical Physics*, vol. 7, no. 5, pp. 339–352, 1939. 1.1

[13] A. M. Glazer, “The classification of tilted octahedra in perovskites,” *Structural Science*, vol. 28, no. 11, pp. 3384–3392, 1972. 1.1

[14] P. M. Woodward, “Octahedral tilting in perovskites. i. geometrical considerations,” *Structural Science*, vol. 53, no. 1, pp. 32–43, 1997. 1.1.1

[15] P. M. Woodward, “Octahedral tilting in perovskites. ii. structure stabilizing forces,” *Structural Science*, vol. 53, no. 1, pp. 44–66, 1997. 1.1.1

[16] N. A. Benedek and C. J. Fennie, “Why are there so few perovskite ferroelectrics?,” *The Journal of Physical Chemistry C*, vol. 117, no. 26, pp. 13339–13349, 2013. 1.1.1, 1.2, 1.2.1, 4.2.2, 5.2.1, 6.2.3

[17] L. D. Landau *et al.*, “On the theory of phase transitions,” *Zh. eksp. teor. Fiz*, vol. 7, no. 19-32, p. 926, 1937. 1.1.1

[18] J. Valasek, “Piezo-electric and allied phenomena in Rochelle salt,” *Physical review*, vol. 17, no. 4, p. 475, 1921. 1.2

[19] H. F. Kay and P. Vousden, “Xcv. symmetry changes in barium titanate at low temperatures and their relation to its ferroelectric properties,” *The London, Edinburgh, and Dublin Philosophical Magazine and Journal of Science*, vol. 40, no. 309, pp. 1019–1040, 1949. 1.2

[20] A. Von Hippel, “Ferroelectricity, domain structure, and phase transitions of barium titanate,” *Reviews of Modern Physics*, vol. 22, no. 3, p. 221, 1950. 1.2

[21] J. F. Scott and C. A. Paz de Araujo, “Ferroelectric memories,” *Science*, vol. 246, no. 4936, pp. 1400–1405, 1989. 1.2

[22] O. Auciello, J. F. Scott, and R. Ramesh, “The physics of ferroelectric memories,” *Physics today*, vol. 51, no. 7, pp. 22–27, 1998. 1.2

[23] C. A.-P. de Araujo, J. Cuchiaro, L. McMillan, M. Scott, and J. Scott, “Fatigue-free ferroelectric capacitors with platinum electrodes,” *Nature*, vol. 374, no. 6523, pp. 627–629, 1995. 1.2

[24] K. Sugibuchi, Y. Kurogi, and N. Endo, “Ferroelectric field-effect memory device using $Bi_4Ti_3O_12$ film,” *Journal of Applied Physics*, vol. 46, no. 7, pp. 2877–2881, 1975. 1.2

[25] S. Mathews, R. Ramesh, T. Venkatesan, and J. Benedetto, “Ferroelectric field effect transistor based on epitaxial perovskite heterostructures,” *Science*, vol. 276, no. 5310, pp. 238–240, 1997. 1.2

[26] E. Y. Tsymbal and H. Kohlstedt, "Tunneling across a ferroelectric," *Science*, vol. 313, no. 5784, pp. 181–183, 2006. 1.2

[27] P. Blom, R. Wolf, J. Cillessen, and M. Krijn, "Ferroelectric schottky diode," *Physical review letters*, vol. 73, no. 15, p. 2107, 1994. 1.2

[28] R. E. Cohen, "Origin of ferroelectricity in perovskite oxides," *Nature*, vol. 358, no. 6382, pp. 136–138, 1992. 1.2, 3.1

[29] R. G. Pearson, "The second-order Jahn-Teller effect," *Journal of Molecular Structure: THEOCHEM*, vol. 103, pp. 25–34, 1983. 1.2

[30] U. Aschauer and N. A. Spaldin, "Competition and cooperation between antiferrodistortive and ferroelectric instabilities in the model perovskite $SrTiO_3$," *Journal of Physics: Condensed Matter*, vol. 26, no. 12, p. 122203, 2014. 1.2, 2, 3.2.1, 3.2.2, 5.2.1

[31] T. Gu, T. Scarbrough, Y. Yang, J. Íñiguez, L. Bellaiche, and H. J. Xiang, "Cooperative couplings between octahedral rotations and ferroelectricity in perovskites and related materials," *Phys. Rev. Lett.*, vol. 120, p. 197602, May 2018. 2, 4.2.3, 5.2.1

[32] V. Torgashev, V. Shirokov, A. Prokhorov, and L. Shuvalov, "Competition between rotational and polar structural distortions in perovskites," *Crystallography Reports*, vol. 50, pp. 637–645, 2005. 1.2, 3.2.1, 4.2.2

[33] A. Devonshire, "Theory of ferroelectrics," *Advances in physics*, vol. 3, no. 10, pp. 85–130, 1954. 1.2.1, 1.4.1, 1.4.5

[34] N. Pertsev, A. Tagantsev, and N. Setter, "Phase transitions and strain-induced ferroelectricity in $SrTiO_3$ epitaxial thin films," *Physical review B*, vol. 61, no. 2, p. R825, 2000. 1.2.1, 1.4.1, 1.5.1, 3.1, 3.2.2, 3.2.2

[35] H. Weaver, "Dielectric properties of single crystals of $SrTiO_3$ at low temperatures," *Journal of Physics and Chemistry of Solids*, vol. 11, no. 3-4, pp. 274–277, 1959. 1.2.1, 3.1, 3.2.1

[36] K. A. Müller and H. Burkard, "$SrTiO_3$: An intrinsic quantum paraelectric below 4 K," *Phys. Rev. B*, vol. 19, pp. 3593–3602, Apr 1979. 1.2.1, 3.1

[37] J. Kiat and T. Roisnel, "Rietveld analysis of strontium titanate in the Müller state," *Journal of Physics: Condensed Matter*, vol. 8, no. 19, p. 3471, 1996. 1.2.1, 3.1, 3.2.1, 3.2.1

[38] W. Zhong and D. Vanderbilt, "Effect of quantum fluctuations on structural phase transitions in $SrTiO_3$ and $BaTiO_3$," *Physical Review B*, vol. 53, no. 9, p. 5047, 1996. 1.2.1, 3.1, 3.2.2

[39] D. Shin, S. Latini, C. Schäfer, S. A. Sato, U. De Giovannini, H. Hübener, and A. Rubio, "Quantum paraelectric phase of $SrTiO_3$ from first principles," *Physical Review B*, vol. 104, no. 6, p. L060103, 2021. 1.2.1, 3.1

[40] S. Saha, T. Sinha, and A. Mookerjee, "Structural and optical properties of paraelectric $SrTiO_3$," *Journal of Physics: Condensed Matter*, vol. 12, no. 14, p. 3325, 2000. 1.2.1, 3.1, 3.2.1

[41] K. van Benthem, C. Elsässer, and R. H. French, "Bulk electronic structure of $SrTiO_3$: Experiment and theory," *Journal of Applied Physics*, vol. 90, pp. 6156–6164, 2001. 1.2.1, 3.1, 3.2.1

[42] S. Piskunov, E. Heifets, R. Eglitis, and G. Borstel, "Bulk properties and electronic structure of $SrTiO_3$, $BaTiO_3$, $PbTiO_3$ perovskites: an ab initio HF/DFT study," *Computational Materials Science*, vol. 29, no. 2, pp. 165–178, 2004. 1.2.1, 3.1, 3.2.1

[43] N. Sai and D. Vanderbilt, "First-principles study of ferroelectric and antiferrodistortive instabilities in tetragonal $SrTiO_3$," *Physical Review B*, vol. 62, no. 21, p. 13942, 2000. 1.2.1, 1.5.1, 3.1

[44] J. Haeni, P. Irvin, W. Chang, R. Uecker, P. Reiche, Y. Li, S. Choudhury, W. Tian, M. Hawley, B. Craigo, *et al.*, "Room-temperature ferroelectricity in strained $SrTiO_3$," *Nature*, vol. 430, no. 7001, pp. 758–761, 2004. 1.2.1, 1.5.1, 3.1, 3.2.2, 3.2.2

[45] T. Yamada, B. W.-v. Eerd, O. Sakata, A. K. Tagantsev, H. Morioka, Y. Ehara, S. Yasui, H. Funakubo, T. Nagasaki, and H. Trodahl, "Phase transitions associated with competing order parameters in compressively strained $SrTiO_3$ thin films," *Physical Review B*, vol. 91, no. 21, p. 214101, 2015. 1.2.1, 1.5.1, 3.1, 3.2.2

[46] T. Yamada, J. Petzelt, A. Tagantsev, S. Denisov, D. Noujni, P. Petrov, A. Mackova, K. Fujito, T. Kiguchi, K. Shinozaki, *et al.*, "In-plane and out-of-plane ferroelectric instabilities in epitaxial $SrTiO_3$ films," *Physical review letters*, vol. 96, no. 15, p. 157602, 2006. 1.2.1, 3.1

[47] T. Mitsui and W. B. Westphal, "Dielectric and x-ray studies of $Ca_xBa_{1-x}TiO_3$ and $Ca_xSr_{1-x}TiO_3$," *Physical Review*, vol. 124, no. 5, p. 1354, 1961. 1.2.1, 3.1

[48] J. Bednorz and K. Müller, "$Sr_{1-x}Ca_xTiO_3$: an xy quantum ferroelectric with transition to randomness," *Physical Review Letters*, vol. 52, no. 25, p. 2289, 1984. 1.2.1, 3.1

[49] A. Chen, Z. Yu, J. Scott, A. Loidl, R. Guo, A. Bhalla, and L. Cross, "Dielectric polarization processes in Bi:$SrTiO_3$," *Journal of Physics and Chemistry of Solids*, vol. 61, no. 2, pp. 191–196, 2000. 1.2.1, 3.1

[50] M. Itoh, R. Wang, Y. Inaguma, T. Yamaguchi, Y. Shan, and T. Nakamura, "Ferroelectricity induced by oxygen isotope exchange in strontium titanate perovskite," *Physical Review Letters*, vol. 82, no. 17, p. 3540, 1999. 1.2.1, 3.1

[51] D. Lee, H. Lu, Y. Gu, S.-Y. Choi, S.-D. Li, S. Ryu, T. Paudel, K. Song, E. Mikheev, S. Lee, *et al.*, "Emergence of room-temperature ferroelectricity at

reduced dimensions," *Science*, vol. 349, no. 6254, pp. 1314–1317, 2015. 1.2.1, 1.5.1, 3.1

[52] K. Klyukin and V. Alexandrov, "Effect of intrinsic point defects on ferroelectric polarization behavior of $SrTiO_3$," *Physical Review B*, vol. 95, no. 3, p. 035301, 2017. 1.2.1, 3.1

[53] H. Jang, A. Kumar, S. Denev, M. D. Biegalski, P. Maksymovych, C. Bark, C. T. Nelson, C. Folkman, S. H. Baek, N. Balke, *et al.*, "Ferroelectricity in strain-free $SrTiO_3$ thin films," *Physical review letters*, vol. 104, no. 19, p. 197601, 2010. 1.2.1, 3.1

[54] W. Burke and R. Pressley, "Stress induced ferroelectricity in $SrTiO_3$," *Solid State Communications*, vol. 9, no. 3, pp. 191–195, 1971. 1.2.1, 3.1

[55] H. Uwe and T. Sakudo, "Stress-induced ferroelectricity and soft phonon modes in $SrTiO_3$," *Phys. Rev. B*, vol. 13, pp. 271–286, Jan 1976. 1.2.1, 3.1

[56] R. Xu, J. Huang, E. S. Barnard, S. S. Hong, P. Singh, E. K. Wong, T. Jansen, V. Harbola, J. Xiao, B. Y. Wang, *et al.*, "Strain-induced room-temperature ferroelectricity in $SrTiO_3$ membranes," *Nature communications*, vol. 11, no. 1, p. 3141, 2020. 1.2.1, 1.5.1, 3.1

[57] R. Haislmaier, R. Engel-Herbert, and V. Gopalan, "Stoichiometry as key to ferroelectricity in compressively strained $SrTiO_3$ films," *Applied Physics Letters*, vol. 109, no. 3, 2016. 1.2.1, 1.5.1, 3.1, 3.2.2

[58] H. Tabata, H. Tanaka, and T. Kawai, "Formation of artificial $BaTiO_3/SrTiO_3$ superlattices using pulsed laser deposition and their dielectric properties," *Applied physics letters*, vol. 65, no. 15, pp. 1970–1972, 1994. 1.2.1, 1.5.1, 3.1

[59] Y. Li, S. Hu, D. Tenne, A. Soukiassian, D. G. Schlom, X. Xi, K. J. Choi, C.-B. Eom, A. Saxena, T. Lookman, *et al.*, "Prediction of ferroelectricity in $BaTiO_3$/ $SrTiO_3$ superlattices with domains," *Applied Physics Letters*, vol. 91, no. 11, 2007. 1.2.1, 1.5.1, 3.1

[60] P. Zubko, N. Jecklin, N. Stucki, C. Lichtensteiger, G. Rispens, and J.-M. Triscone, "Ferroelectric domains in $PbTiO_3/SrTiO_3$ superlattices," *Ferroelectrics*, vol. 433, no. 1, pp. 127–137, 2012. 1.2.1, 1.5.1, 3.1

[61] Q. Li, C. Nelson, S.-L. Hsu, A. Damodaran, L.-L. Li, A. Yadav, M. McCarter, L. Martin, R. Ramesh, and S. Kalinin, "Quantification of flexoelectricity in $PbTiO_3/SrTiO_3$ superlattice polar vortices using machine learning and phase-field modeling," *Nature communications*, vol. 8, no. 1, p. 1468, 2017. 1.2.1, 1.5.1, 3.1

[62] A. Sirenko, C. Bernhard, A. Golnik, A. M. Clark, J. Hao, W. Si, and X. Xi, "Soft-mode hardening in $SrTiO_3$ thin films," *Nature*, vol. 404, no. 6776, pp. 373–376, 2000. 1.2.1, 1.5.1, 3.1

[63] A. Ohtomo and H. Hwang, “A high-mobility electron gas at the $LaAlO_3/SrTiO_3$ heterointerface,” *Nature*, vol. 427, no. 6973, pp. 423–426, 2004. 1.2.1, 1.5.1, 3.1, 5.1, 6.2.4

[64] H. Unoki and T. Sakudo, “Electron spin resonance of Fe^{3+} in $SrTiO_3$ with special reference to the 110 K phase transition,” *Journal of the Physical Society of Japan*, vol. 23, no. 3, pp. 546–552, 1967. 1.2.1, 3.2.1, 3.2.2

[65] J. Zaanen, G. Sawatzky, and J. Allen, “Band gaps and electronic structure of transition-metal compounds,” *Physical review letters*, vol. 55, no. 4, p. 418, 1985. 1.3, 1.3.1

[66] J. B. Torrance, P. Lacorre, C. Asavaroengchai, and R. M. Metzger, “Why are some oxides metallic, while most are insulating?,” *Physica C: Superconductivity*, vol. 182, no. 4-6, pp. 351–364, 1991. 1.3

[67] T. Arima, Y. Tokura, and J. Torrance, “Variation of optical gaps in perovskite-type $3d$ transition-metal oxides,” *Physical Review B*, vol. 48, no. 23, p. 17006, 1993. 1.3

[68] J. Torrance, P. Lacorre, A. Nazzal, E. Ansaldo, and C. Niedermayer, “Systematic study of insulator-metal transitions in perovskites $R\mathrm{NiO}_3$ (R = Pr, Nd, Sm, Eu) due to closing of charge-transfer gap,” *Physical Review B*, vol. 45, no. 14, p. 8209, 1992. 1.3.1

[69] K. Sreedhar, J. Honig, M. Darwin, M. McElfresh, P. Shand, J. Xu, B. Crooker, and J. Spalek, “Electronic properties of the metallic perovskite $LaNiO_3$: Correlated behavior of $3d$ electrons,” *Physical Review B*, vol. 46, no. 10, p. 6382, 1992. 1.3.1, 4.1, 4.2.1

[70] J. B. Torrance, P. Lacorre, A. I. Nazzal, E. J. Ansaldo, and C. Niedermayer, “Systematic study of insulator-metal transitions in perovskites $R\mathrm{NiO}_3$ (R=Pr,Nd,Sm,Eu) due to closing of charge-transfer gap,” *Phys. Rev. B*, vol. 45, pp. 8209–8212, Apr 1992. 1.3.1, 4.1, 4.2.1

[71] M. Imada, A. Fujimori, and Y. Tokura, “Metal-insulator transitions,” *Reviews of modern physics*, vol. 70, no. 4, p. 1039, 1998. 1.3.1, 4.1

[72] F. Hund, “Zur deutung der molekelspektren. i,” *Zeitschrift für Physik*, vol. 40, no. 10, pp. 742–764, 1927. 1.3.1

[73] C. J. Ballhausen, “Introduction to ligand field theory,” *(No Title)*, 1962. 1.3.1

[74] A. Mercy, J. Bieder, J. Íñiguez, and P. Ghosez, “Structurally triggered metal-insulator transition in rare-earth nickelates,” *Nature communications*, vol. 8, no. 1, p. 1677, 2017. 1.3.1, 1.4.4, 4.1, 4.2.2, 4.2.2, 4.2.3

[75] I. Mazin, D. Khomskii, R. Lengsdorf, J. Alonso, W. Marshall, R. Ibberson, A. Podlesnyak, M. Martínez-Lope, and M. Abd-Elmeguid, “Charge ordering as alternative to jahn-teller distortion,” *Physical review letters*, vol. 98, no. 17, p. 176406, 2007. 1.3.1

[76] T. Mizokawa, D. Khomskii, and G. Sawatzky, “Spin and charge ordering in self-doped Mott insulators,” *Physical Review B*, vol. 61, no. 17, p. 11263, 2000. 1.3.1, 6.2.2

[77] H. Park, A. J. Millis, and C. A. Marianetti, “Site-selective Mott transition in rare-earth-element nickelates,” *Physical review letters*, vol. 109, no. 15, p. 156402, 2012. 1.3.1, 6.2.2

[78] S. Johnston, A. Mukherjee, I. Elfimov, M. Berciu, and G. A. Sawatzky, “Charge disproportionation without charge transfer in the rare-earth-element nickelates as a possible mechanism for the metal-insulator transition,” *Physical review letters*, vol. 112, no. 10, p. 106404, 2014. 1.3.1, 6.2.2

[79] A. Subedi, O. E. Peil, and A. Georges, “Low-energy description of the metal-insulator transition in the rare-earth nickelates,” *Physical Review B*, vol. 91, no. 7, p. 075128, 2015. 1.3.1, 6.2.2

[80] J. Varignon, M. N. Grisolia, J. Íñiguez, A. Barthélémy, and M. Bibes, “Complete phase diagram of rare-earth nickelates from first-principles,” *npj Quantum Materials*, vol. 2, no. 1, p. 21, 2017. 1.3.1, 1.4.4, 4.1, 4.2.1, 4.2.1, 6.2.2

[81] J. L. García-Muñoz, J. Rodríguez-Carvajal, P. Lacorre, and J. B. Torrance, “Neutron-diffraction study of $R\mathrm{NiO}_3$ (R=La,Pr,Nd,Sm): Electronically induced structural changes across the metal-insulator transition,” *Phys. Rev. B*, vol. 46, pp. 4414–4425, Aug 1992. 1.3.1, 4.1

[82] J. A. Alonso, M. J. Martínez-Lope, M. T. Casais, J. L. García-Muñoz, and M. T. Fernández-Díaz, “Room-temperature monoclinic distortion due to charge disproportionation in $R\mathrm{NiO}_3$ perovskites with small rare-earth cations (R = Ho, Y, Er, Tm, Yb, and Lu): A neutron diffraction study,” *Phys. Rev. B*, vol. 61, pp. 1756–1763, Jan 2000. 1.3.1, 4.1

[83] J. A. Alonso, M. J. Martinez-Lope, M. T. Casais, M. A. Aranda, and M. T. Fernandez-Diaz, “Metal- insulator transitions, structural and microstructural evolution of $R\mathrm{NiO}_3$ (R = Sm, Eu, Gd, Dy, Ho, Y) perovskites: evidence for room-temperature charge disproportionation in monoclinic HoNiO_3 and YNiO_3,” *Journal of the American Chemical Society*, vol. 121, no. 20, pp. 4754–4762, 1999. 1.3.1, 4.1

[84] J. García-Muñoz, M. Aranda, J. Alonso, and M. Martínez-Lope, “Structure and charge order in the antiferromagnetic band-insulating phase of NdNiO_3,” *Physical Review B—Condensed Matter and Materials Physics*, vol. 79, no. 13, p. 134432, 2009. 1.3.1, 4.1, 4.2.1

[85] T. Mizokawa and A. Fujimori, “Electronic structure and orbital ordering in perovskite-type 3d transition-metal oxides studied by Hartree-Fock band-structure calculations,” *Physical Review B*, vol. 54, no. 8, p. 5368, 1996. 1.3.1

[86] J. B. Goodenough and J.-S. Zhou, “Orbital ordering in orthorhombic perovskites,” *Journal of Materials Chemistry*, vol. 17, no. 23, pp. 2394–2405, 2007. 1.3.1

[87] A. Blanca-Romero and R. Pentcheva, “Confinement-induced metal-to-insulator transition in strained $\mathrm{LaNiO_3/LaAlO_3}$ superlattices,” *Physical Review B—Condensed Matter and Materials Physics*, vol. 84, no. 19, p. 195450, 2011. 1.3.1, 1.4.3, 1.5.2, 4.2.2, 6.1

[88] J. Shi, S. D. Ha, Y. Zhou, F. Schoofs, and S. Ramanathan, “A correlated nickelate synaptic transistor,” *Nature communications*, vol. 4, no. 1, p. 2676, 2013. 1.3.1, 4.1

[89] H.-T. Zhang, T. J. Park, A. N. Islam, D. S. Tran, S. Manna, Q. Wang, S. Mondal, H. Yu, S. Banik, S. Cheng, *et al.*, “Reconfigurable perovskite nickelate electronics for artificial intelligence,” *Science*, vol. 375, no. 6580, pp. 533–539, 2022. 1.3.1, 4.1

[90] Z. Zhang, D. Schwanz, B. Narayanan, M. Kotiuga, J. A. Dura, M. Cherukara, H. Zhou, J. W. Freeland, J. Li, R. Sutarto, *et al.*, “Perovskite nickelates as electric-field sensors in salt water,” *Nature*, vol. 553, no. 7686, pp. 68–72, 2018. 1.3.1, 4.1

[91] R. Jaramillo, S. D. Ha, D. Silevitch, and S. Ramanathan, “Origins of bad-metal conductivity and the insulator–metal transition in the rare-earth nickelates,” *Nature Physics*, vol. 10, no. 4, pp. 304–307, 2014. 1.3.1, 4.1

[92] J. García-Muñoz, J. Rodríguez-Carvajal, and P. Lacorre, “Sudden appearance of an unusual spin density wave at the metal-insulator transition in the perovskites $R\mathrm{NiO_3}$ (R = Pr, Nd),” *Europhysics Letters*, vol. 20, no. 3, p. 241, 1992. 1.3.1, 4.1

[93] J. L. García-Muñoz, J. Rodríguez-Carvajal, and P. Lacorre, “Neutron-diffraction study of the magnetic ordering in the insulating regime of the perovskites $R\mathrm{NiO_3}$ (R =Pr and Nd),” *Phys. Rev. B*, vol. 50, pp. 978–992, Jul 1994. 1.3.1, 4.1

[94] G. Giovannetti, S. Kumar, D. Khomskii, S. Picozzi, and J. van den Brink, “Multiferroicity in rare-earth nickelates $R\mathrm{NiO_3}$,” *Phys. Rev. Lett.*, vol. 103, p. 156401, Oct 2009. 1.3.1, 4.1

[95] V. L. Ginzburg, V. L. Ginzburg, and L. Landau, *On the theory of superconductivity.* Springer, 2009. 1.4.1, 1.4.2

[96] M. Moreau, A. Marthinsen, S. M. Selbach, and T. Tybell, “Strain-phonon coupling in (111)-oriented perovskite oxides,” *Phys. Rev. B*, vol. 96, p. 094109, Sep 2017. 1.4.1, 1.5.1, 3.1, 4.1, 4.2.2

[97] A. Saha and T. Birol, “Effect of (001) and (111) epitaxial strain on *Pnma* perovskite oxides,” *Physical Review Materials*, vol. 8, no. 9, p. 094412, 2024. 1.4.1, 4.1

[98] T. Kim, D. Puggioni, Y. Yuan, L. Xie, H. Zhou, N. Campbell, P. Ryan, Y. Choi, J.-W. Kim, J. Patzner, *et al.*, “Polar metals by geometric design,”

Nature, vol. 533, no. 7601, pp. 68–72, 2016. 1.4.2, 1.5.2, 4.1, 4.2.3, 5.2.1, 6.1, 6.2.5, 6.2.5

[99] B. Halperin, T. Lubensky, and S.-k. Ma, "First-order phase transitions in superconductors and smectic-a liquid crystals," *Physical Review Letters*, vol. 32, no. 6, p. 292, 1974. 1.4.2

[100] F. Schulte, "A theory of thin metal films: electron density, potentials and work function," *Surface Science*, vol. 55, no. 2, pp. 427–444, 1976. 1.4.3

[101] S. Prosandeev, L. Bellaiche, and J. Íñiguez, "Ab initio study of the factors affecting the ground state of rare-earth nickelates," *Phys. Rev. B*, vol. 85, p. 214431, Jun 2012. 1.4.4, 1.5.2, 4.1, 4.2.1, 4.2.2, 4.2.2, 4.2.2

[102] N. Nakagawa, H. Y. Hwang, and D. A. Muller, "Why some interfaces cannot be sharp," *Nature materials*, vol. 5, no. 3, pp. 204–209, 2006. 1.4.5, 5.1

[103] M. Stengel and D. Vanderbilt, "Berry-phase theory of polar discontinuities at oxide-oxide interfaces," *Physical Review B—Condensed Matter and Materials Physics*, vol. 80, no. 24, p. 241103, 2009. 1.4.5, 1.4.5, 1.5.1, 5.1

[104] N. Bristowe, E. Artacho, and P. Littlewood, "Oxide superlattices with alternating p and n interfaces," *Physical Review B—Condensed Matter and Materials Physics*, vol. 80, no. 4, p. 045425, 2009. 1.4.5, 1.5.1, 5.1

[105] M. Stengel, P. Aguado-Puente, N. A. Spaldin, and J. Junquera, "Band alignment at metal/ferroelectric interfaces: Insights and artifacts from first principles," *Physical Review B—Condensed Matter and Materials Physics*, vol. 83, no. 23, p. 235112, 2011. 1.4.5, 5.1, 5.2.3

[106] N. Bristowe, P. Littlewood, and E. Artacho, "The net charge at interfaces between insulators," *Journal of Physics: Condensed Matter*, vol. 23, no. 8, p. 081001, 2011. 1.4.5, 5.2.2

[107] C.-H. Lin, C.-M. Huang, and G. Guo, "Systematic ab initio study of the phase diagram of epitaxially strained $SrTiO_3$," *Journal of applied physics*, vol. 100, no. 8, 2006. 1.5.1, 3.2.2, 4.2.2

[108] A. Erba, K. E. El-Kelany, M. Ferrero, I. Baraille, and M. Rérat, "Piezoelectricity of $SrTiO_3$: An ab initio description," *Physical Review B—Condensed Matter and Materials Physics*, vol. 88, no. 3, p. 035102, 2013. 1.5.1

[109] S. E. Reyes-Lillo, K. M. Rabe, and J. B. Neaton, "Ferroelectricity in [111]-oriented epitaxially strained $SrTiO_3$ from first principles," *Physical Review Materials*, vol. 3, no. 3, p. 030601, 2019. 1.5.1, 3.2.3, 3.2.3

[110] Y. Liang, W. Li, S. Zhang, C. Lin, C. Li, Y. Yao, Y. Li, H. Yang, and J. Guo, "Homoepitaxial $SrTiO_3$ (111) film with high dielectric performance and atomically well-defined surface," *Scientific Reports*, vol. 5, no. 1, p. 10634, 2015. 1.5.1, 3.2.3

[111] S. Thiel, G. Hammerl, A. Schmehl, C. W. Schneider, and J. Mannhart, "Tunable quasi-two-dimensional electron gases in oxide heterostructures," *Science*, vol. 313, no. 5795, pp. 1942–1945, 2006. 1.5.1, 5.1

[112] A. Brinkman, M. Huijben, M. Van Zalk, J. Huijben, U. Zeitler, J. Maan, W. G. van der Wiel, G. Rijnders, D. H. Blank, and H. Hilgenkamp, "Magnetic effects at the interface between non-magnetic oxides," *Nature materials*, vol. 6, no. 7, pp. 493–496, 2007. 1.5.1, 5.1, 6.2.4

[113] A. Caviglia, M. Gabay, S. Gariglio, N. Reyren, C. Cancellieri, and J.-M. Triscone, "Tunable Rashba spin-orbit interaction at oxide interfaces," *Physical review letters*, vol. 104, no. 12, p. 126803, 2010. 1.5.1, 5.1

[114] N. Reyren, S. Thiel, A. Caviglia, L. F. Kourkoutis, G. Hammerl, C. Richter, C. W. Schneider, T. Kopp, A.-S. Ruetschi, D. Jaccard, *et al.*, "Superconducting interfaces between insulating oxides," *Science*, vol. 317, no. 5842, pp. 1196–1199, 2007. 1.5.1, 5.1, 6.2.4

[115] L. Li, C. Richter, J. Mannhart, and R. C. Ashoori, "Coexistence of magnetic order and two-dimensional superconductivity at $LaAlO_3/SrTiO_3$ interfaces," *Nature physics*, vol. 7, no. 10, pp. 762–766, 2011. 1.5.1, 5.1

[116] E. Kane, "Zener tunneling in semiconductors," *Journal of Physics and Chemistry of Solids*, vol. 12, no. 2, pp. 181–188, 1960. 1.5.1, 6.2.4

[117] P. Han, K.-j. Jin, H.-b. Lu, Q.-L. Zhou, Y.-L. Zhou, and G.-Z. Yang, "The mechanism study on transport properties in perovskite oxide pn junctions," *Applied Physics Letters*, vol. 91, no. 18, 2007. 1.5.1, 6.2.4

[118] G. Herranz, F. Sánchez, N. Dix, M. Scigaj, and J. Fontcuberta, "High mobility conduction at (110) and (111) $LaAlO_3/SrTiO_3$ interfaces," *Scientific reports*, vol. 2, no. 1, p. 758, 2012. 1.5.1, 6.2.4

[119] A. Monteiro, D. Groenendijk, I. Groen, J. de Bruijckere, R. Gaudenzi, H. Van Der Zant, and A. Caviglia, "Two-dimensional superconductivity at the (111) $LaAlO_3/SrTiO_3$ interface," *Physical Review B*, vol. 96, no. 2, p. 020504, 2017. 1.5.1, 6.2.4

[120] S. Davis, Z. Huang, K. Han, Ariando, T. Venkatesan, and V. Chandrasekhar, "Magnetoresistance in the superconducting state at the (111) $LaAlO_3/SrTiO_3$ interface," *Physical Review B*, vol. 96, no. 13, p. 134502, 2017. 1.5.1, 6.2.4

[121] C. A.-P. de Araujo, J. Cuchiaro, L. McMillan, M. Scott, and J. Scott, "Fatigue-free ferroelectric capacitors with platinum electrodes," *Nature*, vol. 374, no. 6523, pp. 627–629, 1995. 1.5.1, 5.1

[122] I. P. Batra and B. Silverman, "Thermodynamic stability of thin ferroelectric films," *Solid state communications*, vol. 11, no. 1, pp. 291–294, 1972. 1.5.1

[123] R. Mehta, B. Silverman, and J. Jacobs, “Depolarization fields in thin ferroelectric films,” *Journal of Applied Physics*, vol. 44, no. 8, pp. 3379–3385, 1973. 1.5.1

[124] P. Wurfel and I. Batra, “Depolarization-field-induced instability in thin ferroelectric films—experiment and theory,” *Physical Review B*, vol. 8, no. 11, p. 5126, 1973. 1.5.1

[125] J. Junquera and P. Ghosez, “Critical thickness for ferroelectricity in perovskite ultrathin films,” *Nature*, vol. 422, no. 6931, pp. 506–509, 2003. 1.5.1, 5.1

[126] G. Gerra, A. Tagantsev, and N. Setter, “Ferroelectricity in asymmetric metal-ferroelectric-metal heterostructures: A combined first-principles–phenomenological approach,” *Physical review letters*, vol. 98, no. 20, p. 207601, 2007. 1.5.1, 5.1, 5.2.2

[127] G. Catalan, R. Bowman, and J. Gregg, “Metal-insulator transitions in $NdNiO_3$ thin films,” *Physical Review B*, vol. 62, no. 12, p. 7892, 2000. 1.5.2, 4.1

[128] A. Tiwari, C. Jin, and J. Narayan, “Strain-induced tuning of metal–insulator transition in $NdNiO_3$,” *Applied physics letters*, vol. 80, no. 21, pp. 4039–4041, 2002. 1.5.2, 4.1, 4.2.2

[129] S. Catalano, M. Gibert, V. Bisogni, O. Peil, F. He, R. Sutarto, M. Viret, P. Zubko, R. Scherwitzl, A. Georges, *et al.*, “Electronic transitions in strained $SmNiO_3$ thin films,” *APL materials*, vol. 2, no. 11, 2014. 1.5.2, 4.1

[130] S. Catalano, M. Gibert, V. Bisogni, F. He, R. Sutarto, M. Viret, P. Zubko, R. Scherwitzl, G. A. Sawatzky, T. Schmitt, *et al.*, “Tailoring the electronic transitions of $NdNiO_3$ films through (111) pc oriented interfaces,” *APL materials*, vol. 3, no. 6, 2015. 1.5.2, 4.1, 4.2.3, 6.1, 6.2.4, 6.2.4

[131] J. Chen, H. Hu, F. Meng, T. Yajima, L. Yang, B. Ge, X. Ke, J. Wang, Y. Jiang, and N. Chen, “Overlooked transportation anisotropies in *d*-band correlated rare-earth perovskite nickelates,” *Matter*, vol. 2, no. 5, pp. 1296–1306, 2020. 1.5.2, 4.1

[132] S. Middey, D. Meyers, D. Doennig, M. Kareev, X. Liu, Y. Cao, Z. Yang, J. Shi, L. Gu, P. J. Ryan, *et al.*, “Mott electrons in an artificial graphenelike crystal of rare-earth nickelate,” *Physical review letters*, vol. 116, no. 5, p. 056801, 2016. 1.5.2, 4.1

[133] J. Hwang, J. Son, J. Y. Zhang, A. Janotti, C. G. Van de Walle, and S. Stemmer, “Structural origins of the properties of rare earth nickelate superlattices,” *Physical Review B—Condensed Matter and Materials Physics*, vol. 87, no. 6, p. 060101, 2013. 1.5.2

[134] B. Geisler, A. Blanca-Romero, and R. Pentcheva, “Design of n-and p-type oxide thermoelectrics in $LaNiO_3/SrTiO_3$ (001) superlattices exploiting interface polarity,” *Physical Review B*, vol. 95, no. 12, p. 125301, 2017. 1.5.2

[135] M. Saghayezhian, Z. Wang, H. Guo, Y. Zhu, E. Plummer, and J. Zhang, "Manipulating the polar mismatch at the $LaNiO_3/SrTiO_3$ (111) interface," *Physical Review B*, vol. 95, no. 16, p. 165434, 2017. 1.5.2

[136] E. Schrödinger, "An undulatory theory of the mechanics of atoms and molecules," *Physical review*, vol. 28, no. 6, p. 1049, 1926. 2.1.1

[137] M. Born and R. J. Oppenheimer, "Zur quantentheorie der molekeln," *Annalen der Physik*, 1927. 2.1.2

[138] D. R. Hartree, "The wave mechanics of an atom with a non-Coulomb central field. part i. theory and methods," in *Mathematical Proceedings of the Cambridge Philosophical Society*, vol. 24, pp. 89–110, Cambridge university press, 1928. 2.1.4

[139] D. R. Hartree, "The wave mechanics of an atom with a non-coulomb central field. part ii. some results and discussion," in *Mathematical Proceedings of the Cambridge Philosophical Society*, vol. 24, pp. 111–132, Cambridge University Press, 1928. 2.1.4

[140] W. Pauli Jr, "Zur frage der theoretischen deutung der satelliten einiger spektrallinien und ihrer beeinflussung durch magnetische felder," *Naturwissenschaften*, vol. 12, no. 37, pp. 741–743, 1924. 2.1.5

[141] J. C. Slater, "The theory of complex spectra," *Physical review*, vol. 34, no. 10, p. 1293, 1929. 2.1.5

[142] V. Fock, "Näherungsmethode zur lösung des quantenmechanischen mehrkörperproblems," *Zeitschrift für Physik*, vol. 61, pp. 126–148, 1930. 2.1.5

[143] F. Giustino, *Materials modelling using density functional theory: properties and predictions*. Oxford University Press, 2014. 2.1.5, 2.1, 2.1.12, 2.2

[144] W. Ritz, "Über eine neue methode zur lösung gewisser variationsprobleme der mathematischen physik.," 1909. 2.1.6

[145] P. Hohenberg and W. Kohn, "Inhomogeneous electron gas," *Physical review*, vol. 136, no. 3B, p. B864, 1964. 2.1.6, 2.1.7

[146] W. Kohn and L. J. Sham, "Self-consistent equations including exchange and correlation effects," *Physical review*, vol. 140, no. 4A, p. A1133, 1965. 2.1.7

[147] P. A. Dirac, "Note on exchange phenomena in the Thomas atom," in *Mathematical proceedings of the Cambridge philosophical society*, vol. 26, pp. 376–385, Cambridge University Press, 1930. 2.1.8, A.1

[148] E. Wigner and F. Seitz, "On the constitution of metallic sodium," *Physical Review*, vol. 43, no. 10, p. 804, 1933. 2.1.8

[149] J. C. Slater, "A simplification of the hartree-fock method," *Physical review*, vol. 81, no. 3, p. 385, 1951. 2.1.8, A.1

[150] D. C. Langreth and M. Mehl, “Beyond the local-density approximation in calculations of ground-state electronic properties,” *Physical Review B*, vol. 28, no. 4, p. 1809, 1983. 2.1.8

[151] J. P. Perdew, K. Burke, and M. Ernzerhof, “Generalized gradient approximation made simple,” *Phys. Rev. Lett.*, vol. 77, pp. 3865–3868, Oct 1996. 2.1.8, 2.1.8, 2.1.13, 3.1

[152] J. P. Perdew, J. Chevary, S. Vosko, K. A. Jackson, M. R. Pederson, D. Singh, and C. Fiolhais, “Erratum: Atoms, molecules, solids, and surfaces: Applications of the generalized gradient approximation for exchange and correlation,” *Physical Review B*, vol. 48, no. 7, p. 4978, 1993. 2.1.8

[153] A. D. Becke, “Density-functional thermochemistry. i. the effect of the exchange-only gradient correction,” *The Journal of chemical physics*, vol. 96, no. 3, pp. 2155–2160, 1992. 2.1.8

[154] J. P. Perdew, A. Ruzsinszky, G. I. Csonka, O. A. Vydrov, G. E. Scuseria, L. A. Constantin, X. Zhou, and K. Burke, “Restoring the density-gradient expansion for exchange in solids and surfaces,” *Physical review letters*, vol. 100, no. 13, p. 136406, 2008. 2.1.8, 2.1.13, 3.1, 3.2.2

[155] M. Ernzerhof and G. E. Scuseria, “Assessment of the Perdew–Burke–Ernzerhof exchange-correlation functional,” *The Journal of chemical physics*, vol. 110, no. 11, pp. 5029–5036, 1999. 2.1.8

[156] S. F. Yuk, K. C. Pitike, S. M. Nakhmanson, M. Eisenbach, Y. W. Li, and V. R. Cooper, “Towards an accurate description of perovskite ferroelectrics: exchange and correlation effects,” *Scientific reports*, vol. 7, no. 1, p. 43482, 2017. 2.1.8

[157] D. Langreth, B. I. Lundqvist, S. D. Chakarova-Käck, V. Cooper, M. Dion, P. Hyldgaard, A. Kelkkanen, J. Kleis, L. Kong, S. Li, *et al.*, “A density functional for sparse matter,” *Journal of Physics: Condensed Matter*, vol. 21, no. 8, p. 084203, 2009. 2.1.8

[158] A. D. Becke, “Density-functional thermochemistry. iii. the role of exact exchange,” *The Journal of chemical physics*, vol. 98, no. 7, pp. 5648–5652, 1993. 2.1.8

[159] F. Bloch, “Quantum mechanics of electrons in crystal lattices,” *Z. Phys*, vol. 52, pp. 555–600, 1928. 2.1.9

[160] G. Kresse and J. Furthmüller, “Efficient iterative schemes for ab initio total-energy calculations using a plane-wave basis set,” *Physical review B*, vol. 54, no. 16, p. 11169, 1996. 2.1.9, 3.1

[161] G. Kresse and J. Furthmüller, “Efficiency of ab-initio total energy calculations for metals and semiconductors using a plane-wave basis set,” *Computational Materials Science*, vol. 6, no. 1, pp. 15–50, 1996. 2.1.9, 3.1

[162] E. O. Brigham, *The fast Fourier transform and its applications*. Prentice-Hall, Inc., 1988. 2.1.9

[163] P. E. Blöchl, "Projector augmented-wave method," *Physical review B*, vol. 50, no. 24, p. 17953, 1994. 2.1.11, 2.1.11, 2.1.12, 3.1

[164] G. Kresse and D. Joubert, "From ultrasoft pseudopotentials to the projector augmented-wave method," *Phys. Rev. B*, vol. 59, pp. 1758–1775, Jan 1999. 2.1.11, 2.1.11, 2.1.12, 3.1

[165] H. Hellmann, *Einführung in die Quantenchemie*. Springer, 1937. 2.1.12

[166] R. P. Feynman, "Forces in molecules," *Physical review*, vol. 56, no. 4, p. 340, 1939. 2.1.12

[167] R. M. Martin, *Electronic structure: basic theory and practical methods*. Cambridge university press, 2020. 2.1.12

[168] W. Press, S. Teukolsky, W. Vetterling, and F. BP, "1992. numerical recipes in Fortran 77: the art of scientific computing," 1986. 2.1.12

[169] C. Xiao, "'VASP OPT AXIS: Stress tensor method'." `https://github.com/Chengcheng-Xiao/VASP_OPT_AXIS`. 2.1.12, 3.1

[170] B. Brandow, "Electronic structure of Mott insulators," *Advances in Physics*, vol. 26, no. 5, pp. 651–808, 1977. 2.1.13

[171] J. P. Perdew and A. Zunger, "Self-interaction correction to density-functional approximations for many-electron systems," *Physical review B*, vol. 23, no. 10, p. 5048, 1981. 2.1.13

[172] V. I. Anisimov, J. Zaanen, and O. K. Andersen, "Band theory and Mott insulators: Hubbard u instead of Stoner i," *Physical Review B*, vol. 44, no. 3, p. 943, 1991. 2.1.13

[173] A. I. Liechtenstein, V. I. Anisimov, and J. Zaanen, "Density-functional theory and strong interactions: Orbital ordering in Mott-Hubbard insulators," *Phys. Rev. B*, vol. 52, pp. R5467–R5470, Aug 1995. 2.1.13

[174] A. Shick, A. Liechtenstein, and W. Pickett, "Implementation of the LDA+U method using the full-potential linearized augmented plane-wave basis," *Physical Review B*, vol. 60, no. 15, p. 10763, 1999. 2.1.13

[175] O. Gunnarsson, O. Andersen, O. Jepsen, and J. Zaanen, "Density-functional calculation of the parameters in the Anderson model: Application to Mn in CdTe," *Physical Review B*, vol. 39, no. 3, p. 1708, 1989. 2.1.13

[176] P. Dederichs, S. Blügel, R. Zeller, and H. Akai, "Ground states of constrained systems: application to cerium impurities," *Physical review letters*, vol. 53, no. 26, p. 2512, 1984. 2.1.13

[177] M. Norman and A. Freeman, "Model supercell local-density calculations of the $3d$ excitation spectra in NiO," *Physical Review B*, vol. 33, no. 12, p. 8896, 1986. 2.1.13

[178] A. Svane and O. Gunnarsson, "Transition-metal oxides in the self-interaction–corrected density-functional formalism," *Physical review letters*, vol. 65, no. 9, p. 1148, 1990. 2.1.13

[179] I. Solovyev, P. Dederichs, and V. Anisimov, "Corrected atomic limit in the local-density approximation and the electronic structure of d impurities in Rb," *Physical Review B*, vol. 50, no. 23, p. 16861, 1994. 2.1.13

[180] S. L. Dudarev, G. A. Botton, S. Y. Savrasov, C. Humphreys, and A. P. Sutton, "Electron-energy-loss spectra and the structural stability of nickel oxide: An LSDA+U study," *Physical Review B*, vol. 57, no. 3, p. 1505, 1998. 2.1.13, 4.1, A.2

[181] U. Von Barth and L. Hedin, "A local exchange-correlation potential for the spin polarized case. i," *Journal of Physics C: Solid State Physics*, vol. 5, no. 13, p. 1629, 1972. 2.1.13

[182] H. T. Stokes and D. M. Hatch, "FINDSYM: program for identifying the space-group symmetry of a crystal," *Applied Crystallography*, vol. 38, no. 1, pp. 237–238, 2005. 2.2.1

[183] H. T. Stokes, S. v. Orden, and B. J. Campbell, "ISOSUBGROUP: an internet tool for generating isotropy subgroups of crystallographic space groups," *Journal of Applied Crystallography*, vol. 49, no. 5, pp. 1849–1853, 2016. 2.2.1, 3.1

[184] B. J. Campbell, H. T. Stokes, D. E. Tanner, and D. M. Hatch, "ISODISPLACE: a web-based tool for exploring structural distortions," *Applied Crystallography*, vol. 39, no. 4, pp. 607–614, 2006. 2.2.1

[185] D. M. Hatch and H. T. Stokes, "INVARIANTS: program for obtaining a list of invariant polynomials of the order-parameter components associated with irreducible representations of a space group," *Applied Crystallography*, vol. 36, no. 3, pp. 951–952, 2003. 2.2.1

[186] O. Diéguez, "Perovscripts, a python-based analysis tool," 2012. 2.2.1

[187] G. H. Wannier, "The structure of electronic excitation levels in insulating crystals," *Physical Review*, vol. 52, no. 3, p. 191, 1937. 2.2.2

[188] G. H. Wannier, "Dynamics of band electrons in electric and magnetic fields," *Reviews of Modern Physics*, vol. 34, no. 4, p. 645, 1962. 2.2.2

[189] E. I. Blount, "Formalisms of band theory," in *Solid state physics*, vol. 13, pp. 305–373, Elsevier, 1962. 2.2.2

[190] A. A. Mostofi, J. R. Yates, Y.-S. Lee, I. Souza, D. Vanderbilt, and N. Marzari, “wannier90: A tool for obtaining maximally-localised Wannier functions,” *Computer physics communications*, vol. 178, no. 9, pp. 685–699, 2008. 2.2.2

[191] A. A. Mostofi, J. R. Yates, G. Pizzi, Y.-S. Lee, I. Souza, D. Vanderbilt, and N. Marzari, “An updated version of wannier90: A tool for obtaining maximally-localised Wannier functions,” *Computer Physics Communications*, vol. 185, no. 8, pp. 2309–2310, 2014. 2.2.2

[192] I. Souza, N. Marzari, and D. Vanderbilt, “Maximally localized Wannier functions for entangled energy bands,” *Physical Review B*, vol. 65, no. 3, p. 035109, 2001. 2.2.2, 5.2.2

[193] N. Marzari, A. A. Mostofi, J. R. Yates, I. Souza, and D. Vanderbilt, “Maximally localized Wannier functions: Theory and applications,” *Reviews of Modern Physics*, vol. 84, no. 4, pp. 1419–1475, 2012. 2.2.2, 5.2.2

[194] R. Resta, “Theory of the electric polarization in crystals,” *Ferroelectrics*, vol. 136, no. 1, pp. 51–55, 1992. 2.2.2, 3.1

[195] R. King-Smith and D. Vanderbilt, “Theory of polarization of crystalline solids,” *Physical Review B*, vol. 47, no. 3, p. 1651, 1993. 2.2.2, 2.2.2, 2.2.2, 3.1

[196] R. Resta, “Macroscopic electric polarization as a geometric quantum phase,” *Europhysics Letters*, vol. 22, no. 2, p. 133, 1993. 2.2.2, 2.2.2, 3.1

[197] D. Vanderbilt and R. King-Smith, “Electric polarization as a bulk quantity and its relation to surface charge,” *Physical Review B*, vol. 48, no. 7, p. 4442, 1993. 2.2.2, 3.1

[198] R. King-Smith and D. Vanderbilt, “First-principles investigation of ferroelectricity in perovskite compounds,” *Physical Review B*, vol. 49, no. 9, p. 5828, 1994. 2.2.2

[199] R. Resta, “Macroscopic polarization in crystalline dielectrics: the geometric phase approach,” *Reviews of modern physics*, vol. 66, no. 3, p. 899, 1994. 2.2.2

[200] S. Baroni and R. Resta, “Ab initio calculation of the macroscopic dielectric constant in silicon,” *Physical Review B*, vol. 33, no. 10, p. 7017, 1986. 2.2.3, 2.2.3

[201] M. Gajdoš, K. Hummer, G. Kresse, J. Furthmüller, and F. Bechstedt, “Linear optical properties in the projector-augmented wave methodology,” *Phys. Rev. B*, vol. 73, p. 045112, Jan 2006. 2.2.3, 2.2.3, 3.1

[202] Y. Hinuma, G. Pizzi, Y. Kumagai, F. Oba, and I. Tanaka, “Band structure diagram paths based on crystallography,” *Computational Materials Science*, vol. 128, pp. 140–184, 2017. 2.2.4

[203] A. Togo, K. Shinohara, and I. Tanaka, “Spglib: a software library for crystal symmetry search,” *Science and Technology of Advanced Materials: Methods*, vol. 4, no. 1, p. 2384822, 2024. 2.2.4

[204] S. P. Ong, W. D. Richards, A. Jain, G. Hautier, M. Kocher, S. Cholia, D. Gunter, V. L. Chevrier, K. A. Persson, and G. Ceder, "Python Materials Genomics (pymatgen): A robust, open-source python library for materials analysis," *Computational Materials Science*, vol. 68, pp. 314–319, 2013. 2.2.4

[205] V. Wang, N. Xu, J.-C. Liu, G. Tang, and W.-T. Geng, "VASPKIT: A user-friendly interface facilitating high-throughput computing and analysis using VASP code," *Computer Physics Communications*, vol. 267, p. 108033, 2021. 2.2.4

[206] Y. Watanabe, "Ferroelectricity of stress-free and strained pure $SrTiO_3$ revealed by ab initio calculations with hybrid and density functionals," *Physical Review B*, vol. 99, no. 6, p. 064107, 2019. 3.1, 3.2.1, 3.2.1, 3.2.2

[207] R. Wahl, D. Vogtenhuber, and G. Kresse, "$SrTiO_3$ and BaTiO3 revisited using the projector augmented wave method: Performance of hybrid and semilocal functionals," *Physical Review B—Condensed Matter and Materials Physics*, vol. 78, no. 10, p. 104116, 2008. 3.2.1, 3.2.1, 3.2.2

[208] G. G. Guzmán-Verri, R. T. Brierley, and P. B. Littlewood, "Cooperative elastic fluctuations provide tuning of the metal–insulator transition," *Nature*, vol. 576, no. 7787, pp. 429–432, 2019. 4.1

[209] A. Liechtenstein, V. I. Anisimov, and J. Zaanen, "Density-functional theory and strong interactions: Orbital ordering in mott-hubbard insulators," *Physical Review B*, vol. 52, no. 8, p. R5467, 1995. 4.1, A.2

[210] M. Cococcioni and S. De Gironcoli, "Linear response approach to the calculation of the effective interaction parameters in the LDA+U method," *Physical Review B—Condensed Matter and Materials Physics*, vol. 71, no. 3, p. 035105, 2005. 4.1, A.2

[211] O. K. Orhan and D. D. O'Regan, "First-principles Hubbard U and Hund's J corrected approximate density functional theory predicts an accurate fundamental gap in rutile and anatase TiO_2," *Physical Review B*, vol. 101, no. 24, p. 245137, 2020. 4.1, A.2

[212] D. S. Lambert and D. D. O'Regan, "Use of DFT+$U + J$ with linear response parameters to predict non-magnetic oxide band gaps with hybrid-functional accuracy," *Physical Review Research*, vol. 5, no. 1, p. 013160, 2023. 4.1, A.2

[213] M. L. Medarde, "Structural, magnetic and electronic properties of perovskites (R = rare earth)," *Journal of Physics: Condensed Matter*, vol. 9, no. 8, p. 1679, 1997. 4.1

[214] V. Scagnoli, U. Staub, Y. Bodenthin, M. García-Fernández, A. M. Mulders, G. I. Meijer, and G. Hammerl, "Induced noncollinear magnetic order of Nd^{3+} in $NdNiO_3$ observed by resonant soft x-ray diffraction," *Phys. Rev. B*, vol. 77, p. 115138, Mar 2008. 4.1

[215] T. Arima, Y. Tokura, and J. B. Torrance, “Variation of optical gaps in perovskite-type $3d$ transition-metal oxides,” *Phys. Rev. B*, vol. 48, pp. 17006–17009, Dec 1993. 4.2.1, 4.2.1

[216] A. Hampel and C. Ederer, “Interplay between breathing mode distortion and magnetic order in rare-earth nickelates $R\mathrm{NiO}_3$ within $\mathrm{DFT}+U$,” *Phys. Rev. B*, vol. 96, p. 165130, Oct 2017. 4.2.1

[217] W. Hai-Ping, K. Deng, T. Wei, X. Chuan-Yun, H. Feng-Lan, and Q. Li, “The structural, electronic, and magnetic properties of SrFeO_n ($n = 2$ and 2.5): A GGA+U study,” *Chinese Physics B*, vol. 18, p. 5008, 11 2009. 4.2.2, 4.2.2

[218] A. Caviglia, S. Gariglio, N. Reyren, D. Jaccard, T. Schneider, M. Gabay, S. Thiel, G. Hammerl, J. Mannhart, and J.-M. Triscone, “Electric field control of the $\mathrm{LaAlO}_3/\mathrm{SrTiO}_3$ interface ground state,” *Nature*, vol. 456, no. 7222, pp. 624–627, 2008. 5.1

[219] T. Tybell, C. Ahn, and J.-M. Triscone, “Ferroelectricity in thin perovskite films,” *Applied physics letters*, vol. 75, no. 6, pp. 856–858, 1999. 5.1

[220] E. Stylianidis and P. Zubko, “SrTiO_3 - NdNiO_3 superlattices,” *(unpublished)*, 2025. 5.1, 5.2.3

[221] S. Hayward, F. D. Morrison, S. Redfern, E. Salje, J. Scott, K. Knight, S. Tarantino, A. Glazer, V. Shuvaeva, P. Daniel, *et al.*, “Transformation processes in LaAlO_3: Neutron diffraction, dielectric, thermal, optical, and Raman studies,” *Physical Review B—Condensed Matter and Materials Physics*, vol. 72, no. 5, p. 054110, 2005. 5.1, 6.2.5

[222] J. M. Rondinelli, S. J. May, and J. W. Freeland, “Control of octahedral connectivity in perovskite oxide heterostructures: An emerging route to multifunctional materials discovery,” *MRS bulletin*, vol. 37, no. 3, pp. 261–270, 2012. 5.2.1

[223] J. M. Rondinelli and N. A. Spaldin, “Substrate coherency driven octahedral rotations in perovskite oxide films,” *Physical Review B—Condensed Matter and Materials Physics*, vol. 82, no. 11, p. 113402, 2010. 5.2.1

[224] H. D. Cornean, D. Gontier, A. Levitt, and D. Monaco, “Localised Wannier functions in metallic systems,” in *Annales Henri Poincaré*, vol. 20, pp. 1367–1391, Springer, 2019. 5.2.2

[225] D. Vanderbilt and R. King-Smith, “Electric polarization as a bulk quantity and its relation to surface charge,” *Physical Review B*, vol. 48, no. 7, p. 4442, 1993. 6.1, 6.2.4

[226] N. Bristowe, P. Ghosez, P. B. Littlewood, and E. Artacho, “The origin of two-dimensional electron gases at oxide interfaces: insights from theory,” *Journal of Physics: Condensed Matter*, vol. 26, no. 14, p. 143201, 2014. 6.1

[227] K. S. Knight, “Structural and thermoelastic properties of $CaTiO_3$ perovskite between 7 K and 400 K,” *Journal of alloys and compounds*, vol. 509, no. 22, pp. 6337–6345, 2011. 6.2.1

[228] M. Moreau, A. Marthinsen, S. M. Selbach, and T. Tybell, “First-principles study of the effect of (111) strain on octahedral rotations and structural phases of $LaAlO_3$,” *Physical Review B*, vol. 95, no. 6, p. 064109, 2017. 6.2.5

[229] C. Kittel and P. McEuen, *Introduction to solid state physics.* John Wiley & Sons, 1976. A.1

[230] D. M. Ceperley and B. J. Alder, “Ground state of the electron gas by a stochastic method,” *Physical review letters*, vol. 45, no. 7, p. 566, 1980. A.1

[231] J. P. Perdew and A. Zunger, “Self-interaction correction to density-functional approximations for many-electron systems,” *Physical review B*, vol. 23, no. 10, p. 5048, 1981. A.1